Transactions of the ASME®

Transactions of the ASME, The Journal of Fluids Engineering (ISSN 0098-2202) is published quarterly (Mar., une, Sept., Dec.) for $95 per year by The American Society of Mechanical Engineers, 345 East 47th Street, New York, NY 10017. Second class postage paid at New York, NY and additional mailing offices. POSTMASTER: Send address changes to The Journal of Fluids Engineering, c/o THE AMERICAN SOCIETY OF MECHANICAL ENGINEERS, 22 Law Drive, Box 2300, Fairfield, NJ 07007-2300.
CHANGES OF ADDRESS must be received at Society headquarters seven weeks before they are to be effective. Please send old label and new address.
PRICES: To members, $27.00, annually: to nonmembers, $95. Add $12.00 for postage to countries outside the United States and Canada.
STATEMENT from By-Laws. The Society shall not be responsible for statements or opinions advanced in papers or . . . printed in its publications (B7.1, Par. 3),

INDEXED by Applied Mechanics Reviews and Engineering Information, Inc.

Journal of Fluids Engineering

Published Quarterly by The American Society of Mechanical Engineers

VOLUME 110 • NUMBER 3 • SEPTEMBER 1988

(Contents continued on page 230)

Contents (Continued)

Mohamed Gad-el-Hak
Professor of Aerospace and Mechanical Engineering, University of Notre Dame, Notre Dame, IN 46556
Mem. ASME

Visualization Techniques for Unsteady Flows: An Overview[1]

The purpose of this article is to review some of the novel flow visualization techniques that are particularly suited for studying unsteady flows. While many of these techniques are equally conducive for steady flow fields, the present paper will emphasize applications to time-dependent flows. Possible pitfalls in interpreting the visualization results are elaborated. The flow visualization methods presented include those that make use of scattered light from small particles or other foreign additives as well as those that make use of changes in the index of refraction.

1 Introduction

The understanding of unsteady flow phenomena is of great practical interest in the design of turbomachinery, fixed- or rotating-wing aircraft, missiles, ship propellers, and many other products. Because of the complexity of such flows, they represent a domain of fluid mechanics that is currently beyond the reach of definitive theoretical or numerical analysis, and progress to-date has depended crucially upon experiments. Flow visualization techniques offer a useful tool to establish an overall picture of the unsteady flow field and to delineate broadly its important salient features before embarking on more detailed quantitative measurements using, for example, fast-response velocity or pressure probes. In some instances, it may be impossible to extract useful results from probe measurements alone, and flow visualization can then offer an attractive alternative.

To quote Van Dyke (1982), "We who work in fluid mechanics are fortunate, as are our colleagues in a few other fields such as optics, that our subject is easily visualized." Some flows are, of course, more readily visualized than others. The time-dependent pressure field associated with an unsteady flow often makes it difficult to use classical dye or smoke injection visualization methods. Not only is it difficult to release the tracer uniformly into the flow due to the fluctuating pressure field, but also, as shown below, the observed pattern in an unsteady flow represents streaklines rather than pathlines or mean streamlines. Streaklines are not as well-adapted to the formation of mathematical models, and as a result the visual images are related, subjectively, to the physical modules under consideration (Kline, 1978).

Visualization of unsteady flows can be particularly confusing. While in a steady flow a streamline, a streakline, or a pathline all coincide, this is not the case for a time-dependent flow. To recall briefly, a pathline (or particle path) is the curve that a particular fluid particle traverses in the flow field as a function of time; streamlines are the curves tangential to the instantaneous direction of the flow velocity at all points in the flow field; and a streakline is the instantaneous locus of all fluid particles which have passed through a particular fixed point within the flow. Typically, a tracer is introduced into the flow field at a point or a line and, hence, the observed patterns are streaklines. At any instant, the visualization provides the time history of the tracer but not the local event, even in a frame frozen with the observed phenomenon.

Hama (1962) provided a convincing example of the possible pitfalls in interpreting flow visualization results in an unsteady flow field. He numerically generated the streamlines, pathlines, and streaklines for a shear layer flow perturbed by a traveling sinusoidal wave of neutral stability. The resulting pattern of streamlines changed dramatically when these lines were recorded with a moving "camera" or with a camera at rest in the laboratory frame. Moreover, when "dye" was injected near the critical layer (where the flow speed equals the wave speed), the streaklines had an appearance of amplification and rolling as if to indicate that the flow had developed into discrete vortices. In fact, there was no amplification of the neutrally stable wave and no discrete vortices existed anywhere in the flow. Hama asserted that the rolling-up of a streakline in an unsteady flow cannot constitute a positive identification of the presence of a discrete vortex. Away from the critical layer, the streaklines appeared to show an alternating amplification and damping with the wrong wavelength and wave velocity. Hama clearly showed that information due to pathlines as obtained by tracing marked particles are equally improper in regard to the wave motion. Apparent u and v fluctuations as determined by tracing a particle had no direct bearing on the velocity fluctuations at a point.

In turbulent flows, an additional problem arises due to the large Schmidt numbers involved with typical tracers introduced into the flow, such as dye or smoke. The marker boundary differs from vorticity boundary due to the rapid diffusivity of the tracer introduced upstream of an observation station. This combines with the time history effects to blur out the local events and to make it difficult to differentiate between coherent motion and incoherent turbulence in the flow field (Hussain, 1986).

Another difficulty associated with unsteady flows is the additional time scale imposed by the unsteadiness of the motion.

[1]Based on an invited plenary paper presented at the Fourth International Symposium on Flow Visualization, 26–29 August 1986, ENSTA, Paris, France (Gad-el-Hak, 1987a).

Contributed by the Fluids Engineering Division for publication in the JOURNAL OF FLUIDS ENGINEERS. Manuscript received by the Fluids Engineering Division December 29, 1986.

In any laboratory study, whether visualization techniques or fast-response probes are used, the accurate simulation of field conditions requires that the values of a number of dimensionless parameters attained in the field be matched in the laboratory. Those dimensionless parameters must express the geometric, kinematic, and dynamic similarities of the laboratory modeling with the field. It is generally not difficult to scale down (or up) all geometric objects and all velocities from the field case to the laboratory case, thus satisfying both geometric and kinematic similarities. Dynamic similarity means matching the ratios of a number of forces, such as buoyancy, inertia, viscous, and surface tension. Typical dimensionless ratios of these forces are the Reynolds number, Mach number, Froude (or Richardson) number, Rossby number, etc. Some of these numbers can be matched in most laboratory facilities, while others are more difficult to scale proportionally from the field to the laboratory. For example, in simulating the wake of an underwater vehicle moving in the ocean, the Froude number can be matched in a typical low-speed towing tank although the field Reynolds number is too high to match. However, for unbounded turbulent flows, it is often argued that, if the Reynolds number is high enough, then the large-scale features of the flow will be independent of the Reynolds number (Townsend, 1976). This conjecture must be supported by field or laboratory data for the particular problem under consideration. The unsteadiness of the flow field imposes an additional time scale that must be considered when attempting a laboratory simulation. In fact, unsteady effects often dominate other effects such as viscous, etc. In such cases, a nondimensional frequency would be a more important governing parameter than the Reynolds number.

The present article reviews some of the novel flow visualization techniques that are particularly suited for studying time-dependent flows. Most of these methods can also be used for steady flow fields, but the present paper will emphasize unsteady flow applications. The visualization methods reviewed here are classified into six groups. Section 2 discusses visualization techniques requiring the addition of small particles. Sections 3 and 4 list some of the visualization techniques that use dye and smoke, respectively. In Section 5, visualization methods that make use of index of refraction changes are reviewed, and in Section 6 chemical techniques are discussed. Finally, some flows that can be "naturally" visualized are described in Section 7.

2 Scattered Light From Particles

An important subdivision of flow visualization techniques are those that make use of light scattered by small particles. When foreign particles are added to a flowing fluid, the main concern is whether or not the motion of the particles closely approximates that of the fluid. In general, a tracer particle introduced into the flow deviates in direction and magnitude from the fluid velocity. This concern is, of course, more acute when the flow field is rapidly changing with time. The concentration of the particles and their size must also be so small that the fluid flow is not changed by the presence of the particles. Intuitively, the particle response to fluid velocity changes is faster for smaller particle densities and diameters. As a general rule of thumb, tracer particles should be at least one order of magnitude smaller than the fine structure of the flow under study. In this case, the difference between particle and fluid velocities can virtually be neglected and very reasonable experimental results can be obtained. More rigorous analytical treatments of the motion of a single spherical particle in a nonuniform viscous flow are based on the Bassett-Boussinesq-Oseen equation and can be found in the books by Merzkirch (1974) and Hinze (1975) and the more recent article by Maxey and Riley (1983).

The point in the flow at which the tracer particles are introduced, the rate of particles released to the flow, and the length of the exposure time all determine whether one visualizes streamlines, streaklines or particle paths (Merzkirch, 1974). The relative speed between the flow and the observation frame of reference must also be considered when interpreting flow visualization data. As metioned in Section 1, visualization of time-dependent flows is particularly problematic due to the fact that streaklines, streamlines, and particle paths do not coincide.

For the purpose of this article, we further subdivide the particle visualization techniques to those that use spherical particles and those that utilize disk-shaped particles, where the length scale in one direction is much smaller than that in the other two orthogonal directions. Examples of the use of both kinds of particles in unsteady flows follow.

2.1 Spherical Particles. Examples of spherical particles used for flow visualization are hydrogen bubbles or solid particles, in liquids, and helium bubbles or dust particles, in gases. Solid particles do not change shape during the motion with the fluid, while gaseous bubbles can change shape. Accordingly, the drag on gas bubbles is a function of both the velocity difference between the fluid and the tracer and the deforming forces acting on the particle. This greatly complicates the analysis of bubble motion in a fluid.

The hydrogen-bubbles method, first introduced by Geller (1954; 1955), utilizes very small hydrogen bubbles from a fine wire acting as the cathode of a dc circuit for electrolyzing an electrolytic aqueous solution. Typically, the voltage is supplied in the form of square-wave pulses with peak-to-peak amplitude between 10–100 volts and the size of the bubbles is on the order of one-half the wire diameter. As the diameter of the bubbles is decreased, the buoyancy force is reduced faster than the drag force due to the local liquid motion, and the bubbles follow the fluid.

McAlister and Carr (1978a; 1978b; 1979) used hydrogen bubbles in a water tunnel to study the phenomenon of dynamic stall on an oscillating airfoil. Bubbles were generated at electrodes placed at several chordwise locations along the upper surface of the airfoil, which primarily exposed the viscous domain, as well as from an upstream electrode, which primarily marked the inviscid flow. The sequence of photographs in Fig. 1 show both kinds of visualizations at different phases of the pitching cycle. The NACA 0012 airfoil underwent the large-amplitude harmonic motion $\alpha(t) = 10 \text{ deg} + 10 \text{ deg} \sin \omega t$, at a reduced frequency of 0.25 and a Reynolds number of 21,000. In the figure, the angle of attack changes from 12.1 to 19.7 deg.[2] The photographs vividly show the location of flow separation, the wake pattern, the shear-layer vortices, and the dynamic-stall vortex. McAlister and Carr's visualization experiments clearly demonstrated the basic difference between steady and unsteady separations. For a pitching airfoil, reverse flow starts near the trailing edge and propagates upstream along the surface as the angle of attack increases, without any sign of boundary layer detachment. Clearly, unsteady separation is not related to the point of zero skin friction or to the presence of reverse flow, two conditions always associated with steady separation on two-dimensional bodies (Gad-el-Hak, 1987b).

An example of the use of solid particles for unsteady flow visualizations is provided by the work of Maxworthy (1979), who used small, neutrally buoyant wax particles to observe the flow around a two-dimensional model that simulates the wing motion of a small wasp (Encarsia formosa). By taking streak photographs of the model placed in a large container filled with either water or glycerine and using a camera with a known exposure time, Maxworthy was able to measure the local fluid velocity and, hence, determine the time-dependent

[2] Unless otherwise stated, flow is from left to right in all figures in this paper.

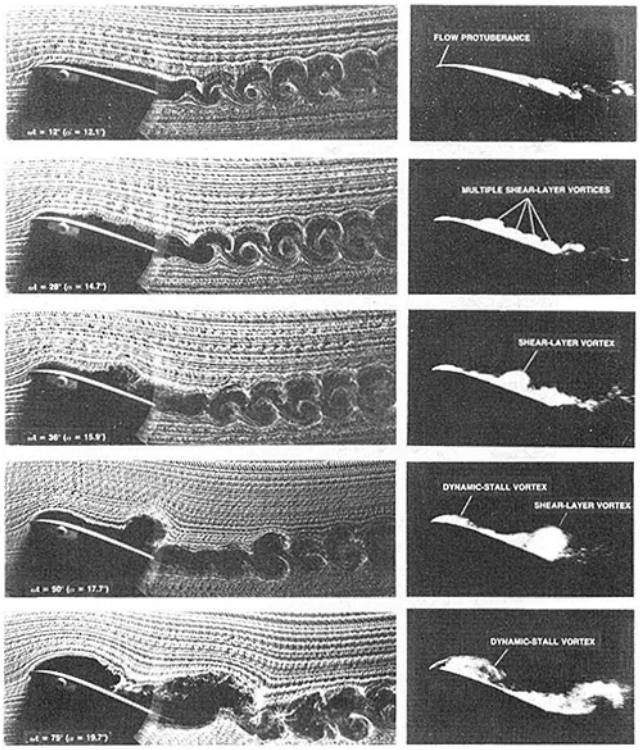

Fig. 1 Hydrogen-bubbles visualization of the critical stages of dynamic stall. $R_c = 21{,}000$; $K = 0.25$; $\alpha(t) = 10$ deg + 10 deg sin ωt (from McAlister and Carr, 1979). (a) Freestream electrode; (b) Model electrodes.

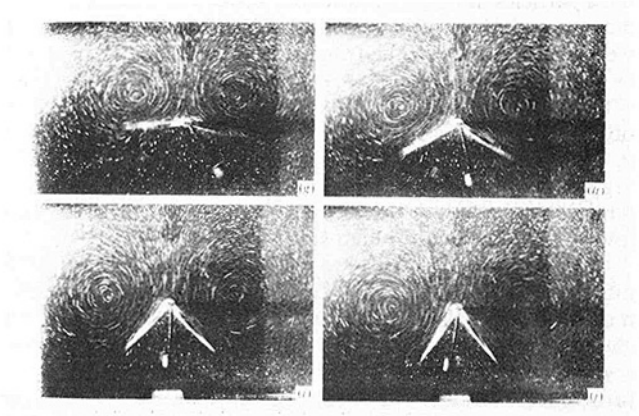

Fig. 2 Particle streak photographs of two-dimensional flow over rotating wings. $\bar{R}_\theta$ 13,000; time between photographs 0.5 s; camera exposure time 0.06 s (from Maxworthy, 1979).

circulation around the model at any instant. Figure 2 depicts a sequence of four photographs of the two-dimensional flow over the rotating wings at a mean Reynolds number of 13,000. The approximate time between photographs is 0.5 s and the camera exposure time is about 0.06 s. The dominant presence of the two separate vortices is apparent in the pictures. Maxworthy observed that the major part of the circulation created by the wing motion is contained within these vortices and that the circulation around the wing surface alone is of opposite sign to that of the vortex, being dominated by the vortex induced flow directed towards the wing tip on the upper surface. Maxworthy was able to account for the large lift forces generated by small wasps in hovering flight by use of the so-called "clap and fling" mechanism (Lighthill, 1973).

A similar flow visualization technique was used by Koromilas and Telionis (1980) to study the unsteady laminar separation over moving walls. A glycerol-water mixture was used to achieve low-Reynolds-number flow with a measurable magnitude of velocity, and neutrally buoyant surface pellets were used to capture the instantaneous two-dimensional flow field around downstream- or upstream-moving circular cylinders. Accurate quantitative information was provided by the visualization methods and was complemented by laser Doppler anemometer measurements. Koromilas and Telionis's experiments were able to capture, for the first time, the saddle-point-streamline pattern predicted earlier by the theoretical work of Moore (1958), Rott (1956), and Sears (1956). Koromilas and Telionis (1980) also used the same visualization technique to determine boundary-layer velocity profiles for transient and oscillatory ambient velocity fields. Their results reveal that unsteady laminar separation responds with time lag to external disturbances, in agreement with unsteady stall data (McAlister et al., 1978).

Helium-filled soap bubbles are ideal for visualizing airflow in wind tunnels because the particle size and buoyancy can be readily controlled. An interesting history of the method is provided in the article by Mueller (1983). Examples of the use of helium bubbles for visualizing complex, three-dimensional flows with unsteady velocity components are given in the paper by Santanam and Tietbohl (1985), who considered flow fields occurring in power generation equipment such as burners, furnaces, piping networks, pulverizers, and steam drums. Ambient air was blown through a scale model of a particular power generation setup, and 3-mm-diameter helium-filled soap bubbles were injected into the airflow. Santanam and Tietbohl determined the actual flow directions from observation of the flow pattern of the bubble streaks.

Using solid tracers, accurate quantitative data were deduced from observing the flow pattern in the two-dimensional wake induced by an impulsively started thin airfoil placed in an oil mixture (Monnet et al., 1985). The different velocity fields resulting from the experiments were used to improve the corresponding numerical simulations made by treating the Navier-Stokes equations with a high-order, compact finite difference scheme.

In recent years, the utility of particle-tracering visualization techniques has been considerably enhanced by the development of digital image processing systems, holography, and speckle photographic methods. These novel techniques allow effective and efficient means of obtaining quantitative information in complex flows. In fact, the extent to which any new flow visualization method can be used for quantitative analysis is probably its most important feature in future applications. The second edition of Merzkirch's (1987) book provides a useful overview of these novel methods.

2.2 Scattered Light from Disk-Shaped Particles. Disk-shaped particles, where the length scale in one direction is much smaller than that in the other two orthogonal directions, behave quite differently from other foreign materials, such as dye, smoke, or bubbles, added to a fluid for the purpose of visualizing its motion. A single photograph using the latter kind of tracers shows the cumulative results of all the various processes that have transported and concentrated or dispersed the tracer material, whether or not these processes are still active (Cantwell et al., 1978). On the other hand, disk-shaped particles are oriented in a systematic way by the three-dimensional rate-of-strain field in the fluid. Moreover, if these particles are small enough, they respond very rapidly to changes in the rate-of-strain field. Thus, information contained in a single picture is essentially information about the current state of the motion, providing dynamic visualization of the flow field. Examples of small reflective particles commonly used in flow visualization studies are aluminum flakes, titanium-dioxide-coated mica platelets, and fish flakes.

According to Savas (1985), the commonly quoted view that

disk-shaped particles align themselves along the axes of principal normal stresses in the flow field is unsubstantiated. Savas presented a rational analysis of the nature of flow visualization using such flakes. His analyses are based on the stochastic treatment of Jeffery's (1922) solution for the motion of ellipsoidal particles in a viscous fluid, where thin flakes tend to align with stream surfaces. Savas (1985) asserted that the probability density function of Euler angles that describe the orientations of the flakes is adequate to explain the observed light field in flow visualization experiments, provided that the initial conditions of the particle's equation of motion are treated as random variables. The flakes tend to align themselves with the stream surfaces, but their finite thickness causes rapid turnovers. Savas confirmed the predicted light fields using several examples.

In his milestone presentation in which he introduced the boundary-layer theory, Prandtl (1904) used very small flakes of mica to visualize the initial motion of water as set up by a plate moving from rest at right angles to itself. Prandtl discussed the time-dependent development of the shear layer that originated from the plate's edge. He stated that this shear layer may be regarded as a Helmholtz surface of discontinuity (vortex sheet) in the case of small viscosity (high Reynolds number). Vortical motions were particularly easy to see with these thin flakes because a great number of the particles had the same orientation.

Many other examples of the use of mica or aluminum flakes for both steady and unsteady flow visualizations can be seen in the books by Prandtl and Tietjens (1934), Batchelor (1967), and Van Dyke (1982). Weidman (1976) used aluminum flakes to visualize the spinup and spindown of a cylindrical cavity.

In order to visually study unsteady separation, Taneda (1977) used both aluminum powder and an electrolytic precipitation method to mark the instantaneous streamline and streakline patterns around several two-dimensional bodies of simple shape. His paper provided many clear photographs of the water flow patterns around circular cylinders, elliptic cylinders, flat plates, and flexible plates, all performing basic unsteady motions in an incompressible, viscous fluid. The time-dependent motions considered were impulsive start from rest, change of velocity, translatory oscillation, change of angle of incidence, uniform rotation, rotatory oscillation, and swimming motion. The streamline patterns, marked by the disk-shaped particles, revealed the velocity field, while the streaklines, marked by the colloidal cloud generated at the surface of the body by electrolysis of water, tagged the vortex sheets shed from the surface.[3] Taneda (1977) provided a pragmatic criterion for unsteady separation. He asserted that the separation point is the point at which the boundary layer is shed from the surface of the body and that it can be determined experimentally as the point at which the streakline separates from the surface (for a recent review of steady and unsteady separation, see Gad-el-Hak, 1987b). Taneda reiterated that although the streamline pattern changes according to the reference frame, the streaklines are invariant.

Turbulent spots developing in a laminar boundary layer were visualized by Cantwell et al. (1978) using aluminum flakes that were about 0.2 micron in thickness with their largest dimension ranging from 5 to 30 microns. An extremely dense suspension of aluminum powder was used to allow a striking visualization of the low-speed streaks in the lower part of the viscous sublayer. Wygnanski et al. (1979) conducted hot-wire measurements in the back of a turbulent spot and reported the existence of oblique wave packets trailing the spot. Cantwell et al. (1978) were not able to visualize these Tollmien-Schlichting waves using the aluminum flakes and argued that their Reynolds number may not have been high enough. However, Savas (1985) convincingly showed that the reflective-flake flow-visualization technique may be rather unsuitable for observing low-amplitude shear waves in a unidirectional high shear flow, and due caution must be exercised in interpreting the visualization results in such applications.

[3] This is only true, of course, near the body before the vorticity (or the tracer material) is appreciably diffused.

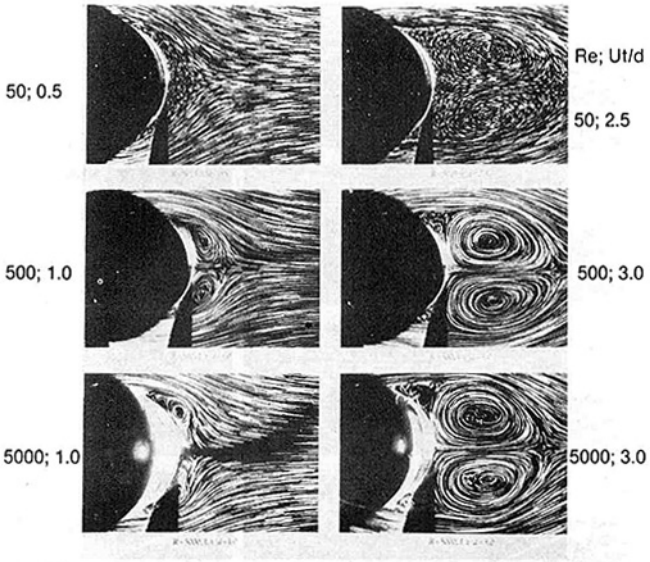

Fig. 3 Tracer particles visualization of an impulsively starting cylinder. Camera moves with the cylinder. Photographs by M. Coutanceau and R. Bouard.

Carlson et al. (1982) observed the evolution of turbulent spots in plane Poiseuille flow using titanium-dioxide-coated mica particles having a thickness of about 3 to 4 microns and a diameter of 10 to 12 microns. Strong oblique wave packets were observed at both the front of the arrowhead-shaped spot as well as trailing from the rear tips. Once again, Savas (1985) offered an explanation of why these wave packets were observed in the Poiseuille flow of Carlson et al. (1982) but not in the boundary layer flow of Cantwell et al. (1978). Savas argued that shallow angles, almost parallel to the flow, of illumination and observation are necessary to observe these low-amplitude waves in high shear flows.

Compared to classical dye or smoke visualization techniques, the method used by Carlson et al. (1982) provided a more dynamic visualization of the flow disturbances, including those that propagated through the fluid and formed regions of strong shear waves, vorticity, and breakdown to turbulence. Unlike turbulent spots growing in laminar boundary layers (Gad-el-Hak et al. 1981; Riley and Gad-el-Hak, 1985), the spots in Poiseuille flow were observed to undergo pronounced splitting. Carlson et al. offered a possible explanation for the lack of splitting in the case of a boundary layer.

Coutanceau and Bouard (see p. 36 of Van Dyke, 1982) used fine magnesium cuttings in an oil tank to visualize an impulsively starting circular cylinder. The six photographs in Fig. 3 are taken with a camera moving with the cylinder, of which only the lighted rear surface is seen. Three different Reynolds numbers, 50, 500 and 5000, are shown at different normalized times after the start of the motion, Ut/d, where U is the instantaneous velocity and d is the diameter of the cylinder.

The present author used titanium-dioxide-coated mica platelets to visualize the wall region of a fully-developed turbulent boundary layer. A water suspension of the microplatelets was made at a concentration of 2 percent by weight and was injected through a spanwise slot on the surface of a flat plate that was towed in a low-speed water tank. The left-to-right near-wall flow is shown in Fig. 4(*a*). A ciné film from

(a) Visualization using micro-platelets suspension.

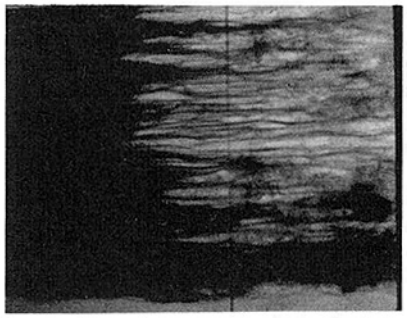

(b) Visualization using conventional food-coloring dye.

Fig. 4 Low-Speed streaks in a turbulent boundary layer. $R_\delta^* = 700$. Photographs by M. Gad-el-Hak.

which this photograph was taken clearly showed the low-speed streaks and the accompanying bursting events.

3 Dye Visualization Techniques

Another kind of foreign material that could be added to a liquid to render it visible is dye. In his famous experiment, Reynolds (1883) was the first to demonstrate the transition from laminar to turbulent flow by injecting a thin thread of liquid dye into a flow of water through a glass tube. Since then, numerous steady and unsteady flows have been visualized using different dye-injection methods, including the significant work at ONERA in France reviewed by Werlé (1973). Some of the more recent work is described in this section, classified according to the method of introducing the dye to the flow.

3.1 Classical Dye-Injection Methods. The dye is usually introduced to the flow from small holes or slots provided in the model under consideration or from a source external to the body, such as a small hypodermic needle. The disturbance to the main flow due to the ejecting device must be minimized. A wide variety of dyes is available, including different food-coloring dyes, ink, milk, and the more recently used fluorescent dyes. Illumination can be accomplished with banks of floodlights, for an overall view of the flow region, or sheets of laser light, most suited for the use with fluorescent dye where any particular plane within the flow field can be visualized, thus providing an extra degree of freedom in observing the flow patterns.

The present author used food-coloring dye to visualize the low-speed streaks and the bursting events in the near wall region of a low-Reynolds-number turbulent boundary layer. Figure 4 shows a comparison between conventional dye visualization (Fig. 4(*b*)) and that using reflective microplatelets (Fig. 4(*a*)). The displacement thickness Reynolds number for the two runs is about 700.

Pullin and Perry (1980) used household blue dye mixed with alcohol to visualize the growth of a two-dimensional starting flow vortex formed at a wedge-like sharp edge. The neutrally buoyant dye mixture was injected into the accelerating-decelerating water flow through several small holes at various points on the centerline of the wedge model. Pullin and Perry were able to mark the flow streaklines by carefully injecting the dye before the commencement of each run, when very slow residual motions existed in the water tank due to previous runs. They observed various secondary-flow details that result from the temporal primary vortex growth for different wedge angles and different values of the time exponent in the velocity-time power law describing the starting flow.

In the more complex flow of an oscillatory boundary layer, Ohashi and Hayashi (1985) visualized the resulting laminar-turbulent transition by placing a thin layer of powdered milk dissolved in water on the bottom of a U-shaped water channel. A piston stroke caused the water to undergo a sinusoidal movement, and the disturbance pattern at the milk-water interface indicated the generation, development, and decay of turbulence occurring during each cycle of the oscillatory motion. Ohashi and Hayashi observed primary and secondary instabilities as well as turbulent bursts similar to those seen in unidirectional-flow boundary layers.

Although fluorescent dyes have been available for a long time, the more recent availability of coherent light sources and the ability to generate thin sheets of laser light have made possible an extremely powerful visualization technique. A dilute solution of fluorescent dye is more or less transparent but becomes bright when excited with a light source of the appropriate wavelength. Thus, one can readily view a particular plane in the interior of the flow region. In conventional dye techniques, on the other hand, one can only see the outer boundaries or the "skin" of the flow region marked by the tracer.

The present author has used the laser/fluorescent dye technique to visualize the turbulent spots or turbulent wedges growing in a laminar boundary layer (Gad-el-Hak et al., 1981), the transition events in a decelerating boundary layer (Gad-el-Hak et al., 1984a), the discrete vortices shed from the leading edge of a delta wing in steady flight (Gad-el-Hak and Blackwelder, 1985; 1987a), the time-dependent flow around three-dimensional lifting surfaces undergoing pitching motions (Gad-el-Hak, 1987b; Gad-el-Hak and Ho, 1985; 1986a; 1986b), the natural and artificial bursting events in a turbulent boundary layer (Gad-el-Hak and Blackwelder, 1988; Gad-el-Hak and Hussain, 1986), and the large-eddy structures in a turbulent boundary layer (Gad-el-Hak and Blackwelder, 1987b). All the above experiments were conducted in a unique towing tank where the model's carriage rides on two tracks supported by an oil film (Gad-el-Hak, 1987c). Thin sheets of light were generated from a 5-Watt argon-ion laser beam using either a cylindrical lens or an oscillating mirror. Fluorescein, Rhodamine-B, and Rhodamine-6G dyes were used, which fluoresced green, dark red, and yellow, respectively, when excited by the green laser light. Under floodlights, the first two dyes fluoresced green and dark red while the Rhodamine-6G dye had a faint red color. The dye in these experiments was seeped into the flow through slots and holes machined into the different models. Dye was also released uniformly from a model by covering its entire surface with a thin, porous cloth saturated with dry dye crystals. As the body moved through the towing tank, the dye dissolved slowly into the surrounding water and marked the flow in the boundary layer and separation region (Gad-el-Hak and Ho, 1986b).

Two examples of the above visualizations are depicted in Fig. 5. A top view of a typical turbulent spot is shown in Fig. 5(*a*). The dynamics within the spot appear to be controlled by many individual eddies, similar to those within a fully developed turbulent boundary layer. Figure 5(*b*) shows the breakdown of a decelerating laminar boundary layer. A well-defined route to turbulence was identified by Gad-el-Hak et al. (1984a). First, the boundary layer became unstable to two-dimensional waves, which, due to the inflectional character of

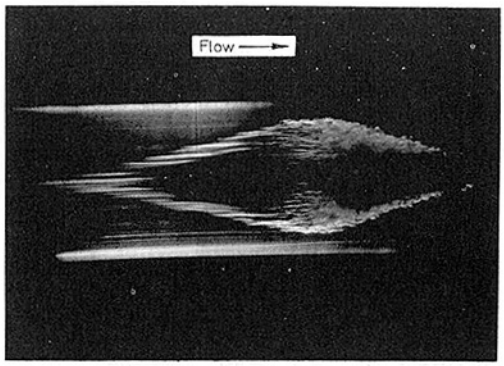

(a) Turbulent spot (from Gad-el-Hak et al., 1981).

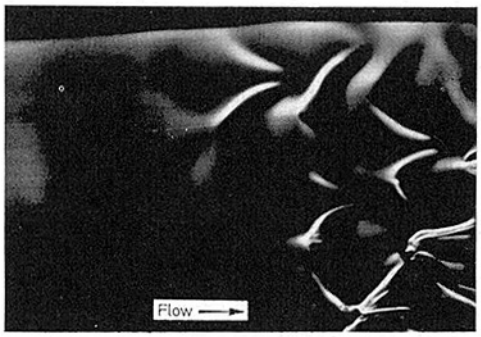

(b) Decelerating laminar boundary layer (from Gad-el-Hak et al., 1984a).

Fig. 5 Laser/fluorescent dye visualization.

the velocity profiles associated with the decelerating plate, have substantially larger growth rates than their Tollmien-Schlichting counterparts. Secondly, the two-dimensional waves were themselves unstable and developed a regular spanwise modulation. This in turn led to the formation of hairpin vortices (Fig. 5(*b*)) that lifted away from the wall, stretched and burst into turbulence.

A comparative analysis of the visualization techniques using floodlight/conventional dyes, laser/fluorescent dyes or disk-shaped particles was presented by Gad-el-Hak et al. (1985). It was shown that each method gives a unique and complementary view of a given flow field. The conventional dye provides a spatially integrated view of the observed flow structure. Thus, details of the internal flow field are difficult to obtain. By using sheets of laser light, the fluorescent dye enables the investigator to obtain the anatomy of a flow structure. As mentioned before, however, both the conventional and fluorescent dyes show the cumulative result, or the integrated history, of all the various processes that they experience from the time of their release into the flow. The disk-shaped particles, on the other hand, align themselves along the axes of principal normal stresses imposed upon them by the flow; thus, giving a more instantaneous view of the stress within the flow field.

3.2 The Dye-Layer Technique. The time-dependent pressure field associated with an unsteady flow often makes it difficult to use classical dye or smoke injection visualization methods. Not only is it difficult to release the tracer uniformly into the flow due to the fluctuating pressure field, but also the observed patterns are difficult to interpret. The dye-layer technique, described by Gad-el-Hak (1986a) overcomes some of these difficulties. This visualization method can be used in a water towing tank facility. In brief, cotton strings with a diameter of 1 mm are stretched horizontally on a rake and painted with a concentrated solution of alternating-color fluorescent dye and alcohol. The alcohol is allowed to evaporate, leaving the strings saturated with dye crystals. The rake is then placed in the water channel, which has a weak, stable stratification, and towed at a relatively low speed (1 cm/s) so that the wakes behind the strings are laminar. As the dye is washed away from the strings, it forms several thin horizontal sheets. These alternating-color layers of dye remain thin, about 1 mm in thickness, due to the inhibition of vertical motion caused by the saline stratification in the tank. The density gradient in the tank is about 10^{-4} gm/cm^4, which yields a Brunt-Väisälä frequency (Turner, 1973) of $N = 0.05$ Hz. This provides a time scale for gravity-driven motion that is far longer than a typical time scale in the flow under consideration; hence the stratification should have negligible effect on the dynamics of the flow. This conclusion was verified experimentally by Gad-el-Hak (1986a) who used conventional dye injection methods to conduct two similar runs in the presence and in the absence of stratification in the towing tank. The visualization patterns in the two runs were indistinguishable.

The dye-layer technique has been particularly useful in investigating the complex, time-dependent flow fields around three-dimensional lifting surfaces undergoing large-amplitude pitching harmonic oscillations (Gad-el-Hak and Ho, 1985; 1986a; 1986b). Sheets of laser light were projected in the desired plane to excite the fluorescent dye layers. The alternating horizontal sheets of different color dyes remained quiescent until disturbed by the moving lifting surface. Each dye layer was in a sense a fluid material surface whose evolution in time was visually recorded. Unlike conventional dye injection techniques, the dye layers marked the flow in the separation region, the flow in the wake region, and the potential flow away from the surface. This was particularly useful for observing the irrotational motion induced by the leading and trailing edge vortices associated with changing the angle of attack of the lifting surface.

Figure 6 shows dye-layer visualization of small-aspect-ratio, sharp-leading-edge rectangular wing undergoing the large amplitude pitching motion $\alpha(t) = 15 \text{ deg} + 15 \text{ deg} \sin(2\pi ft)$ at three reduced frequencies, $K = 0.2$, 1.0 and 3.0. All three pictures were taken during the upstroke at an angle of attack of 20 deg. Figure 7 is a sequence of photographs depicting the complete pitching cycle for the same wing at a reduced frequency of 3.0 and a chord Reynolds number of 8.63×10^3.

Along the same lines, the complex flow around a model of a rotating-wing aircraft was visualized using the same dye-layer method (Jenks et al. 1987). A 1:40 scale model of an H-34 helicopter rotor was towed in the author's towing tank facility and the collective pitch angle, the advance ratio, and the longitudinal and lateral cyclings were adjusted independently over normal field operating conditions. Under certain run parameters, a negative loading was present near the tip of the advancing blade and a pair of counter-rotating vortices was shed from that tip. For the first time, the interaction of these vortices with the succeeding blade, believed to be a major source of helicopter noise and vibration, was observed directly in these experiments. It is obvious that classical dye-injection techniques would be extremely difficult to implement for such a model where the blades are simultaneously moving forward, rotating, and undergoing cyclical pitching.

4 Visualization Techniques Using Smoke

Smoke is used to visualize gaseous flows much the same as dye is used in liquid flows. Unlike dye, however, "smoke" is commonly a very concentrated field of extemely small particles. These particles, usually less than 1 micron in diameter, are large enough to scatter a sufficient amount of light for observation but too small to be seen individually under normal circumstances. Smoke or smoke-like materials, such as

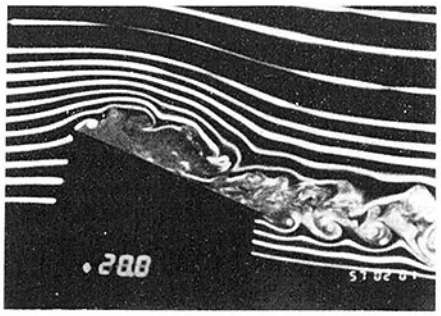

a. Reduced Frequency = 0.2

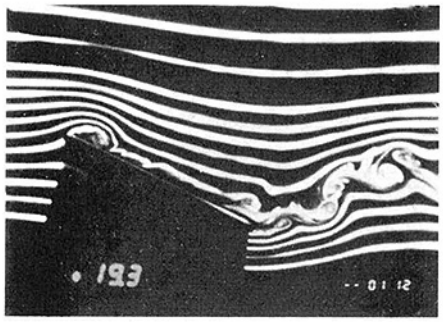

b. Reduced Frequency = 1.0

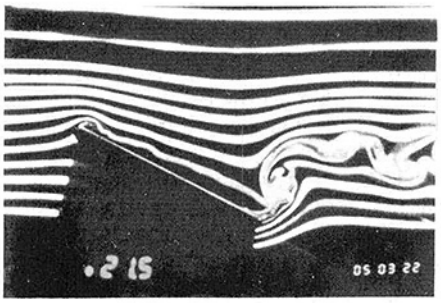

c. Reduced Frequency = 3.0

Fig. 6 Dye-Layer technique used to visualize a pitching lifting surface. $R_c = 1.25 \times 10^4$; AR = 4; $\alpha(t) = 15$ deg + 15 deg sin ωt (from Gad-el-Hak, 1986a).

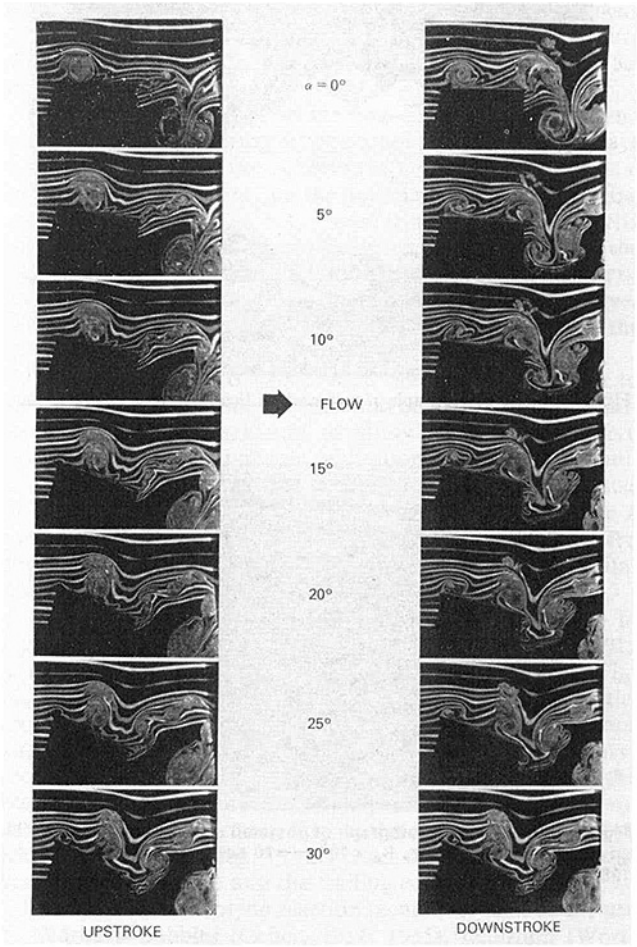

Fig. 7 A complete pitching cycle of a low-aspect-ratio rectangular wing. $R_c = 8.63 \times 10^3$; AR = 4; $K = 3.0$, $\alpha(t) = 15$ deg + 15 deg sin ωt (from Gad-el-Hak and Ho, 1986a).

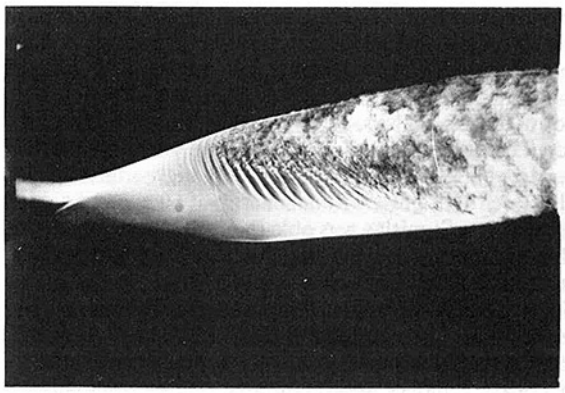

Fig. 8 Smoke photograph of a spinning body of revolution. $R_L = 3.2 \times 10^5$; $V/U_\infty = 1.0$; $\alpha = -10$ deg (from Mueller et al., 1981b).

vapors, fumes, and mists, can be introduced to the flow from slots and holes machined into the model or from an external source such as a smoke tube or smoke wire. The first use of smoke visualization in a scientific experiment was reported by Mach (1896). The development and refinement of the so-called smoke tunnel are due largely to the work of Brown (1953) at the University of Notre Dame. An interesting history of the early development of smoke visualization facilities is given by Mueller (1980).

Transition events in the boundary layer on spinning and nonspinning axisymmetric bodies were observed using a single smoke filament issuing from an upstream tube (Kegelman and Mueller, 1986; Kegelman et al., 1979; 1980; Mueller et al., 1981a; 1981b; 1985). The spectacular flow visualization photographs that were produced showed clearly the formation of two-dimensional Tollmein-Schlichting waves in the nonspinning case and the subsequent breakdown of these waves into vortex trusses. For the spinning body, vortices originated in the crossflow and spiraled around the body. These crossflow vortices eventually broke down into turbulence, but did so in a distinctly different manner than axisymmetric waves. For certain run parameters, both two-dimensional waves and crossflow vortices appeared on the spinning axisymmetric body. A typical example of the spinning case is shown in Fig. 8. The axisymmetric model is at a negative angle of attack of 10 deg and the flow is from left to right. The Reynolds number based on the body length is 3.2×10^5 and the spin rate is 1500 rpm (ratio of peripheral velocity to freestream = 1.0).

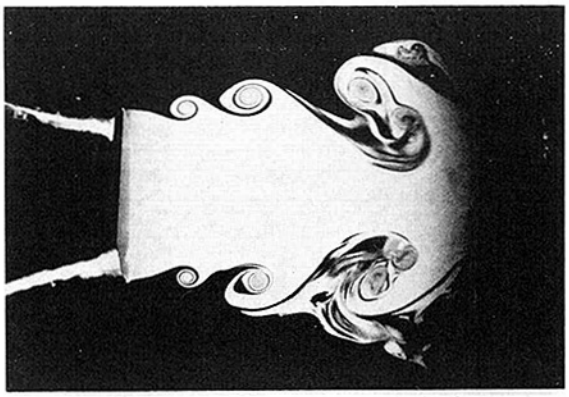

Fig. 9 Smoke photograph of a forced jet (from Ng and Bradley, 1988).

Fig. 10 Smoke wire photograph of poststall separation on an airfoil in an oscillating freestream. $R_c = 10^5$; $\alpha = 20$ deg; $K = 0.64$ (from Brendel, 1986).

Kerosene vapor was also used to study the effects of acoustically forcing an axisymmetric jet with low-level disturbances containing more than one frequency component (Bradley and Ng, 1988; Ng and Bradley 1988). Figure 9 shows a side view of the jet illluminated with a vertical sheet of argon-ion laser light. The response of the shear layer to the artificial forcing depends on the frequency content, the amplitude, and the relative phase angles and amplitudes among the different frequency components.

For high-speed flows, Stanislas (1985) used a sheet of light generated from a pulsed ruby laser to visualize the smoke-generated patterns of an air intake at high angles of attack. With a laser light pulse with an energy of 60 mJ and a duration of 15 to 20 ns, Stanislas was able to more or less freeze the turbulent motion and obtain ultrahigh-speed pictures of an incompressible, high-Reynolds-number flow.

To produce small but discrete smoke streaklines, the smoke-wire technique was developed by Raspet and Moore in the early 1950's (see Cornish, 1964) and subsequently refined by Cornish (1964), Sanders and Thompson (1966), Yamada (1973; 1979), Corke et al. (1977), Nagib et al. (1978), and Nagib (1979). In this technique, a 0.1-mm-diameter wire is uniformly coated with minute droplets of lubricating or mineral oil that is vaporized by the use of resistive heating, resulting in sheets of discrete streaklines. The Reynolds number based on the wire diameter must be small, less than 50, which limit application of the technique to low-speed wind tunnels (less than 8 m/s). A synchronization circuit controls the duration of the time the wire is supplied with the heating current and triggers a camera and accompanied lighting after an adjustable delay. Several techniques are available to coat the smoke wire with oil, including a pressurized gravity-feed method (Corke et al., 1977) and a "windshield-wiper" device (Nagib, 1979). Nagib et al. (1978) reported several applications of the smoke-wire technique, including studying flows near building models in simulated atmospheric boundary layers, investigating wakes of bluff bodies, examining transitional and turbulent boundary layers, and recording shear layer instabilities.

A variety of unsteady separated flows was studied by Adler et al. (1985) using synchronized flow visualization techniques. They used both a smoke rake and a smoke wire to deliver dense, stable, and reproducible smokelines capable of providing a highly reliable base for measurement and comparison of flow disturbances. Single and multiple phase-locked stroboscopic pictures were taken of the vortical flow field induced by an airfoil oscillating at high reduced frequencies and high angles of attack. The visualization approach used by Adler et al. permitted rapid assessment of the spatial and temporal dependence and the three-dimensionality of an unsteady flow across a wide range of variables.

Chambers and Thomas (1983) used the smoke-wire technique to study the initial formation and growth of turbulent spots. They were the first to visually observe the oblique waves trailing the spot. Recall from Section 2.2 that Wygnanski et al. (1979) detected these waves using a hot-wire probe, while Cantwell et al. (1978) were not able to visualize the oblique waves using aluminum flakes.

Brendel (1986) used a vertical smoke wire to visualize poststall separation on a Wortmann FX63-137 airfoil at a Reynolds number of 100,000 subjected to an oscillating freestream. Figure 10 depicts the airfoil at a constant angle of attack of 20 deg. The freestream oscillated sinusoidally at a frequency of 11 Hz (reduced frequency = 0.64) and a maximum amplitude of 4 percent of the mean speed. Brendel's results illustrated the dynamic character of a laminar separation bubble subjected to a low amplitude oscillation in the Reynolds number.

5 Optical Techniques

Visualization techniques that make use of variations in the refractive index within a flow field are considered under this topic. These include the shadowgraph technique, schlieren method, interferometry, flow birefringence, and the more recently available holographic techniques (Lauterborn and Vogel, 1984). The optical index of refraction of a fluid is a function of its density, so any of the above techniques can be used where there are sufficient spatial and/or temporal density changes in the flow field. This is the case in high-speed gaseous flows or in liquids with salinity or temperature stratification. Mueller (1985) reviewed the role of optical visualization techniques in providing the necessary insight for the development of theoretical models of complex afterbody and base flows.

A unique flow visualization technique, particularly suited for low-speed unsteady flows, was described by Pierce (1961). He investigated the shedding of vorticity from the edges of a plate that was accelerated normal to itself from rest in still air. At the relatively low speeds used in Pierce's experiments, an ordinary shadowgraph technique cannot be used directly because of insufficient density changes in the flow field. However, artificially introduced density changes in the flow allowed the use of a spark-lighted shadowgraph system to show the details of the vortex sheet. Density changes were caused either by heating a column of air just outboard of the edge of the plate or by coating the upper and lower surfaces of the plate with benzene. Using the former method, the plate acceleration caused hot air to be drawn behind its lee side and to be on the inner side of the resulting vortex sheet, yielding very clear pictures of the surface of discontinuity. In the second method, the vaporization of the benzene was increased due to the air flowing over the surface and, because of the difference in density between the vapor and the air, the paths of their boundaries were clearly seen in a shadowgraph picture.

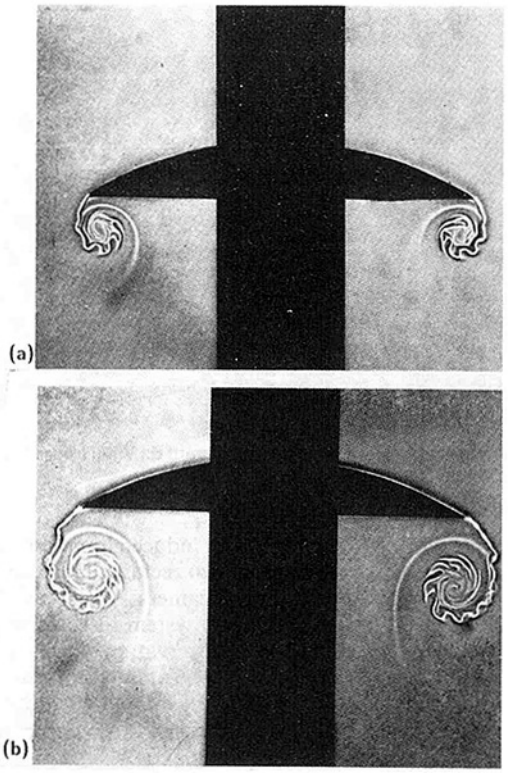

Fig. 11 Shadowgraphs of an accelerating plate with a sharp edge (from Pierce, 1961). (*a*) $t = 7$ ms; $U_\infty = 3.7$ m/s; (*b*) $t = 11$ ms; $U_\infty = 3.7$ m/s.

This is shown in Figure 11 at two different times after the stopping of the plate. The resulting photographs show small-scale undulations and the formation of a number of centers of vorticity along the well-known large-scale vortex sheet that roll up along the edges of the plate (Prandtl, 1904).

As mentioned before, visualization techniques that make use of variations in the index of refraction within a flow field can also be used in liquid flows. Several examples of visualization methods used in a stratified water channel can be found in the article by Lin and Pao (1979). Both shadowgraph and dye visualization were used to study turbulence decay, wake collapse, and horizontal vortices in a stratified medium. These techniques can be used for both steady and time-dependent flows.

Holographic high-speed interferometry was used by Eisfeld (1985) to observe large fields of fast-changing flows and the propagation of highly turbulent flames. A rotating-mirror camera with an external electro-optical shutter was specifically developed to yield the very short exposure time, the very high framing rate, and the high optical resolutions required for recording the events inside a model of an internal combustion engine.

6 Chemical Techniques

Flow visualization techniques that utilize a chemical process include the hydrogen-bubbles method described in Section 2.1 (chemical/electrolytic reaction), the titanium tetrachloride technique (chemical reaction), the tellurium method (ionization/electrolytic reaction), thymol blue dye (electrolytic reaction), and several chemical excitation techniques such as flash photolysis, spark tracing, luminescence, and fluorescence (described in Section 3.1).

The use of titanium tetrachloride for visualizing air flow was first reported by Simmons and Dewey (1931). This colorless liquid with a pungent acid smell reacts with the moisture in the air to produce a dense, white fume (smoke). This technique has been used for visualizing unsteady flows by Taneda (1977) and more recently by Freymuth and his colleagues (Freymuth, 1985; Freymuth et al., 1985a; 1985b; 1985c; 1985d).

Taneda (1977) investigated the time-dependent flow around a flexible body performing a large-amplitude progressive wave motion. He observed the behavior of a thin layer of titanium tetrachloride introduced into the boundary layer at the leading edge of a waving rubber sheet placed in a wind tunnel. Taneda concluded that, when the wave velocity is smaller than the freestream velocity, the boundary separates at the back side of the first wave crest. On the other hand, the boundary layer never separates when the wave velocity is larger than the freestream velocity.

Freymuth and his colleagues used titanium tetrachloride to visualize the accelerating flow around an airfoil placed at different angles of attack and to study the vortical pattern development during dynamic separation. Their results, summarized in the review article by Freymuth (1985), emphasize the unity of the field of dynamic separation and include a useful descriptive vocabulary for different vortex pattern developments, such as vortex aggregation, crowding, elicitation, nipping, pairing, shedding, and splitting.

Two examples of Freymuth's visualization are shown in Figs. 12 and 13. The accelerating flow around an NACA 0015 airfoil at $\alpha = 30$ deg is depicted in the three photographs in Fig. 12. The flow starts from rest and uniformly accelerates at the rate of 2.4 m/s^2. The Reynolds number based on the chord and acceleration ($\mathrm{Re} \equiv a^{1/2} c^{3/2} / \nu$) was 5.2×10^3. Primary, secondary and tertiary separation vortices appear near the leading edge of the airfoil as time proceeds. Figure 13 compares the same accelerating flow at the two extreme angles of attack of 80 and 90 deg. In this case, separation occurs near both the leading edge and the trailing edge of the airfoil.

Examples of electrolytic reaction techniques include the use of hydrogen bubbles (Geller, 1954; 1955), tellurium (Wortmann, 1953), and thymol blue dye (Baker, 1966). In all three methods, two electrodes are introduced into an aqueous solution, the negative electrode (cathode) being usually a thin straight wire placed perpendicular to the mean flow direction. A dc voltage is then applied continuously or intermittently to effect the electrolytic reaction. In the hydrogen bubbles method, the water molecules are electrolyzed into hydrogen bubbles at the cathode and oxygen at the anode. In the tellurium method, the thin wire cathode is made of, or coated with, tellurium that is ionized with the application of an external voltage. With oxygen present in the surrounding fluid, the tellurium ions are brought into a state of colloidal suspension that appears in the form of a black dye. The thymol blue method relies on the change of color of the aqueous solution of thymol blue dye when voltage is applied, causing the fluid to become acidic near the anode and basic near the cathode. Since thymol blue is orange-yellow in an acidic environment and turns to blue if the solution becomes alkaline, a small cylinder of dark blue solution is formed around the cathode every time a voltage is applied between the electrodes.

Unlike the three visualization methods described above, the flash photolysis technique does not require the presence of a cathode wire in the flow. Introduced by Popovich and Hummel (1967), the technique utilizes a photoactive solution and a suitable light source. Examples of photoactive solutions include pyridine dissolved in ethyl alcohol and nitrospyran dissolved in kerosene. A pulsed ruby laser can be used to initiate photochemical dye production along the whole path of the laser beam through the fluid. The main drawback of this technique is the unusual working fluids that must be used.

Other chemical excitation techniques include the luminescence method used by Nakatani and Yamada (1985) for measuring the instantaneous velocity distribution in a nonstationary flow of glycerine aqueous solution containing

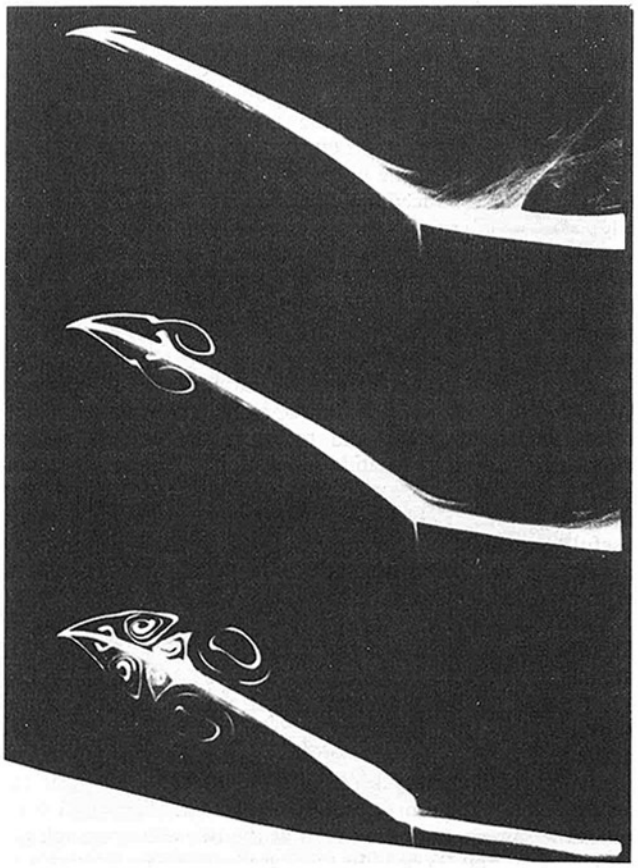

Fig. 12 Titanium tetrachloride visualization of an accelerating flow around an airfoil. $Re = 5.2 \times 10^3$; $\alpha = 30$ deg; acceleration = 2.4 m/s^2 (from Freymuth, 1985).

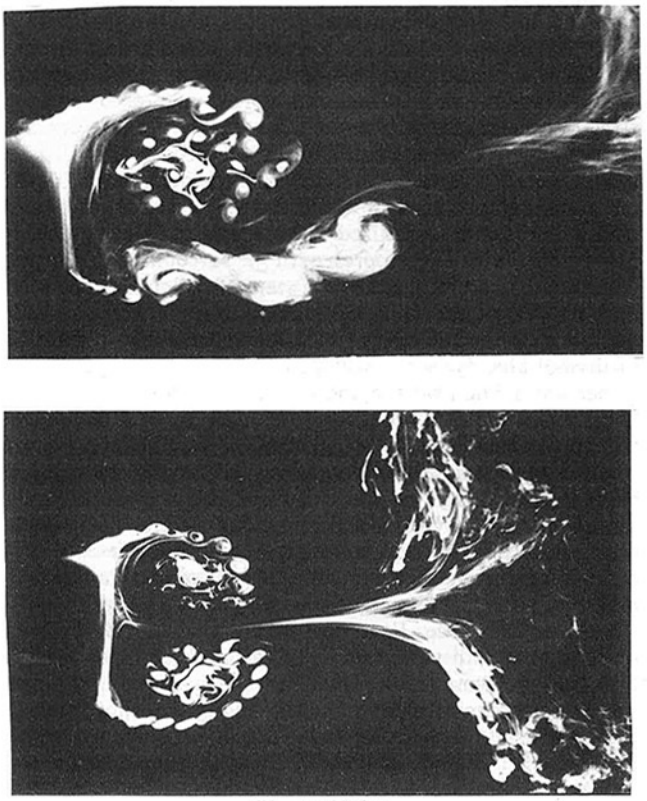

(*b*) $\alpha = 90$ deg.

Fig. 13 Titanium tetrachloride visualization of an accelerating flow around an airfoil at very high incidence. $Re = 5.2 \times 10^3$; acceleration = 2.4 m/s^2 (from Freymuth, 1985).

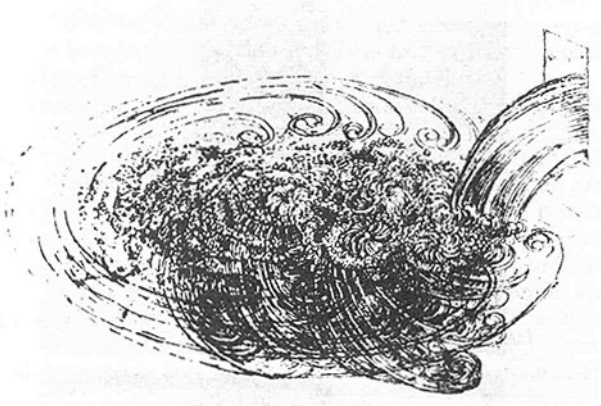

Fig. 14 Vortical flow as depicted by Leonard da Vinci (reproduced from Cornish, 1982).

zinc sulfide particles. A pulsed laser induced luminescence patterns in the turbulent flow inside two rectangular tubes of different aspect ratios. A video camera with night-vision capability was used together with a system of rotating prisms to record those patterns at high observation rates. From the visualization results, Nakatani and Yamada concluded that the dimensionless spanwise spacing of the longitudinal vortices in the boundary layer increases by about 260 percent as the tube aspect ratio increases from 1 to 4.

7 Naturally Visualized Flows

Some flows can be visualized naturally because of the presence of foreign additives that have not been added by the experimentalist, the existence of a liquid-gas interface, or some other occurrences that result in sufficient contrast to render the flow pattern visible. Leonardo da Vinci sketched and wrote about such a flow around 1509. He observed the formation of bubbles and eddies as a free waterjet issues from a square hole into a pool and drew the sketch reproduced in Fig. 14. Da Vinci wrote (translated): "So moving water strives to maintain the course pursuant to the power which occasions it and, if it finds an obstacle in its path, completes the span of the course it has commenced by a circular and revolving movement." This is perhaps the earliest reference to the importance of vortices in fluid motion.

A look at the sea on a windy day, the clouds, water from a faucet, smoke from a chimney, or even a lighted cigarette provides many examples of "naturally" visualized natural and man-made flows. The lecture by Cornish (1982) contains colored photographs of an ocean whirlpool, a hurricane, a tornado, a swirling spiral galaxy, satellite picture of the vortex wake behind an island, the explosion of an atomic bomb, and vortical clouds on the surface of Jupiter. It is, of course, impossible to seed, artificially, any of these large-scale flows. We who work in fluid mechanics are indeed fortunate that our subject is, sometimes, naturally visualized!

High-speed liquid jets issuing in air can also be directly observed because of the sudden change of the index of refraction at the air-water interface. For example, Hoyt and Taylor (1977a; 1977b) visualized the instabilities occurring in high-Reynolds-number waterjets discharging into stagnant air using a specially designed high-speed camera and lighting to furnish maximum detail. These instabilities include the axisymmetric mode accompanying the transition from laminar to turbulent flow, spray formation as a culmination of axisymmetric disturbances, and, further downstream, helical disturbances that result in the entire jet assuming a helical form. The final disruption of the jet is due to amplification of the helical waves. In the example shown in Fig. 15, a water jet is discharged into surrounding air that moves at 8, 40, and 80 percent of

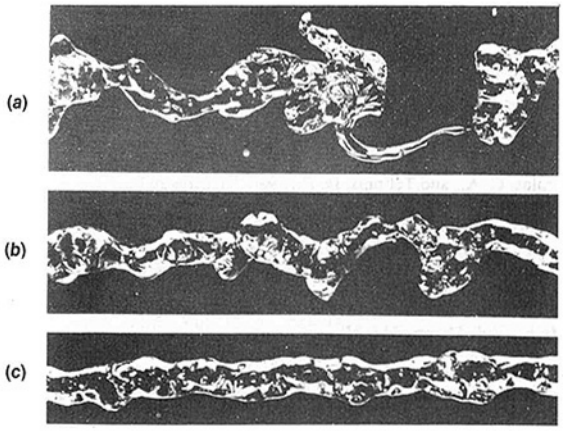

Fig. 15 High-speed water jet in a coaxial air stream. The jet is emerging from the axisymmetric nozzle at 27 m/s; nozzle diameter = 3 mm; distance from nozzle = 760 mm (from Hoyt and Taylor, 1977b). (a) Air speed = 2 m/s; (b)Air speed = 11 m/s; (c) Air speed = 22 m/s.

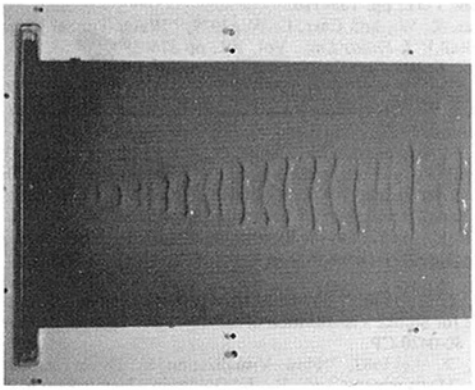

(a) Turbulent wedge embedded in a laminar boundary layer.

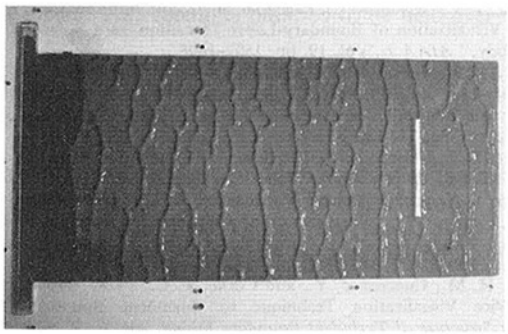

(b) Fully-developed turbulent boundary layer.

Fig. 16 Flow-induced waves on a compliant surface (from Gad-el-Hak et al., 1984b).

the jet speed as it merges from the nozzle. All three pictures are taken 238 diameters downstream. It is clear that helical instabilities are suppressed as the relative speed between the jet and the surrounding fluid is reduced. Hoyt and Taylor (1977b) concluded that the amplification of helical disturbances is due in part to aerodynamic form drag, which decreases as the relative speed diminishes.

Unstable waves forming on the surface of an elastic or a viscoelastic (compliant) material due to the pressure fluctuations in a turbulent boundary layer have been directly observed by many investigators including Hansen and Hunston (1983), Hansen et al. (1980), Gad-el-Hak et al. (1984b), Gad-el-Hak (1986b; 1986c; 1987d), and Riley et al. (1988). The static-divergence waves forming on a viscoelastic surface were more readily visualized due to their sharp crests and broad, shallow valleys. Typical examples of these waves on a soft PVC plastisol are shown in Fig. 16. In the first picture, a localized turbulent wedge is created in a laminar boundary layer by placing a single roughness element on the surface of a flat plate towed at low speed in a water channel. The static-divergence waves appeared only under the turbulent wedge. In a fully-developed turbulent boundary layer, the waves appeared everywhere as shown in Fig. 16(*b*).

8 Concluding Remarks

Many flow visualization techniques that were developed for observing time-independent flows can be readily adopted for unsteady flows. The examples given in this paper include methods that require the addition of foreign materials, optical techniques, chemical methods, and "naturally" visualized flows. Possible pitfalls in interpreting the visualization results from unsteady flow experiments were elaborated in this article.

The present review is by no means exhaustive, and many more visualization methods not mentioned here can be used in both steady and unsteady flows. A look at the number of papers presented during the past four International Symposiums on Flow Visualization (Tokyo, 1977; Bochum, 1980; Ann Arbor, 1983; and Paris, 1986) is enough to convince the reader of the fecundity of flow visualization researchers.

Acknowledgments

The writing of this article, together with the research of the author for the past five years, has been supported by the National Science Foundation Grant ISI-8560825, the Air Force Office of Scientific Research Contract F49620-85-C-0131, the Office of Naval Research Contract N00014-81-C-0453, and the National Aeronautics and Space Administration-Langley Research Center Contracts NAS1-17951, NAS1-18292 and NAS1-18213.

References

Adler, J. N., Robinson, M. C., Luttges, M. W., and Kennedy, D. A., 1985, "Visualizing Unsteady Separated Flows," *Flow Visualization III*, ed. W. J. Yang, Hemisphere, Washington, D. C., pp. 342–347.

Baker, D. J., 1966, "A Technique for the Precise Measurement of Small Fluid Velocities," *J. Fluid Mech.*, Vol. 26, pp. 573–575.

Batchelor, G. K., 1967, *An Introduction to Fluid Dynamics*, Cambridge University Press, London.

Bradley, T. A., and Ng, T. T., 1988, "Phase-Locking in a Jet Forced with Two Frequencies," *Exp. Fluids*, in press.

Brendel, M., 1986, "Experimental Study of the Boundary Layer on a Low Reynolds Number Airfoil in Steady and Unsteady Flow," Ph.D. thesis, University of Notre Dame, Notre Dame, IN.

Brown, F. N. M., 1953, "A Photographic Technique for the Mensuration and Evaluation of Aerodynamic Patterns," *Photog. Eng.*, Vol. 4, pp. 146–156.

Cantwell, B., Coles, D., and Dimotakis, P., 1978, "Structure and Entrainment in the Plane of Symmetry of a Turbulent Spot," *J. Fluid Mech.*, Vol. 87, pp. 641–672.

Carlson, D. R., Widnall, S. E., and Peeters, M. F., 1982, "A Flow Visualization Study of Transition in Plane Poiseuille Flow," *J. Fluid Mech.*, Vol. 121, pp. 487–505.

Chambers, F. W., and Thomas, A. S. W., 1983, "Turbulent Spots, Wave Packets, and Growth," *Phys. Fluids*, Vol. 26, pp. 1160–1162.

Corke, T., Koga, D., Drubka, R., and Nagib, H., 1977, "A New Technique for Introducing Controlled Sheets of Smoke Steaklines in Wind Tunnels," *Proc. Int. Cong. on Instrum. in Arosp. Simulation Facilities*, IEEE Publ. 77 CH1251-8 AES, New York, pp. 74–80.

Cornish, J. J., 1964, "A Device for the Direct Measurements of Unsteady Air Flows and Some Characteristics of Boundary Layer Transition," Mississippi State University, State College, Aerophysics Res. Note 24.

Cornish, J. J., III, 1982, *Vortex Flows*, Lockheed-Georgia Company, Marietta, GA.

Eisfeld, F., 1985, "The Investigation of Fast Changing Flows Using the High Speed Interferometry," *Flow Visualization III*, ed. W. J. Yang, Hemisphere, Washington, D. C., pp. 150–154.

Freymuth, P., 1985, "The Vortex Pattern of Dynamic Separation: A

Parametric and Comparative Study," *Prog. Aerospace Sci.*, Vol. 22, pp. 161–208.

Freymuth, P., Bank, W., and Palmer, M., 1985a, "Further Experimental Evidence of Vortex Splitting," *J. Fluid Mech.*, Vol. 152, pp. 289–299.

Freymuth, P., Bank, W., and Palmer, M., 1985b, "Reynolds Number Dependence of Vortex Patterns in Accelerated Flow Around Airfoils," *Exp. Fluids*, Vol. 3, pp. 109–112.

Freymuth, P., Bank, W., and Palmer, M.. 1985c "Use of Titanium Tetrachloride for Visualization of Accelerating Flow Around Airfoils," *Flow Visualization III*, ed. W. J. Yang, Hemisphere, Washington, D. C., pp. 99–105.

Freymuth, P., Finaish, F., and Bank, W., 1985d, "Three-Dimensional Vortex Patterns in a Starting Flow," *J. Fluid Mech.*, Vol. 161, pp. 239–248.

Gad-el-Hak, M., 1986a, "The Use of the Dye-Layer Technique for Unsteady Flow Visualization," ASME JOURNAL OF FLUIDS ENGINEERING, Vol. 108, pp. 34–38.

Gad-el-Hak, M., 1986b, "The Response of Elastic and Viscoelastic Surfaces to a Turbulent Boundary Layer," ASME *Journal of Applied Mechanics*, Vol. 53, pp. 206–212.

Gad-el-Hak, M., 1986c, "Boundary Layer Interactions with Compliant Coatings: An Overview," *Appl. Mech. Rev.*, Vol. 39, pp. 511–523.

Gad-el-Hak, M., 1987a, "Review of Flow Visualization Techniques for Unsteady Flows," *Flow Visualization IV*, ed. C. Véret, Hemisphere, Washington, D. C., pp. 3–14.

Gad-el-Hak, M., 1987b, "Unsteady Separation on Lifting Surfaces," *Appl. Mech. Rev.*, Vol. 40, pp. 441–453.

Gad-el-Hak, M., 1987c, "The Water Towing Tank as an Experimental Facility: An Overview," *Exp. Fluids*, Vol. 5, pp. 289–297.

Gad-el-Hak, M., 1987d, "Compliant Coatings Research: A Guide to the Experimentalist," *J. Fluids & Structures*, Vol. 1, pp. 55–70.

Gad-el-Hak, M., and Blackwelder, R. F., 1985, "The Discrete Vortices from a Delta Wing," *AIAA J.*, Vol. 23, pp. 961–962.

Gad-el-Hak, M., and Blackwelder, R. F., 1987a, "Control of the Discrete Vortices from a Delta Wing," *AIAA J.*, Vol. 25, pp. 1042–1049.

Gad-el-Hak, M., and Blackwelder, R. F., 1987b, "Simulation of Large Eddy Structures in a Turbulent Boundary Layer," *AIAA J.*, Vol. 25, pp. 1207–1215.

Gad-el-Hak, M., and Blackwelder, R. F., 1988, "Selective Suction for Controlling Bursting Events in a Boundary Layer," *AIAA J.*, Vol. 26, No. 12.

Gad-el-Hak, M., Blackwelder, R. F., and Riley, J. J., 1981, "On the Growth of Turbulent Regions in Laminar Boundary Layers," *J. Fluid Mech.*, Vol. 110, pp. 73–95.

Gad-el-Hak, M., Blackwelder, R. F., and Riley, J. J., 1984b, "On the Interaction of Compliant Coatings with Boundary Layer Flows," *J. Fluid Mech.*, Vol. 140, pp. 257–280.

Gad-el-Hak, M., Blackwelder, R. F., and Riley, J. J., 1985, "Visualization Techniques for Studying Transitional and Turbulent Flows," *Flow Visualization III*, ed. W. J. Yang, Hemisphere, Washington, D. C., pp. 568–575.

Gad-el-Hak, M., Davis, S. H., McMurray, J. T., and Orszag, S. A., 1984a, "On the Stability of the Decelerating Boundary Layer," *J. Fluid Mech.*, Vol. 138, pp. 297–323.

Gad-el-Hak, M., and Ho, C.-M., 1985, "The Pitching Delta Wing," *AIAA J.*, Vol. 23, pp. 1660–1665.

Gad-el-Hak, M., and Ho, C.-M., 1986a, "Unsteady Vortical Flow Around Three-Dimensional Lifting Surfaces," *AIAA J.*, Vol. 24, pp. 713–721.

Gad-el-Hak, M., and Ho., C.-M., 1986b, "Unsteady Flow Around an Ogive-Cylinder," *J. Aircraft*, Vol. 23, pp. 520–528

Gad-el-Hak, M., and Hussian, A.K.M.F., 1986, "Coherent Structures in a Turbulent Boundary Layer. Part 1. Generation of 'Artificial' Bursts," *Phys. Fluids*, Vol. 29, pp. 2124–2139.

Geller, E. W, 1954, "An Electrochemical Method of Visualizing the Boundary Layer," M.Sc. thesis, Mississippi Stage College, State College.

Geller, E. W., 1955, "An Electrochemical Method of Visualizing the Boundary Layer," *J. Aeronaut. Sci.*, Vol. 22, pp. 869–870.

Hama, F. R., 1962, "Streaklines in a Perturbed Shear Flow" *Phys. Fluids*, Vol. 5, pp. 644–650.

Hansen, R. J., and Hunston, D. L., 1983, "Fluid Property Effects on Flow-Generated Waves on a Compliant Surface," *J. Fluid Mech*, Vol. 133, pp. 161–177.

Hansen R. J., Hunston, D. L., Ni, C. C., and Reischman, M. M., 1980, "An Experimental Study of Flow-Generated Waves on a Flexible Surface," *J. Sound & Vibration*, Vol. 68, pp. 317–334.

Hinze, J. O., 1975, *Turbulence*, Second Edition, McGraw-Hill, New York.

Hoyt, J. W., and Taylor, J. J., 1977a, "Turbulence Structure in a Water Jet Discharging in Air," *Phys. Fluids*, Vol. 20S, pp. 253–257.

Hoyt, J. W., and Taylor, J. J., 1977b, "Waves on Water Jets," *J. Fluid Mech.*, Vol. 83, pp. 119–127.

Hussain, A.K.M.F., 1986, "Eduction of Coherent Structures," AIAA Paper No. 86-0026.

Jeffery, G. B., 1922, "The Motion of Ellipsoidal Particles Immersed in a Viscous Fluid," *Proc. R. Soc. Lond. A*, Vol. 102, pp. 161–179.

Jenks, M., Dadone, L., and Gad-el-Hak, M., 1987, "Towing Tank Flow Visualization Test of a Scale Model H-34 Rotor," *Proc. 43rd Annual Forum*, American Helicopter Society, St. Louis, MO.

Kegelman, J. T., and Mueller, T. J., 1986, "Experimental Studies of Spontaneous and Forced Transition on an Axisymmetric Body," *AIAA J.*, Vol. 24, pp. 397–403.

Kegelman, J. T., Nelson, R. C., and Mueller, T. J., 1979, "Smoke Visualization of the Boundary Layer on Axisymmetric Body," AIAA Paper No. 79-1635.

Kegelman, J. T., Nelson, R. C., and Mueller, T. J., 1980, "Boundary Layer and Side Force Characteristics of a Spinning Axisymmetric Body," AIAA Paper No. 80-1584-CP.

Kline, S. J., 1978, "The Role of Visualization in the Study of the Structure of the Turbulent Boundary Layer," *Coherent Structure of Turbulent Boundary Layers*, eds. C. R. Smith and D. E. Abbott, Lehigh University, Bethlehem, PA, pp. 1–26.

Koromilas, C. A., and Telionis, D. P., 1980, "Unsteady Laminar Separation: An Experimental Study," *J. Fluid Mech.*, Vol. 97, pp. 347–384.

Lauterborn, W., and Vogel, A., 1984, "Modern Optical Techniques in Fluid Mechanics," *Ann. Rev. Fluid Mech.*, Vol. 16, pp. 223–244.

Lighthill, M. J., 1973, "On the Weis-Fogh Mechanism of Lift Generation," *J. Fluid Mech.*, Vol. 60, pp. 1–17.

Lin, J.-T., and Pao, Y.-H., 1979, "Wakes in Stratified Fluids," *Ann. Rev. Fluid Mech.*, Vol. 11, pp. 317–318.

Mach, L., 1896, "Über die Sichtbarmachung von Luftstromlinien," *Z. Luftschiffahrt Phys. Atm.*, Vol. 6, pp. 129–139.

Maxey, M. R., and Riley, J. J., 1983, "Equation of Motion for a Small Rigid Sphere in a Nonuniform Flow," *Phys. Fluids*, Vol. 26, pp. 883–889.

Maxworthy, T., 1979, "Experiments on the Weis-Fogh Mechanism of Lift Generation by Insects in Hovering Flight. Part 1. Dynamics of the 'Fling'," *J. Fluid Mech.*, Vol. 93, pp. 47–63.

McAlister, K. W., and Carr, L. W., 1978a, "Water-Tunnel Experiments on an Oscillating Airfoil at Re=21,000," NASA TM-78446.

McAlister, K. W., and Carr, L. W., 1978b, "Water Tunnel Visualization of Dynamic Stall," *Nonsteady Fluid Dynamics*, eds. D. E. Crow & J. A. Miller, ASME, New York, pp. 103–110.

McAlister, K. W., and Carr, L. W., 1979, "Water Tunnel Visualization of Dynamic Stall," *J. Fluids Eng.*, Vol. 101, pp 376–380.

McAlister, K. W., Carr, L. W., and McCroskey, W. J., 1978, "Dynamic Stall Experiments on the NACA 0012 Airfoil," NASA Tech. Paper 1100.

Merzkirch, W., 1974, *Flow Visualization*, Academic Press, New York (also Second Edition, 1987).

Monnet, P., Coutanceau, M., Daube, O., and Ta Phuoc Loc, 1985, "The Use of Visualization as a Guide in the Numerical Determination of the Flow Around an Abruptly Accelerated Elliptic Cylinder or Airfoil," *Flow Visualization III*, ed. W. J. Yang, Hemisphere, Washington, D. C., pp. 363–368.

Moore, F. K., 1958, "On the Separation of the Unsteady Laminar Boundary Layer," in *Boundary-Layer Research*, ed. H. G. Görtler, Springer, Berlin, pp. 296–310.

Mueller, T. J., 1980, "On the Historical Development of Apparatus and Techniques for Smoke Visualization of Subsonic and Supersonic Flows," AIAA Paper No. 80-0420-CP.

Mueller, T. J., 1983, "Flow Visualization by Direct Injection," *Fluid Mechanics Measurements*, ed. R. J. Goldstein, Hemisphere, Washington, D. C., pp. 307–375.

Mueller, T. J., 1985, "The Role of Flow Visualization in the Study of Afterbody and Base Flows," *Exp. Fluids*, Vol. 3, pp. 61–70.

Mueller, T. J., Nelson, R. C., Kegelman, J. T., and Morkovin, M. V., 1981a, "Smoke Visualization of Boundary-Layer Transition on a Spinning Axisymmetric Body," *AIAA J.*, Vol. 19, pp. 1607–1608.

Mueller, T. J., Nelson, R. C., Kegelman, J. T., and Zehentner, R. J., 1981b, "Boundary Layer and Side Force Characteristics of Non-Spinning and Spinning Axisymmetric Bodies," Department of Aero. & Mech. Eng., Univ. of Notre Dame, Report No. TN-127.

Mueller, T. J., Nelson, R. C., Kegelman, J. T., and Zehentner, R. J., 1985, "A New Single Filament Smoke Tube Injection Device," *Flow Visualization III*, ed. W. J. Yang, Hemisphere, Washington, D. C., pp. 45–48.

Nagib, H. M., 1979, "Visualization of Turbulent and Complex Flows Using Controlled Sheets of Smoke Streaklines," *Flow Visualization I*, ed. T. Asanuma, Hemisphere, Washington, D. C., pp. 181–186.

Nagib, H. M., Guezennec, Y., and Corke, T. C., 1978, "Application of a Smoke-Wire Visualization Technique to Turbulent Boundary Layers," *Coherent Structure of Turbulent Boundary Layers*, eds. C. R. Smith & D. E. Abbot, Lehigh University, Bethlehem, PA, pp. 372–379.

Nakatani, N., and Yamada, T., 1985, "Measurement of Non-Stationary Flow by the Pulse-Laser Induced Luminescence Method: Increase of Observation Rate," *Flow Visualization III*, ed. W. J. Yang, Hemisphere, Washington, D. C., pp. 82–86.

Nelson, R. C., 1986, "The Role of Flow Visualization in the Study of High-Angle-of-Attack Aerodynamics," in *Tactical Missile Aerodynamics*, eds. M. J. Hemsch & J. N. Nielsen, AIAA, New York, pp. 46–88.

Ng, T. T., and Bradley, T. A., 1988, "Effect of Multi-Frequency Forcing on the Near Field Development of a Jet," *AIAA J.*, in press.

Ohashi, M., and Hayashi, T., 1985, "Visualization of the Phenomenon of Transition to Turbulence of Wall Boundary Layers by Means of Thin-Layered Milk Method," *Flow Visualization III*, ed. W. J. Yang, Hemisphere, Washington, D. C., pp. 563–567.

Pierce, D., 1961, "Photographic Evidence of the Formation and Growth of Vorticity Behind Plates Accelerated from Rest in Still Air," *J. Fluid Mech.*, Vol. 11, pp. 460–464.

Popovich, A. T., and Hummel, R. L., 1967, "A New Method for Nondisturbing Turbulent Flow Measurements Very Close to a Wall," *Chem. Eng. Sci.*, Vol. 22, pp. 21–25.

Prandtl, L., 1904, "Über Flüssigkeitsbewegung bei sehr kleiner Reibung," *Proc. Third Intern. Math. Congr.*, Heidleberg, Germany, pp. 484–491.

Prandtl, L., and Tietjens, O. G., 1934, *Applied Hydro- and Aeromechanics*,

(Translated from the German edition, Springer, 1931), McGraw-Hill, New York.

Pullin, D. I., and Perry, A. E., 1980, "Some Flow Visualization Experiments on the Strating Vortex," *J. Fluid Mech.*, Vol. 97, pp. 239–255.

Reynolds, O., 1883, "An Experimental Investigation of the Circumstances which Determine Whether the Motion of Water Shall be Direct or Sinuous, and of the Law of Resistance in Parallel Channels," *Phil Trans. Roy. Soc. London*, Vol. 174, pp. 935–982.

Riley, J. J., and Gad-el-Hak, M., 1985, "The Dynamics of Turbulent Spots," *Frontiers in Fluid Mechanics*, eds. S. H. Davis & J. L. Lumley, Springer, Berlin, pp. 123–155.

Riley, J. J., Gad-el-Hak, M., and Metcalfe, R. W., 1988, "Compliant Coatings," *Ann. Rev. Fluid Mech.*, Vol. 20, pp. 393–420.

Rott, N., 1956, "Unsteady Viscous Flow in the Vicinity of a Stagnation Point," *Q. Appl. Math.*, Vol. 13, pp. 444–451.

Sanders, C. J., and Thompson, J. F., 1966, "An Evaluation of the Smoke-Wire Technique for Measuring Velocities in Air," Mississippi State University, State College, Aerophysics Res. Report 70.

Santanam, C. B., and Tietbohl, G. L., 1985, "Complex Flow Visualization by a Unique Method," *Flow Visualization III*, ed. W. J. Yang, Hemisphere, Washington, D. C., pp. 1–6.

Savas, Ö., 1985, "On Flow Visualization Using Reflective Flakes," *J. Fluid Mech.*, Vol. 152, pp. 235–248.

Sears, W. R., 1956, "Some Recent Developments in Airfoil Theory," *J. Aerospace Sci.*, Vol. 23, pp. 490–499.

Simmons, L. F. G., and Dewey, N. S., 1931, "Photographic Records of Flow in the Boundary Layer," Aeronautical Research Council, London, R&M Nos. 134 and 135.

Stanislas, M., 1985, "Ultra High Speed Smoke Visualization of Unsteady Flows Using a Pulsed Ruby Laser," *Flow Visualization III*, ed. W. J. Yang, Hemisphere, Washington, D. C., pp. 41–44.

Taneda, S., 1977, "Visual Study of Unsteady Separated Flows Around Bodies," *Prog. Aerospace Sci.*, Vol. 17, pp. 287–348.

Townsend, A. A., 1976, *The Structure of Turbulent Shear Flow*, Second Edition, Cambridge University Press, London.

Turner, J. S., 1973, *Buoyancy Effects in Fluids*, Cambridge University Press, London.

Van Dyke, M., 1982, *An Album of Fluid Motion*, Parabolic Press, Stanford, CA.

Weidman, P. D., 1976, "On the Spin-Up and Spin-Down of a Rotating Fluid. Part 2. Measurements and Stability," *J. Fluid Mech.*1, Vol. 77, pp. 709–735.

Werlé, H., 1973, "Hydrodynamic Flow Visualization," *Ann. Rev. Fluid Mech.*, Vol. 5, pp. 361–382.

Wortmann, F. X., 1953, "Eine Methode zur Beobachtung und Messung von Wasserströmungen mit Tellur," *Z. Angew Phys.*, Vol. 5, pp. 201–206.

Wygnanski, I., Haritonidis, J. H., and Kaplan, R. E., 1979, "On a Tollmien-Schlichting Wave Packet Produced by a Turbulent Spot," *J. Fluid Mech.*, Vol. 92, pp. 505–528.

Yamada, H., 1973, "Instantaneous Measurements of Airflows by Smoke-Wire Technique," *Trans. Jpn. Mech. Eng.*, Vol. 39, pp. 726–731.

Yamada, H., 1979, "Use of Smoke Wire Technique in Measuring Velocity Profiles of Oscillating Laminar Air Flows," *Flow Visualization I*, ed. T. Asanuma, Hemisphere, Washington, D. C., pp. 187–192.

Exploration of the Iceformation Method Applied to a Diffuser

R. S. LaFleur
Graduate Student,
Mechanical Engineering
The University of Connecticut,
Storrs, Ct. 06268

The design of optimum flow surfaces has been a challenging task for fluid dynamicists ever since the concept of fluid drag was realized. This paper will serve to introduce another method of flow surface design which has the potential to overcome the difficulties of present analytic and experimental methods. Natural design is introduced as an alternative to scientific design. The iceformation method is defined as harnessing the natural process of ice formation to perform geometric variations. The flow field has the direct opportunity to influence and optimize the geometry development. The hypothesis of design optimization is tested by an exploratory example of the method. The example is a fundamental but nevertheless difficult design problem of a diffuser. Use of the iceformation method resulted in the design of diffusers with higher pressure recovery performance than conical diffusers of the same length and area ratio.

1 Introduction

Surface Geometry Design Goals. In internal and external flows the fluid field is deformed by the fixture or body surface. Fluid flow changes to meet, flow over, and finally leave the surface. The shape of the surface relative to these three intervals determines the performance. The transfer of energy between the flow and the surface is in the form of viscous work and heat transfer. Typically the goal is to design optimum body or fixture surfaces that transfer the least energy with the flow. This has direct significance on fuel or maintenance costs of turbomachinery and transportation devices. For an external flow, the body would have least drag for a given speed. For an internal flow, the flow would retain the maximum of available energy when interacting with the fixture.

1.A The Classification of Design Tree. To discuss the iceformation method, it is necessary to examine the relevance of present geometric design approaches and distinguish the basic philosophical differences this new method offers. The classification of major design philosophies can be displayed by a relative tree (Fig. 1).

The initial basic surface geometry is the "parent shape." About this, variations in geometry occur to obtain another shape. The first tree level signifies the mechanism of the geometric variations. With the introduction of natural processes as design tools, a new class of design methods is obtained. The mechanism of geometry variation can then be categorized into natural and scientific designs. The second tree level signifies the type of environment which causes the geometric variations. The further left the branch, the more human controlled the design environment. Below each second level branch is an evolution loop. Each loop is made of two components: the conditions and geometry reaction to those conditions. Evolution of a geometry occurs when the conditions of the design environment change. The loop forms an iteration of variations applied to a starting parent shape geometry.

Scientific Design Mechanisms. The scientific design methods are common and can be subdivided into analytical and experimental methods. Analytic design consists of using a mathematical simulation of the flow and altering the surface geometry until the surface satisfies given criteria or constraints. For example, optimal external shapes were obtained by varying the geometry under constraints such as constant wing profile area, contour moment of inertia and length, volume or enclosed area [1, 2, 3,]. In describing a high speed aircraft or missile nose, Pike [4] showed how a parent shape could be conceived and then optimized numerically. The analytical approach contains approximations in the physical modeling of the flow and in the mathematical procedures used

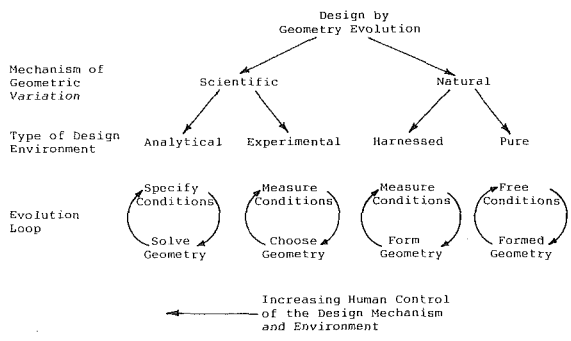

Fig. 1 Design classification tree

Contributed by the Fluids Engineering Division for publication in the JOURNAL OF FLUIDS ENGINEERING. Manuscript received by the Fluids Engineers Division April 10, 1987.

to solve for the geometry. Accordingly, these calculations may result in a less than optimum geometry for real conditions.

The experimental approach utilizes scale models of the parent shape in actual flow field conditions. The geometric variations are influenced by flow measurements and the human decision for surface movement. The development of an optimum flow surface using experimental means is arbitrary and local optimization does not guarantee a global optimum. One example [5] is the design of a converging/diverging nozzle for a two phase transonic flow (water/steam). The axisymmetric nozzle was designed by random variation of a finite number of wall sections starting with a De Laval nozzle (55 percent efficiency). Improvement in performance was the criterion for acceptance of the next generation. The process was stopped at step 45, a nozzle with multiple rings and 80 percent efficiency. The limitation is that the variations are finite in number and magnitude and the randomness is indirect and expensive to evaluate.

The alternative to random variations would be to vary the geometry based on the experience of the designer. The geometry search would benefit but also be limited by the designer's understanding of what is good or bad in similar design problems (creativity). Often design optimization employs simultaneous or iterative use of both scientific classes: analysis and experimentation.

Natural Design Mechanisms. The natural approach is unexploited when compared to scientific methods. Geometric variations occur naturally to satisfy an extremum principle. This principle is a central theme in the science of thermodynamics and calculus of variations. The natural designs can be categorized into harnessed designs and pure designs. In one class, the natural processes which provide geometric variations are harnessed by utilizing them in a controlled environment. The flow surface geometry then forms by the natural application of the geometric variations. The flow can influence the surface; simultaneously, the surface alters the flow and performance. In natural designs, humans have no influence on the geometry result other than specifying constraints. The order of the geometry variation is not limited by scientific understanding.

The pure natural design class encompasses all objects existing in nature. By definition the designs have evolved under conditions and constraints not specified by humans. The pure natural designs are seldom useful in human devised mechanisms because of the free conditions during the design evolution.

1.B An Exploration of the Iceformation Method. One approach of harnessed natural design is the iceformation method. This involves the use of water as a flow medium which flows over a cooled (sub-freezing) surface. Over time, water will solidify naturally on the parent surface forming an altered surface geometry (Fig. 2). The new geometry perturbs the flow field. The word "formation" is used to represent the global variation of the interface geometry by either local ice growth or ice decay. The phrase "ice formation" refers to the natural process and the word "iceformation" refers to the harnessed process as a design method. The mechanism resembles measurement of heat transfer by use of Reynolds analogy and the chemical species transfer of naphthalene. However, the change in ice geometry is carried beyond the small deformations used in the naphthalene method and the ice allows material deposition on the surface, not just decay.

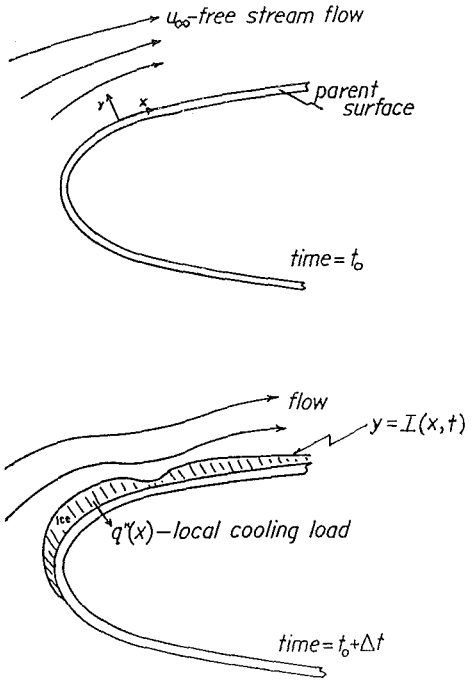

Fig. 2 External iceformation

The distribution of geometric change is governed by a design criterion. For the iceformation method, the design criterion is natural but can be understood in an analytical statement by formulating the heat transfer problem at the interface. The ice formation can be described by an interface equation which balances the ice and water heat transfers at the interface. Thus the interface equation as a function of the tangent coordinate, x, which describes the formation in the normal direction, y, is shown in equation (1).

$$Q\,\rho_I \frac{dI}{dt} = k_I\left[\frac{dT_I}{dy}\right]_{y=I} - k_W\left[\frac{dT_W}{dy}\right]_{y=I} \tag{1}$$

Using the Reynolds analogy we can put the formation rate in terms of fluid shear on the surface. Equation (2) shows a chain rule.

$$\left[\frac{\partial T_W}{\partial y}\right]_{y=I} = \left[\frac{\partial T_W}{\partial u}\right]_{u=0}\left[\frac{\partial u}{\partial y}\right]_{y=I} = \frac{\tau}{\mu}\left[\frac{\partial T_W}{\partial u}\right]_{u=0} \tag{2}$$

Substituting equation (2) into equation (1) and solving for formation rate we obtain equation (3).

Nomenclature

y = parent shape normal coordinate
x = parent shape tangent coordinate
I = interface position
δ = water channel width
P = static pressure
h = hydrostatic pressure head
ϵ = experimental quantity
n = population size
σ = standard deviation, S.D.
Δh = differential h across fixture
$\bar{V}_1$ = inlet average velocity
Re = Reynolds number
g_c = gravitational conversion, mass to force
g = gravity on the earth
C_P = pressure recovery coefficient
β_d = tailpipe correction factor
T_W, T_I = temperature
k_W, k_I = conductivity; water, ice
μ, ρ_I = water viscosity, Ice density
τ = fluid shear at the ice interface
dt = time differential
Q = latent heat of fusion

$$\frac{dI}{dt} = \frac{k_I}{\rho_I Q}\left[\frac{\partial T_I}{\partial y}\right]_{y=I} - \tau \frac{k_W}{\mu\, Q\, \rho_I}\left[\frac{\partial T_W}{\partial u}\right]_{u=0} \quad (3)$$

The flow field will adjust the ice surface through the shear force and the ice boundary geometry will adjust the flow field through melting and growing. Regions of low shear, such as separation, may accumulate ice due to low shear stress and stagnating fluid. High shear stress areas will tend to decay the surface and allow more room for the flow. The process will continue until a global steady state is reached: when the local fluid convection matches the local surface conduction. Once the parent shape, cooling load, and fluid boundaries are fixed, the geometry evolves without any human interference.

Understanding of the Ice Formation Process. Basic fluid regimes involving ice formation have been studied both experimentally and analytically to provide a thorough understanding of the heat transfer and phase change mechanisms. The ice formation has been treated as an interference to the water flow or as a predictable interface transient. With this view, one can only seek to predict and control or eliminate the phenomena. However, these studies many be used to understand the ice growth/decay process for various parent surfaces and flow regimes and how it may be utilized as a design tool instead of eliminated. Basic geometries of flat plates, rectangular channels, cylinders and tubes portray a fundamental illustration of what occurs during ice formation.

The fundamental external problem of a flat plate flow with ice formation has been thoroughly examined by Hirata et al. [6] and analytically by Stephan [7]. Ashton and Kennedy [8] studied the natural ice ripples forming on the underside of a river ice cover. The internal flat plate, a flow channel, has also been studied. This regime is related to rectangular ducts and slots which may occur within fluid machinery. Analytical work by Cheng and Wong [9] and Bowley and Coogan [10] uncovered the phenomena in a developing boundary layer flow.

The cylindrical problem has also been studied extensively because the simple curved geometry of a cylinder is a good partial model of complicated geometries. The external cylinder problem has been studied experimentally by Cheng, Inaba, and Gilpin [11] and Carlson [12]. These experiments have displayed the iceformation phenomena about a flow separation. Carlson's approach discussed the possibility of an optimized geometry. Unfortunately, flow testing of the cylindrical shapes did not show differences in drag because the test apparatus error overwhelmed the measurements. The internal cylinder, in tube form, has been examined fully by Zerkle and Sunderland [13] and Thomason, Mulligan, and Everhart [14]. Gilpin [15] demonstrated the phenomenon exposed to a turbulent transition flow.

The references cited may be used as a basis for designing an ice formation apparatus. Complicated geometry problems may be separated into simpler models such as cylinders and flat plates. The information provides the relationship between ice geometry and relevant parameters to be varied and measured.

Internal Iceform–Sudden Enlargement Diffuser. The example treated in this paper examines the geometry transition region of an internal diffuser. The diffuser problem has become important because the increasing technology in turbomachinery has demanded the highest performance of all flow components. The diffuser has been a difficult device to design because flow separation (stall) often occurs in the adverse pressure gradient. This three dimensional fluctuating flow is complicated by effects of inlet and exit conditions. Heskestad [16] has shown that suction at the inlet greatly improves the performance of sudden enlargement diffusers. Another approach by Adkins [17] deals with utilizing a controlled vortex to aid in the flow expansion. Bleed flow off the vortex is necessary to maintain a stable vortex. The treatment in the present paper varies the wall geometry, not the flow field; therefore no suction is used.

Parent Surface Description. A diffuser geometry was studied as a fundamental example to apply the iceformation method. The parent shape chosen was the extreme diffuser geometry of a sudden enlargement in a pipe flow (Fig. 3). The diametral step and enlarged cylinder were cooled to allow an ice layer to be maintained. Inlet water flowed downward through a nozzle of diameter 3.8 cm to the enlarged diameter of 10.2 cm. An inlet nozzle served to fully develop the inlet velocity profile and provided insulation to form an adiabatic boundary condition in the small diameter. The exit was a sudden contraction to the previous small diameter. The maximum steady state area ratio is different since ice growth forced by refrigeration into the flow field decreased the channel opening. The flow rate and bulk tank temperature can be adjusted to allow laminar to turbulent inlet conditions which cause different flow fields and resulting iceforms. The geometry results are categorized by these two experimental constraints.

2 Iceformation Technique

2.A Iceformation Apparatus and Method. The apparatus is made of two systems: a water system and a refrigeration system. As shown in Fig. 4, the two systems meet at the ice column. This vertical chamber is an open evaporator containing

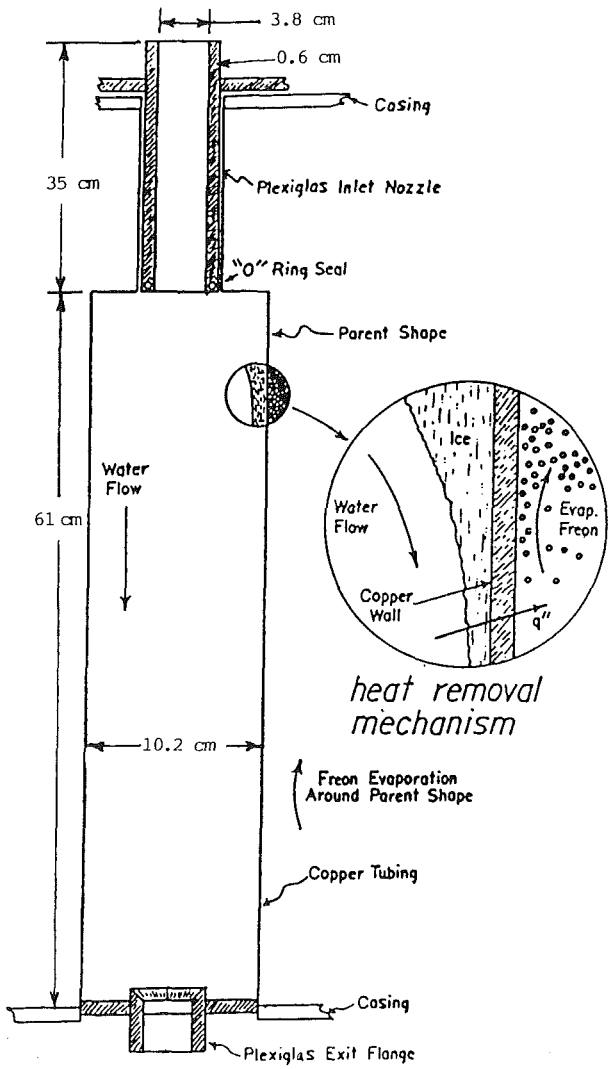

Fig. 3 Sudden enlargement parent shape

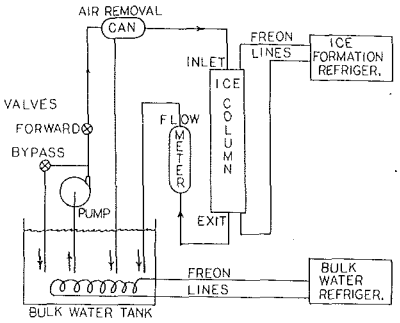

Fig. 4 Iceformation apparatus

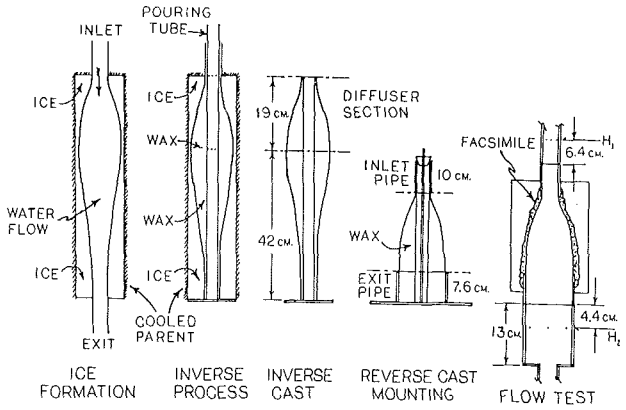

Fig. 5 Capturing process

the parent surface: a copper walled sudden enlargement. The enlargement is made of copper which has low resistance to conductive heat removal from the ice layer. It is surrounded by evaporating (boiling) freon which facilitates heat removal at constant temperature and high film coefficient. The ice column refrigeration system is the backbone of the iceform technique. It provides the cooling load necessary to support convective cooling of the water channel and ice growth into the water.

Water System. Water flow to the ice column is provided by a 1/3 H.P. Goulds pump. The water flow to the ice column is regulated by a bypass and a forward valve. This system supplies a maximum of Re = 12,000 based on the inlet diameter of 3.8 cm. During the experiment, the flow rate is maintained by adjusting the control valves sufficiently to keep the flow meter reading constant. It is desirable for the maximum equilibrium area ratio obtained to be the same for each iceform experiment. This can be obtained approximately by maintaining a constant thermal capacity (above freezing reference) flow rate to the inlet of the ice chamber. This is obtained by multiplying flow rate by the bulk water temperature (in Celsius) and water specific heat.

At some time the iceformation transient will approach a steady state geometry. The capturing time approximates the steady state time. The specimens were captured approximately one hour after the bulk tank temperature transient reached a constant value. The nominal capturing time was 6 hours. Actual steady state time is an unknown parameter. Many experiments would have to be run to detail the variation of geometry versus capturing time.

Capturing. The internal iceform diffusers may be optimum in pressure recovery due to minimization of energy dissipation. To check this hypothesis, each iceform diffuser was flow tested and compared to the performance of standard diffusers (equivalent cone and sudden enlargement diffusers). The steady state ice surface cannot be tested for different flow rates as this will cause transients to begin. Instead, the iceform shape must be captured in a solid condition.

This capturing involves two procedures. The first is to cast the internal shape with wax. Secondly, the inverse shape must be externally cast to obtain the previous iceform shape (Fig. 5). This was accomplished by using a composite of Facsimile (*R*) impression material and plaster of paris for the bulk support of the reverse cast. An inlet pipe of diameter 3.9 cm and an exit pipe of diameter 8.9 cm are used for each specimen. Individual specimens are slightly altered near the maximum area point to meet the exit pipe diameter (Fig. 8). Six diffusers were constructed with the Facsimile/plaster composite. Four are iceform results and the others are sudden enlargement and a 15 deg cone (Table 1).

Iceform shapes grown at different flow rates can be compared with standard diffuser geometries including the sudden enlargement for the given area ratio. Individual iceforms have different diffusion lengths. Therefore, the specimens will be compared to the traditional scientific result of equivalent conical diffusers: cones of equal length and area ratio to each iceform specimen.

2.B Flow Testing. The casting procedures yield a test section of the original iceform. The diffuser can be tested for static pressure recovery, (P exit-P entrance), versus flow rate and thus provide a dimensionless coefficient C_P, a ratio of static pressure recovery over inlet dynamic head.

$$C_P = \frac{P_2 - P_1}{\rho \bar{V}_1^2} 2g_c = \frac{h_2 - h_1}{\bar{V}_1} 2g$$

If the pressure losses decrease in a diffuser, C_P increases. Flow tests of different diffusers provide comparison between the friction signatures in each specimen. The inlet flow in the performance tests was fully developed due to 14 diameters of pipe length upstream of the diffusers. Statistical reduction of the data yielded C_P and a measurement confidence. From this we may test the hypothesis: Does the iceformation method produce diffusers of improved performance over conical diffusers?

Measurement Instruments. The pressure sensing is done with an instrument called a Hooke gauge. This resembles a manometer except that the vertical tubes are relatively large in cross-sectional area and the water-air interface heights are measured with depth micrometers (Fig. 6). The pressure probes mounted on the test section circumferentially average static pressure. The flow meter used during the performance experiment is of the turbine counter type. The display of the rotation is provided by a digital readout. The meter calibration data was used to compute an equivalent inlet dynamic head. The raw data consists of 12 flow rate and differential head measurements for 16 different flow rates.

Data Reduction. The differential head data is reduced by a set algorithm (Fig. 7). The flow rate and differential head data is processed by first finding an average and standard deviation (S.D.) for the 12 raw data samples for each nominal flow rate. The population is trimmed of outliers by Chavenet's Criterion (18). Using the population size and S.D. the point is rejected if

$$erfc\left[\frac{\epsilon - \bar{\epsilon}}{\sigma\sqrt{2}}\right] \leq \frac{1}{2n}$$

where $erfc(\ )$ is the complimentary error function. After outlier rejection, a mean and S.D. are calculated for the remaining flow rate and differential head populations. Then the flow rate is converted to inlet Re and inlet dynamic head using the meter calibration curve and inlet pipe geometry. The mean

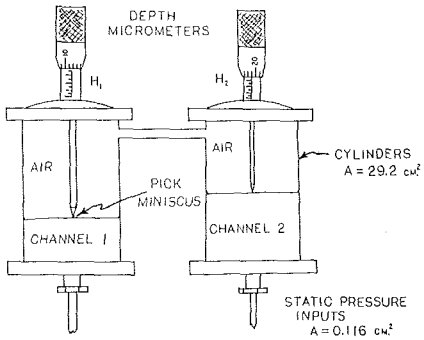

Fig. 6 Hooke gauge

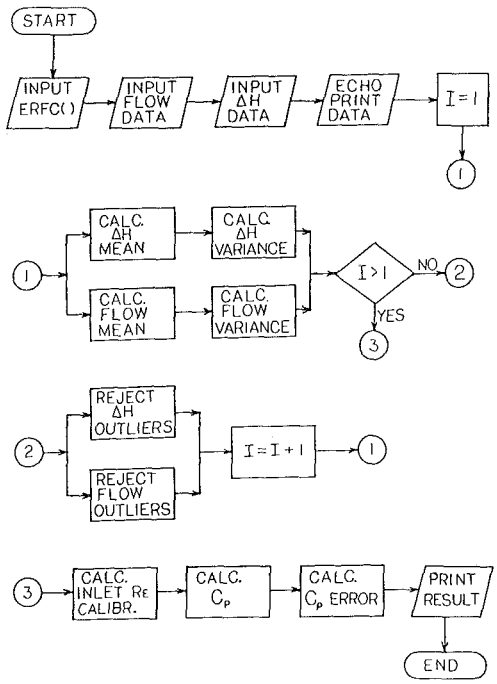

Fig. 7 Data reduction algorithm

C_P and S.D. of C_P are then calculated using the Δh and inlet dynamic head means and standard deviations.

3 Results and Discussion

The iceformation design technique can be examined both qualitatively and quantitatively. The results of the ice formation and flow testing for each type of diffuser are examined by comparing the surface contours and pressure recovery performance.

3.A Surface Plots. The surface plots are diffuser profiles obtained by linear tracing of the surface contours. Shown are six different diffuser geometries (Fig. 8). The plots are profiles of a cylindrical surface. Axisymmetry is apparent on a global scale. With many contours on a plot, one can see the actual differences of the surface contours.

The wall slope directly after the inlet pipe is one important characteristic of the diffusers. Steep inlet slopes have a higher adverse pressure gradient than shallower ones. The pressure gradient will control the performance by the condition of separation and subsequent reverse flow. Typically a stalled diffuser has lower performance than one that does not separate. The reverse flow is a result of higher pressure downstream than upstream. In a diffuser, the performance increases when the pressure downstream can be increased for a

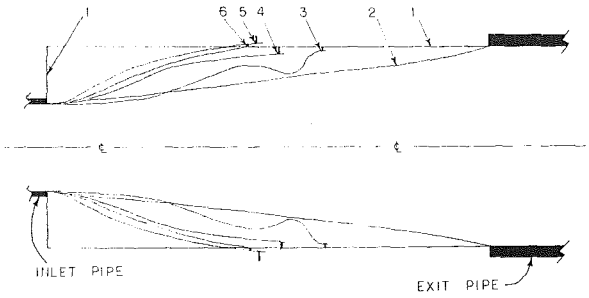

Fig. 8 Diffuser surface contours

Table 1 Diffuser specimens and equivalent cones

Specimen Number	Ice Formation Water Condition Flow Re	Temp. °C	Steady State Area Ratio	Equivalent Cone Geometry Length cm	Angle 2θ	Tailpipe Length Ratio ℓ_t/D_2
1	sudden enlargement		5.44	0.0	180.0	3.5
2	conical		5.44	19.1	15.0	1.36
3	6800	3	5.06 ring	12.1	22.3	2.14
4	6800	3	4.69	10.2	24.7	2.36
5	5100	5	6.00	9.33	33.0	2.46
6	3400	8	5.44	8.89	31.9	2.50

given inlet flow, length and area ratio. If the reverse flow could be controlled, the loss mechanism can be controlled to increase pressure downstream. Often suction in the adverse pressure gradient region is used to control the separation. For example, Adkins [17] discussed the use of cusped wall at the inlet and bleed off to control the vortex. This resulted in short diffusers with relatively low total pressure loss. One iceform diffuser appears to have a vortex control in the form of a ring on the contour. An uncontrolled vortex would shed off the inlet and reduce performance. However, the ring may serve to control the vortex and resist the shedding.

The monotonic diffuser contours, viewed separately, look similar in shape but the combined plot clearly shows the differences in the surface shapes. The normalized thermal capacitance flow rate of the inlet water can be calculated approximately by multiplying the growth Re by the bulk tank temperature (Celcius). The higher thermal fluxes tend to yield higher equivalent cone angles and a larger equilibrium water space. This can be supported by the interface equation in the form of higher water heat transfer. Specimen 6 diverges slightly from the correlation of thermal flow rate to resulting equivalent cone angle. This indicates a higher order correlation between experimental conditions and resulting geometry. A higher order correlation is seen in other regimes such as a flat plate [6].

Specimens 3 and 4 were formed under the same flow rate and bulk water temperature. Apparently another experimental quantity is different between them due to the differences in the steady state surface contours. Specimen 3 was captured 7 hours after starting and specimen 4, 6 hours. Perhaps specimen 3 is closer to steady state than specimen 4. Locally, small scale geometry variation may occur slowly after a general shape, specimen 4, is reached. This effect indicates a fine tuning of the interface geometry as steady state is approached. The Reynolds number of specimens 3 and 4 was the highest that was considered in this exploration. The transition of the flow from laminar to turbulent may also be the ex-

perimental constraint that varied. Verification of turbulence by measurement or flow visualization was prevented by the complexity of the internal ice chamber.

These results show the complexity of the flow/ice interaction. Further experiments should include a study of geometry variation as the capturing time varies including inlet laminar/turbulent determination. A study with wider variations in inlet flow temperature, inlet mass flow rate, inlet velocity profile, and changes in the parent shape temperature will be necessary to "nail down" the correlation between experimental conditions and the resulting iceform diffuser geometries.

3.B Pressure Recovery Performance. Flow testing the test sections (Table 1) for static pressure indicates the diffuser performance in terms of the pressure recovery coefficient C_P (Table 2). Shown is the result of flow testing of six different diffusers. The results are displayed on the performance plot (Fig. 9). Both axes are non-dimensional but universality cannot be expected because the iceforms are grown at particular thermal and inlet flow conditions. The iceform diffuser performance is presented as a function of flow rate. The limit values (higher inlet Re) of the C_P are recorded for comparison in Table 3. The lower inlet Re gives higher variation about the mean C_P thus comparisons would be "cloudy" in this range. The 2σ values indicate variations in the flow field and instrument reaction thus it is not "error" but confidence for the mean value.

Equivalent Diffusers. The iceform diffusers are compared to conical diffusers of the same length and area ratio. Conical diffuser performance in the literature indicates great diversity in presentation of the final curves. Ward-Smith (19) has combined many sources to indicate conical diffuser performance as a function of cone angle, tailpipe length and inlet conditions. The remaining task is then interpolating the curves to obtain reasonable equivalent cone performance.

Table 1 shows a list of the diffuser specimens tested. The geometric data is used to obtain equivalent cone performance from Ward-Smith [19]. Tailpipe effect is accounted for using a factor, β_d. The conditions for iceformation included a fully developed inlet profile and resulted in relatively short tailpipes. The reference cone data is given for long tailpipes and is reduced by dividing by β_d for shorter tailpipe effect. The equivalent cone performance is listed in Table 3.

Performance Comparison. A comparison is made between the constructed sudden enlargement performance, specimen 1, and the ideal pressure recovery for a sudden enlargement of the same area ratio. The constructed enlargement performed below the ideal. This is due to real flow conditions such as separation and turbulent mixing. These mechanisms may exist during other specimen testing. The sudden enlargement test shows the maximum amount of losses expected and the maximum deviation from a theoretical (ideal) performance. The 15 deg cone comparison shows that the two correspond to the nearest percent of pressure recovery performance. Therefore, the use of the charts in Ward-Smith and tailpipe correction yielded a reasonable set of equivalent cones for comparison to iceform diffusers.

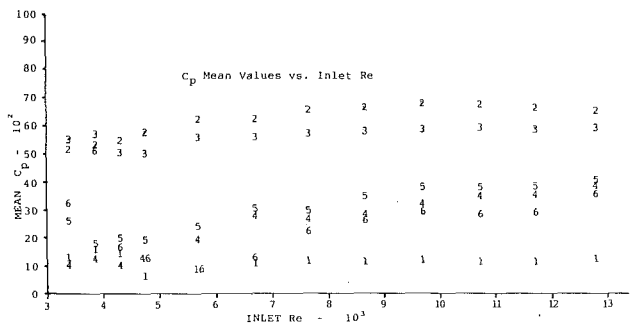

Fig. 9 Flow test of diffuser performance

Table 2 Diffuser pressure recovery versus Reynolds number

($C_p \pm 2\sigma$) 10^2

Nominal Re	Specimen # 1	2	3	4	5	6
3350	12+7.7	51+10	54+13	10+7.2	26+11	32+14
3850	16+7.4	52+8.1	57+8.6	13+5.6	17+6.9	51+23
4300	14+5.0	54+8.0	50+4.5	10+2.7	20+4.9	16+11
4750	6+3.8	57+2.2	50+3.1	13+2.7	19+4.0	13+6.1
5700	9+2.6	62+2.6	55+3.1	19+2.6	24+1.5	9+3.3
6700	11+1.7	62+1.1	56+2.6	28+4.0	29+1.4	13+2.7
7650	12+1.7	65+1.1	57+1.3	27+1.3	29+2.1	22+1.2
8650	11+1.2	66+1.5	58+1.7	29+1.5	35+0.8	26+1.3
9700	11+0.8	67+0.8	58+1.5	32+0.7	38+0.5	30+0.5
10700	12+0.8	67+0.6	59+0.6	37+1.8	38+1.1	29+1.8
11700	12+0.7	67+1.0	58+0.4	36+0.5	38+1.1	29+2.4
12800	13+0.7	66+0.6	59+0.4	40+0.9	41+0.5	36+1.5

Table 3 Iceform diffuser comparison to equivalent cones

Specimen	Equivalent Cones, Ref. Ward-Smith: Tailpipe>8*D pp. 338 C_p'	Tailpipe Factor β_d pp. 341	$C_p = \frac{C_p'}{\beta_d}$	Iceform Asymtote C_p
1	Ideal= 30	1.00	30	13
2	73	1.09	67	67
3	59	1.35	44	59
4	55	1.45	38	40
5	40	1.55	26	41
6	43	1.55	28	36

The comparison of the iceform specimens to their equivalent cones show that the iceform diffuser performance for pressure recovery is higher than equivalent conical diffuser performance. In particular, specimens 3 and 5 show a much greater pressure recovery than the cones. As discussed previously, specimen 3 has a controlling ring which improves the pressure recovery. Specimen 5 has the largest water space within the diffusion length and has the largest equivalent cone angle.

Overall the iceform contours would be an improvement over the conical diffuser components in a flow system. The cones are simple geometries made by placing a first order fit between inlet and exit end points. The iceform geometries are not limited by mathematical fit or other scientific concepts. Rather, due to specified constraints the ice interface reaches a steady state geometry through natural geometry variation.

4 Conclusions

In conclusion, the iceformation method produced short diffusers with significantly higher pressure recovery performance over conical diffusers of the same length and area ratio. The short diffusion is obtained without any bleed flow. Resulting iceform diffuser length and area ratios are related to flow rate and inlet water temperature. The indication of nonlinear relationships and geometry dependence on capturing time and inlet velocity profile must be explored further.

The natural variation in geometry is not limited by our knowledge of the flow field. This is displayed by the unconventional results of the "ring" diffuser contour. It is unlikely that a diffuser with a ring constriction could be obtained through scientific methods. A constriction (decrease in area) in a diffuser (increase in area) goes against the grain of scientific understanding. These characteristics would make the iceformation method suited for design problems where high secondary flows occur due to space limitations. The application is direct because the design is arrived at in a working flow environment.

This experiment constituted an exploration of the natural design technique of iceformation. The diffuser design example illustrated positive results but also identified points for improvements. Further study covering wide ranges of parent shape and inlet flow conditions is necessary to clarify the usefulness of this method and determine detailed cause-and-effect relationships between experimental conditions, capturing time, and the resulting ice geometry.

Acknowledgments

There are many people without whom this paper could not have been written. First the author would like to thank Professor Wallace Bowley for originating the idea of using ice formation for design and for his inspiration and encouragement. Thanks also go to Mr. Glenn Rivard and Mr. Harold Craig for their interest and support. The author would also like to thank Mr. Brian Molinari, Mr. Peter Craig, and Ms. Sue Bowley for assistance in the laboratory. Finally, the author would like to thank his wife, Laura, for assistance with the development of this document.

References

1 Miele, A., "Theory of Optimum Aerodynamic Shapes," *Applied Mathematics and Mechanics*, Vol. 9, Academic Press, New York, 1965.

2 Pironneau, O., "On Optimum Profiles in Stokes Flow," *J. of Fluid Mechanics*, Vol. 59, Part 1, 1973, pp. 117–128.

3 Sano, M., and Sakai, H., "Numerical Determination of Minimum Drag Profile in Stokes Flow," *Trans. Japan Soc. Aero. Space Sci.*, Vol. 26, 1983, pp. 1–9.

4 Pike, J., "Minimum Drag Bodies of Given Length and Base Using Newtonian Theory," *AIAA Journal*, 1977, pp. 769–770.

5 *Ingo Rechenberg Evolutionsstrategie Optimierung technischer Systeme nach Prinzipien der biologischen Evolution*, mit einem Nachwort von Manfred Eigen, Friedrich Frommann Verlag, Struttgart-Bad Cannstatt, 1973, pp. 33–37.

6 Hirata, T., Gilpin, R. R., Cheng, K. C., and Gates, F. M., "The Steady State Ice Layer Profile on a Constant Temperature Plate in a Forced Convection Flow," *Int. J. of Heat and Mass Transfer*, Vol. 22, 1979, pp. 1425–1443.

7 Stephan, K., "Influence of Heat Transfer on Melting and Solidification in Forced Flow," *Int. J. of Heat and Mass Transfer*, Vol. 12, 1969, pp. 199–214.

8 Ashton, G. D., and Kennedy, J. F., "Ripples on Underside of River Ice Covers," *J. of Hydraulic Div. ASCE*, Vol. 98, 1972, pp. 1603–1624.

9 Cheng, K. C., and Wong, Sum-Lok, "Liquid Solidification in a Convectively Cooled Parallel Plate Channel," *Canadian J. of Chemical Engineering*, Vol. 55, 1977, pp. 149–155.

10 Bowley, Wallace W., Coogan, and Charles H., "Two-Dimensional Melting in a Channel," ASME *Publication 67-Ht-75*, 1967.

11 Cheng, K. C., Inaba, H., and Gilpin, R. R., "An Experimental Investigation of Ice Formation around an Isothermally Cooled Cylinder in a Cross-Flow," ASME *Journal of Heat Transfer*, Vol. 103, 1981, pp. 733–738.

12 Carlson, Frederick Michael, "An Investigation of the Solidification of a Flowing Liquid on a Circular Cylinder in Crossflow and Its Effect on the Drag Coefficient," Ph.D. thesis, University of Connecticut, 1975.

13 Zerkle, R. D., and Sunderland, J. E., "The Effect of Liquid Solidification in a Tube Under Laminar Flow Heat Transfer and Pressure Drop," ASME *J. of Heat Transfer*, Vol. 90, 1968, p. 183.

14 Thomason, S. B., Mulligan, J. C., and Everhart, J., "The Effect of Internal Solidification on Turbulent Flow Heat Transfer and Pressure Drop in a Horizontal Tube," ASME *Journal of Heat Transfer*, Vol. 100, 1978, p. 387.

15 Gilpin, R. R., "Ice Formation in a Pipe Containing Flows in the Transition and Turbulent Regimes," ASME *Journal of Heat Transfer*, Vol. 103, 1981, pp. 363–368.

16 Heskestad, G., "Further Experiments With Suction at a Sudden Enlargement in a Pipe," ASME *Journal of Basic Engineering*, Sept. 1970, pp. 437–449.

17 Adkins, R. C., "A Short Diffuser with Low Pressure Loss," ASME JOURNAL OF FLUIDS ENGINEERING, 1975, p. 297.

18 Schenck, Hilbert, *Theories of Engineering Experimentation*, McGraw-Hill, New York, 1968.

19 Ward-Smith, A. J., *Internal Fluid Flow*, Oxford: Clarendon Press, 1980, pp. 337–338.

20 LaFleur, Ronald Samuel, "Ice Formation as a Natural Design Tool," Master's thesis, University of Connecticut, 1985.

Unified Equation of Motion (UEM) Approach as Applied to S1 Turbomachinery Problems

S. Abdallah

C. F. Smith

M. W. McBride
Mem. ASME

Applied Research Laboratory,
The Pennsylvania State University,
State College, PA 16804

Incompressible, blade-to-blade (S1 surface) flow solutions for stators and rotors of turbomachines are obtained utilizing an approach which combines the equations of motion into a single elliptic, second-order partial differential equation for the streamline field. This Unified Equation of Motion (UEM) is obtained from the momentum equation which is modified by using a stream function that satisfies the continuity equation identically. The unified equation is solved numerically by use of a finite difference technique. The velocity field is determined by differentiation of the stream function field and use of the computed streamlines. The pressure field is then determined from an energy relation along the streamlines. The present method is similar to the classical Streamline Curvature Method (SLCM) in that a computation grid is not required; however, the ellipticity of the flow field is preserved directly by the unified equation of motion. The UEM solution is substantially more stable than the SLC method and yields the periodic stagnation streamlines directly. Body-fitted curvilinear coordinates (quasi-orthogonals and streamlines) are generated naturally by the UEM solution. A number of comparisons of the results of the present method are made with experimental data and results of other numerical methods. These comparisons are made for incompressible two dimensional and quasi-three dimensional stationary and rotating blade sections. There is general agreement with accepted analysis procedures.

Introduction

Calculations of three-dimensional flow in rotating and stationary blade passages of turbomachinery are approximated by assuming that the three-dimensional flows can be represented by separate, nearly orthogonal, two-dimensional flows. This appproach, originally proposed by Wu [1], leads to blade-to-blade (S1 surface) solutions and a meridional (S2 surface) solution representing the spanwise variation of the blade-to-blade flow. A further simplification is then introduced which eliminates the twist of the S1 surface by assuming rotational symmetry. The S2 surfaces are then streamsurfaces describing the spanwise variation of the mean blade-to-blade flow.

The methods which have been employed to solve the governing flow equations on the S1 and S2 surfaces include the Matrix method [1], [2], and [3] for example, and the Streamline Curvature Method (SLCM), [4] and [5]. The difference between these methods is the form of the equations of motion and the approach used to obtain a numerical solution. The Matrix method solves for the stream function in the region of interest while the SLCM determines the velocity field from the tangential momentum equation. A comparison of the two methods in obtaining solutions in the S2 surface is given in reference [6].

Contributed by the Fluids Engineering Division and presented at the Gas Turbine Conference, Anaheim, Calif., May 31–June 4, 1987, of THE AMERICAN SOCIETY OF MECHANICAL ENGINEERS. Manuscript received by the Fluids Engineering Conference, June 26, 1987.

Novak and Hearsey [5] describe a SLCM which provides a solution of the flow on the S1 surface by solving for the velocity field. This approach is similar to that employed by Wilkinson [4] and formulates the momentum and energy equations in terms of the velocity gradients occurring in the flow. A comparison of the predicted surface velocities with those measured in a NACA 65(18) 10 compressor cascade show that the SLCM is a very effective approach.

In a previous paper, Abdallah and Henderson [10] used a second-order elliptic differential equation, in the meridional direction, to trace the streamlines throughout the flow field on the S1 surface. The velocity field was then determined from the continuity equation by differentiation of the stream function. This method is different from the traditional SLCM approach in which a first-order velocity gradient equation is solved for the velocity field. The streamline positions are subsequently determined by integration of the equation of continuity.

The analysis described in this paper introduces a new formulation of the governing momentum equation. A second-order, elliptic, partial differential equation in the tangential and meridional directions is derived by combining the continuity and momentum equations. This equation is referred to as the Unified Equation of Motion (UEM). The UEM is used to trace streamlines on the blade-to-blade surface. The velocity field is then determined by differentiating the stream function field, which satisfies the continuity equation.

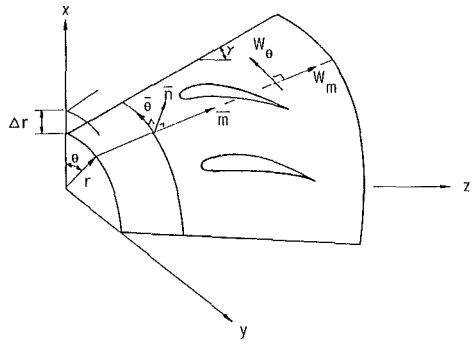

Fig. 1 S_1 stream surface and coordinates

The advantage of the present approach is that the elliptic characteristic of the flow in the meridional and tangential directions is preserved by the governing equation. This method does not require under-relaxation of the iterative numerical solution of the governing equations. Body-fitted curvilinear coordinates from the streamlines and quasi-orthogonals are naturally generated.

Governing Equations

The continuity and momentum equations are written in a coordinate system that rotates with angular velocity ω.

$$\nabla \cdot (\rho \bar{W}) = 0 \tag{1}$$

$$\bar{W} x (\nabla x \bar{V}) = \nabla I - T \nabla S \tag{2}$$

$$\bar{V} = \bar{W} + \bar{\omega} x \bar{r} \tag{2a}$$

Where $\bar{V}$ and $\bar{W}$ are the absolute and relative velocity vectors respectively, I is the relative stagnation rothalpy, S is the entropy, ρ is the density, $\bar{r}$ is the radius vector, and T is the temperature.

Consider the orthogonal curvilinear coordinates (m,θ,n) on the stream surface S_1 as shown in Fig. 1. The S_1 surface is assumed to be a body of revolution (variations in r are neglected in the θ-direction). The coordinates m and θ lie on the surface while n is normal to the surface. The velocity vector $\bar{W}$ has two non-zero components, the meridional velocity W_m and the tangential velocity W_θ. The normal velocity component $W_n = 0$.

The Continuity Equation. Equation (1) is written in the orthogonal coordinates m, θ, and n as

$$\frac{\partial}{\partial m}(\rho b r W_m) + \frac{\partial}{\partial \theta}(\rho b W_\theta) = 0 \tag{3}$$

Equation (3) can be identically satisfied using the relations

$$W_m = \frac{1}{\rho b r}\frac{\partial \psi}{\partial \theta} \tag{4a}$$

and

$$W_\theta = \frac{\tan(\beta)}{\rho b r}\frac{\partial \psi}{\partial \theta} \tag{4b}$$

where β is the streamline angle relative to the meridional direction and b is the streamtube thickness (normal distance between two stream surfaces).

The stream function ψ in equations (4a) and (4b) is determined from the mass flow in each streamtube at the upstream reference station.

The Velocity Gradient Equation. The θ-component of the momentum equation (2) is

$$-W_m\left[\frac{\partial}{\partial m}(rV_\theta) - \frac{\partial}{\partial \theta}(V_m)\right] = \frac{\partial I}{\partial \theta} - T\frac{\partial S}{\partial \theta}. \tag{5}$$

Using equation (2a) and the relation

$$W_m{}^2 = W^2 - W_\theta{}^2$$

and substituting in equation (5), one obtains:

$$W\frac{\partial W}{\partial \theta} - \left[W_m \frac{\partial}{\partial m}(rW_\theta) + \frac{W_\theta}{r}\frac{\partial}{\partial \theta}(rW_\theta)\right] - \omega W_m \frac{dr^2}{dm} = \frac{\partial I}{\partial \theta} - T\frac{\partial S}{\partial \theta} \tag{6}$$

The second term in equation (6) is rewritten as:

$$W_m \frac{\partial}{\partial m}(rW_\theta) + \frac{W_\theta}{r}\frac{\partial}{\partial \theta}(rW_\theta) = W\frac{d}{dl}(rW_\theta) = W_m \frac{d}{dm}(rW_\theta) \tag{6a}$$

Nomenclature

A = blade spacing
a,b,c,d = coefficients defined in equation (13)
b = streamtube thickness (normal distance between two stream surfaces
I = relative stagnation rothalpy
m = distance along meridional stream surface
m,θ,n = orthogonal curvilinear coordinates, Fig. 1
M = numberf of grid points in m-direction
ML = number of grid points upstream of the leading edge in m-direction
MT = number of grid points upstream of the trailing edge in m-direction
N = number of streamlines
P_0 = total pressure
P = static pressure
r = radius of meridional stream surface
S = entropy
S_1,S_2 = Wu's stream surfaces; S_1: blade-to-blade S_2: meridional
SLCM = streamline curvature method
SSL = stagnation streamlines
T = temperature
V,W = absolute and relative velocity vectors, respectively
ρ = density
ω = rotation speed
$\Delta\theta$ = blade tangential thickness
θ_s = suction surface relative tangential coordinate
β = relative flow angle, (Tan^{-1} $(rd\theta/dm)$, Fig. 2)
γ = tan^{-1} (dr/dz), Fig. 1
ζ = transformed meridional coordinate = $\int dm/r$
ψ = stream function
Δr = radial thickness increment between two meridional stream surfaces

Subscripts

m,θ,n = refer to components in m, θ and n directions respectively
e = refer to exit conditions
i = refer to inlet conditions
p = refer to pressure surface
s = refer to suction surface

where d/dl is the derivative along a streamline (l). Using the above identity, equation (6) takes the form

$$W\frac{\partial W}{\partial \theta}-W_m\frac{d}{dm}(rW_\theta)-\omega W_m\frac{dr^2}{dm}=\frac{\partial I}{\partial \theta}-T\frac{\partial S}{\partial \theta}. \quad (7)$$

Since $W_\theta = W_m r d\theta/dm$, then equation (5) becomes

$$r^2 W_m\frac{d^2\theta}{dm^2}+\frac{d}{dm}(r^2W_m)\frac{d\theta}{dm}=\frac{W}{W_m}\frac{\partial W}{\partial \theta}$$

$$-\omega\frac{dr^2}{dm}-\left(\frac{\partial I}{\partial \theta}-T\frac{\partial S}{\partial \theta}\right)\Big/W_m \quad (8)$$

Equation (8) is an elliptic second-order differential equation in terms of $\theta(m)$ which is known as the velocity gradient equation.

The ellipticity of the flow field in the meridional direction, m, is explicitly modeled in equation (8). However, the ellipticity in the tangential direction, θ, (the first term in the right-hand side of equation (8)) lags by one iteration because the relative velocity, W, is computed at the previous iteration. In the present study the term

$$\frac{W}{Wm}\frac{\partial W}{\partial \theta}$$

in equation (8) is expressed in terms of the stream function, ψ. The dependent and independent variables ψ and θ are exchanged in order to express the ellipticity in the tangential direction explicitly. This term is rewritten as

$$\frac{W}{W_m}\frac{\partial W}{\partial \theta}=\frac{1}{\cos^2(\beta)}\frac{1}{\rho br}\frac{\partial^2\psi}{\partial\theta^2}+W_m\frac{\sin(\beta)}{\cos^3(\beta)}\frac{\partial\beta}{\partial\theta} \quad (9)$$

Using the chain rule [13] and noting that ψ is constant along each streamline, one obtains:

$$\frac{\partial^2\psi}{\partial\theta^2}=-\left(\frac{\partial\psi}{\partial\theta}\right)^3\frac{\partial^2\theta}{\partial\psi^2} \quad (9a)$$

Using equations (9a) and (4a), equation (9) is rewritten as

$$\frac{W}{W_m}\frac{\partial W}{\partial\theta}=-\frac{1}{\cos^2(\beta)}(\rho br)^2{W_m}^3\frac{\partial^2\theta}{\partial\psi^2}$$

$$+W_m\frac{\sin(\beta)}{\cos^3(\beta)}\frac{\partial\beta}{\partial\theta} \quad (9b)$$

Substituting the above relation in equation (8), one obtains:

$$\frac{d}{dm}\left(r^2W_m\frac{d\theta}{dm}\right)+\left(\frac{\rho br}{\cos(\beta)}\right)^2{W_m}^3\frac{\partial^2\theta}{\partial\psi^2}=\sigma \quad (10)$$

where

$$\sigma=W_m\frac{\sin(\beta)}{\cos^3(\beta)}\frac{\partial\beta}{\partial\theta}-\omega\frac{dr^2}{dm}-\left(\frac{\partial I}{\partial\theta}-T\frac{\partial S}{\partial\theta}\right)\Big/W_m \quad (10a)$$

Equation (10) is a second-order, elliptic, partial differential equation in both the meridional and tangential directions. This unified equation of motion is the result of combining the continuity equation (3) and the momentum equation (5). Boundary conditions are specified along all the solution domain boundaries since equation (10) is elliptic.

Boundary Conditions. Referring to Fig. 2, the following boundary conditions are used

(1) At the blade suction surface ($\psi=0$)

$$\theta=\theta_s \quad (11a)$$

(2) At the blade pressure surface ($\psi=1$)

$$\theta=\theta_p \quad (11b)$$

The upstream and downstream stagnation streamlines are determined from the solution of equation (10) and the periodic condition

$$\theta_P=\theta_s+A \quad (11c)$$

where θ_P, θ_s, and A refer to the pressure surface, the suction surface, and the blade spacing in the θ-direction, respectively.

(3) Far-Upstream ($m=0$)

$$r\frac{d\theta}{dm}=\tan(\beta_i) \quad (11d)$$

(4) Far-Downstream ($m=m_e$)

$$r\frac{d\theta}{dm}=\tan(\beta_e) \quad (11e)$$

Where β_i and β_e are the relative flow inlet and exit angles respectively, Fig. 2.

In case the flow exit angle β_e is not known, an iterative procedure is adopted to satisfy a Kutta condition. We start by estimating the exit angle β_e and solve for the flow field. An increment $\Delta\beta$ is then added to the exit angle and the flow field is recalculated. The process is repeated until the magnitudes of the velocity at the cutoff points [4] of the blade are equal. This leads to the unique determination of the flow exit angle.

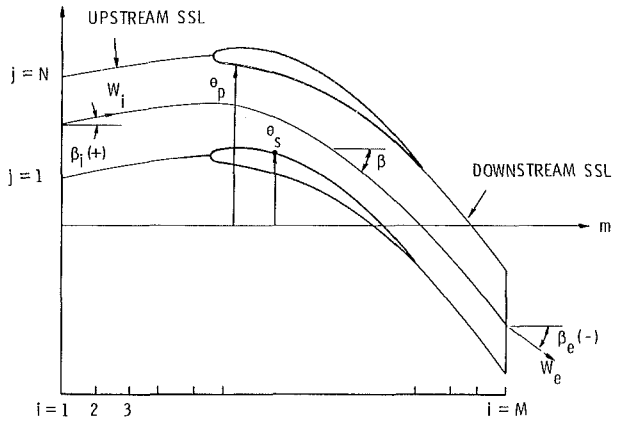

Fig. 2 Blade-to-blade geometry

Numerical Solutions

Numerical solutions for the governing equations (4) and (10) with the boundary conditions equation (11) are obtained using the finite-difference method. Finite difference equations are derived using central difference approximations for the first and second order derivatives in equations (4) and (10).

Finite-Difference Equations for Equation (4)

$$W_m(j)=\frac{\Delta j^2\omega_{j+1}-\Delta^2{}_{j+1}\psi_{j-1}-(\Delta_j{}^2-\Delta_{j+1})\psi_j}{\Delta_j\Delta_{j+1}(\Delta_j+\Delta_{j+1})\rho b_j r_j} \quad (12a)$$

$$W_\theta(j)=W_m(j)\tan(\beta_j) \quad (12b)$$

where

$$\Delta_j=\theta_j-\theta_{j-1} \quad (12c)$$

$$\Delta_{j+1}=\theta_{j+1}-\theta_{j-1} \quad (12d)$$

$$2\le j\le N-1 \quad (12e)$$

At the solid boundaries, $j=1$ and $j=N$, second-order, one-sided formulas are used to approximate equations (4a) and (4b).

Finite-Difference Equations for Equation (10)

$$(a\theta)_{i-1,j}+(a\theta)_{i+1,j}+(a\theta)_{i,j+1}+(a\theta)_{i,j-1}-d_{i,j}=(a\theta)_{i,j} \quad (13)$$

where

$$a_{i-1,j} = \frac{2(r^2 W_m)_1}{(m_{i+1,j} - m_{i-1,j})(m_{i,j} - m_{i-1,j})}, \quad (13a)$$

$$a_{i+1,j} = \frac{2(r^2 W_m)_2}{(m_{i+1,j} - m_{i-1,j})(m_{i+1,j} - m_{i,j})}, \quad (13b)$$

$$a_{i,j-1} = \frac{2b_{i,j}}{(\psi_{i,j+1} - \psi_{i,j-1})(\psi_{i,j} - \psi_{i,j-1})}, \quad (13c)$$

$$a_{i,j+1} = \frac{2b_{i,j}}{(\psi_{i,j+1} - \psi_{i,j-1})(\psi_{i,j+1} - \psi_{i,j})}, \quad (13d)$$

$$a_{i,j} = a_{i-1,j} + a_{i+1,j} + a_{i,j+1} + a_{i,j-1}, \quad (13e)$$

$$b_{i,j} = \left(\frac{pbr}{\cos(\beta)}\right)^2 W_m{}^3 \quad (13f)$$

$$d_{i,j} = \sigma, \quad (13g)$$

$$2 \le i \le M-1. \quad (13h)$$

M is the number of grid points in the meridional direction. The subscripts 1 and 2 in the above equations refer to the grid locations $(i-1/2)$ and $(i+1/2)$, respectively.

Equation (13) is solved numerically using the successive over-relaxation method.

The iterative procedure adopted for solving the governing equations (6) to (10) is as follows:

(1) An initial estimate is made of the position of the streamlines and the velocity field. The number and location of the streamlines at the inlet station are sepcified by the user. The mass flow in each streamtube is defined and consequently the distribution of the stream function ψ (ψ is constant on each streamline). The initial flow exit angle is taken as equal to the blade exit angle.

(2) Equation (10) is solved for the location of the streamlines with the boundary conditions (11).

(3) The velocity field is computed from equations (4*a*) and (4*b*).

(4) Steps (2) and (3) are repeated until convergence is achieved.

(5) The flow exit angle is adjusted to satisfy the Kutta condition (5 adjustments in flow angle were typically required).

Results and Discussion

Numerical results are obtained by solving the unified equation of motion using the successive over-relaxation technique. The over-relaxation factor was varied between 1.0 and 1.2. Under-relaxation parameters were not required for any of the cases considered. All cases computed here required approximately 20 CPU minutes on a VAX 11/780 computer.

Initially, solutions were obtained for the Sawyer stator [9] using a uniform distribution of streamlines. The number of streamlines used varied between 3 and 51. It was found by numerical experimentation that by using streamlines that were closely spaced near the blade surfaces, a smaller number of streamlines could be used to obtain accurate results. Specifically, eleven streamlines, distributed non-uniformly, see Figs. 7 and 9, provided the same results as twenty one uniformly distributed streamlines. By using eleven streamlines, instead of twenty one, the computation time was reduced by approximately a factor of two.

A major consideration for determining the spacing of the meridional calculation stations is the stagger angle of the blade row. The higher the stagger angle becomes, the more difficult it is to resolve the leading edge well. Therefore, for large stagger angles, a nonuniform spacing of the calculation stations was specified with the closest spacing occurring at the leading edge. At low stagger angles, a more uniform spacing of the calculation stations resolved the leading edge well.

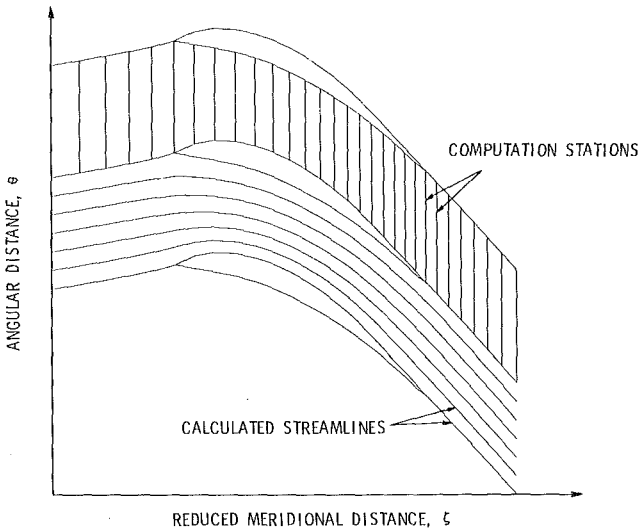

Fig. 3 Computation stations and streamlines

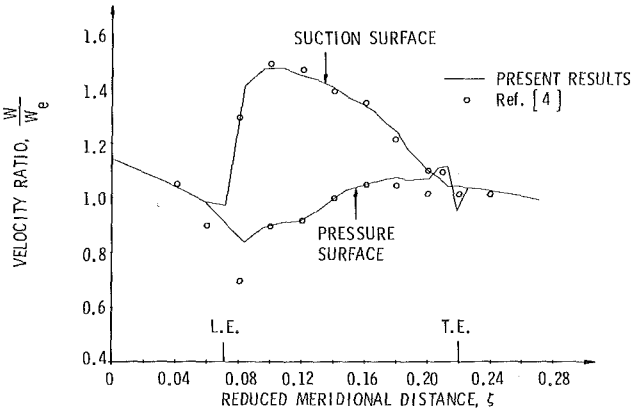

Fig. 4 Blade surface velocity distribution

Several cascades were analyzed, for the incompressible case, in order to verify the method. The numerical results were compared with experimental data and with results obtained using other numerical methods. The effects of rotation, stream sheet thickness and radius change were investigated for the Wilkinson [4] stator and rotor having the same geometry. The first case was the stator in which the effects of radius change and stream sheet thickness variations were investigated. The second case was the rotor which had the additional effect of rotation included. The effects of stagger were investigated with the present analysis and with an independent analysis which used the matrix method [11] with a C-grid. Two blades were analyzed, one having a high stagger angle and one with a low stagger angle. The first case was the Axial Flow Research Fan (AFRF) rotor [8] which was constant stream sheet thickness and radius. The second case was the Sawyer stator [9] which also had constant stream sheet thickness and radius.

The computation stations and calculated streamlines for the Wilkinson stator are shown in Fig. 3. The axial stations are specified while the streamlines are computed. The blade geometry given by Wilkinson [4] did not define the leading edge well. The calculated relative velocity ratio (W/We) distribution is shown in Fig. 4 along with the numerical results from reference [4], which uses the traditional formulation of the streamline curvature method.

The computation stations and calculated relative streamlines for the Wilkinson rotor [4] are shown in Fig. 5. The blade is identical to the previous stator case. The relative inlet flow angle is the same as for the stator. These streamlines

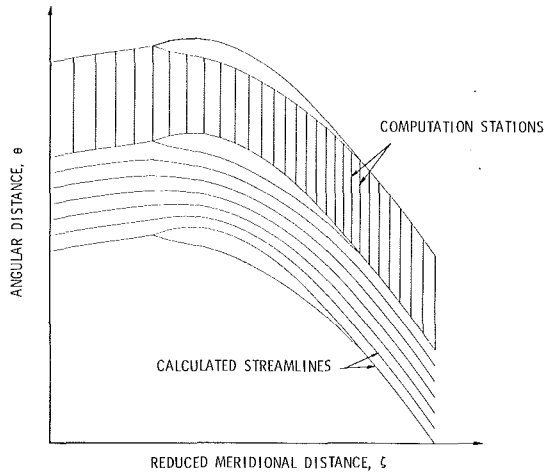

Fig. 5 Computation stations and streamlines

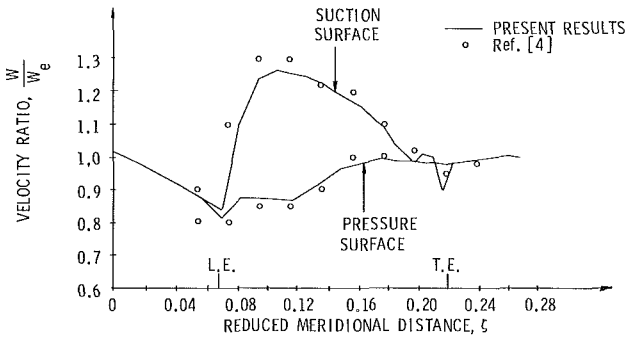

Fig. 6 Blade surface velocity distribution

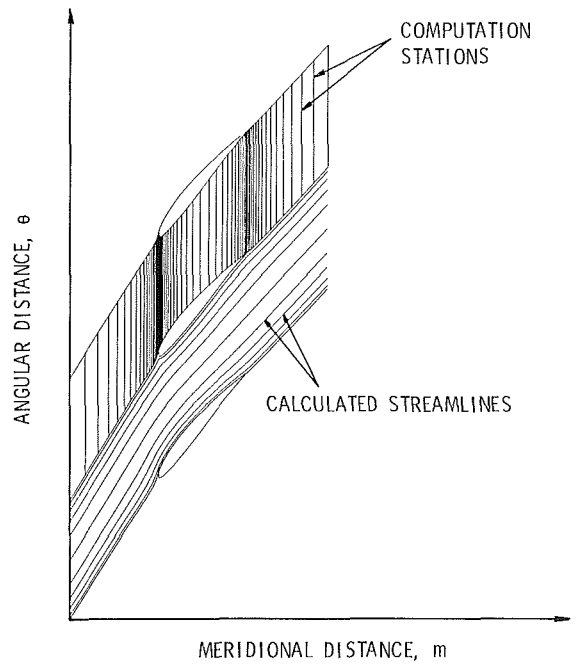

Fig. 7 Computation stations and streamlines

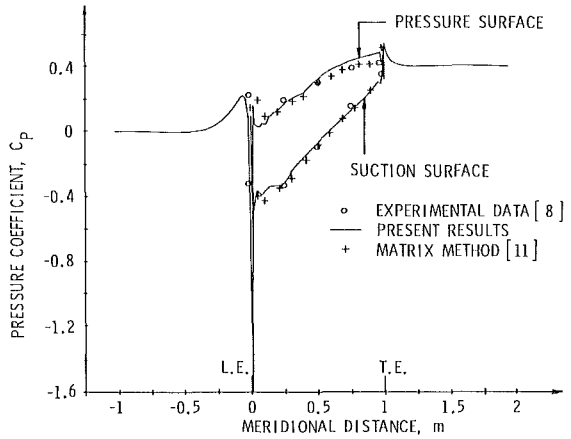

Fig. 8 Blade surface pressure distribution

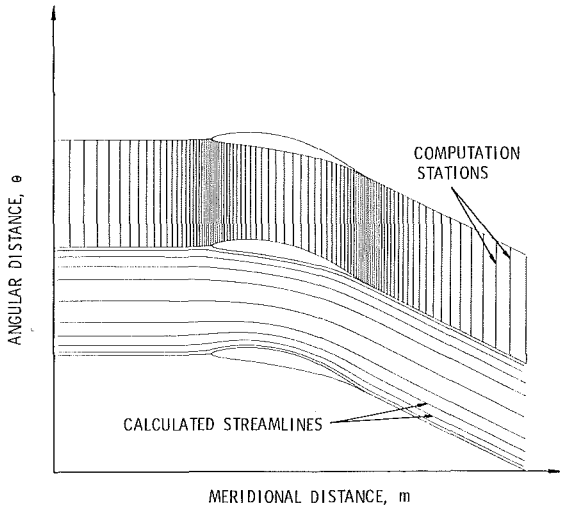

Fig. 9 Computation stations and streamlines

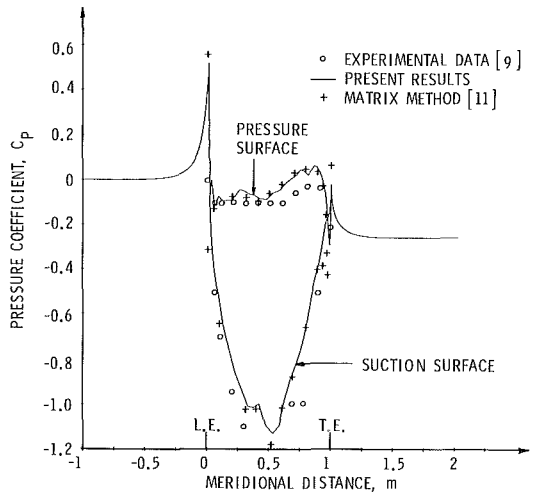

Fig. 10 Blade surface pressure distribution

compare well with Wilkinson's calculated streamline. The velocity ratio distribution for the rotor is shown in Fig. 6, along with the results from reference [4].

The computation stations and calculated relative streamlines for the highly staggered AFRF rotor [8] are shown in Fig. 7. These results are obtained by combining the present method with a meridional solution obtained using the method of reference [3]. The leading edge is not resolved well due to the high stagger angle. The calculated pressure distribution is shown in Fig. 8. Also shown are experimental data [8] and the results of a numerical method which solves the stream function equation in rectilinear coordinates. The stream function solver uses a C-grid which provides better resolution of the leading edge than the present method. This is an especially im-

portant consideration when highly staggered blades are being analyzed.

The computation stations and calculated streamlines for the Sawyer stator [9] are shown in Fig. 9. For low stagger angles, the leading edge pressure distribution is resolved well in the present analysis. The calculated pressure distributions are presented in Fig. 10. Also shown are the experimental results [9] and the numerical results of the stream function solver. The results from both analyses agree well with the experimental data, with the exception of the last quarter chord. This is due to separated flow in this region. Both methods predict a spike on the pressure surface.

Conclusions

A simple approach is developed for the solution of inviscid blade-to-blade flow in turbomachines. The method is applied for the solution of blade-to-blade flow in both rotating and non-rotating passages. The computed results show that the method is stable and does not require any under-relaxation parameters. The present method is similar to the classical SLCM in that both methods do not require the generation of a computational grid. It is different from the classical SLCM in two respects. First, the streamline positions are determined from the momentum equation (UEM) and the velocity field is computed from the continuity equation. The continuity equation here is identically satisfied by using a stream function. The use of the momentum equation to trace the streamline models the ellipticity of the flow field in the tangential and meridional directions explicitly. Second, the present method does not require curve-fitting or under-relaxation that is commonly used in the SLCM.

The most significant problem with the present method is the resolution of the blade leading edge when the cascade stagger angle is large. One approach to eliminating this problem would be to rotate the blade coordinates to reduce the stagger angle. Another method of eliminating this problem would be to use an embedded C-grid in the leading edge region [12].

At the present time, blade-to-blade lossses have not been incorporated into any of the results presented here. However, a loss model is planned to be incorporated to account for losses in both the meridional and tangential directions by modifying the total pressure term in the right hand side of equation (10).

Acknowledgments

This work was conducted at the Applied Research Laboratory of the Pennsylvania State University under the sponsorship of the Naval Sea Systems Command.

References

1 Wu, Chung-Hua, "A General Through-Flow Theory of Fluid Flow With Subsonic or Supersonic Velocity in Turbomachines of Arbitrary Hub and Casing Shapes," NACA TN 2302, 1951.

2 March, H., "A Digital Computer Program for the Through-Flow Fluid Mechanics in an Arbitrary Turbomachine Using a Matrix Method," Aeronautical Research Council R&M No. 3509, 1968.

3 Katsanis, T., and McNally, W. D., "Fortran Progam for Calculating Velocities and Streamlines on Hub-Shroud Mid-Channel Flow Surface of an Axial or Mixed-Flow Turbomachine," NASA TN D-7343, 1973.

4 Wilkinson, D. H., "Calculation of Blade-to-Blade Flow in a Turbomachine by Streamline Curvature," Aeronautical Research Council R&M No. 3704, 1972.

5 Novak, R. A., and Hearsey, R. M., "A Nearly Three-Dimensional Intrablade Computing System for Turbomachinery," ASME JOURNAL OF FLUIDS ENGINEERING, Vol. 99, 1977, pp. 154–166.

6 Marsh, H., "The Through-Flow Analysis of Axial-Flow Compressor," AGARD Lecture Series on Advanced Compressor, AGARD-LS-39-70, 1970.

7 Emery, J. C. et al., "Systematic Two-Dimensional Cascade Test of NACA 65-Series Compressor Blades at Low Speeds," NACA Report 1368, 1958.

8 Pierzga, M. J., "Experimental Verification of the Streamline Curvature Numerical Analysis Method Applied to the Flow Through an Axial Flow Fan," M.S. Thesis, Department of Aerospace Engineering, Pennsylvania State University, Nov. 1980.

9 Sawyer, W. T., "Experimental Investigation of a Stationary Cascade of Aerodynamic Profiles," Institute for Aerodynamics, Swiss Federal Institute of Technology, Zurich, Circa 1950.

10 Abdallah, S., and Henderson, R. E., "Improved Approach to the Streamline Curvature Method in Turbomachinery," ASME JOURNAL OF FLUIDS ENGINEERING, Vol. 109, 1987, pp. 213–217.

11 McBride, M. W., Powers, D. J., and Wagner, M. J., "Calculation of the Exterior Pressure Distribution on an Axisymmetric Propulsor Duct," Applied Research Laboratory, The Pennsylvania State University, TM 83-211, Dec. 1983.

12 Wenquan, Wu, and Jiang, Honge, "A Development in Calculation of Flow Past Cascade on Arbitrary Surface of Revolution," *Computational Methods in Turbomachinery*, IMechE 1984-3, papers read at the conference held at the University of Birmingham on 10-21 Apr. 1984, pp. 265–270.

13 Courant, R., *Differential and Integral Calculus*, Vol. II, Chapter III, Interscience, New York, 1957.

Mean Flow and Turbulence Measurements of Annular Swirling Flows

F. M. Yowakim
Graduate Student.

R. J. Kind
Professor.

Department of Mechanical and Aeronautical Engineering, Carleton University, Ottawa, Canada K1S 5B6

This paper presents the results of a detailed experimental investigation of swirling flows in a cylindrical annulus. Flows having nominal swirl angles of 0, 15, 30, and 45 degrees were measured. Mean velocity components, total and static pressures, wall shear and Reynolds stresses were measured. Mixing length and eddy viscosity distributions were deduced from the data. The majority of the flow field measurements were made with single-sensor hot-wire anemometer probes; six independent readings, each with a different sensor orientation, were made at each point. Consistency checks were applied wherever possible and indicate that the data are of high quality.

1 Introduction

Swirling flows occur in many devices including turbomachinery, cyclone separators, and combustion equipment (Gupta et al., 1984). Swirling flows are physically complex: they are three-dimensional with strongly curved streamlines and their behaviour, especially near solid surfaces, is therefore substantially different from that in nonswirling flows. This paper reports an experimental investigation of several incompressible swirling flows in an annular duct having constant inner and outer radii, r_i and r_o, respectively. Current methods are unable to satisfactorily predict even this relatively simple class of swirling flows (Yamamoto and Millar, 1979; Reddy et al., 1987); the difficulty of course lies in turbulence modelling.

Experimental data, including turbulence measurements, are needed to aid in development of improved turbulence models. The literature contains only mean flow data for swirling flow in annuli (Yeh, 1958; Scott and Rask, 1973; Scott and Bartelt, 1976). The present investigation included comprehensive measurements of Reynolds stresses in four flows, having nominal swirl angles of 0, 15, 30, and 45 degrees; initial swirl numbers, SN, were 0, 0.23, 0.47, and 0.87. The radii r_i and r_o had values of 0.127 and 0.20m, respectively, and the Reynolds number based on mean axial velocity, $\bar{U}$, and hydraulic diameter was 3.1×10^5. $\bar{U}$ was about 32m/s. The data are of high quality and the purpose of this paper is to make them available for guidance of turbulence modelling and for validation of calculation methods. The experimental methods are described and selected data are presented, with emphasis on the 45 degree swirl flow, the most difficult to predict. Complete data for all four flows are presented in the thesis of Yowakim (1985).

Contributed by the Fluids Engineering Division for publication in the JOURNAL OF FLUIDS ENGINEERING. Manuscript received by the Fluids Engineering Division October 10, 1987.

2 Description of Experiments

2.1 Apparatus. Figure 1 shows a schematic of the swirl tunnel used to produce the measured flows. Air from a 2-stage axial blower passed through a honeycomb into a settling chamber. The settling chamber was fitted with three screens, the first one graded, to produce uniform stagnation pressure in the flow entering the contraction leading into the annular working section.

A row of inlet guide vanes (IGV's) at the start of the working section was used to impart swirl to the flow. There were 26 vanes, each having a constant chord of 62 mm and 5.6 mm maximum camber. The vane angle was adjustable to give the desired swirl angle; the vanes were removed to obtain the nonswirling flow. The IGV's were hollow, with a slot in the trailing edge so that air could be ejected to minimize the momentum defect in the wakes; unfortunately the blowing-air supply was insufficient to eliminate the momentum defect and substantial wakes remained. These decayed quite rapidly with downstream distance and no total-pressure defects were detected at the first measurement station, $x/D_h = 1.67$.

The working section ended with a row of straightening vanes so that the flow was discharged with negligible swirl. This avoided mismatch of radial pressure gradient at the annulus exit. The straightening vanes were 1.8m downstream of the IGV's, giving a test section length of 12.3 hydraulic diameters. Values of radii and Reynolds number are stated in the Introduction. The test section was made of mild steel; working surfaces were machined to a smooth finish and segments were accurately aligned so that inner and outer annulus walls were concentric and there were no significant discontinuities at joints. The inner wall was supported by four streamlined struts about 0.5 hydraulic diameters upstream of the IGV's and by the straightening vanes. There were no struts or other obstructions between the IGV's and straightening vanes. The test section was fitted with static pressure taps in the outer and inner walls and five axially aligned ports at

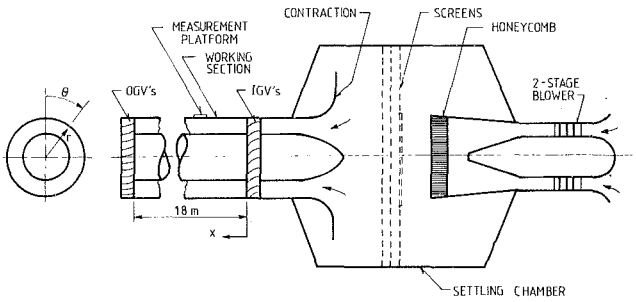

Fig. 1 Schematic of swirl tunnel (not exactly to scale)

which instrumentation could be traversed radially across the flow. Only one port was used at any given time, other ports being smoothly sealed.

Instrumentation consisted of a 3-hole cobra probe, a single channel of constant-temperature hot-wire anemometry (TSI-1053A), single-sensor hot wire probes and Rosemount Model 831A3 pressure transducers. The transducer sensitivity was about 0.12mm of water per mV of output voltage. The cobra probe used tubes of 0.44mm ID, 0.73mm OD, the side tubes being chamfered at 60°. The mouth of the central tube was located on the axis of the 3.2mm diameter probe stem so that the probe could be rotated about this axis without changing the location of the mouth. DISA single-sensor normal (90 deg) and slant (45 deg) hot wire probes, models 55P11 and 55P12, respectively, were used. Sensors were tungsten wires, 5μm diameter and 1.25 mm long. Support prongs and probe holders were straight.

The cobra and hot wire probes were traversed radially at each of the five instrumentation ports using a manual traversing gear. Probe stems or holders were radial with respect to the annular duct and the traverse gear allowed rotation about this radial axis. Radial position, absolute angular orientation and changes in angular orientation (yaw) of the probes could be determined within 0.03 mm, ±1 deg and ±0.1 deg, respectively.

A Hewlett-Packard 3054A data acquisition and control system was used to acquire and process the pressure and hot-wire anemometer data. The system comprised a HP-85A computer, a 3497A acquisition/control unit and a 3456A digital voltmeter. The latter had a nominal sensitivity of 1μV. RMS voltages were measured using a true RMS voltmeter set at a 3 s integration time constant.

Table 1 Azimuth angles for slant and normal hot wire probes with different swirl angles

Nominal swirl angle (degrees)	Slant probes (degrees)	Normal probes (degrees)
45	0, 45, 90	−45, 0, 90
30	0, 45, 90	−45, 0, 90
15	0, 45, 90	−45, 45, 90
0	0, 45, 90	−45, 45, 90

2.2 Experimental Methods. The cobra probe was used only to measure the radial distribution of total pressure and as a Preston tube at the inner wall of the annular duct. At each measurement point the probe was nulled by yawing it until both side tubes gave the same pressure reading. Calibration showed that the central tube gave the correct total pressure when aligned within 5° of the resultant velocity direction in uniform flow. No displacement corrections were applied; available corrections were not expected to be valid because the mouth of this particular probe was very close to the stem (within 3 mm).

When resting against the inner wall, the centre of the cobra probe's mouth was 0.37 mm above the wall, corresponding to $y^+ = 70$. Previous work by Rajaratnam and Muralidhar (1968) and Prahlad (1972) indicates that under such conditions a nulled yaw probe can be used to determine the resultant wall shear stress and its direction. The Preston-tube calibration of Head and Vasanta Ram (1971) was used.

At each measurement point in the flow, six separate readings of mean and RMS anemometer output voltage were taken, three with the normal wire probe and three with the slant wire probe. The probes were rotated about their stems to a different azimuth angle, ψ, for each of the three readings. Mean velocity and Reynolds stress components were deduced from these data as outlined below. Azimuth angles were selected as in Table 1 to minimize wake interference effects from the sensor-support prongs.

For the hot wire probes, the instantaneous effective cooling velocity was assumed to follow the relationship suggested by Jorgenson (1971):

Nomenclature

D_h = hydraulic diameter, $2(r_0 - r_i)$
h, k = probe yaw and pitch sensitivity factors; see equation (1)
K = von Karman constant
l = mixing length; see equation (5)
p = static pressure
p_a = ambient pressure
p_t = total pressure
$\bar{Q}$ = mean resultant velocity
r = radius from axis of annular duct
SN = swirl number; $SN = \int_{r_i}^{r_o} UWr^2 dr / \int_{r_i}^{r_o} r_o U^2 r dr$
$\bar{U}$ = mean axial velocity, the radial average of U
$U_b, U_{\text{eff}}, U_n, U_t$ = components of sensor cooling velocity; see equation (1)
U, V, W = axial (x), radial (r) and tangential (θ) components of mean velocity
u, v, w = axial, radial, and tangential components of turbulent fluctuating velocity
x = axial distance from inlet guide vanes
y = distance from wall
α = complementary angle of sensor to probe stem; see Fig. 2
θ = tangential coordinate
ν = kinematic molecular or eddy viscosity; see equation (4)
ρ = density
τ = shear stress
ψ = sensor azimuth angle; see Fig. 2

Subscripts and Superscripts

i = inner wall
lam = laminar
o = outer wall
w = wall
$rx, r\theta$ = axial and tangential components of Reynolds shear stress, eddy viscosity or mixing length
x, θ = axial and tangential components of wall shear stress
$\bar{}$ = time-averaged (except for U and Q)

$$U_{\text{eff}}^2 = U_n^2 + k^2 U_t^2 + h^2 U_b^2 \quad (1)$$

U_n, U_t, and U_b are, respectively, the velocity components normal to the sensor in the plane of the prongs, tangential to the sensor and normal to the sensor and the prongs (see Fig. 2). The relationship between anemometer bridge output voltage and U_{eff} was found by calibrating the probes in the potential core of a free jet, with the probes oriented such that $U_t = U_b = 0$. This relationship is highly nonlinear and it was fitted with a fourth-order polynomial. This polynomial relationship was used to calculate a linearized output voltage for any given bridge DC output. Multiplication of bridge RMS outputs by the local slope of the polynomial relation gave corresponding "linearized" RMS voltages. This procedure is equivalent to that implemented in hardware form by the TSI Model 1052 linearizer (TSI, 1975) but with the availability of a computer data acquisition system the present method was judged to be more accurate and reliable. Checks showed that it gave the same results as when the hardware linearizer was used. The yaw and pitch sensitivity factors, k and h, were determined by separate calibration steps, using a procedure similar to that suggested by Bruun and Tropea (1980). For k, two separate probe orientations in the calibration flow are used such that $U_b = 0$ and $U_t \neq 0$. Given equation (1) and the other calibration data, k can then be calculated. h is found similarly, using two orientations for which $U_t = 0$, $U_b \neq 0$. Orientations representative of those prevailing during the flow measurements were used for determining k and h.

The velocity components of equation (1) can be re-expressed in terms of the axial, radial and tangential velocity components, $(U + u)$, $(V + v)$ and $(W + w)$ in the annulus. Together with the calibration information, this yields a relationship between instantaneous anemometer output voltage and velocity components. Assuming low turbulence intensity (maximum of 14 percent in the present flows), this relationship can be expanded and split into two equations, one between linearized DC anemometer voltage and the mean velocity components, U, V, and W and the other between linearized RMS voltage and the turbulence parameters $\overline{u^2}$, $\overline{v^2}$, $\overline{w^2}$, $\overline{uv}$, $\overline{uw}$, and $\overline{vw}$. Of course these equations also contain the sensor orientation angles α and ψ (see Fig. 2). α was 0 and 45 deg for the normal and slant-wire probes, respectively (these values were checked and found accurate within 0.2 degrees for all probes). As mentioned, a variety of values was used for azimuth angle ψ (see Table 1). These equations can be written

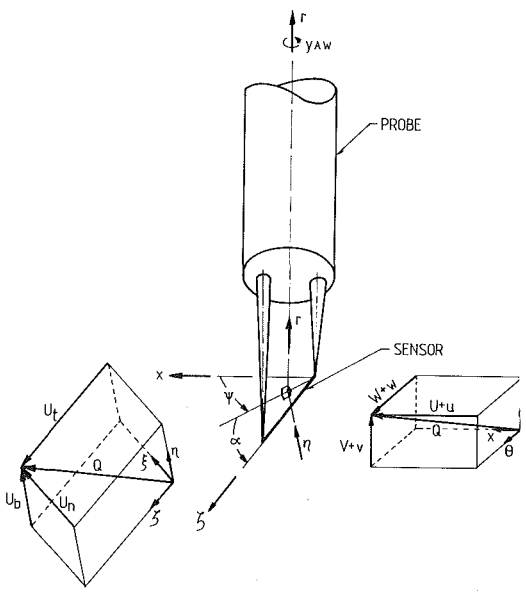

Fig. 2 Probe-fixed and annulus-fixed coordinate systems and velocity components

for each of the six DC and RMS readings made at each measurement point and solved simultaneously for the flow parameters. The system would be over-defined for the mean velocity components and the mean equations were only written and solved for the three readings made with the slant wire probes. The slant wire probes were judged to have the best sensitivity for this purpose.

The above method of measuring mean flow and turbulence parameters is similar to the rotating probe method used by other investigators, for example Bissonette and Mellor (1974) and So and Mellor (1973). Bruun (1977) suggested that all six readings at each point could be taken with the same slant wire probes. Acrivlellis (1978), as modified by Bartenwerfer (1979), suggested a maximum of five measurements with a slant probe and the sixth with a normal probe. In the present work, attempts to take five readings with a single probe were unsuccessful; the resulting equations lacked linear independence. The procedure of three readings with each probe worked best. It should also be noted that Comte-Bellot et al. (1971) found that orienting hot wire probes normal to the flow was not markedly inferior to aligning them with the stream direction.

Hot wire probes were recalibrated about every three hours.

3 Results and Discussion

3.1 Consistency Checks on Data. A number of checks for axisymmetry and consistency were applied to the data. Such checks included: (*a*) mean axial velocity, $\bar{U}$, constant within ± 0.7 percent; (*b*) outer wall static pressure near start of annulus circumferentially uniform within ± 1.5 percent of $0.5\rho\bar{U}^2$; (*c*) dynamic pressure at mid-radius circumferentially uniform within ± 3 percent at all stations; (*d*) axial and angular momentum between stations 1 and 5 conserved within ± 1.7 percent, or better, of the initial momentum or angular momentum. (*e*) comparison of static pressures measured by inner-wall taps with those determined by integration of the radial momentum equation from the outer wall; (*f*) comparison of total pressures measured with the 3-hole probe with those computed from the static pressures and the mean velocity and normal Reynolds stress data; (*g*) comparisons of wall shear stresses measured by Preston tube with those determined from Clauser plots and by extrapolation of the Reynolds shear stresses measured within the flow. The comparisons of (*e*), (*f*), and (*g*) were always very satisfactory; examples can be seen in the figures which present the experimental results.

3.2 Error Estimates. Errors can arise from effects of velocity gradients over the slant wire probes, neglect of higher order turbulence terms in the data reduction equations, imperfect calibration and linearization, position and orientation errors, and sensitivity and repeatability limitations. A detailed error analysis is given by Yowakim (1985). The maximum error on the mean velocity components U and W is estimated at 4 percent and is mainly due to neglect of turbulence terms, calibration errors and repeatability limitations. The radial velocity V is very small and estimated errors on it were over 100 percent; consequently no data for V are presented and it was set to zero in the data reduction calculations. The maximum error is estimated at 15 percent on the Reynolds stresses $\overline{uv}$, $\overline{vw}$, $\overline{u^2}$, and $\overline{w^2}$ and at 20 percent on $\overline{uw}$ and $\overline{v^2}$. As outlined, the Reynolds stresses are obtained by simultaneous solution of six equations representing six separate readings; the errors arise mainly from sensitivity and repeatability limitations.

The quality of the data is perhaps best indicated by the small scatter seen in the figures and by the very good agreement between results obtained by different techniques. Uncertainty estimates are summarized in Table 2.

3.3 Experimental Results. Complete data for all four flows are presented by Yowakim (1985). Only selected data are presented in this paper, with the emphasis on the flow with

strongest swirl. Unless otherwise noted, the solid curves through the data are fitted by eye; they are intended simply to facilitate reading of the graphs.

Figure 3 shows radial distributions of total pressure for the 45 deg swirl flow. A substantial 'core' flow with uniform total pressure is evident at station 1. This core disappears somewhat upstream of station 3. The wall boundary layers thus thicken and merge quite rapidly. There is good agreement between directly measured total pressures and those calculated from the relation

$$p_t = p + 0.5\rho(U^2 + W^2 + \overline{u^2} + \overline{v^2} + \overline{w^2}) \quad (2)$$

Figure 4 shows radial distributions of static pressure for the 45 deg swirl flow. These were calculated by integration of the radial momentum equation, that is

$$p = p_{wo} - \rho\left(\overline{v^2} + \int_r^{r_0} \frac{W^2 + \overline{w^2} - \overline{v^2}}{r}\, dr\right) \quad (3)$$

At the inner wall the static pressure given by equation (3) is generally in excellent agreement with the directly measured values (see Fig. 4); this inspires confidence in the values at intermediate radii.

Figures 5(*a*) and (*b*) present radial distributions of the axial and swirl mean velocity components. Figure 6 presents results for the axial and tangential components of wall and Reynolds shear stresses. Both figures are for the 45 degree swirl flow. The wall shear stresses were determined using a Clauser plotting technique based on an extended form of the law-of-the-wall, suitable for swirling flows (Yowakim, 1985; Kind et al., 1988). These wall values are seen to be entirely consistent with the Reynolds shear stresses measured in the flow using the hot-wire anemometer. Preston-tube data are available at the inner wall and are in good agreement with the other results. The

Table 2 Uncertainty estimates

Quantity	Estimated uncertainty at 20:1 odds
radial position $(r-r_i)/(r_o-r_i)$	±0.0005
wall static pressures, $(p-p_a)/0.5\ \rho\bar{U}^2$	±0.02
total pressures $(p_t-p_a)/0.5\rho\bar{U}^2$	±0.05
mean velocity components, U, W	±4 percent
wall shear stress $\tau_{xw}, \tau_{\theta w}/0.5\rho\bar{U}^2$	±0.0002 from Clauser plots ±0.0003 from Preston tube
Reynolds stresses $\overline{uv}$, $\overline{vw}$, $\overline{u^2}$, $\overline{w^2}$	±15 percent
Reynolds stresses $\overline{uw}$, $\overline{v^2}$	±20 percent
mixing lengths l_{rx}, $l_{r\theta}$	±10 percent
eddy viscosities ν_{rx}, $\nu_{r\theta}$	±15 percent

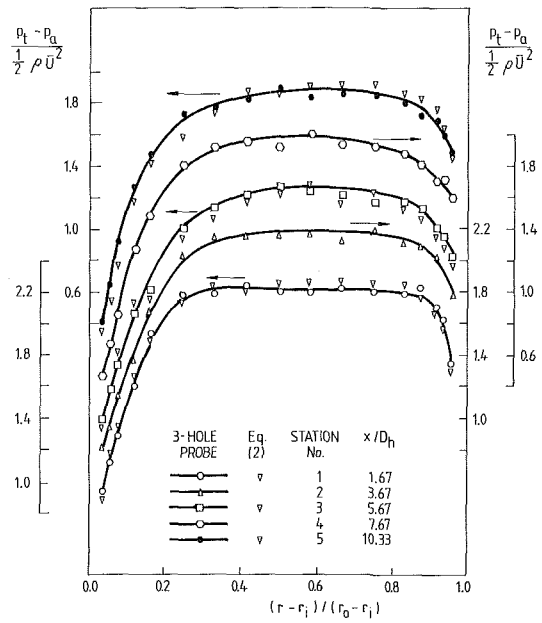

Fig. 3 Radial distributions of total pressure for 45 degree swirl flow ($\bar{U}$ = 32.6 m/s)

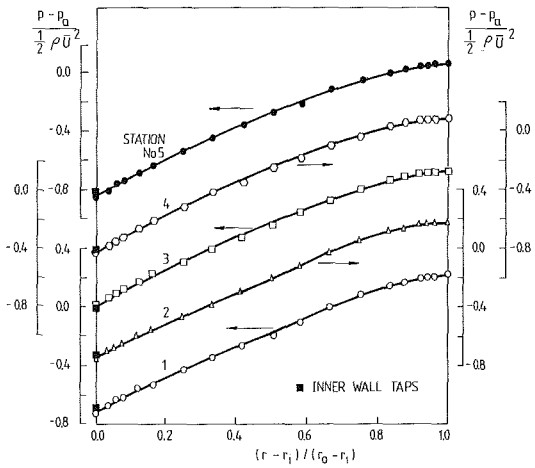

Fig. 4 Radial distributions of static pressure for 45 degree swirl flow

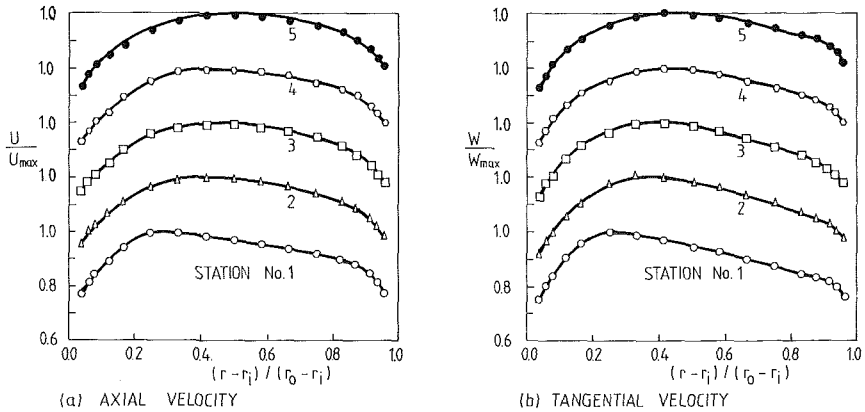

Fig. 5 Radial distributions of axial and tangential mean velocity components in 45 degree swirl flow. U_{max} = 36.8, 36.0, 35.6, 35.5, 35.2 m/s; W_{max} = 37.8, 36.4, 34.7, 33.6, 33.1 m/s; $\bar{U}$ = 32.7, 32.6, 32.8, 32.6, 32.9 m/s; at stations 1 to 5 respectively.

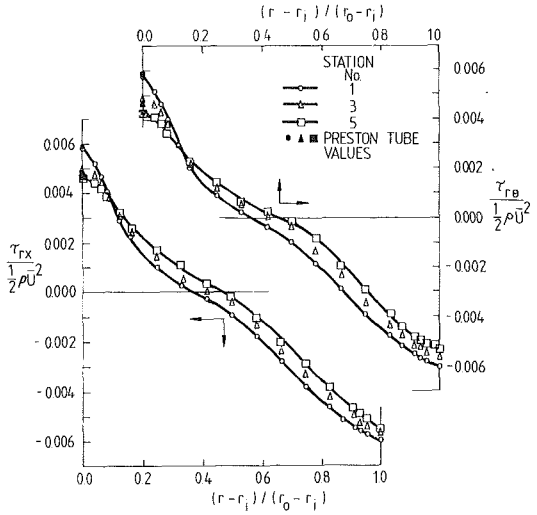

Fig. 6 Radial distributions of axial and tangential shear stress in 45 degree swirl flow (wall values are from Clauser plots; Preston-tube values are also shown for inner wall)

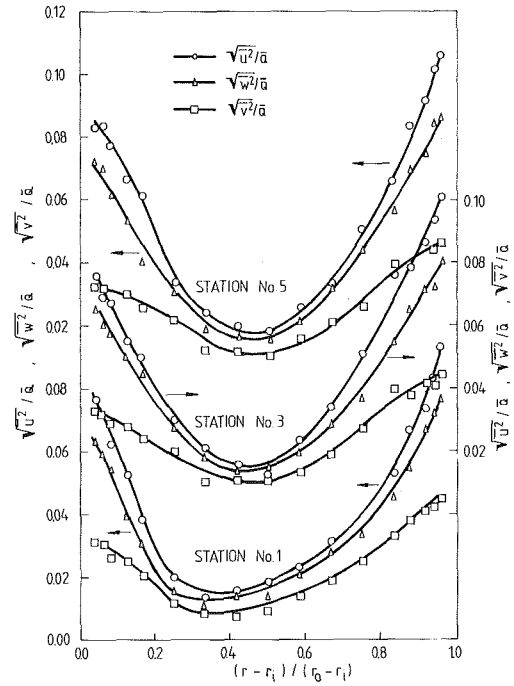

Fig. 7 Radial distributions of turbulent fluctuation velocities in 45 degree swirl flow ($\bar{Q}$ = 45.5, 43.9, 43.1 m/s at stations 1, 3, 5 respectively)

radial gradients of the measured shear stress distributions near the walls were also found to be in excellent agreement with those given by the axial and tangential momentum equations with convection terms neglected.

Figure 7 presents data for the turbulent fluctuation velocities for the 45 degree swirl flow.

Figures 8 to 11 present additional data for mean velocities, wall static pressures and wall shear stresses. The data are sufficient to enable predictive calculations. The shear stresses on the outer wall are seen to be generally higher than those on the inner wall for the swirling flows. This reflects the unstable and stable gradients of angular momentum near the outer and inner walls, respectively. Transverse curvature also has some influence; the ratio of inner to outer wall shear stress for the non-swirling flow is in excellent agreement with the work of Pletcher and Malik (1979).

For present purposes, eddy-viscosities and mixing lengths are defined by the relations suggested by Lilley and Chigier (1971):

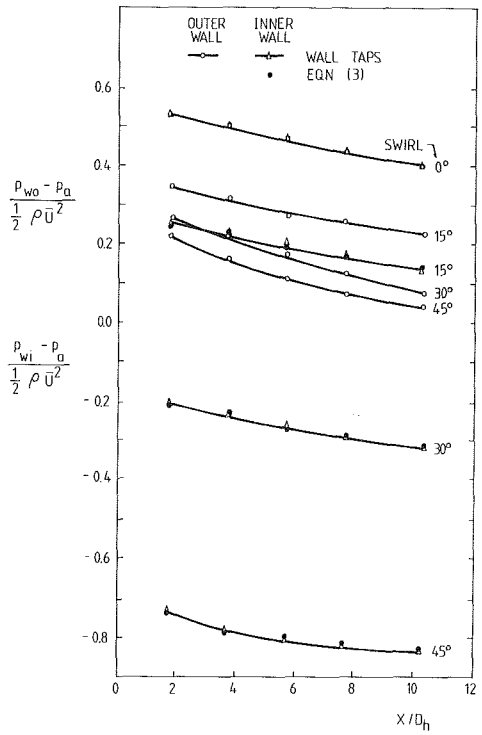

Fig. 9 Axial distributions of wall static pressures

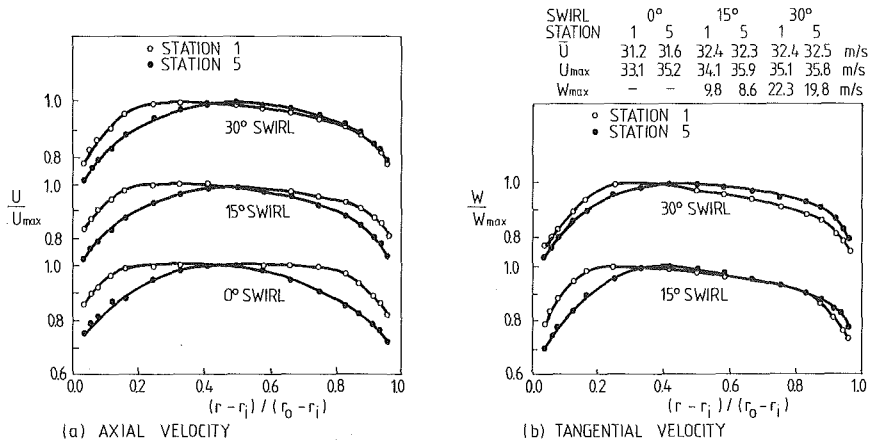

Fig. 8 Radial distributions of axial and tangential mean velocity components in 0, 15, and 30 degree swirl flows

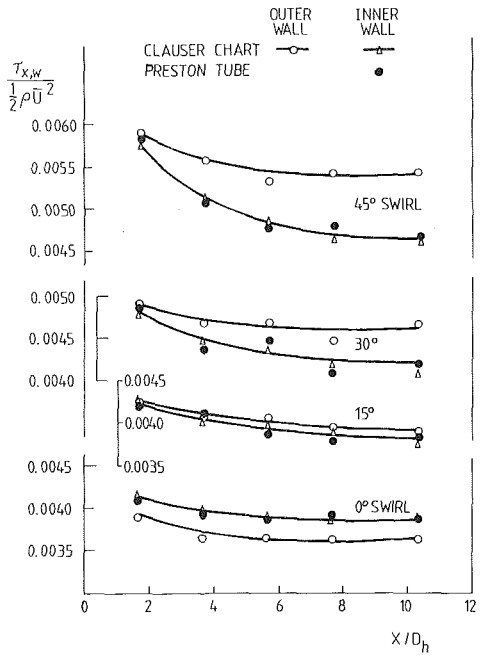

Fig. 10 Axial distributions of axial component of wall shear stress

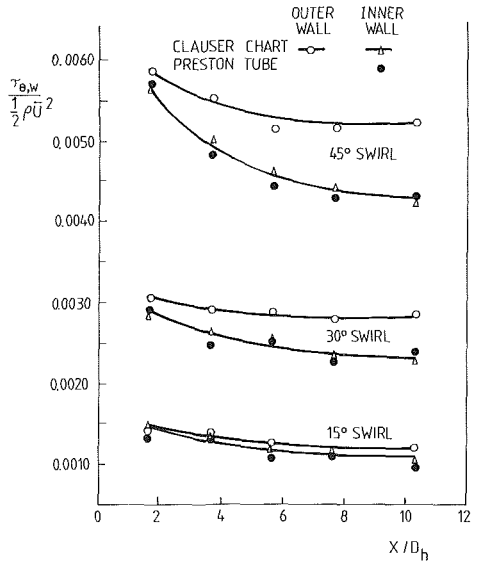

Fig. 11 Axial distributions of tangential component of wall shear stress

$$\nu_{rx} = -\overline{uv}/\left(\frac{\delta U}{\delta r}\right) \quad \nu_{r\theta} = -\overline{vw}/\left(r\frac{\delta}{\delta r}\left(\frac{W}{r}\right)\right) \tag{4}$$

$$l_{rx}^2 = \nu_{rx}/\left[\left(\frac{\delta U}{\delta r}\right)^2 + \left(r\frac{\delta}{\delta r}\left(\left(\frac{W}{r}\right)^2\right)\right]^{1/2} \quad l_{r\theta}^2 = l_{rx}^2\,\frac{\nu_{r\theta}}{\nu_{rx}} \tag{5}$$

Figure 12 presents data for the mixing lengths at the last measurement station. The mixing lengths are seen to be almost independent of the degree of swirl, especially near the inner wall, and to be approximately isotropic. Geometry, as represented by the ratio r_o/r_i, appears to have more effect than swirl. The mixing lengths are seen to agree rather well with the relations

$$l_{rx} = Ky\sqrt{\frac{\tau_{rx}}{\tau_{x,w}}} \quad l_{r\theta} = Ky\sqrt{\frac{\tau_{r\theta}}{\tau_{\theta,w}}} \tag{6}$$

suggested by the work of Galbraith et al. (1977). The extended law of the wall is based on equation (6). Some eddy viscosity

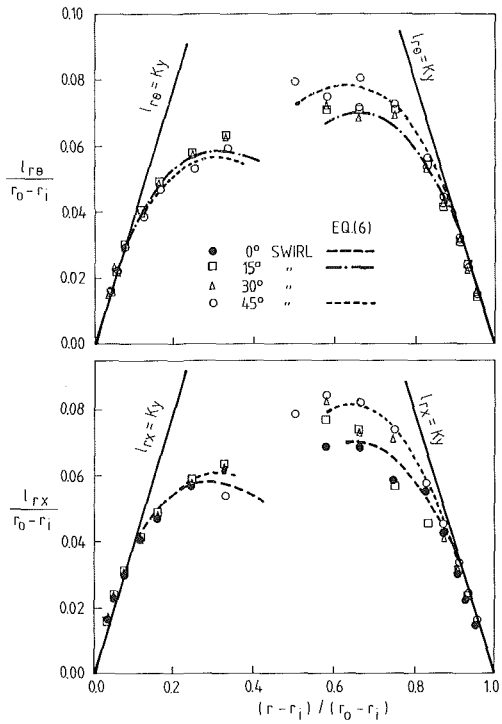

Fig. 12 Radial distributions of mixing lengths at station 5

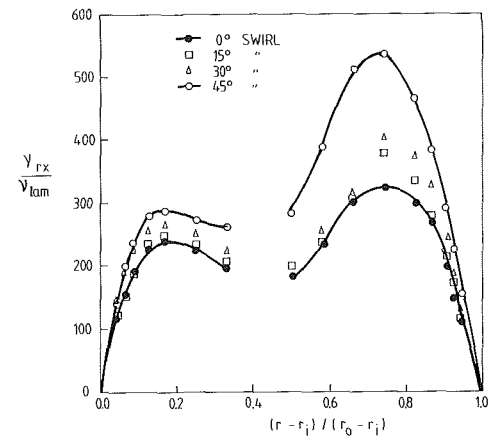

Fig. 13 Radial distributions of axial component of eddy viscosity at station 5

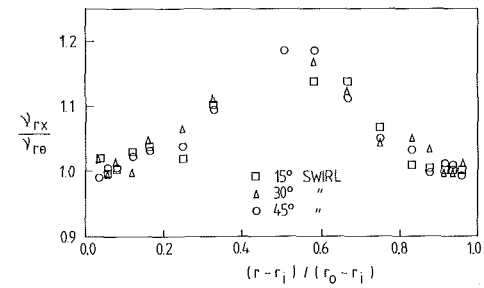

Fig. 14 Radial distributions of eddy viscosity ratio $\nu_{rx}/\nu_{r\theta}$ at station 5

data are presented in Figs. 13 and 14. The eddy viscosities exhibit more dependence on degree of swirl than the mixing lengths. They also exhibit some anisotropy (Fig. 14) but this is not pronounced.

4 Conclusions

Detailed mean flow and turbulence measurements have been obtained for several swirling flows in a cylindrical annulus. Consistency checks have been applied to the data wherever possible and the quality of the data appears to be very good. The data are considered suitable to guide development of and assess computational methods for this important class of three-dimensional flows.

Acknowledgments

Acknowledgments are due to D. A. J. Millar who developed the swirl tunnel and initiated this work. Financial support from the Natural Sciences and Engineering Research Council is also gratefully acknowledged.

References

Acrivlellis, M., 1978, "An Improved Method for Determining the Flow Field of Multidimensional Flows of Any Turbulence Intensity," *DISA Information*, No. 23.

Bartenwerfer, M., 1979, "Letters to the Editors—Comments on: The Method for Analyzing Hot-wire Signals," *DISA Information*, No. 24.

Bissonnette, L. R., and Mellor, G. L., 1974, "Experiments on the Behaviour of an Axisymmetric Turbulent Boundary Layer With a Sudden Circumferential Strain," *J. Fluid Mech.*, Vol. 63, pp. 369–413.

Brunn, H. H., and Tropea, C., 1980, "Calibration of Normal, Inclined and X-Array Hot Wire Probes," University of Karlsruhe SFB 80/M/170.

Bruun, H. H., 1977, "A Review of Conventional and Some Advanced Hot-wire Measurements and Their Physical Interpretation," von Karman Inst. for Fluid Dynamics, Lecture Series 96.

Comte-Bellot, G., Strohl, A., and Alcaraz, E., 1971, "On Aerodynamic Disturbances Caused by Single Hot-Wire Probes," ASME *Journal of Applied Mechanics*, Vol. 38, pp. 767–774.

Galbraith, R. A., McD., Sjolander, S., and Head, M. R., 1977, "Mixing Length in the Wall Region of Turbulent Boundary Layers," *Aero. Quart.*, Vol. XXVII, pp. 97–110.

Gupta, A. K., Lilley, D. G., and Syred, N., 1984, *Swirl Flows*, Abacus Press, Tunbridge Wells, U. K. and Cambridge, Mass., 1984.

Head, M. R., and Vasanta Ram, M. R., 1971, "Simplified Presentation of Preston Tube Calibration," *Aero Quarterly*, Vol. XXII, pp. 295–300.

Jorgensen, F. E., 1971, "Directional Sensitivity of Wire and Fiber-film Probes," *DISA Information*, No. 11.

Kind, R. J., Yowakim, F. M., and Sjolander, S. A., 1987, "The Law of The Wall for Swirling Flow in Annular Ducts," to be published in ASME JOURNAL OF FLUIDS ENGINEERING.

Lilley, D. G., and Chigier, N. A., 1971, "Nonisotropic Turbulent Stress Distribution in Swirling Flows from Mean Value Distributions," *Int. J. Heat Mass Transfer*, Vol. 14, pp. 573–585.

Pletcher, R. H., and Malik, M. R., 1979, "Prediction of Turbulent Flow Heat Transfer in Annular Geometries," in: *Turbulent Forced Convection in Channels and Bundles, Theory and Applications to Heat Exchangers and Nuclear Reactors*, Vol. 1, Advanced Study Institute book, ed., Kakac, S., and Spalding, D. B., Hemisphere Pub. Corp., N.Y.

Prahlad, T. S., 1979, "Yaw Characteristics of Preston Tubes," *AIAA J.*, Vol. 10, No. 3, pp. 357–359.

Rajaratnam, N., and Muralidhar, D., 1968, "Yaw Probe Used as Preston Tube," *The Aeronautical Journal*, Vol. 72, pp. 1059–1060.

Reddy, P. M., and Kind, R. J., and Sjolander, S. A., 1987, "Computation of Turbulent Swirling Flow in an Annular Duct," *Proc. 5th International Conference on Numerical Methods in Laminar and Turbulent Flow*, Montreal.

Scott, C. J., and Rask, D. R., 1973, "Turbulent Viscosities for Swirling Flow in a Stationary Annulus," ASME JOURNAL OF FLUIDS ENGINEERING, Vol. 95, pp. 557–566.

Scott, C. J., and Bartelt, K. W., 1976, "Decaying Annular Swirl Flow With Inlet Solid Body Rotation," ASME JOURNAL OF FLUIDS ENGINEERING, Vol. 98, pp. 33–40.

So, R. M. C., and Mellor, G. L., 1973, "Experiment on Convex Curvature Effects in Turbulent Boundary Layers," *J. Fluid Mech.*, Vol. 60, pp. 43–62.

TSI Inc., 1975, "TSI Instruction Manual for Model 1052 Linearizer," Thermo-Systems Inc., St. Paul, Minnesota.

Yamamoto, A., and Millar, D. A. J., 1979, "A Calculation of Laminar and Turbulent Swirling Flows in Cylindrical Annuli," in: *Flow in Primary, Non-Rotating Passages in Turbomachines*, ed. Herring, H. J., Soler, A., and Steltz, W. G., ASME, N. Y., pp. 89–98.

Yeh, H., 1958, "Boundary Layer Along Annular Walls in a Swirling Flow," ASME *Journal of Basic Engineering*, Vol. 80, pp. 767–776.

Yowakim, F. M., 1985, "Experimental Investigation of Turbulent Swirling Flow in an Annulus," Ph.D. thesis, Carleton University, Ottawa, Ontario, Canada.

Turbulence Measurements With Symmetrically Bent V-Shaped Hot-Wires. Part 1: Principles of Operation

M. Hishida[1]
Professor.

Y. Nagano
Professor.
Mem. ASME

Department of Mechanical Engineering,
Nagoya Institute of Technology,
Gokiso-cho, Showa-ku,
Nagoya 466, Japan

A new anemometry technique has been developed for turbulence measurements near the wall, where the conventional X-wire method is subject to large errors due to aerodynamic disturbances caused by the tips of wire supports. The technique proposed in this study is founded on the principle of convective heat transfer from a symmetrically bent V-shaped hot-wire, which can be supported just like a cantilever. The present paper describes the details of effective cooling velocities of a V-shaped hot-wire, together with the related comments on its aeroelastic deformation and vibration.

Introduction

The hot-wire anemometers have been and will likely continue to be among the most versatile and widely used instruments for obtaining quantitative information on turbulent flows. The anemometry technique, however, is not yet fully established, and vigorous efforts are still being devoted to deepen the understanding of hot-wire anemometer systems and/or to develop a new anemometry technique. The present state-of-the-art is given by Blackwelder [1], Perry [2], Fingerson and Freymuth [3], and Smol'yakov and Tkachenko [4].

It is now well known that the structure of near-wall turbulence plays an important role in the dynamics of wall-turbulent shear flows, and many of the attributes of wall-turbulent flows can be ascribed to the coherent motions near the wall (e.g., see Kim, Kline and Reynolds [5], Willmarth and Bogar [6], and Hussain [7]). Studies by various visualization methods in shear layers and wall-bounded flows offer abundant qualitative knowledge of coherent structures. On the other hand, until recent years little quantitatively authentic information has been available on the near-wall layer structure. Thus, an accumulation of quantitative information on the structure of near-wall turbulence is now evidently required.

A lack of quantitative results of the flow structure close to the wall is mainly due to the great difficulties of accurate hot-wire measurements of the Reynolds stresses near the wall. Such experiments have usually been performed by using an X-wire anemometry technique. However, when this technique is employed in a turbulent flow near the wall, the support system which comprises of prongs (i.e., support needles) and the probe body signficantly distorts the flow field and introduces serious errors into the measurements. In addition, the conventional X-wire probe is kept somewhat away from the wall by its supports. Hence, for the study of near-wall turbulence, a development of a novel technique for measurements is of prime importance.

The technique proposed in this study is based on the principle of convective heat transfer from a symmetrically bent V-shaped hot-wire. In our previous paper [8], the heat transfer characteristics of a bent hot-wire in an extremely narrow 'V' shape were investigated. The recognized anomalous attributes of such hot-wires may be ascribed to the effects of aerodynamic and thermal wake disturbances caused by the hot-wire filaments composing the legs of the 'V' shape. The present series of investigations are designed to obtain universal information on the V-shaped hot-wires with large vertex angles, which are free from undesirable wire interference, and to establish a new anemometry technique for turbulence measurement. In this paper the principles of operation of a single V-shaped hot-wire are given, together with some remarks on its aeroelastic behaviour. In our next report, the principles of turbulence measurements are to be described along with associated probe arrangements, and it will be shown that the proposed technique is highly effective for the measurement of turbulence in close proximity to the wall, where the conventional X-wire anemometry technique is either subject to large errors or at worst cannot be used.

A Conventional Inclined Straight Hot-Wire

The directional dependence of heat transfer characteristics of an inclined straight hot-wire can properly be expressed by the effective cooling velocity [1–3]. Several expressions for the effective cooling velocity U_e have been suggested [9–14]. Among others, the following functional form evolved by Hinze [9] is now widely used [1–3]:

[1] Present address: Chubu University, Department of Mechanical Engineering, Matsumoto-cho, Kasugai 487, Japan.

Contributed by the Fluids Engineering Division for publication in the JOURNAL OF FLUIDS ENGINEERING. Manuscript received by the Fluids Engineering Division August 7, 1985.

$$U_e^2 = U_n^2 + k^2 U_t^2$$

$$= U^2\{1-(1-k^2)\cos^2\gamma\} \quad (1)$$

where U is the instantaneous fluid velocity, γ is the angle between U and the axis of the hot-wire, and U_n and U_t are the components of the velocity vector normal and parallel to the hot-wire, respectively. For a given type of wire, the tangential sensitivity coefficient of hot-wire, k, is generally dependent upon the wire orientation and the fluid velocity.

The relationship between the average heat transfer coefficient of a hot-wire, h, and the effective cooling velocity is customarily expressed as:

$$h = A + BU_e^n \quad (2)$$

with n, A, and B constants.

The corresponding thermal equilibrium of a hot-wire operated in constant-temperature mode can be written as:

$$\pi d h(T - T_a) = i^2 R \quad (3)$$

where T and T_a are the wire and the fluid temperatures, respectively, and R denotes the electric resistance of the wire per unit length. The temperature dependence of the wire resistance can adequately be expressed as:

$$R = R_0\{1+\beta(T-T_0)\} \quad (4)$$

With equation (4), rewriting equation (3) gives:

$$h(R-R_a) = Ci^2R \quad (5)$$

in which R_a denotes the wire resistance corresponding to an ambient fluid temperature T_a, and C is a constant given by:

$$C = \beta R_0/\pi d$$

A V-Shape Hot-Wire

A fine wire is symmetrically bent into a V-shape at an angle 2α (an angle of vertex) and oriented at a certain angle to the flow, as shown in Fig. 1. The axis of symmetry of V-shaped wire is in the xy-plane and the velocity vector in the xz-plane. Let ϕ be the angle between the xz-plane and the plane in which the V-shaped wire is located, and ψ be the angle between the velocity vector and the x-axis. In what follows, ϕ and ψ are referred to as the pitch and the side-slip angles, respectively, and the subscripts 1 and 2 pertain to each side of the V-shaped wire.

In case a V-shaped wire is operated as a constant temperature hot-wire, the overall resistance of the V-shaped wire is kept constant, so that:

$$R_1 + R_2 = 2R_m = \text{const.}$$

where R_m is the average resistance of the V-shaped hot-wire.

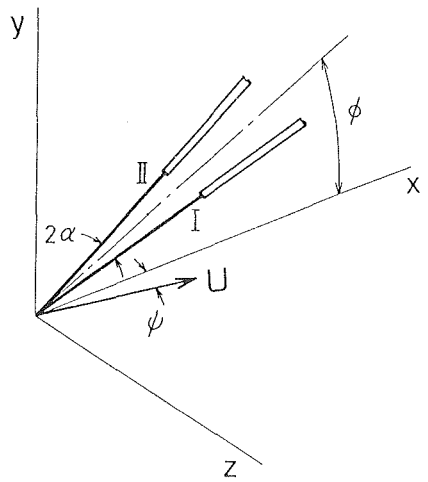

Fig. 1 Orientation of a V-shaped hot-wire with respect to flow

Following the thermal equilibrium for a conventional inclined straight hot-wire, given by equation (5), the energy equation for a V-shaped hot-wire can be written as:

$$h_{ov}(R_m - R_a) = Ci^2R_m \quad (6)$$

where h_{ov} is the "overall" heat transfer coefficient of the V-shaped hot-wire, or conversely equation (6) may be regarded as the defining equation of h_{ov}. As is demonstrated in Appendix A, h_{ov} can be approximated with a high accuracy as:

$$h_{ov} \simeq h_m = (h_1 + h_2)/2 \quad (7)$$

If the convective cooling from a V-shaped hot-wire obeys the law similar to that for a straight wire, the relation between the overall heat transfer coefficient h_{ov} and the overall effective cooling velocity U_{eov} can be written as:

$$h_{ov} = A + BU_{eov}^n \quad (8)$$

with n, A, and B constants (but may differ from those for straight hot-wires).

The 'overall' effective cooling velocity U_{eov} is, as derived in Appendix B, nearly identical to the average effective cooling velocity of the V-shaped hot-wire, so that:

$$U_{eov} \simeq U_{em} \quad (9)$$

where $U_{em} = (U_{e1} + U_{e2})/2$.

Effective Cooling Velocity of a V-Shaped Hot-Wire

Using the coordinate system shown in Fig. 1, one of the angles γ which a flow velocity vector U makes with the axis of

Nomenclature

d = wire diameter
F = direction-sensitivity characteristic, equation (16)
h = convective heat transfer coefficient
i = current through wire
k = tangential sensitivity coefficient
m = resistive overheat ratio
Nu = Nusselt number
n = exponent of Reynolds number (velocity) in heat transfer correlations
R = wire resistance per unit length
Re = Reynolds number
T = wire temperature
T_a = ambient temperature of fluid
U = fluid velocity past wire
U_e = effective cooling velocity of wire
α = half of the vertex angle of V-shaped wire
γ = angle which velocity vector makes with wire axis
λ = thermal conductivity of fluid
ν = kinematic viscosity of fluid
ϕ = pitch angle of V-shaped wire
ψ = side-slip angle of V-shaped wire

Subscripts

a = conditions at ambient temperature T_a
1, 2 = each side of V-shaped wire
m = mean value

the hot-wire (hereafter referred to as an angle of attack) is expressed for each side of the wire as follows:

$$\cos\gamma_1 = \cos\alpha\cos\phi\cos\psi + \sin\alpha\sin\psi \tag{10a}$$

$$\cos\gamma_2 = \cos\alpha\cos\phi\cos\psi - \sin\alpha\sin\psi \tag{10b}$$

The effective cooling velocity for the V-shaped hot-wire can be written, from equations (1) and (10), as:

$$U_{em} = U(\{1-(1-k_1^2)\cos^2\alpha\cos^2\psi(\cos\phi+\tan\alpha\tan\psi)^2\}^{1/2} + \{1-(1-k_2^2)\cos^2\alpha\cos^2\psi(\cos\phi - \tan\alpha\tan\psi)^2\}^{1/2})/2 \tag{11}$$

Let $\cos\gamma_m$ be the average of $\cos\gamma_1$ and $\cos\gamma_2$, and we get:

$$\cos\gamma_m = (\cos\gamma_1 + \cos\gamma_2)/2 = \cos\alpha\cos\phi\cos\psi \tag{12}$$

Under typical working conditions $\phi = 30$ deg, $\alpha = 15$ deg, and $\psi < 11.3$ deg (which corresponds to $\tan\psi = w/\bar{U} < 0.2$, where w and $\bar{U}$ are the fluctuating velocity component in the z-direction and the time-averaged velocity in the x-direction, respectively), as described later, we can approximate equation (11) as:

$$U_{em} \simeq U[\{1-(1-k_m^2)\cos^2\alpha\cos^2\psi(\cos\phi+\tan\alpha\tan\psi)^2\}^{1/2} + \{1-(1-k_m^2)\cos^2\alpha\cos^2\psi(\cos\phi-\tan\alpha\tan\psi)^2\}^{1/2}]/2 \tag{13a}$$

where k_m denotes the value of k for $\gamma = \gamma_m$.

The absolute error due to the approximation of U_{em} to equation (13*a*) remains less than 0.4 percent. The following provides a fairly good approximation to equation (13*a*):

$$U_{em} \simeq U\{1-(1-k_m^2)\cos^2\alpha\cos^2\psi(\cos^2\phi+\tan^2\alpha\tan^2\psi)\}^{1/2} \tag{13b}$$

And further approximation yields:

$$U_{em} \simeq U\{1-(1-k_m^2)\cos^2\alpha\cos^2\psi\cos^2\phi\}^{1/2} \tag{13c}$$

The resulting errors in U_{em} associated with the approximation of equation (13*a*) to equations (13*b*) and (13*c*) do not exceed 0.57 and 0.90 percent, respectively.

Heat Transfer Function

The average heat transfer rate from the V-shaped hot-wire placed normal to the air flow, i.e., $\psi = 0$ deg and $\phi = 90$ deg, is a function of both the fluid velocity and the vertex angle of the wire, as presented in Fig. 2, where $\mathrm{Nu} = h_{ov}d/\lambda$ and $\mathrm{Re} = Ud/\nu$. The hot-wire tested was $d = 5\mu$m diameter and $2L = 1$ mm length (effective total length), and the temperature loading of the hot-wire was $T_f/T_a = 1.265$ where T_f is the film temperature given by $T_f = (T_w + T_m)/2$. The thermal conductivity λ and the kinematic viscosity ν of the fluid were evaluated at T_f.

As seen from Fig. 2, the relationship between Nusselt number Nu and Reynolds number Re can be written as:

$$\mathrm{Nu} = A + BR_e^n \tag{14}$$

with n, A, and B shown to be functions of vertex angle α. For $\alpha = 90$ deg, which corresponds to a straight normal wire, equation (14) becomes:

$$\mathrm{Nu} = 0.615 + 0.683\mathrm{Re}^{0.45} \quad \text{for } 0.2 < \mathrm{Re} < 6.8 \tag{15}$$

In the case of the conventional normal wire, various empirical heat transfer formulae have been proposed [1–3, 9, 15]. The correlation of Collis and Williams [16] is now considered to express well the heat transfer rate from a fine wire of very large aspect ratio, say $2L/d > 1000$. However, the aspect ratio $2L/d$ of hot-wires commonly used in anemometry practice

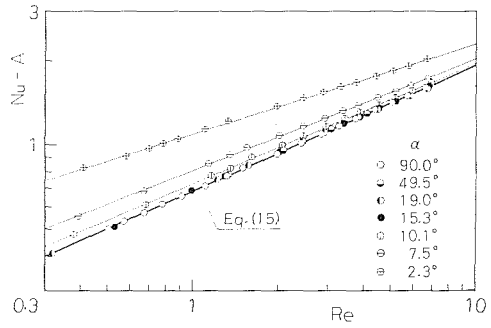

Fig. 2 Heat transfer rate from a V-shaped hot-wire placed normal to flow ($\psi = 0$ deg, $\phi = 90$ deg). Uncertainty in Nu is ±1.8 percent, in Re ± 2.1 percent at 20:1 odds.

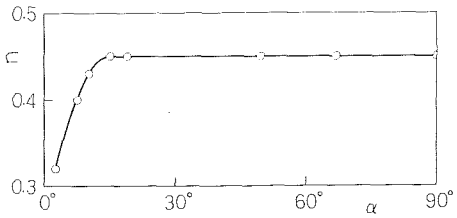

Fig. 3 Dependence of the exponent of Reynolds numbers in heat transfer correlations on the half vertex angle of a V-shaped hot-wire

ranges from 150 to 300, and hence their effect on heat transfer characteristics becomes significant [15]. Equation (15) is established for wires of $2L/d = 200$, and is found to be in excellent agreement with the relation obtained by Koch and Gartshore [17] for DISA miniature hot-wire probe ($2L/d = 230$). It should be noted that equation (15) covers the fluid velocity range from 1 m/s to 30 m/s.

From Fig. 2, it is found that the heat transfer coefficient of the V-shaped hot-wire for half vertex angle larger than 15 deg becomes a single function of fluid velocity regardless of the value of the vertex angle. This suggests that a symmetrically bent V-shaped hot-wire of $\alpha > 15$ deg works in the same manner as a straight hot-wire. The exponent n in equation (14) for wires of $\alpha < 15$ deg, however, changes with the vertex angle, as is evidenced in Fig. 3. This can be attributed to the anomalous effects of aerodynamic and thermal wake disturbances caused by the hot-wire filaments composing the adjacent legs of the 'V' shape. In turbulent flows, the instantaneous direction of the fluid velocity vector changes with time. Thus, in order to minimize any unexpected problems introduced by the wire interference effects, the half vertex angle of a V-shaped hot-wire should be made larger than 15 deg. (For practical applications, it is to be recommended that the limiting value of the vertex angle is determined by the calibration for a given type of wire.)

Tangential Sensitivity Coefficient

In a qualitative sense, the role of convective cooling by the tangential velocity component in heat transfer characteristics of inclined hot-wires is fairly well understood. Yet, the reported discrepancies in the measured values of the tangential sensitivity coefficient of inclined hot-wire, k, are far too great [10, 13, 14, 18, 19]. Although these results are helpful in the understanding of the problem, the lack of agreement is a source of concern. Further work is evidently still needed. In general, the value of k for inclined straight hot-wires depends upon the type of probe, the wire Reynolds number and the probe orientation with respect to the flow. Particularly the aerodynamic effects from both the support needles and the probe body significantly affect the readings [13, 20, 21]. In the

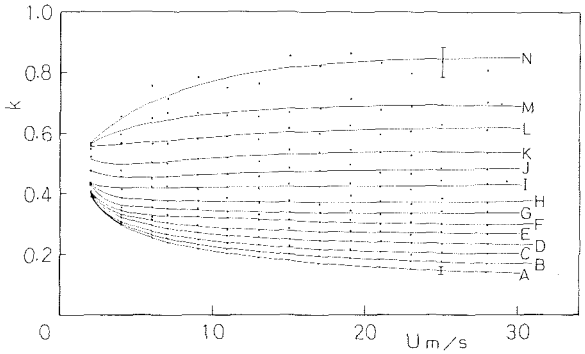

Fig. 4 Tangential sensitivity coefficient of a V-shaped hot-wire. A, $\gamma = 15.3$ deg; B, 19.6 deg; C, 24.3 deg; D, 28.9 deg; E, 33.9 deg; F, 39.1 deg; G, 43.5 deg; H, 48.0 deg; I, 53.4 deg; J, 57.9 deg; K, 62.5 deg; L, 67.1 deg; M, 71.7 deg; N, 77.3 deg. Uncertainty intervals are at 20:1 odds.

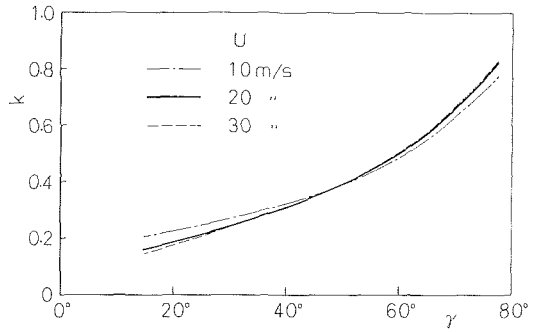

Fig. 5 Variation in k with angles of attack and fluid velocity

case of the present V-shaped hot-wires, there are no upstream prongs disturbing the flow field, and hence the most crucial problem due to support interference can be evaded in evaluating the tangential sensitivity k.

Typical values of k obtained with a V-shape hot-wire of $\alpha = 15.25$ deg and $L = 0.5$ mm are shown in Fig. 4 as functions of fluid velocity U for various angles of attack γ. In this case, the side-slip angle is kept at $\psi = 0$ deg. The variation in k with the angle of attack γ is given in Fig. 5 for three different velocities.

The tangential sensitivity is naturally expected to be dependent upon the fluid velocity and the angle of attack to the flow. As seen from Figs. 4 and 5, the value of k increases markedly with increasing γ and changes little with fluid velocity. As described later and in our next paper, turbulence measurements with inclined V-shaped hot-wires are usually done by placing wires at an angle of 30 deg $< \gamma <$ 50 deg. Within this range, the tangential sensitivity can be considered to be dependent primarily upon the angle of attack γ and almost independent of the fluid velocity U at least for $U > 6$ m/s. Thus, in evaluating effective cooling velocities from equation (13), it causes no practical problems to regard k as a single function of γ.

Directional Characteristics of V-Shaped Hot-Wires

Since it is mainly the effective cooling velocity U_{em} that determines the directional dependence of heat transfer characteristics of V-shaped hot-wires, their directional characteristics can be represented as functions of the probe configuration (i.e., half of the vertex angle α) and the orientation of the velocity vector with respect to the probe (i.e., pitch angle ϕ and side-slip angle ψ). The tangential sensitivity k due to the flow parallel to the hot-wire depends, as described above, almost entirely upon the angle of attack γ. Thus the effective cooling has a functional form given as:

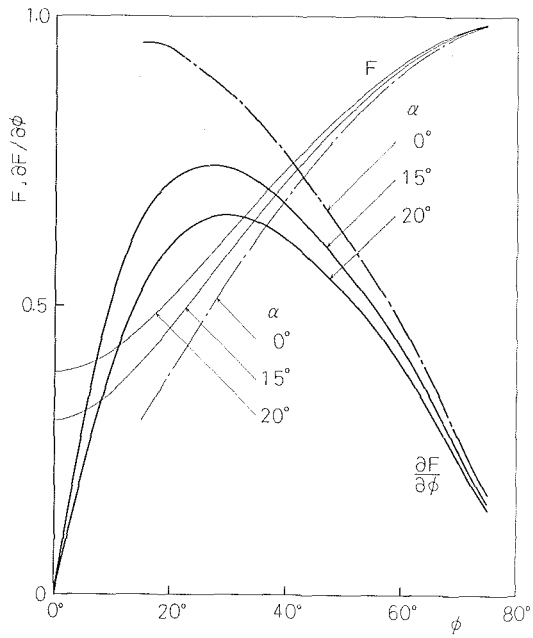

Fig. 6 Direction-sensitivity characteristics

$$U_{em} = U \cdot F(\phi, \psi, \alpha) \tag{16}$$

where

$$F(\phi, \psi, \alpha) = [\{1 - (1 - k_1^2)\cos^2\alpha\cos^2\psi(\cos\phi + \tan\alpha\tan\psi)^2\}^{1/2} + \{1 - (1 - k_2^2)\cos^2\alpha\cos^2\psi(\cos\phi - \tan\alpha\tan\psi)^2\}^{1/2}]/2 \tag{17}$$

The profiles of direction-sensitivity characteristic F and its derivative $\partial F/\partial\phi$, with k given in Fig. 5 assigned to k_1 and k_2 in equation (17), are presented as a function of ϕ in Fig. 6 for $\psi = 0$ deg, $\alpha = 15$ deg, and 20 deg. For comparison, the corresponding profiles for the conventional inclined straight hot-wire (i.e., $\alpha = 0$ deg) are also shown by chain lines in the figure. It is seen that the value of F increases with an increase of pitch angle ϕ, and $\partial F/\partial\phi$ reaches a maximum at about $\phi = 30$ deg, although the maximum point is somewhat dependent upon the half vertex angle α. In the measurement of turbulence with inclined hot-wires, the value of F is nothing but the sensitivity to streamwise velocity fluctuations, and $\partial F/\partial\phi$ determines the prime sensitivity to normal velocity fluctuations. Accordingly, for V-shaped hot-wires with practically no probe interference effects (i.e., $\alpha > 15$ deg), the best probe orientation to the flow is seen from Fig. 6 to be in the range of 30 deg $< \phi <$ 45 deg, where both sensitivities become of the same order of magnitude.

The Aeroelastic Behavior of V-Shaped Hot-Wires

A typical configuration of a V-shaped hot-wire used in the investigation is shown in Fig. 7. A 5μm dia. 1 mm-long straight tungsten wire was symmetrically bent into a V-shape at an angle of 30.5 deg. To avoid any influence of aerodynamic disturbances caused by the wire supports, the diameter of the copper-plated ends was made smaller (20μm), and the length of each plated end fixed on to the tapered wire support was made sufficiently longer (2 mm).

A V-shaped hot-wire can be supported just like a cantilever. Thus, some comments on the elastic deformation and vibration of V-shaped wires due to the fluid drag appear to be useful for practical applications. The maximum wire deformation occurs when the V-shaped wire is set in a flow in such a way that $\psi = 0$ deg and $\phi = 90$ deg. By the use of the beam

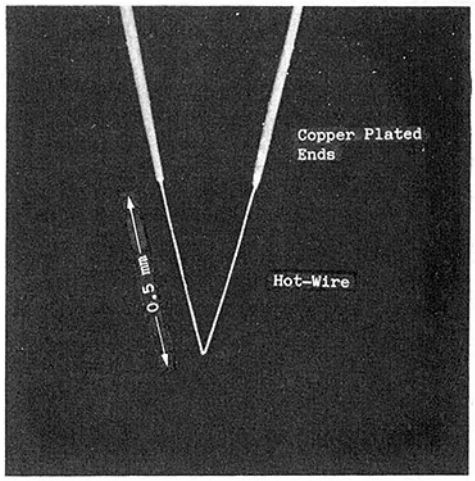

Fig. 7 Typical configuration of a V-shaped hot-wire

theory, it can be shown that the maximum wire deformation is proportional to L^4 and U^2, and inversely proportional to d^3 and the Young's modulus of elasticity. The computed maximum deformation of a tungsten wire for $d=5$ μm, $L=0.5$ mm, and $U=20$ m/s is about 2.8 μm thus indicating a visually unobservable, very small value. In fact, the deformation could hardly be observed under a microscope. Moreover, no deformation of a V-shaped hot-wire was noticed after its repeated uses.

The wire vibration, on the other hand, becomes a matter of great concern when the V-shaped hot-wire is used in a high speed flow. The natural frequencies of V-shaped wires are usually much higher than the range of interest for most turbulence research. However, it is advisable for a V-shaped hot-wire to be used in the absence of any wire vibration. It is the authors' opinion that the best way to detect the wire vibration is to measure a rough frequency spectrum with the wire in the free stream by using a plug-in spectrum analyser which displays the power spectrum on an oscilloscope screen. It should be definitely stated here that no vibrations occurred at all with the V-shaped hot-wire shown in Fig. 7 for $U<30$ m/s.

Conclusions

The heat transfer characterisitics of a hot-wire bent into a 'V' shape, which is developed for reliable measurements of near-wall turbulence, are investigated. The results can be summarized in the following conclusions:

1 The heat transfer coefficients of V-shaped hot-wires for half vertex angles larger than 15 deg are found to become a single function of effective cooling velocity regardless of the value of the vertex angle: the convective cooling from a V-shaped hot-wire obeys the same law as that for a straight hot-wire.

2 The effective cooling of the V-shaped hot-wire has the functional form given by equations (16) and (17).

3 The tangential sensitivity coefficient of the V-shaped hot-wire is dependent mainly upon the angle of attack and almost independent of the fluid velocity for $U>6$ m/s.

4 Prime sensitivities of the V-shaped hot-wire to fluctuating velocity components are dependent upon both the configuration of the wire and its orientation to the flow. A typical dependence is demonstrated.

5 The aeroelastic deformation and vibration of the V-shaped hot-wire are examined, and it becomes evident that both of them do not occur in an air flow of $U<30$ m/s.

References

1 Blackwelder, R. F., "Hot-Wire and Hot-Film Anemometers," *Methods of Experimental Physics: Fluid Dynamics*, (ed. Emrich, R. J.), Vol. 18, Part A, Academic Press, 1981, pp. 259–314.

2 Perry, A. E., *Hot-Wire Anemometry*, Oxford University Press, 1982.

3 Fingerson, L. M., and Freymuth, P., "Thermal Anemometers," *Fluid Mechanics Measurements*, (ed. Goldstein, R. J.), Hemisphere, 1983, pp. 99–154.

4 Smol'yakov, A. V., and Tkachenko, V. M., *The Measurement of Turbulent Fluctuations*, Springer-Verlag, 1983.

5 Kim, H. T., Kline, S. J., and Reynolds, W. C., "The Production of Turbulence Near a Smooth Wall in a Turbulent Boundary Layer," *J. Fluid Mech.*, Vol. 50, 1971, pp. 133–160.

6 Willmarth, W. W., and Bogar, T. J., "Survey and New Measurements of Turbulent Structure Near the Wall," *Phys. Fluids*, Vol. 20, No. 10, Point 2, 1977, pp. S9–S21.

7 Hussain, A. K. M. F., "Coherent Structures–Reality and Myth," *Phys. Fluids*, Vol. 26, No. 10, 1983, pp. 2816–2850.

8 Hishida, M., Nagano, Y., Tsuji, T., and Fukuda, K., "Measurement of Turbulence by V-Shaped Hot Wire," *Trans. JSME*, Vol. 46, No. 408, 1980, pp. 1467–1475.

9 Hinze, J. O., *Turbulence*, (2nd ed.), McGraw-Hill, 1975, pp. 83–174.

10 Champagne, F. H., Sleicher, C. A., and Wehrmann, O. H., "Turbulence Measurements with Inclined Hot-Wires," *J. Fluid Mech.*, Vol. 28, 1967, pp. 153–175.

11 Fujita, H., and Kovasznay, L. S. G., "Measurement of Reynolds Stress by a Single Rotated Hot Wire Anemometer," *Rev. Sci. Instrum.*, Vol. 39, No. 9, 1968, pp. 1351–1355.

12 Friehe, C. A., and Schwarz, W. H., "Deviations from the Cosine Law for Yawed Cylindrical Anemometer Sensors," ASME *Journal of Applied Mechanics*, Vol. 16, 1968, pp. 655–662.

13 Jorgensen, F. E., "Directional Sensitivity of Wire and Fiber-Film Probes," *DISA Information*, No. 11, 1971, pp. 31–37.

14 Bruun, H. H., "Interpretation of a Hot Wire Signal Using a Universal Calibration Law," *J. Phys. E.*, Vol. 4, 1971, pp. 225–231.

15 Mahajan, R. L., and Gebhart, B., "Hot-Wire Anemometer Calibration in Pressurized Nitrogen at Low Velocities," *J. Phys. E.*, Vol. 13, 1980, pp. 1110–1118.

16 Collis, D. C., and Williams, M. J., "Two-Dimensional Convection from Heated Wires at Low Reynolds Numbers," *J. Fluid Mech.*, Vol. 6, 1959, pp. 357–384.

17 Koch, F. A., and Gartshore, I. S., "Temperature Effects on Hot Wire Anemometer Calibrations," *J. Phys. E.*, Vol. 5, 1972, pp. 58–61.

18 Webster, C. A. G., "A Note on the Sensitivity to Yaw of a Hot-Wire Anemometer," *J. Fluid Mech.*, Vol. 13, 1962, pp. 307–312.

19 Müller, U. R., "On The Accuracy of Turbulence Measurements with Inclined Hot-Wires," *J. Fluid Mech.*, Vol. 119, 1982, pp. 155–172.

20 Strohl, A., and Comte-Bellot, G., "Aerodynamic Effects Due to Configuration of X-Wire Anemometers," ASME *Journal of Applied Mechanics*, Vol. 40, 1973, pp. 661–666.

21 Bremhorst, K., "Effect of Mounting Systems on Heat Transfer from Inclined Cylinders in Cross-Flow," *Int. J. Heat Mass Transfer*, Vol. 24, 1981, pp. 243–250.

APPENDIX A

The energy equation for each side of the V-shaped hot-wire can be written as:

$$h_1(R_1-R_a)=Ci^2R_1$$

$$h_2(R_2-R_a)=Ci^2R_2$$

where $R_1+R_2=2R_m=$ const. holds. Eliminating R_1, R_2, and Ci^2 from the above equations and equation (6) then yields:

$$\frac{h_1R_a}{h_1R_m-h_{ov}(R_m-R_a)}+\frac{h_2R_a}{h_2R_m-h_{ov}(R_m-R_a)}=2$$

The overall heat transfer coefficient, h_{ov} of the V-shaped hot-wire derived from the above equation becomes:

$$h_{ov}=h_m(1+1/2m)\left[1-\left\{1-\frac{4(1+1/m)h_1h_2}{(2+1/m)^2h_m{}^2}\right\}^{1/2}\right]$$

where m denotes the resistive overheat ratio defined by:

$$m=R_m/R_a-1$$

For $m=0.5$ and $h_2/h_1=0.9$, we obtain $h_{ov}=0.9959h_m$. Thus,

in ordinary situations, the approximation of $h_{ov} \simeq h_m$ is quite satisfactory.

APPENDIX B

The relation between the heat transfer coefficient and the effective cooling velocity can be written for each side of the V-shaped hot-wire as:

$$h_1 = A + BU_{e1}^n,\ h_2 = A + BU_{e2}^n$$

Thus, we get:

$$h_{ov} \simeq h_m = A + B(U_{e1}^n + U_{e2}^n)/2$$

Now, writing $U_{em} = (U_{e1} + U_{e2})/2$ and $U_{e2} = (1+\Delta)U_{e1}$, we get from the above equation and equation (8):

$$\begin{aligned} U_{eov} &= \{(U_{e1}^n + U_{e2}^n)/2\}^{1/n} \\ &= U_{e1}\{1 + \Delta/2 - \Delta^2(1-n)/8 + \Delta^3(1-n)/16 + \ldots\} \\ &= U_{em} - U_{e1}\{\Delta^2(1-n)/8 - \Delta^3(1-n)/16 + \ldots\} \end{aligned}$$

For $\Delta = 1/10$ and $n = 0.45$, we obtain $(U_{em} - U_{eov})/U_{e1} = 6 \times 10^{-4}$, and hence the approximation of $U_{eov} \simeq U_{em}$ has no practical problems.

Turbulence Measurements With Symmetrically Bent V-Shaped Hot-Wires. Part 2: Measuring Velocity Components and Turbulent Shear Stresses

M. Hishida[1]
Professor.

Y. Nagano
Professor.
Mem. ASME

Department of Mechanical Engineering,
Nagoya Institute of Technology,
Gokiso-cho, Showa-ku,
Nagoya 466, Japan

An analysis of the response of a V-shaped hot-wire to velocity component fluctuations is presented. A V-shaped hot-wire works in the same manner as a conventional inclined straight wire. The great differences are: the V-shaped wire is less sensitive to the w component of velocity; the V-shaped wire can be supported just like a cantilever, and thus the wire may be brought closer to the wall until it touches the wall surface, whereas an inclined straight wire is kept away from the wall by the supports, and a probe body distorts the flow field.

Introduction

In turbulence studies, two velocity components are often measured with an X-wire, while three components can be measured by adding a third wire [1]. There are, however, limitations that must be observed. As demonstrated by Tutu and Chevray [2], cross-wire or X-wire anemometry is found to be erroneous due to the rectification, which stems from the inherent insensitivity of hot-wires to the direction of the instantaneous velocity vector, and the effect of the w component of velocity, when employed in high intensity turbulence. The use of 3-wire probes can reduce these errors considerably [3], and hence the performance of triple hot-wire probes has been actively studied and improved upon in the last five years (e.g., Acrivlellis [4], Frota [5], and Andreopoulos [6]). The primary practical limitations or drawbacks of triple hot-wire probes are imperfect spatial resolution and a high possibility of the existence of probe interference effects. To allow an essentially point measurement, it is necessary to construct hot-wire arrays as small as possible. On the other hand, to minimize any probe interference, a certain spacing between wires is needed [7]. A large probe should suffer from the effects of imperfect spatial resolution on turbulence measurements. As a matter of fact, it is not rare that misleading information is obtained on the flow structure [8–11].

More crucial is that measurements of components of the Reynolds stresses near the wall are very difficult when using a conventional X-wire probe because the probe is kept away from the wall by the supports, and a probe body significantly distorts the flow fields. In an earlier paper [12], it was reported that symmetrically bent V-shaped hot-wires have been developed to permit the aforementioned problems to be solved, and that the basic heat-transfer characteristics of V-shaped wires obey the law similar to that for straight wires. The present paper deals with the measurements of the turbulent velocity components and the Reynolds shear stresses with V-shaped hot-wires. First, an analysis is given of the behavior of V-shaped hot-wires set in a fluctuating velocity field, which provides the principle of turbulence measurements. Secondly, the complete procedure for measuring velocity components with two V-shaped wires in an X arrangement is described. Finally, some results are given of measurements of Reynolds shear stress in the immediate vicinity of a wall.

Basic Equations for the Instantaneous Effective Cooling Velocity

The effective cooling velocity for the V-shaped hot-wire, as presented in our earlier paper [12], is given by the following equations

$$U_{em} = U \cdot F \tag{1}$$

with

$$F = \{(1 - K_1 \cos^2\gamma_1)^{0.5} + (1 - K_2 \cos^2\gamma_2)^{0.5}\}/2 \tag{2}$$

In these equations, U is the instantaneous fluid velocity; $K_i = 1 - k_i^2 (i = 1,2)$ where k denotes the tangential sensitivity coefficient introduced to account for the effect of heat transfer due to the flow parallel to the hot-wire; γ is the instantaneous angle between U and the axis of the hot-wire; the subscripts 1 and 2 pertain to each side of the V-shaped wire (sides no. I and no. II in Fig. 1). Consider a V-shaped hot-wire oriented at a fixed angle ϕ_0 with respect to the mean velocity U_m in an x- or streamwise direction, as depicted in Fig. 1. Let

[1] Present address: Chubu University, Department of Mechanical Engineering, Matsumoto-cho, Kasugai 487, Japan.

Contributed by the Fluids Engineering Division for publication in the JOURNAL OF FLUIDS ENGINEERING. Manuscript received by the Fluids Engineering Division August 7, 1985.

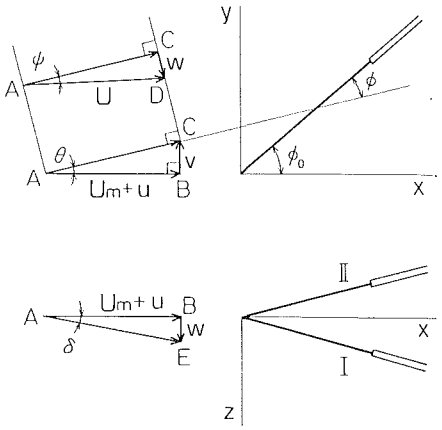

Fig. 1 Coordinate system and velocity components with respect to the sensing element

u, v, and w be the velocity component fluctuations in the x, y, z directions, respectively. Write $\overline{AB}=U_m+u$, $\overline{BC}=v$, $\overline{CD}=w$, and $\overline{AD}=U$ in Fig. 1, and let ϕ be the angle that $\overline{AC}$ makes with the plane in which the V-shaped wire is located, and ψ, θ, and δ be the angles CAD, CAB, and BAE, respectively. The so-called instantaneous pitch angle is ϕ and the instantaneous side-slip angle is ψ. As shown in the previous paper [12], the direction-sensitivity characteristic F in equation (2) becomes a single function of α, ϕ, and ψ except in very low velocity situations. The relationships between these angles can be given as:

$$\phi=\phi_0-\theta \tag{3}$$

$$\tan\theta=v/(U_m+u) \tag{4}$$

$$\tan\delta=w/(U_m+u) \tag{5}$$

$$\tan\psi=\cos\theta\tan\delta \tag{6}$$

By following the same procedure as in the previous paper [12], the instantaneous angle of attack γ, which an instantaneous flow velocity U makes with the axis of the hot-wire, can be expressed in terms of the half vertex angle of V-shaped hot-wire α, the pitch angle ϕ and the side-slip angle ψ so that:

$$\cos\gamma_i=\cos\alpha\cos\phi_0(1+\tan\phi_0\tan\theta \pm\tan\alpha\tan\delta/\cos\phi_0)/(1+\tan^2\theta+\tan^2\delta)^{0.5} \tag{7}$$

where some modifications are made with equations (3)-(6), and plus and minus signs in the right hand side refer to $i=1$ and 2, respectively. Substituting equation (7) for equation (2) yields:

$$F=\left[\left\{1-K_1\frac{\cos^2\alpha\cos^2\phi_0}{1+v^{*2}+w^{*2}}(1+v^*\tan\phi_0+w^*\tan\alpha/\cos\phi_0)^2\right\}^{0.5} +\left\{1-K_2\frac{\cos^2\alpha\cos^2\phi_0}{1+v^{*2}+w^{*2}}(1+v^*\tan\phi_0 -w^*\tan\alpha/\cos\phi_0)^2\right\}^{0.5}\right]/2 \tag{8}$$

where $v^*=v/(U_m+u)$ and $w^*=w/(U_m+u)$. Thus, the instantaneous effective cooling velocity in a fluctuating velocity field can be written as:

$$U_{em}'=U_{em}/U_m=[\{(1+u')^2+v'^2+w'^2 -K_1\cos^2\alpha\cos^2\phi_0(1+u'+v'\tan\phi_0+w'\tan\alpha/\cos\phi_0)^2\}^{0.5} +\{(1+u')^2+v'^2+w'^2-K_2\cos^2\alpha\cos^2\phi_0(1+u' +v'\tan\phi_0-w'\tan\alpha/\cos\phi_0)^2\}^{0.5}]/2 \tag{9}$$

where the velocity fluctuations are normalized in such a way that $u'=u/U_m$, $v'=v/U_m$ and $w'=w/U_m$. By solving equation (9), with measured values U_{em}' for different sets of ϕ_0, we obtain a mean velocity and velocity components.

Effects of Velocity Component Fluctuations on the Effective Cooling Velocity

In order to transform equation (9) into a more convenient form, the effects of velocity component fluctuations u', v', and w' on the effective fluctuating cooling velocity should be examined independently. Define U_{eo} as the effective cooling velocity for $u'=v'=w'=0$. Then equation (9) yields:

$$U_{eo}'=U_{eo}/U_m=(1-K_0\cos^2\alpha\cos^2\phi_0)^{0.5} \tag{10}$$

where $K_0=1-k_0^2$, and k_0 is the tangential sensitivity coefficient at the fixed angle of attack γ_0 given by:

Nomenclature

a, b, c = absolute values of S_{uo}, S_{vo}, and C_{wo}
F = direction-sensitivity characteristic, equation (2)
G = parameter defined in equation (16)
K = deviation factor of V-shaped hot-wire, equation (2)
k = tangential sensitivity coefficient
S_{uo}, S_{vo}, C_{wo} = sensitivities of V-shaped wire to velocity fluctuations u,v, and w^2.
u, v, w = velocity component fluctuations in x, y, and z directions
U = instantaneous flow velocity
U_m = mean velocity
U_{em} = instantaneous effective cooling velocity
U_{eo} = effective cooling velocity for the case $u=v=w=0$
ΔU_{em} = variation in U_{em} with velocity component fluctuations $=U_{em}-U_{eo}$
(ΔU_e) = ΔU_{em} for inclined straight hot-wire
x, y, z = coordinates, see Fig. 1
α = half vertex angle of V-shaped wire
γ = angle which velocity vector makes with wire axis
ϕ = instantaneous pitch angle
ψ = instantaneous side-slip angle

Superscript

$'$ = value normalized by U_m

Subscripts

0 = value for the case $u=v=w=0$
1,2 = each side of V-shaped wire

$$\cos\gamma_0 = \cos\alpha\cos\phi_0$$

1 Variation in U_{em}' with u'. If we let $\Delta U_{emu}'$ be the variation in U_{em}' with u' for the case $v' = w' = 0$, then the following equation is obtained from equations (9) and (10):

$$\Delta U_{emu}' = U_{em}' - U_{eo}'$$
$$= (1 - K\cos^2\alpha\cos^2\phi_0)^{0.5} u'$$
$$= S_{uo} u' \tag{11}$$

where S_{uo} is the sensitivity to streamwise velocity fluctuations u' given by:

$$S_{uo} = (1 - K\cos^2\alpha\cos^2\phi_0)^{0.5} \tag{12}$$

The calculated values of $\Delta U_{emu}'$ from equation (11) with the measurements of k reported in the earlier paper [12] are presented as a function of u' in Fig. 2 for a typical configuration of a V-shaped hot-wire ($\alpha = 15$ deg and $\phi_0 = 35$ deg). This probe configuration was found to provide the better result of measurements [12].

2 Variation in U_{em}' with v'. The variation in U_{em}' with v', denoted as $\Delta U_{emv}'$ for $u' = w' = 0$ is obtained in much the same way as the above, so that:

$$\Delta U_{emv}' = U_{em}' - U_{eo}' = \{(1 + v'^2$$
$$- K\cos^2\alpha\cos^2\phi_0(1 + v'\tan\phi_0)^2\}^{0.5} - U_{eo}' \tag{13}$$

Note that $K(= 1 - k^2)$ in equation (13) changes at the same time as v', since

$$\cos\gamma = \cos\alpha\cos\phi_0(1 + v'\tan\phi_0)/(1 + v'^2)^{0.5}$$

holds and k changes with an angle of attack γ [12].
The relationship between $\Delta U_{emv}'$ and v' is demonstrated in Fig. 2 for $\alpha = 15$ deg and $\phi_0 = 35$ deg. It is seen that $\Delta U_{emv}'$ for v' of up to 0.2 can be represented by a linear variation indicated by the chain line in the figure so that:

$$\Delta U_{emv}' = S_{vo} v' \tag{14}$$

where S_{vo} is the prime sensitivity to normal velocity fluctuations v' given by:

$$S_{vo} = (\partial\Delta U_{emv}'/\partial v')_{v'=0} = -(G/2)\cos^2\alpha\sin 2\phi_0 \tag{15}$$

Here G is the unique function of γ as:

$$G(\gamma) = \{K - (\partial K/\partial\gamma)\cot\gamma/2\}/(1 - K\cos^2\gamma)^{0.5} \tag{16}$$

The resulting errors due to the approximation of $\Delta U_{emv}'$ to equation (14), $S_{vo} v'/\Delta U_{emv}' - 1$, are generally dependent upon both α and ϕ_0. The calculated errors for $\alpha = 15$ deg are shown as a function of ϕ_0 in Fig. 3.

For the practical applications of V-shaped hot-wires, it is often of great convenience to allow the sensitivities S_{uo} and S_{vo} to become of the same order of magnitude. As seen in Fig. 3, the best probe orientation to the flow is in the range of 35 deg $< \phi_0 <$ 45 deg for $\alpha = 15$ deg. In Fig. 3, the corresponding sensitivities for a conventional inclined straight hot-wire ($\alpha = 0$ deg) are also presented for comparison by the broken lines.

3 Variation in U_{em}' with w'. The variation in U_{em}' with w', $\Delta U_{emw}'$, for $u' = v' = 0$ can be written from equations (9) and (10) as:

$$\Delta U_{emw}' = U_{em}' - U_{eo}' = [\{(1 + w'^2$$
$$- K_1\cos^2\alpha\cos^2\phi_0(1 + w'\tan\alpha/\cos\phi_0)^2\}^{0.5} + \{(1 + w'^2$$
$$- K_2\cos^2\alpha\cos^2\phi_0(1 - w'\tan\alpha/\cos\phi_0)^2\}^{0.5}]/2 \tag{17}$$

As illustrated in Fig. 4 for the case $\alpha = 15$ deg, $\Delta U_{emw}'$ changes almost linearly with w'^2 in such a way that:

$$\Delta U_{emw}' = C_{wo} w'^2 \tag{18}$$

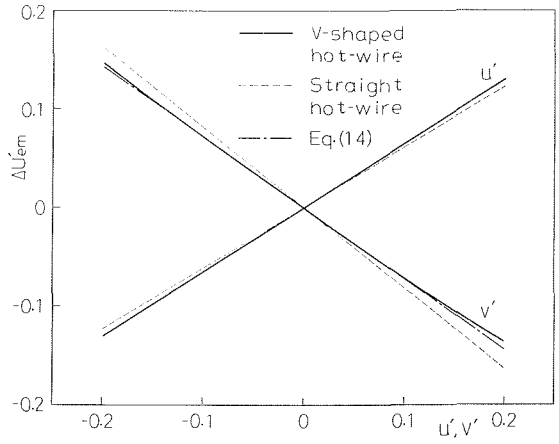

Fig. 2 Variation in the effective cooling velocity with velocity component fluctuations u' and v' for $\alpha = 15$ deg and $\phi_0 = 35$ deg

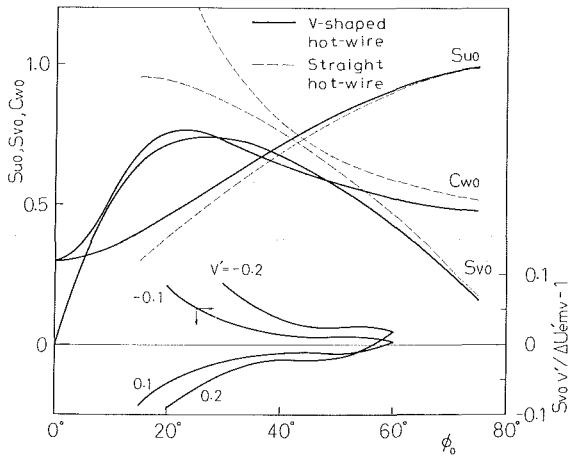

Fig. 3 Variations in the sensitivities S_{uo}, S_{vo}, and C_{wo} with pitch angle ϕ_0, and the resulting errors due to the approximation of $\Delta U_{emv}'$ to a linear variation with v' for $\alpha = 15$ deg

The differentiation of equation (17) with respect to w'^2 yields:

$$C_{wo} = (\partial\Delta U_{emw}'/\partial w'^2)_{w'=0} = \{(1 - K\cos^2\alpha\cos^2\phi_0)^{0.5}$$
$$+ G(\cos^2\alpha\cos^2\phi_0 - \sin^2\alpha) + (\partial G/\partial\gamma)_{\gamma 0}\cot\gamma_0\sin^2\alpha\}/2 \tag{19}$$

The change of C_{wo} with ϕ_0 is shown in Fig. 3 for $\alpha = 15$ deg, together with that for an inclined straight hot-wire. For ordinary orientation to the flow, i.e., $\phi_0 > 25$ deg, C_{wo} decreases as ϕ_0 increases. The errors in $\Delta U_{emw}'$ due to the approximation with equation (18) are 0.1 percent and 1.3 percent for $\alpha = 15$ deg, $\phi_0 = 35$ deg, according as $w' = 0.1$ and $w' = 0.2$.

4 The Response Equation of a V-Shaped Hot-Wire to the Three Components of Velocity. From the foregoing consideration, the resulting response equation of a V-shaped hot-wire to velocity fluctuations can be expressed as:

$$U_{em}' = U_{eo}' + S_{uo} u' + S_{vo} v' + C_{wo} w'^2 \tag{20}$$

for $|v'| < 0.2$ and $|w'| < 0.2$.
Equation (20) is valid for a conventional inclined straight hot-wire, although a set of coefficients S_{uo}, S_{vo}, and C_{wo} takes different values. This suggests that a V-shaped hot-wire works in the same manner as an inclined straight hot-wire.

It should be noted here that the sensitivity S_{vo} in equation (20), strictly speaking, holds true for v' fluctuations under $u' = w' = 0$. However, the sensitivity, $S_v = \partial\Delta U_{em}'/\partial v'$, for $w' = 0$ and $u' = 0.1$ becomes larger only by 0.3 percent than the value of S_{vo}. The same conclusions have proven true for

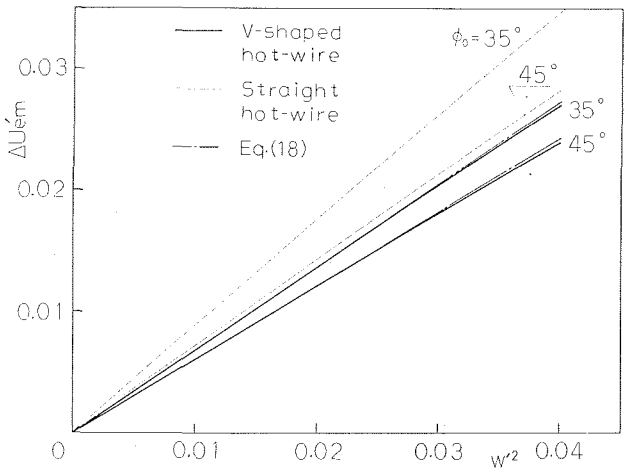

Fig. 4 Variation in the effective cooling velocity with w'

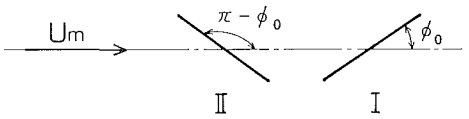

Fig. 5 Orientation of two V-shaped wires in an X arrangement with respect to flow

both S_{uo} and C_{wo}. Accordingly, the use of equation (20) is satisfactory for the measurements of velocity components except in very high intensity turbulence.

Values of S_{uo}, S_{vo}, and C_{wo} are of the same order of magnitude. Thus, the effective cooling velocity changes with u' and v' approximately to the same degree, while the influences of w' on the effective cooling velocity are of order w'^2 and hence much smaller than those of u' and v'.

Comparison of V-Shaped and Straight Hot-Wires

All of the attributes of conventional inclined straight hot-wires can be derived simply by putting $\alpha = 0$ deg in the governing equations for V-shaped hot-wires. The variation in the effective cooling velocity for straight wires, $\Delta U_e'$, with velocity component fluctuations, u', v', and w' can be written respectively as:

$$(\Delta U'_e)_u = (1 - K\cos^2\phi_0)^{0.5} u',$$

$$(\Delta U_e')_v = \{1 + v'^2 - K\cos^2\phi_0(1 + v'\tan\phi_0)^2\}^{0.5} - U_{eo}',$$

$$(\Delta U_e')_w = (1 + w'^2 - K\cos^2\phi_0)^{0.5} - U_{eo}'$$

Equations for sensitivities S_{uo}, S_{vo}, and C_{wo} yields:

$$S_{uo} = (1 - K\cos^2\phi_0)^{0.5}$$

$$S_{vo} = -(G/2)\sin 2\,\phi_0$$

$$C_{wo} = \{(1 - K\cos^2\phi_0)^{0.5} + G\cos^2\phi_0\}/2$$

In the above set, K and G are functions of γ given by:

$$\cos\gamma = \cos\phi_0(1 + v'\tan\phi_0)/(1 + v'^2 + w'^2)^{0.5}$$

The variations in the effective cooling velocity for straight hot-wires in the typical case of $\phi_0 = 35$ deg are compared with those for V-shaped hot-wires in Figs. 2 and 4. The corresponding comparison of sensitivities is made in Fig. 3.

These results indicate that the sensitivities to u' and v' fluctuations, S_{uo} and S_{vo}, do not differ significantly between V-shaped and straight hot-wires, while C_{wo} for V-shaped wires becomes much smaller than that for straight hot-wires. The latter result is important, for this proves that V-shaped hot-wires are less sensitive to w' fluctuations.

Table 1 Comparison of error-producing factors

ϕ_0	c/a	
	V-Shaped Hot-Wire	Straight Hot-Wire
35°	1.05	1.45
45°	0.79	0.97

Measurement of Turbulent Quantities With Multiple Probe Arrays

As in conventional X-wire or triple-wire anemometry, velocity components can be measured simultaneously by using probes containing more than one V-shaped hot-wire. The quality of velocity information obtainable, however, is different from that of X-wire or triple hot-wire probes, since parameters S_{uo}, S_{vo}, and C_{wo} are different between newly developed and conventional types of hot-wires.

Let's examine the array with two V-shaped wires in an X arrangement and measure the streamwise and the normal velocity components, u' and v'. Consider two identical V-shaped hot-wires, I and II, inclined at an angle ϕ_0 and $\pi - \phi_0$ with respect to the mean flow direction, as shown in Fig. 5. Define a, b, and c as the asbolute values of S_{uo}, S_{vo}, and C_{wo}, respectively. For each wire, equation (20) yields:

$$U_{e1}' = U_{e0}' + au' + bv' + cw'^2 \tag{21}$$

$$U_{e2}' = U_{e0}' + au' - bv' + cw'^2 \tag{22}$$

Rearranging these equations then gives the following expressions for u' and v':

$$u' + (c/a)w'^2 = (\Delta U_{e1}' + \Delta U_{e2}')/(2a) \tag{23}$$

$$v' = (\Delta U_{e1}' - \Delta U_{e2}')/(2b) \tag{24}$$

where $\Delta U_{e1}' = U_{e1}' - U_{e0}'$ and $\Delta U_{e2}' = U_{e2}' - U_{e0}'$.

As seen from equation (23) and (24), the dominant error-producing factor in the measurement of u' and v' is w' fluctuations, represented by the additional term $(c/a)w'^2$. This is also true in conventional X-wire anemometry, as discussed in [2, 3]. The values of c/a for V-shaped hot-wires, as given in Table 1 for the case $\alpha = 15$ deg, are 38 percent and 23 percent smaller for $\phi_0 = 35$ and 45 deg than those for conventional X-wires, thus indicating the superiority of the present method over the conventional one. For instance, if $w' = u'/2$ in high intensity turbulence, then the error in u' for V-shaped hot-wires at $\phi_0 = 35$ deg becomes about 5 percent for $u' = 0.2$. This error is 0.72 times as large as that produced in X-wires.

To verify the effectiveness of the present method, measurements of Reynolds stress $\overline{uv}$ near the wall were made in fully developed pipe flow for a Reynolds number (based on bulk velocity and pipe diameter) of 40,000. A hot-wire array used was one with two V-shaped wires in an X arrangement (X-probe), as shown in Fig. 6. Each wire of the X-probe was separately operated in constant-temperature mode and set at angles of ± 45 deg to the flow. The spacing, l_z, between the wire centers was 0.26 mm. Note that the probe was constructed as small as was practicable in order to detect the small scale flow phenomena near the wall, i.e., $l_z = 0.26$ mm $= 9.8\,\nu/u^* \simeq 3\eta$, where ν is the kinematic viscosity, u^* is the friction velocity, and η is the Kolmogorov microscale.

From the theory of fully developed pipe flow, the Reynolds stress is given by:

$$-\overline{uv}/u^{*2} = (1 - y/r_0) - \nu/u^{*2}\partial U/\partial y \tag{25}$$

where r_0 is the pipe radius and y is the distance from the wall.

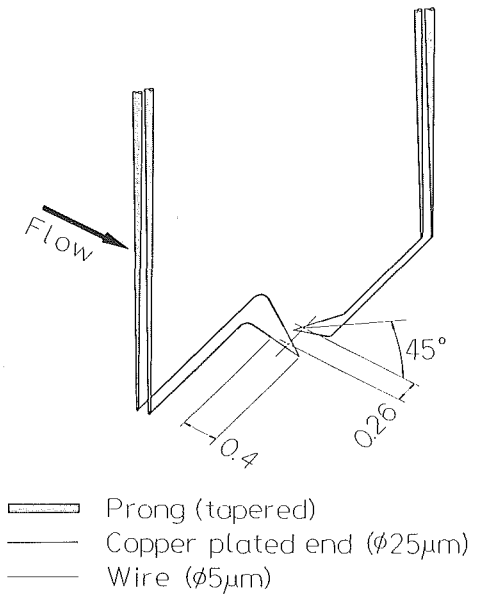

Fig. 6 Probe configuration (all dimensions in millimeters)

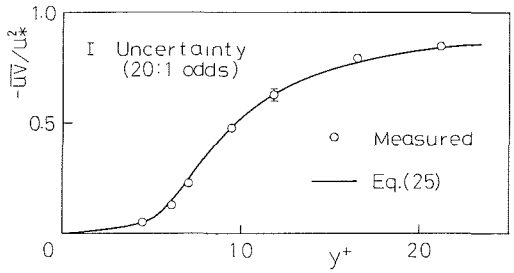

Fig. 7 Measurements of Reynolds stress near the wall

The values of $\overline{uv}$ from equation (25), calculated by using measurements of $u*$ and U [13, 14], are compared with the present direct measurements of $\overline{uv}$ in Fig. 7. It can be seen that the present values of $\overline{uv}$ are in almost complete agreement with those calculated from equation (25). The onset of the wall proximity effect was observed at a sensor-to-wall distance of about 0.07 mm or $y^+ \simeq 3.3$ (nearly touching the wall surface). It should be mentioned here that measurements of Reynolds stress in the near-wall region $y^+ < 20$ can hardly be performed by using the conventional X-wire.

Conclusions

The characteristics of symmetrically bent V-shaped hot-wires in a fluctuating velocity field are investigated, and a new method for the measurement of three components of velocity and turbulent shear stresses with these wires is presented. The technique described eliminates various errors due to aerodynamic disturbances caused by the wire supports and is shown to be highly effective for the measurement of turbulence in close proximity to the wall, where a conventional X-wire anemometry technique is either subject to large errors or at worst cannot be used. The results can be summarized in the following conclusions:

1 Basically, a V-shaped hot-wire is found to work in the same manner as an inclined straight hot-wire, the effective cooling velocity varying linearly with u, v, and w^2 except in high intensity turbulent flows. The great difference is that a V-shaped hot-wire is less sensitive to w fluctuations than a conventional inclined straight wire.

2 As the pitch angle ϕ_0 increases, the sensitivity of V-shaped hot-wire to u fluctuations increases, while that of v fluctuations decreases accordingly. Thus, the best probe orientation to the flow is in the range of $30 \text{ deg} < \phi_0 < 45$ deg, where both sensitivities become of the same order of magnitude.

3 An important source of error in measurements of u and v fluctuations with an X-wire is the effect of the w component of velocity. This error can be reduced considerably by using two V-shaped hot-wires in an X arrangement.

4 The proposed technique has been tested in measurements of Reynolds shear stress very near the wall where a conventional X-wire could hardly be used, and the results obtained have proven very satisfactory.

References

1 Fingerson, L. M., and Freymuth, P., "Thermal Anemometers," *Fluid Mechanics Measurements* (ed. by Goldstein, R. J.) , Hemisphere, 1983, pp. 99–154.

2 Tutu, N. K., and Chevray, R., "Cross-Wire Anemometry in High Intensity Turbulence," *J. Fluid Mech.*, Vol. 71, 1975, pp. 785–800.

3 Kawall, J. G., Shokr, M., and Keffer, J. F., "A Digital Technique for the Simultaneous Measurement of Streamwise and Lateral Velocities in Turbulent Flows," *J. Fluid Mech.*, Vol. 133, 1983, pp. 83–112.

4 Acrivlellis, M., "Measurements by Means of Triple-Sensor Probes," *J. Phys. E: Sci. Instrum.*, Vol. 13, 1980, pp. 986–992.

5 Frota, M. N., "Analysis of the Uncertainties in Velocity Measurements Technique for Turbulence Measurements in Complex Heated Flows with Multiple Hot-Wires," Ph.D. thesis, Stanford University, 1982.

6 Andreopoulos, J., "Improvements of the Performance of Triple Hot Wire Probes," *Rev. Sci. Instrum.*, Vol. 54, No. 6, 1983, pp. 733–739.

7 Strohl, A., and Comte-Bellot, G., "Aerodynamic Effects Due to Configuration of X-Wire Anemometers," ASME *Journal of Applied Mechanics*, Vol. 40, 1973, pp. 661–666.

8 Wyngaard, J. C., "Measurement of Small-Scale Turbulence Structure with Hot Wires," *J. Phy. E: Sci. Instrum.*, Vol. 1, 1968, pp. 1105–1108.

9 Johansson, A. V., and Alfredsson, P. H., "Effects of Imperfect Spatial Resolution on Measurements of Wall-Bounded Turbulent Shear Flows," *J. Fluid Mech.*, Vol. 137, 1983, pp. 409–421.

10 Johnson, F. D., and Eckelmann, H., "Has a Small-Scale Structure in Turbulence been Experimentally Verified?" *Phys. Fluids*, Vol. 26, No. 9, 1983, pp. 2408–2414.

11 Willmarth, W. W., and Sharma, L. K., "Study of Turbulent Structure with Hot-Wires Smaller than the Viscous Length," *J. Fluid Mech.*, Vol. 142, 1984, pp. 121–149.

12 Hishida, M., and Nagano, Y., "Turbulence Measurements with Symmetrically Bent V-Shaped Hot-Wires. Part 1: Principles of Operation," JOURNAL OF FLUIDS ENGINEERING, published in this issue, pp.

13 Hishida, M., and Nagano, Y., "Structure of Turbulent Velocity and Temperature Fluctuations in Fully Developed Pipe Flow," ASME *Journal of Heat Transfer*, Vol. 101, No. 1, 1979, pp. 15–22.

14 Hishida, M., Nagano, Y., and Morimoto, Y., "Structure of Pipe Flow Turbulence. Part 1. Characteristics of Velocity Fluctuations and Reynolds Shear Stress," *Trans. JSME*, Vol. 46, No. 408, 1980, pp. 1455–1466.

An LDA Study of the Backward-Facing Step Flow, Including the Effects of Velocity Bias

E. W. Adams[1]

J. K. Eaton

Mechanical Engineering Department,
Stanford University,
Stanford, Calif. 94305

The subsonic, backward-facing step flow was studied experimentally to provide structural information and test data for modelers. A single-component laser-Doppler anemometer was the primary measurement instrument. The effects of velocity bias on the LDA results were examined in detail. It was concluded that velocity bias was small (< 4 percent) in the uncorrected measurements and nonexistent when a periodic sampling strategy was employed. The measurements show that the pressure gradient at reattachment is lower in the present experiment than in most previous work, due to the thick boundary layer at separation. Turbulence levels in the separated shear layer are also reduced by the thick upstream boundary layer. Scaling of the streamwise coordinate on the reattachment length produced the best agreement with previous data. Agreement of turbulence quantities was particularly good downstream of reattachment.

1 Introduction

Flow fields containing regions of turbulent separated flow occur frequently, both in the natural environment and in man-made devices. Separated flows play an important role in establishing and limiting the performance of such varied devices as diffusers, airfoils, combustors, and sewage-treatment-plant settling basins. Historically, much information about turbulent separated flows was gained visually (e.g., Abbott and Kline (1)) or inferred from hot-wire and pressure measurements (Chapman et al. [2], Bradshaw and Wong [3], Kim et al. [4]). However, the detailed structure of the flows remained largely a mystery, because the velocity field contains regions of instantaneously reversing flow in which conventional instruments are not accurate. It was not until the development of the laser-Doppler anemometer (LDA) in the 1970s that potentially accurate measurements throughout a turbulent separated flow could be made. Unfortunately, much of the LDA data may be subject to undocumented errors caused by velocity bias.

The objective of the present paper is to present a detailed data set for the two-dimensional, backward-facing step flow, including structural information for turbulence-model development. Such a presentation must include documentation of the two-dimensionality of the flow as well as a reasonable assessment of the experimental uncertainty. The most serious question regarding the uncertainty is how to evaluate or eliminate the velocity bias in LDA measurements. It is widely recognized that velocity bias can occur in LDA measurements in which a counter-type signal processor is used. Many "corrections" and sampling strategies have been proposed to eliminate the bias, but its elusive nature has led some investigators to abandon all velocity-bias corrections (e.g., Driver and Seegmiller [5]).

The first phase of the present study, then, was to make a detailed examination of the uncertainty of LDA measurements in turbulent, separated flows. The performance was studied by comparing LDA measurements in a turbulent, separated flow to data obtained from a pulsed-wire anemometer and a thermal tuft. In addition, the results of several different LDA sampling strategies were compared. This work was intended to help clarify the inaccuracies in past LDA-based separated flow studies, as well as to supply guidelines for uncertainty estimation in the present work. Phase 2 documented the flow two-dimensionality and the initial conditions, and the final data set was produced in phase 3. The present paper follows this same outline.

2 Experiment

The experiments were conducted in a single-sided, sudden expansion wind tunnel. The channel height upstream of the expansion was 15.2 cm, and the step height was 3.8 cm, giving an expansion ratio of 1.25. The upstream reference velocity (U_{ref} measured 12.7 cm upstream of the step in the freestream) was 15 m/s, resulting in a step-height Reynolds number of 36,000. The boundary layer at the step edge was relatively thick ($\delta/h = 1.0$) and fully turbulent ($Re_\theta = 3500$). The step aspect ratio was 11:1, which is sufficient to ensure two-dimensional flow according to the criteria of deBrederode and Bradshaw [6]. The reattachment distance for these conditions was 6.6 step heights.

An open-circuit wind tunnel supplied filtered air to the test section at the reference speed. Flow conditioning was per-

[1]Present address: Institut fur Hydromechanik, Univ. of Karlsruhe, Karlsruhe, Federal Republic of Germany

Contributed by the Fluids Engineering Division for publication in the JOURNAL OF FLUIDS ENGINEERING. Manuscript received by the Fluids Engineering Division January 7, 1986.

formed by a large-pressure-drop heat exchanger, five fine mesh screens, and a 4:1 contraction ratio nozzle. These components were designed to reduce the turbulence intensity and to ensure uniform inlet conditions for the test section velocity and temperature. Measurement upstream of the test section indicated a free-stream turbulence level of 0.2–0.4 percent. The documentation of tunnel two-dimensionality is presented in a later section.

A dual-beam, forward-scatter LDA system was the primary velocity measurement instrument. Light was supplied by a Lexel two-Watt argon-ion laser, and all measurements were made using the green line at 514.5 nm. The LDA optics were obtained from TSI, Inc., with the exception of two front surface mirrors (Newport Research Co.), which were used to steer the beams 180° as required due to space limitations in the experimental area. The focusing-lens focal length was 490 mm, and beam intersection half angle, 7.5 deg. The receiving optics were placed 1 cm above the measuring plane at a distance of 450 mm. A Bragg cell with a shift frequency of 5 mHz (about 10 m/s in velocity units) was used at all times. Tests indicated that a doubling of the shift frequency had no effect on the measured velocities anywhere in the flow field. A TSI model 1980A counter processor was used. Data were transferred to the PDP-11 laboratory computer using a direct-memory-access interface (TSI Model 1998).

The LDA was calibrated with a one-point calibration against a pitot tube in situ. This was judged easier than any attempt to measure beam intersection angles. Since all data are presented normalized by U_{ref}, and the LDA is a linear instrument, the calibration method is rather irrelevant. By using averaging times greater than 40 seconds and more than 2000 points at every location, the statistical uncertainty was estimated to be less than 1 percent throughout the flow. It is important to note that the statistical uncertainty is not an estimate of *bias*, but rather an estimate of repeatability. Bias is considered in the next section.

The use of an LDA system in air usually requires the introduction of seed material to serve as scattering centers. The present study used a TEM Ltd. NPL-type smoke generator positioned in the filter box upstream of the blower inlet. By locating the seeder upstream of the blower, flowfield seeder interactions were minimized, and the blower itself could be used to help distribute the seed uniformly. The seeding particles were mineral-oil droplets (White Mineral Oil #9). "Smoke" was generated by pumping a thin film of the oil onto the external surface of a heated cylinder. The vaporized oil recondensed in the air stream to form the seed particles.

The conventional instruments used to judge the accuracy of the LDA were the pulsed-wire anemometer and the thermal tuft. Extensive tests (Westphal et al. [7], Eaton and Johnston [8]) have shown good agreement between the pulsed wire and a hot wire in regions where both instruments should be accurate. Typical uncertainty estimates for the PWA are about 2–3 percent of U_{ref} (Westphal, et al. [7]). The thermal tuft (Eaton et al. [9]) is a near-wall probe capable of sensing instantaneous flow direction. Its ouput was sampled to determine the fraction of time the flow moves in the downstream direction, γ. Because of the thermal tuft's simplicity, it is felt that it is the most reliable conventional measurement instrument in the separated region. The LDA may be compared to the thermal tuft by extrapolating the LDA results to 0.3 mm from the wall.

Wall skin friction was measured using the pulsed wall probe of Westphal et al. [10]. This probe, like the pulsed wire, is a three-wire probe in which the center wire is pulse heated and the outer wires act as resistance thermometers to measure the time of flight. In the present instrument, the three wires are parallel and very close to the wall. The probe measures the velocity of the fluid within the sublayer and infers skin friction from a calibration performed in a reference flow—at the same distance from the wall. Westphal showed that the calibrations performed in laminar or turbulent channel flows differed from each other by less than 5 percent.

3 LDA Performance

3.1 Simplified Analysis. The performance of the LDA was studied specifically with regard to possible bias effects, in order to choose the best averaging scheme for the conditions of the present experiment and to obtain accuracy estimates. In turbulent flow, velocity bias occurs when the particle measurement rate, f_p, is correlated to the magnitude of the instantaneous velocity vector at a point in the flowfield (McLaughlin and Tiederman [11]). For uniformly seeded incompressible flows, during periods of relatively high velocity, more particles can be measured per unit time than in periods of relatively low velocity. If the sample mean is calculated by summing the velocities of all the measured particles and dividing by the number of particles, this calculated mean (a particle average) will be higher than the true time average—it will be biased. Thus bias results, because the measurement frequency of any velocity class, u_i, is proportional to the velocity.

The bias may be "calculated" by assuming the relationship between the measurement frequency and velocity, assuming the shape of the velocity probability density function, PDF, and assuming one-dimensional flow. Such calculations have been performed, for example, by McLaughlin and Tiederman [11], by Buchhave [12], and recently by Erdmann and Tropea [13]. Calculations can often be useful as a guide to where to expect the worst bias. Since the past results were valid only for attached flows, a new estimate of the magnitude of the velocity bias is made using a simple square-wave velocity signal, 1-D flow, and assuming a direct proportionality between velocity and measurement frequency. The resulting "calculated" bias, normalized on the reference velocity is:

Nomenclature

C_f = $\tau_w / 1/2\ \rho U_{ref}^2$
C_p = $p - p_{ref} / 1/2\ \rho U_{ref}^2$.
f_p = frequency of valid particle arrival
f_s = sample frequency
f_t = turbulence frequency scale
H = step height
N = number of velocity samples
p = pressure
Re = Reynolds number
T = sampling time interval
T_{bd} = time between data samples
U = instantaneous streamwise velocity
U_N = maximum reversed-flow velocity
U_{ref} = reference freestream velocity
u' = fluctuating component of streamwise velocity
v' = fluctuating component of normal velocity
x = streamwise coordinate, origin at step
x_r = reattachment point
x^* = $(x - x_r)/x_r$
δ = boundary-layer thickness
θ = momentum thickness
ν = kinematic viscosity
τ = shear stress
ρ = density

Superscripts

$\bar{}$ = time averages
$'$ = fluctuating quantity

$$\frac{\langle U\rangle_p - \bar{U}}{U_{\text{ref}}} = \begin{cases} \dfrac{U_{\text{ref}}}{\bar{U}} \dfrac{u'^2}{U_{\text{ref}}} & ; u' < \bar{U} \\ \dfrac{\bar{U}}{U_{\text{ref}}} & ; u' > \bar{U} \end{cases} \quad (1)$$

The reference velocity is used rather than the local velocity because separated flow results are generally presented in this way, and thus it is the error relative to U_{ref} which is of primary importance. It should be pointed out that, although a square wave is hardly a realistic velocity signal, the present results agree with the results of McLaughlin and Tiederman [11] and Buchhave [12] for low turbulence intensities. This occurs because at low turbulence intensity the bias is proportional to the square of the turbulence intensity, regardless of the shape of the velocity PDF. The present formulation has the advantage of being a simple, closed-form solution, valid throughout the separated region. Though it will be shown later to be quantitatively inaccurate, qualitatively the right trends are predicted.

Equation (1) above suggests two things. First, as has long been recognized, the magnitude of the velocity bias is a strong function of turbulence intensity. Second, equation (1) suggests that the magnitude of the bias can never be any worse than the magnitude of the mean velocity. At the reattachment point itself, there can be no bias because, as the mean velocity decreases, the velocity PDF becomes relatively more symmetric around zero velocity. Since the bias is proportional to the magnitude of velocity, the negative velocity regions balance out the positive ones—decreasing the bias. Applying equation (1) to a typical separated-flow velocity profile suggests that the maximum bias will occur in the free shear layer where the turbulence intensity is large but the mean velocity is still significant. This finding was confirmed by experiment.

3.2 Averaging Schemes. Many sampling and averaging schemes to reduce or eliminate velocity bias have been proposed. Those tested in this program are described below.

Particle Average. The velocity of each valid particle is measured, and the average is formed arithmetically.

$$\langle U\rangle_p = \sum_{i=1}^{N} U_i/N$$

As previously discussed, this average may be biased if the particle arrival rate is correlated to U_i.

T_{bd} Average. Barnett and Bentley [14] proposed that the best way to eliminate the velocity bias was to start with the definition of the time average,

$$\bar{U} = \frac{1}{T}\int_0^T u(t)dt$$

and approximate that expression as a sum replacing the differential time, dt, with the time between measured data points, T_{bd}. Thus

$$\langle U\rangle_{T_{bd}} = \sum_{i=1}^{N} (U_i \times T_{bd,i}) / \sum_{i=1}^{N} T_{bd,i}$$

This method is called the T_{bd} method after the weights assigned to each velocity sample. If the sampling is periodic, the expression reduces to the arithmetic average. The T_{bd} scheme may also be viewed as a correction scheme. Since $T_{bd,i} = 1/f_{p,i}$ if $f_{p,i} \propto U_i$, weighting by T_{bd} should correct for the bias.

Periodic Sampling. A possible method of eliminating the velocity/data-rate correlation, and therefore the velocity bias, would be to enable the counter at regular intervals and process the next Doppler burst to arrive (Stevenson and Thompson [15]). With this method, the counter analyzes the Doppler bursts at an almost uniform rate f_s which is slower than f_p. Uniform sampling is assumed, and a simple average is used to obtain $\langle U\rangle_{ps}$. Since exactly equally spaced intervals are not possible, it would seem likely that a turbulence frequency scale, f_t, might also be important. If the velocities of two consecutively sampled bursts are strongly correlated, the waiting time might be a function of f_p and U_i, resulting in bias.

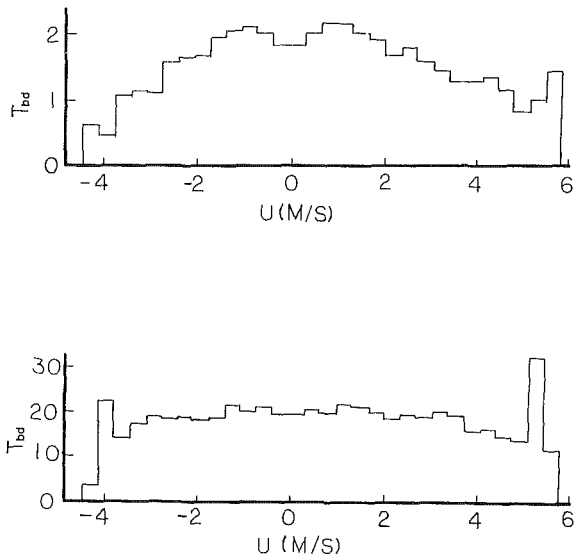

Fig. 1 Comparison of the average interdetection time (in milliseconds) for different velocity classes.
$x/H = 3.3$, $y/H = -0.5$ (a) $f_p = 500$ Hz 10,000 bursts; (b) $f_p = 50$ Hz, 2000 bursts.

Erdmann and Tropea [13] analyzed this situation and also concluded that the three important frequency scales were f_s, f_p, and f_t. We feel that, if $f_p \gg f_s$, then $\langle U\rangle_p$ would represent an unbiased estimate of $\bar{U}$, while if $f_p \sim f_s$, velocity bias would result. On the other hand, Erdmann and Tropea predict that it is f_p/f_t which is most important. While data presented by Stevenson et al. [15] suggest that, when $f_p/f_s > 10$, the result is independent of f_p/f_s, it is difficult to assess the effect of f_t because a wide enough range of seed rates was not available. In the present study, $f_p/f_s > 10$ was used at all times.

D/A Method. Mayo [16] in the discussion which followed Barnett and Bentley's paper, suggested that a time average could be generated by a sample-and-hold circuit, turning an inherently digital signal from the counter into an analog-like signal. The signal can then be processed by sampling with an A/D converter at a frequency f_s. Dimensional analysis again suggests that f_p, f_s, and f_t all influence the magnitude of the bias. Thus the same cautions and limitations apply as for the periodic sampling method.

The T_{bd} method, the periodic sampling method, and the D/A method all approximate the true time average in a slightly different manner. In practice, it was found that these methods behaved almost identically. Because of this agreement, the three methods are collectively referred to as time-average methods.

3.3 LDA Performance Results. As previously discussed, if the measurement rate, f_p, is correlated to the velocity, the particle average should be biased. To examine the correlation of U_i with $f_{p,i}$, Durao, Laker, and Whitelaw [17] suggest that the intermeasurement time distribution be examined. If $U_i \propto f_{p,i}$, then $U_i \propto 1/T_{bd}$. In Fig. 1a, the average T_{bd} falls with *increasing* magnitude of velocity. This is a clear indication that, if the particle average is used to calculate the mean,

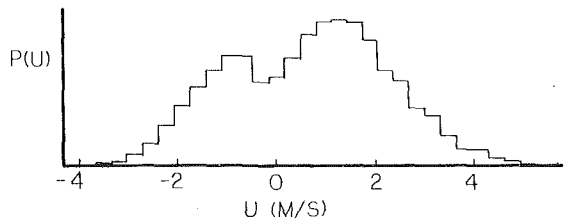

Fig. 2 Histogram of streamwise velocity at $x/H = 4.5$, $y/H = -0.5$ showing "hole" centered around $U = 0$

velocity bias would result. On the other hand, T_{bd} appears to be independent of the velocity in Fig. 1(*b*). Here there is no correlation between U_i and $f_{p,i}$. Thus a particle avarage would not be biased in this case. In fact, the mean velocity, as calculated by the particle average, shifted from 0.6 m/s for the conditions of Fig. 1a to 0.45 m/s for the conditions of Fig. 1b. The flow conditions for the two histograms are identical except that in (*a*) the laser power has been increased, increasing f_p.* The importance of this experimental result is that the bias can "disappear" rather unexpectedly. Thus any proposed bias-correction scheme must be able to handle such occurrences. Bias-elimination methods such as the 1-D or 2-D McLaughlin-Tiederman correction, or the residence-time weighting scheme, which always "corrects" the mean velocity, will fail in the general case—if the bias can suddenly disappear. For example, for the conditions of Fig. 1(*b*), any of these methods would result in an overcorrection of the bias.

Since a lowering of laser power lowers the average measurement rate attainable, it appears as if the bias has been eliminated by lowering the data rate. These results are in contrast to the results of Johnson et al. [18], who found that the bias remained constant below the fastest measurement rate of the detector.

The explanation for this seeming contradiction lies in signal-to-noise ratio (SNR) effects. Consider any velocity class, U_i. The larger the velocity, the fewer total photons are scattered from the measuring volume, because the particle is physically present in the measuring volume for a shorter time. However, the background light level would generally be independent of velocity. For this reason, faster-moving particles have lower SNR, on average, than slower-moving particles, and a smaller percentage of available faster-moving particles are processed than slower-moving particles, counteracting the bias. For this mechanism to be important, the total SNR must also be relatively low, so that the total fraction of particles affected is large. As the laser power is lowered, the fraction of particles affected by this mechanism might be increased if the level of light from the background sources, i.e., experimental setup, is not reduced as much as the level of light scattered from the measuring volume. Clearly, this is an extremely configuration-dependent result. Thus, the experiment of Johnson et al. [18] probably had higher SNR than the present one, and a smaller fraction of particles was affected by the present mechanism.

A second interesting anomaly in the performance of the LDA was observed, as illustrated by Fig. 2. This velocity PDF was processed using the T_{bd} method and was taken well away from the wall and near the line of $U = 0$. Figure 2 contains a "hole" in the PDF centered around the $U = 0$ point. The hole is always centered around zero velocity, regardless of the mean. PDFs obtained using periodic sampling and the *D/A* method also have this feature, while when data were processed using the particle average, the hole was not always present (about 60 percent of the time). Even though some bimodal PDF's have been reported in the literature (Durst and Tropea [19]), the authors believe this hole is not physical and thus represents an LDA error. The obvious explanation is that the particles did not cross enough fringes to make a measurement possible at speeds near zero. However, this explanation suggests that, by reducing the number of fringes required for a measurement, the "hole" would disappear. When the number of fringes required for a measurement was reduced from 32 to 16, 8 or even 4, there was no apparent effect—the "hole" still existed.

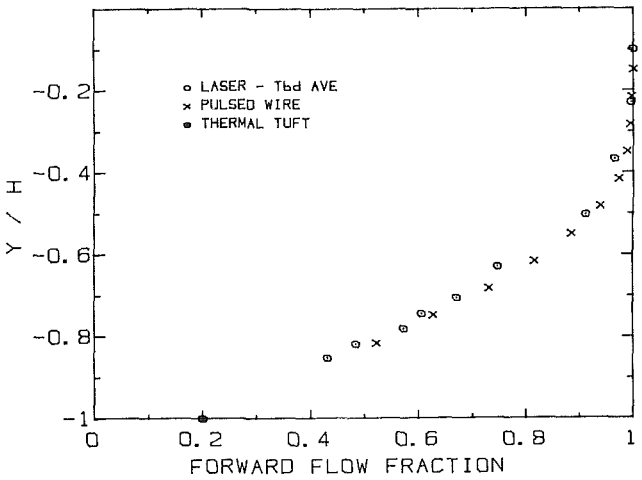

Fig. 3 Forward-flow fraction in the recirculation region. $x/H = 5.87$

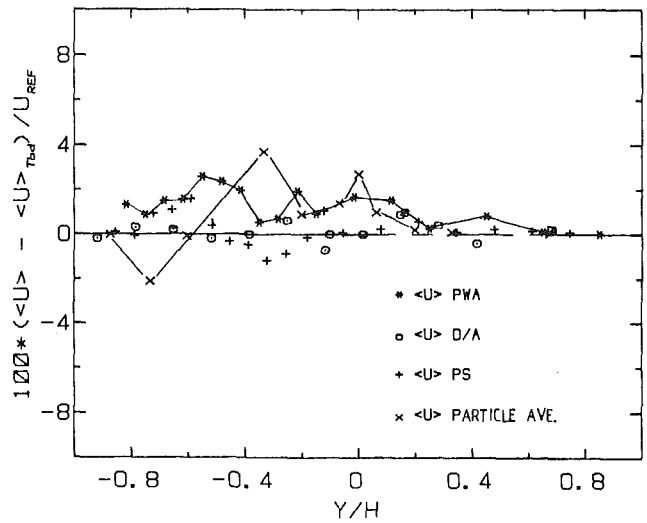

Fig. 4 Errors of various LDA bias correction schemes compared with the Pulsed Wire (PWA) and the Uncorrected LDA (PARTICLE AVE). ($x/H = 4.5$).

The effect of the bimodal structure on the mean RMS quantities was evaluated. In the worst case, the effect was 1/2 percent on the mean and 1 percent on the measured turbulence intensity (percent of U_{ref}). While PDFs such as those seen in Fig. 2 are annoying, the magnitude of the effect was rather small in the present experiment and should not detract from the conclusions of the study.

The effectiveness of the bias-reducing methods studied here can be seen in Figs. 3 and 4. Figure 3 contains profiles of the fraction of time the flow moves downstream, γ, measured with the pulsed wire, the LDA, and the thermal tuft just downstream of the reattachment point. Here, very good agreement is seen between the various instruments. While the thermal tuft always agreed with the time-averaged LDA methods to within 5 percent, the agreement between the pulsed wire and the thermal tuft was often no better than 20 percent, the pulsed wire often giving erroneously high results. This lack of perfect agreement between the pulsed wire and the thermal tuft is typical of past results in our lab. It is believed that this effect is due to the pulsed wire "dropout" near zero velocity,

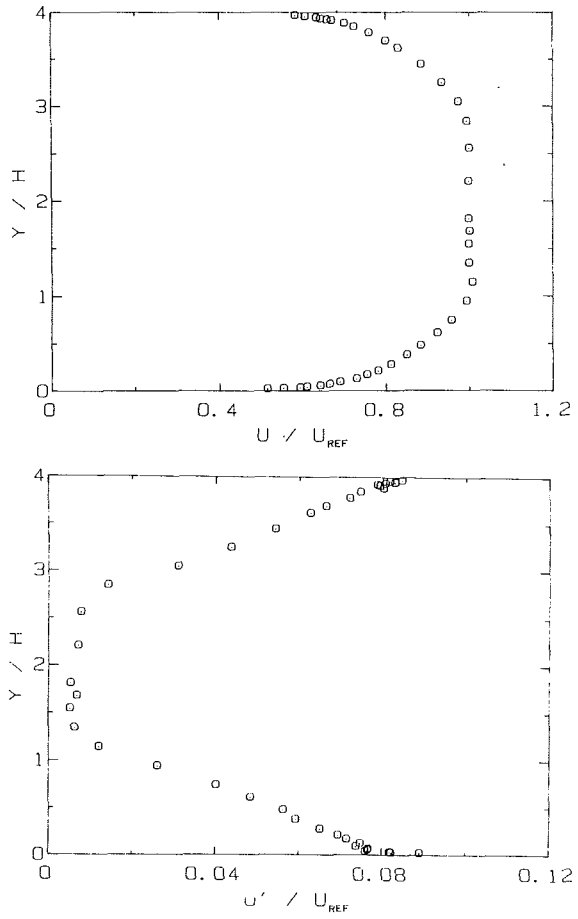

Fig. 5 Inlet conditions for the case $Re_H = 36{,}000$, $\delta/H = 1.0$, ER = 1.25

due to viscous diffusion effects (Bradbury and Castro [20]). The good agreement between the LDA time-average methods and the thermal tuft is critical, because the thermal tuft is the most reliable conventional instrument for separated flows.

Figure 4 presents the differences among the mean velocity results from the separated flow region ($x/H = 4.5$), as measured by the various LDA methods and the PWA. The reference velocity used to form the differences shown in the figure is the T_{bd} method. The most striking feature of Fig. 4 is the small differences among the various LDA methods and the PWA. The D/A method, periodic sampling method, and the T_{bd} method all lie quite close together and 1/2 to 2 percent below the PWA results, within the uncertainty of the PWA. Note also that the region of the largest differences between the PWA and the LDA is also the region of the largest velocity gradient. In regions of high gradient and high turbulence intensity, "turbulent diffusion" might cause the mean velocity as measured by the pulsed wire to be too high. Therefore, the region of the largest uncertainty in the PWA results corresponds to the region of the largest difference between the LDA and the PWA.

Figure 4 also shows that the particle average, uncorrected for any bias effects, also lies quite close to the PWA as well as the other LDA methods. Choosing any LDA method or the PWA as the reference, the worst "bias" seen in the experiment was less than 4 percent of the reference velocity. The behavior of $\langle U \rangle_p$ relative to the time-average methods is explained qualitatively using the bias calculation of equation (1), though the measured LDA bias is only a fraction of that predicted. Specifically, equation (1) predicts negative bias where the mean velocity is negative, in accordance with the results shown in Fig. 4. Note that, near the point where $\bar{U} = 0$, there is no difference between the particle average and the time average, again as predicted by equation (1). In addition, the point where the largest differences occur between the time-average methods and the particle average is in the free shear layer, away from where $\bar{U} = 0$.

There are at least two explanations for the quantitative difference between the model and the measured bias. First, the analysis leading to equation (1) is quite crude—a square wave is hardly a realistic velocity signal. Second, the results shown earlier indicate that the measured bias changes with SNR, and thus other experimental setups could result in a measured bias different from that of the present experiment.

Considering the results presented here, it is not surprising that several investigators have not found a bias effect in boundary-layer-type flows. The bias is significant only in highly turbulent regions. Even in the separated region, uncorrected LDA data appear to be as accurate as those of the PWA. In fact, uncorrected LDA data are often closer to the PWA results than are the corrected LDA data. Buchhave [12] found a similar result comparing hot-wire data with LDA data in a free jet. This is just an indication that the LDA bias observed in the present flow is no worse than the accuracy of the appropriate conventional technique in the same flow.

While Fig. 4 shows that all LDA methods lie quite close to the PWA results, LDA-thermal tuft comparisons indicated the time-average LDA methods agreed better with the thermal tuft than with the pulsed wire. Since the thermal tuft is considered the most accurate conventional instrument in the separated flow zone, the time-average methods are concluded to be bias-free. The qualitative behavior of the difference $\langle U \rangle_p - \langle U \rangle_{T_{bd}}$, which follows the expected bias trends, adds further evidence to the belief that, although the bias is small, it evidently exists. Thus, this report concludes that any of the time-average methods tested here, when properly used, corrects for the effects of LDA bias. For this reason, the periodic sampling method was used to process the LDA data described in the next sections.

4 Tunnel Qualification

Tunnel qualification consisted of four main tests: (1) a spanwise-uniformity check of the total pressure at the step edge, (2) a comparison of the separating boundary layer to well-known data, (3) reattachment-position spanwise uniformity check, and (4) mass and momentum balance checks over the entire test section to determine the two-dimensionality of the flow. Inlet spanwise uniformity was checked by making spanwise traverses with a total pressure probe 2.5 cm upstream of the step edge. Traverses were made at four different heights in the boundary layer, including one mounted flush on the wall. This proved to be the most sensitive test, indicating that total pressure was uniform to within 2 percent over the mid-75 percent of the span.

Mean-velocity and turbulence data (Fig. 5) show that the upstream boundary layer behaves like an ordinary flat-plate boundary layer. The mean velocity follows the log-law quite closely. The computed shape factor for the data is 1.35, and the Clauser G parameter is 6.26. The skin friction, as computed by the log-law, was 0.0034, within 1 percent of that given by the Ludwieg-Tillman correlation. Clearly, mean results indicated a well developed normal boundary layer. The agreement between the present turbulence intensity results and those of Klebanoff [21] is fair. The present results are five percent higher than Klebanoff's in the inner region between $y/\delta = 0.1$ and 0.4. Beyond $y/\delta = 0.4$, the present results are higher than those of Klebanoff, because of the higher free-stream turbulence.

The spanwise uniformity of the reattachment line was checked and found to be uniform within 0.3 h over the middle

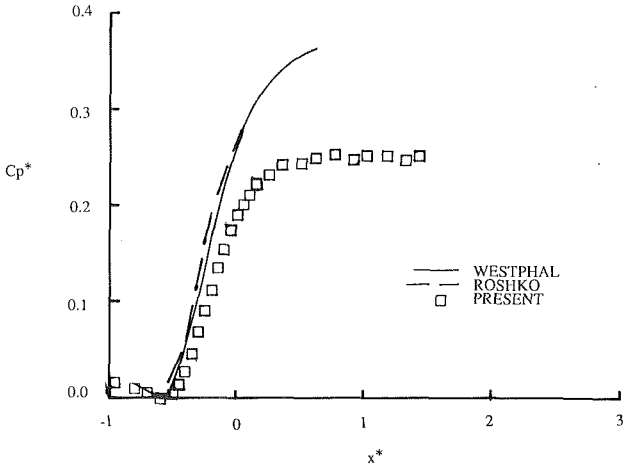

Fig. 6 A comparison of the present pressure data with that of Westphal and Roshko and Lau. $C_p = (C_p^* - C_{p_{min}})/(1 - C_{p_{min}})$.

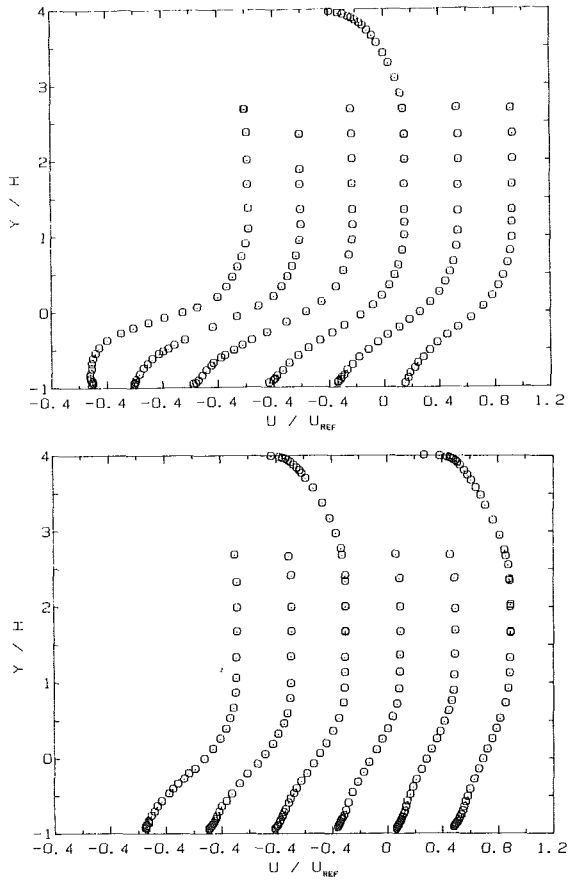

Fig. 7 Mean velocity profiles downstream of the step. $Re_H = 36{,}000$, $\delta/H = 1.0$. Profile locations (left to right):
Top: $x/H = 2.0, 3.33, 4.67, 6.0, 6.67, 7.33$;
Bottom: $x/H = 8.67, 10.0, 12.0, 14.0, 16.0, 18.0$.

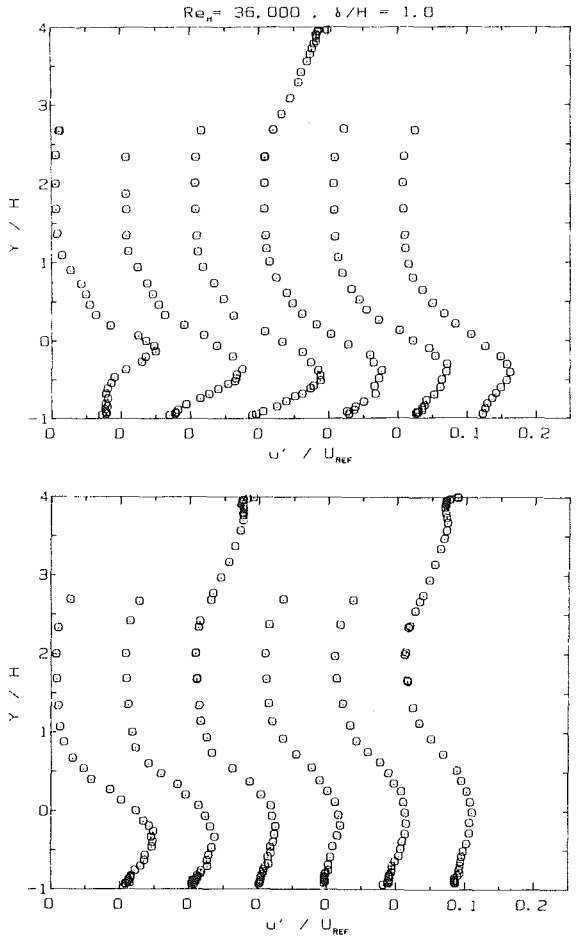

Fig. 8 Streamwise turbulence intensity profiles downstream of the step. $Re_H = 36{,}000$, $\delta/H = 1.0$. Profile locations (left to right):
Top: $x/H = 2.0, 3.33, 4.67, 6.0, 6.67, 7.33$;
Bottom: $x/H = 8.67, 10.0, 12.0, 14.0, 16.0, 18.0$.

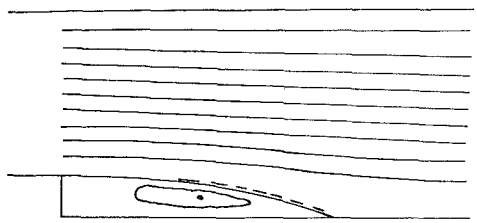

Fig. 9 Comparison of the computed streamlines for the present experiment with the reattachment streamline of Eaton and Johnston—present exp.---Eaton and Johnston

70 percent of the span. There were no ports outside this region, so this estimate may be conservative.

Mass and momentum balance checks, assuming flow two-dimensionality, were performed. The mass flux balanced to within 3 percent, even at the outlet of the test section. The momentum balance was performed by considering a control volume within the entire test section. The momentum deficit in the outflow was necessarily balanced by the pressure rise in the tunnel and the skin friction on the step wall and opposite wall. The momentum balance was performed at one location upstream of reattachment and at two locations downstream of reattachment. At all three locations, the momentum equation balanced to within 3 percent of the inlet momentum flux.

5 Final Results

Figures 6–11 present the final results of the one-component LDA study of the backward facing step. Uncertainty estimates for all measurands are tabulated in Table 1. Uncertainties were estimated using a worst case analysis which is more conservative than the 95 percent confidence interval typically used. Reattachment as measured with the thermal tuft was 6.6H. All data are normalized on the reattachment length in the streamwise direction and on step height in the vertical direction. Figure 6 presents the pressure data normalized on

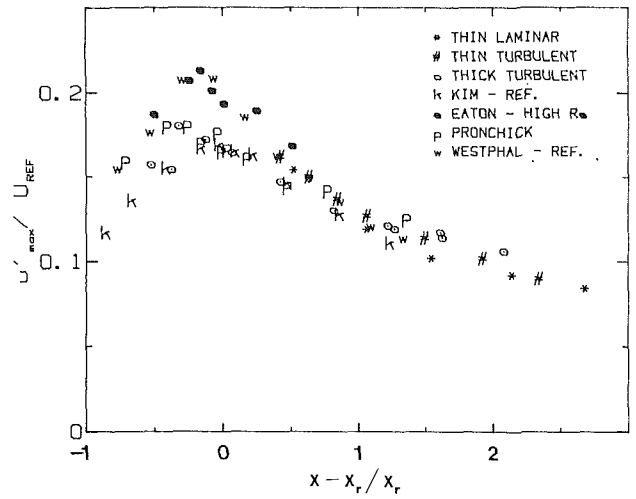

Fig. 10 Recovery region behavior of the streamwise component of turbulence intensity for several experiments

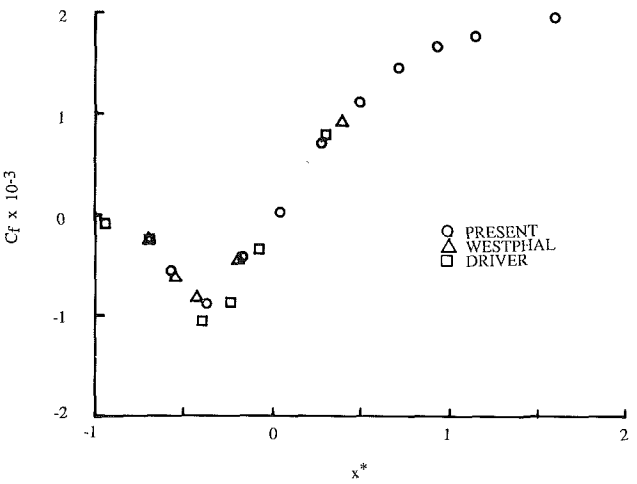

Fig. 11 Comparison of C_f data between several experiments

the reference dynamic head and then renormalized, following the suggestion of Westphal et al. [7] and Roshko and Lau [22]. Westphal collapses several different backstep cases, including the results of a backstep angled at 10° to the step and the blunt body results of Roshko and Lau, onto a single curve, through the reattachment point. This normalization is significant, because it eliminates the effect of geometry (including expansion ratio) on the pressure rise through reattachment. It is interesting to note that the present results *do not* lie on the correlation of Westphal et al. Further checking indicated that all of the results plotted by Westphal had thin boundary layers at separation, while the present results have a thick boundary layer at the step edge. Further evidence of this effect is that the pressure measurements of Driver and Seegmiller [5], who had a thick boundary layer at the step edge, also deviate from the correlation.

Figures 7 and 8 present the LDA-measured mean and rms fluctuating components of streamwise velocity. While the present results look much like previous backstep data, there are some subtle changes. As with most backstep flows, the maximum backflow velocity is about $-0.2\ U_{\text{ref}}$ and occurs about 0.1 h above the bottom wall. Thus the entire backflow region is supplied by a very thin region near the wall. This is possible because of the strong streamwise pressure gradient in this region. In fact, if this thin region of backflow were to be considered a boundary layer growing in the $-x$ direction, the

Table 1 Uncertainty estimates

Measurand	Uncertainty
C_p	±0.005
C_f	±0.05
x_R	±0.1H
$\bar{U}/U_{\text{ref}}$ (LDA)	±0.01
$\bar{U}/U_{\text{ref}}$ (PWA)	±0.03
u'/U_{ref} (LDA)	±0.03
u'/U_{ref} (PWA)	±0.03
γ	±0.03 @γ=50%
	±0.01 @γ=95%

computed acceleration parameter $(\nu/U_N^2)/(\partial U_N/\partial x)$ would be two orders of magnitude higher than the relaminarization limit! (U_N is the maximum velocity in the $-x$ direction.)

The turbulence-intensity results in the region of reattachment are 10–15 percent lower than the results of Eaton and Johnston [8] and Westphal et al. [7]. The turbulence-intensity results do correspond with those of Pronchick et al. [23], who also had a thicker boundary layer at the step edge. The lower u' is not surprising, considering the pressure results. Since

$$\frac{\partial p}{\partial x} = \frac{\partial \tau}{\partial y}\bigg|_{y=0}$$

at reattachment, peak $\overline{u'v'}$ is probably lower in the present case than in that of Eaton. If the normal structural assumptions hold true, u' would also be expected to be lower. Thus it appears that the effect of a thicker initial boundary layer is to reduce the pressure rise and the pressure gradient at reattachment and to lower the turbulence intensity at reattachment compared with what it would normally be.

Streamlines computed from the mean-velocity profiles (see Fig. 9) are in excellent agreement with those of Eaton and Johnston [8] when the x-coordinate is normalized on x_r. The reattachment length in the present experiment (6.6 h) is considerably shorter than that of Eaton and Johnston (8.0 h), primarily due to the different expansion ratio used. Thus, scaling of the coordinate on x_r is seen to be effective in collapsing data from different experiments.

Figure 10 presents a comparison of values of peak streamwise turbulence intensity through the reattachment region with some data downstream of reattachment for other initial boundary-layer thicknesses and the results of other workers. Though there are fairly large differences ahead of the reattachment point, the data roughly collapse downstream of reattachment when the streamwise coordinate is normalized on x_r. Normalization on h was attempted and found to be much less successful. Though the data presented represent a range of initial δ/h and expansion ratios, it should be remembered that the flow in this region is so complex that Bradshaw and Wong (1972) comment, "Attempts to correlate properties of the relaxation regions downstream of different obstacles in terms of a few parameters describing the perturbations are not likely to succeed."

Figure 11 presents the skin-friction measured on the step wall with the pulsed wall probe. These results agree nicely with the results of Westphal et al. [9] using the pulsed wall probe and of Driver and Seegmiller [5] using a laser-based viscosity-balance method. Note here that, although the experiments compared have quite a range of expansion ratio and initial boundary-layer thickness resulting in large differences in reattachment length, the results of skin friction are the same in the separated region for these flows.

Though the value of C_f is small in the separation zone when normalized on the upstream reference velocity, when normalized on the maximum backflow velocity, $C_f \sim 0.02$. It is interesting to note that such large values are more typical of laminar than of turbulent flows.

The good collapse of C_f and u', among several experiments

when the streamwise coordinate is normalized by x_r is encouraging. Westphal et al. [7] also found an excellent collapse of static pressure data. The reason for the success of this normalization, which was suggested by Westphal et al. is undoubtedly due to the physical importance of x_r both in downstream-flow development and in the recirculation zone. Because of the success of the x_r normalization the authors recommend that comparisons of computations with experiments take place at the same x/x_r location, rather than the same x/h position. This normalization eliminates any effect of the miscalculation of the reattachment location.

6 Summary of Conclusions

Comparison of the LDA results reduced by several different schemes and pulsed-wire anemometer data showed that velocity bias was not a major problem in the present experiment. A small amount of velocity bias (<4 percent) was measurable in particle averages but was eliminated by the time-average methods tested here. The periodic sampling method of Stevenson and Thompson [15] was selected for the main data acquisition.

The present LDA results for the backward-facing step flow indicate the importance of upstream initial conditions on the development of the free shear layer. A thick boundary layer causes a lower pressure rise to reattachment and a lower pressure gradient at reattachment than cases with thinner initial separating boundary layers.

The present skin-friction results have strong similarities to the results of others in the separated region, despite the large differences in expansion ratio and initial shear-layer thickness. Finally, because of the importance of the reattachment length in the correlation of all the data, it is recommended that computational comparisons take place at the same x/x_r location to emphasize structural features of the flow.

7 Acknowledgments

We gratefully acknowledge the support of the National Science Foundation under grant MEA 80-17860-A1. We also thank Dr. John Vogel for his assistance in many phases of the experiment, particularly with the pulsed-wire probe. Finally, we thank Professor James P. Johnston for his guidance and assistance throughout the experiment.

References

1 Abbott, D. E., and Kline, S. J., "Theoretical and Experimental Investigation of Flow over Single and Double Backward-Facing Steps," Report MD-5, Thermosciences Div., Mech. Engrg. Dept., Stanford Univ., June 1961.

2 Chapman, D. R., Kuehn, D. M., and Larson, H. K., "Investigation of Separated Flows with Emphasis on the Effect of Transition," NACA Report 1356, 1958.

3 Bradshaw, P., and Wong, F. Y. F., "The Reattachment and Relaxation of a Turbulent Shear Layers," *J. Fluid Mech.*, Vol. 152, 1972, pp. 113–135.

4 Kim, J., Kline, S. J., and Johnston, J. P., "Investigation of Separation and Reattachment of a Turbulent Shear Layer: Flow over a Backward-Facing Step," Report MD-37, Thermosciences Div., Mech. Engrg. Dept., Stanford University, 1978.

5 Driver, D. M., and Seegmiller, H. L., "Features of a Reattaching Turbulent Shear Layer in Divergent Channel Flow," *AIAA J.*, Vol. 23, No. 2, 1985, pp. 163–171.

6 de Brederode, V. A. S. L., and Bradshaw, P., "Three-Dimensional Flow in Nominally Two-Dimensional Separation Bubbles. I. Flow behind a Rearward-Facing Step," I.C. Aero Report #72-19, 1972.

7 Westphal, R. V., Johnston, J. P., and Eaton, J. K., "Experimental Study of Flow Reattachment in a Single-Sided Sudden Expansion," NASA CR-3765, 1984.

8 Eaton, J. K., and Johnston, J. P., "Turbulent Flow Reattachment: An Experimental Study of the Flow and Structure behind a Backward-Facing Step," Report MD-39, Thermosciences Div., Mech. Engrg. Dept., Stanford Univ., June 1980.

9 Eaton, J. K., Jeans, A. H., Ashjaee, and Johnston, J. P., "A Wall-Flow-Direction Probe for Use in Separating and Reattaching Flows," ASME J. FLUIDS ENGRG., Vol. 101, 1979, pp. 364–366.

10 Westphal, R. V., Eaton, J. K., and Johnston, J. P., "A New Probe for Measurement of Velocity and Wall Shear Stress in Unsteady, Reversing Flow," ASME J. FLUIDS ENGRG., Vol. 103, Sept. 1981, p. 478.

11 McLaughlin, D. K., and Tiederman, W. G., "Biasing Corrections for Individual Realization Laser Anemometer Measurements in Turbulent Flows," *Phys. of Fluids*, Vol. 16, No. 12, Dec. 1973, pp. 2082–2088.

12 Buchhave, P., "Biasing Errors in Individual Particle Measurements with the LDA-Counter Signal Processor," *Proc. of the LDA Symposium*, Copenhagen, 1975, pp. 258–279.

13 Erdmann, J. C., and Tropea, C., "Statistical Bias in Laser Anemometry," SFB 80/ET/198, Univ. Karlsruhe, August 1981.

14 Barnett, D. O., and Bentley, H. T., III, "Statistical Bias of Individual Realization Laser Velocimetry," *Proc. of 2nd Int. Workshop on Laser Velocimetry* (H. D. Thompson and W. H. Stevenson, eds.), Purdue Univ. Bulletin No. 144, 1974, pp. 428–444.

15 Stevenson, W. H., and Thompson, H. D., "Direct Measurement of Laser Velocimeter Bias Errors in a Turbulent Flow," *AIAA Journal*, Vol. 20, No. 12, Dec. 1982, pp. 1720–1723.

16 Mayo, W. T., Jr., Discussion of Ref. 12, Purdue Univ. Bulletin No. 144, p. 444.

17 Durão, D. F. G., Laker, J., and Whitelaw, J. H., "Bias Effects in Laser-Doppler Anemometry," *J. Phys. E: Sci. Instrum.*, Vol. 13, 1980, pp. 442–445.

18 Johnson, D. A., Modarress, D., and Owen, F. K., "An Experimental Verification of Laser-Velocimeter Sampling Bias and Its Correction," *ASME J. Fluids Engrg.*, Vol. 106, 1984, pp. 5–12.

19 Durst, F., and Tropea, C., "Flows over Two-Dimensional Backward-Facing Steps," *Proc. Structure of Complex Turbulent Shear Flows*, (R. Dumas and L. Fulachier, eds.), Springer, LUTAM Symposium, Marseille, France, 1982.

20 Bradbury, L. J. S., and Castro, I. P., "A Pulsed Wire Technique for Velocity Measurements in Highly Turbulent Flows," *J. Fluid Mechanics*, Vol. 149, Part 4, 1971, pp. 657–691.

21 Klebanoff, P. S., "Characteristics of Turbulence in a Boundary Layer with Zero Pressure Gradient," NACA Report 1347, 1955.

22 Roshko, A., and Lau, J. C., "Some Observations on Transition and Reattachment of a Free Shear Layer in Incompressible Flow," *Proc. of 1965 Heat Transfer and Fluid Mechanics Institute* (A. F. Charwat, ed.), Stanford Univ. Press, pp. 157–167, 1965.

23 Pronchick, S. W., and Kline, S. J., "An Experimental Investigation of the Structure of a Turbulent Reattaching Flow behind a Backward-Facing Step," Report MD-42, Thermosciences Div., Mech. Engrg. Dept., Stanford Univ., June 1983.

B. M. Argrow
Graduate Student.

G. Emanuel
Professor.

School of Aerospace and Mechanical Engineering, The University of Oklahoma, Norman, Okla. 73019

Comparison of Minimum Length Nozzles

A second-order accurate method-of-characteristics algorithm is used to determine the flow field and wall contour for a supersonic, axisymmetric, minimum length nozzle with a straight sonic line. Results are presented for this nozzle and compared with three other minimum length nozzle configurations. It is shown that the one investigated actually possesses the shortest length as well as the smallest initial wall turn angle at the throat. It also has an inflection point on the wall contour, in contrast to the other configurations.

1 Introduction

Traditionally, supersonic nozzle design is done in two parts. Since the supersonic portion of the nozzle is independent of conditions upstream of the sonic line, it can be designed independent of the subsonic portion [1–9]. The converging portion of the nozzle is then designed to produce the required sonic line shape. In this tradition, we discuss a class of nozzles with a minimum throat-to-exit length and a uniform exit flow. This type of nozzle is referred to as a minimum length nozzle (MLN).

There are two fundamentally different MLN types. The first assumes a straight sonic line at the throat and is referred to as a straight sonic line MLN. For this type, the wall at the throat generates a centered expansion. The second type has a circular arc sonic line which is followed by a conical flow region with no centered expansion. This type is referred to as the curved sonic line MLN. Both types exist for two-dimensional and axisymmetric flows resulting in four possible configurations. All configurations have a sharp corner at the throat, in contrast to the smoothly contoured throats of conventional nozzles.

The two-dimensional straight sonic line MLN (often referred to as the classical sharp-cornered MLN) is investigated in references [1–6]. Reference [9] contains the first analysis of the axisymmetric straight sonic line MLN. Reference [4] presents the first complete analysis of the two-dimensional curved sonic line MLN. Finally, references [4, 7, 8] present analyses of the axisymmetric curved sonic line MLN.

Figure 1 is a sketch of a straight sonic line MLN. The flow between the throat, OA, and the downstream uniform flow consists of two regions. For both two-dimensional and axisymmetric flows, the kernel region, OAB, is a non-simple wave region. The transition region, ABC, is a simple wave region when the flow is two-dimensional, and its solution can be obtained analytically [4]. However, it is a non-simple region when the flow is axisymmetric, and a numerical solution is required.

In contrast to Fig. 1, the curved sonic line MLN has a source flow (non-simple wave) region just downstream of the sonic line [4]. This is followed by a transition region in which the flow expands to a uniform state. At a low exit Mach number M_f, the source flow region is roughly triangular, as in Fig. 1. At higher M_f values this region has a quadrilateral shape [4]. In this circumstance, the first wall section, starting at point A, is adjacent to a source flow and has a constant slope θ^*. As a consequence, the variation of the initial wall angle θ^* with M_f has a sharp change in slope. This variation, which depends on the ratio of specific heats γ, is shown in later figures.

All lengths can be normalized by the throat radius or half width r_i. The wall contour of any MLN is then fully determined by γ and M_f. These parameters fix θ^*, the length x_f of the nozzle, etc. The throat radius or half width r_i is determined by the mass flow rate.

Application of MLNs has largely been limited to the gas dynamic laser [10], where only the two-dimensional, straight sonic line nozzle has been utilized. However, a hypersonic wind tunnel using an axisymmetric, curved sonic line MLN has been in operation for years [8].

Somewhat surprisingly, the literature for one MLN type does not discuss the other [1, 3]. Consequently, a systematic comparison between configurations has not been previously done. Furthermore, except for references [4] and [5], published comprehensive results are not available. Of course, any comparison of the different configurations should include the

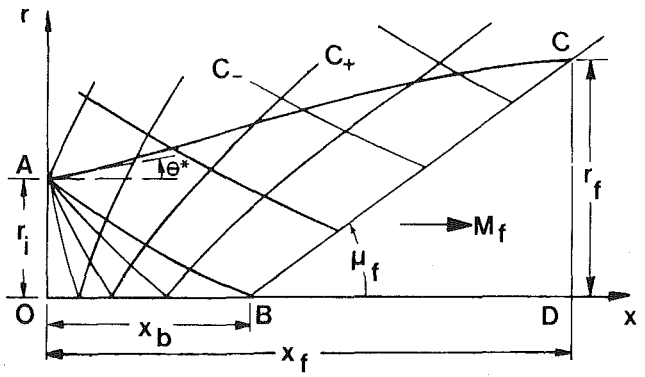

Fig. 1 Schematic of the flow field

Contributed by the Fluids Engineering Division for publication in the JOURNAL OF FLUIDS ENGINEERING. Manuscript received by the Fluids Engineering Division June 26, 1987.

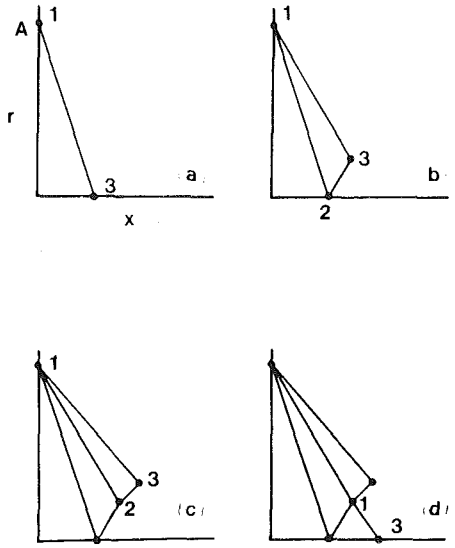

Fig. 2 Three unit processes used in constructing the kernel region

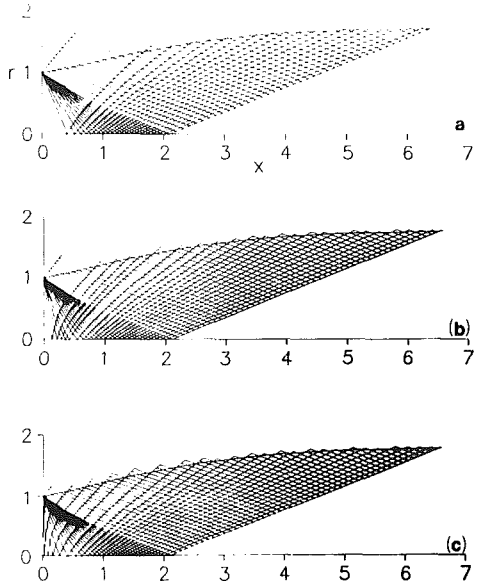

Fig. 3 Computer plots illustrating the effect of grid compression. All plots are for $\gamma = 1.4$, $\theta^* = 10°$. (a) has no grid compression, (b) and (c) have moderate compression.

axisymmetric, straight sonic line MLN. The published literature, however, does not provide any discussion or results for this specific MLN type. (Possibly, the fragmentary status of MLN theory is one reason why MLNs are not more widely used.)

In order to provide a systematic comparison of all four configurations, we have developed a computer code for the axisymmetric, straight sonic line MLN. Its computation is appreciably more difficult than the other three configurations, and it was not obvious that the flow would be free of shock waves. We present the first published results for this configuration.

Section 2 describes the formulation and numerical method used for the axisymmetric, straight sonic line MLN. The remaining two sections present results for this MLN and a comparison of the four configurations.

2 Formulation

For steady, supersonic, irrotational, axisymmetric flow of a perfect gas, the MOC equations can be written as

$$\frac{(M^2-1)^{1/2}}{1+(\gamma-1)M^2/2}\frac{dM}{M}+d\theta-\frac{\tan\theta}{(M^2-1)^{1/2}+\tan\theta}\frac{dx}{r}=0 \quad (1a)$$

$$\frac{dr}{dx}=\tan[\theta-\sin^{-1}(1/M)] \quad (1b)$$

$$\frac{(M^2-1)^{1/2}}{1+(\gamma-1)M^2/2}\frac{dM}{M}-d\theta-\frac{\tan\theta}{(M^2-1)^{1/2}\tan\theta+1}\frac{dr}{r}=0 \quad (2a)$$

$$\frac{dr}{dx}=\tan[\theta+\sin^{-1}(1/M)] \quad (2b)$$

where x and r are the axial and radial coordinates, respectively, and θ is the flow inclination angle. Equations (1) hold on the right-running C_- characteristics, while equations (2) hold on the left-running C_+ characteristics. In order to save computation time, the Prandtl-Meyer function ν is not used.

The differenced form of equations (1) and (2) are easily solved for the x, r, M, and θ variables. The resulting equations for a grid point in the kernel or transition region are listed in the Appendix. The sweep procedure for the kernel is evident in Fig. 2. For the upstream-most characteristic (Fig. 2(*a*)) unit process 3 is used. For the next point (Fig. 2(*b*)) unit process 2 is used. In Fig. 2(*c*) the interior point unit process is utilized, while the unit 3 process is again used in Fig. 2(*d*).

The kernel computation starts at point A with a known value for θ^*. We set $\Delta\theta = \Delta\nu = \theta^*/N$, which results in N rays whose angular spacing decreases as AB is approached; see Fig. 3(*a*). This results in a nearly uniform grid in the downstream part of the flow, but in a highly nonuniform grid near the throat. As a consequence, the wall contour downstream of A is poorly represented. At only a slight increase in computational time, this defect is corrected by a grid compression scheme. Additional characteristics, starting at point A, are inserted between the sonic line and the first regular C_- characteristic. A power law distribution

$$\nu_j=\left(\frac{j}{N_j}\right)^{M_j}\Delta\nu, \quad j=1, 2, \ldots, N_j$$

is utilized, where M_j and N_j are fixed integers that are not incremented with j.

Figure 3 shows the effect of grid compression. In this figure, $\gamma = 1.4$, $\theta^* = 10°$, $N = 20$, and M_f is 2.681. Figure 3(*a*) is the basic grid with no compression. Figure 3(*b*) has moderate compression with $N_j = 5$ and $M_j = 2$. Five additional characteristics have been inserted upstream of the first regular one. A greater degree of compression is used in Fig. 3(*c*), where N_j and M_j are both five. The number of additional characteristics is still five, but they now start closer to the sonic line, and result in a more satisfactory wall contour.

Control of the grid geometry in the transition region is achieved by prescribing an aspect ratio

$$\mathrm{AR}=\frac{S_+}{S_{\mathrm{ave}}}$$

for the cell closest to point B. The length S_{ave} is the average distance between grid points on the AB characteristic, while S_+ is the equally spaced distance between grid points on the BC characteristic. Figure 4 illustrates the procedure and shows the sweep direction in the transition region. Each sweep is in the C_- direction and terminates after the addition of a wall segment.

The wall is determined by

$$\frac{dr_w}{dx}=\tan\theta_w$$

subject to the initial condition, $\theta_w = \theta^*$ at $x = 0$. This equation

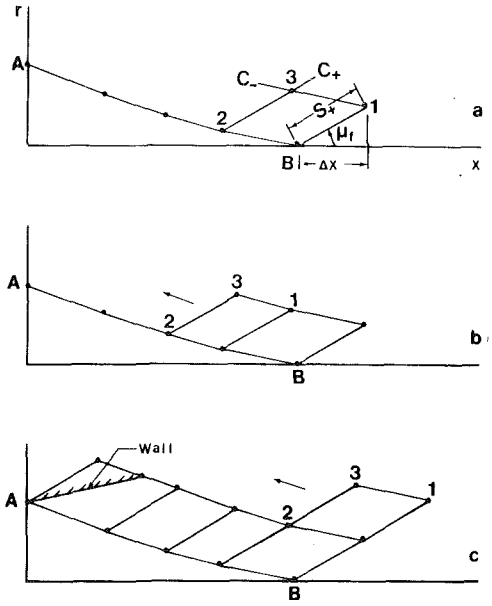

Fig. 4 Characteristic grid in the transition region

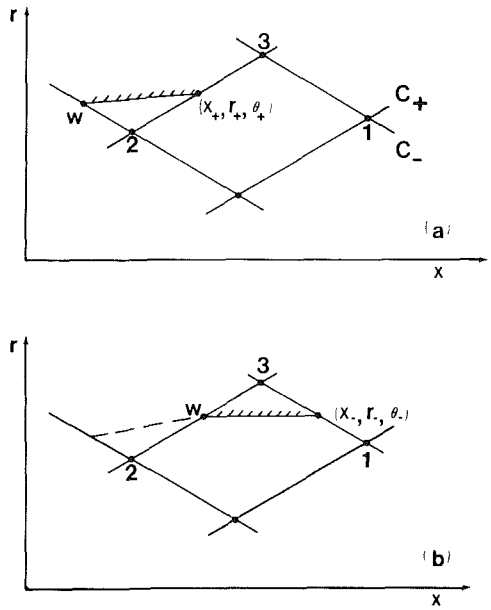

Fig. 5 Intersection of the wall and the $C_{\pm}$ characteristics

is solved iteratively using an average property, Euler predictor-corrector scheme.

As shown in Figs. 5(*a*) and (*b*), the characteristic segments 1-3 and 2-3, and the wall segments are assumed to be straight. The upstream wall point w and the characteristic points 1, 2, and 3 are known. The intersection point of the wall and the C_+ characteristic is (x_+, r_+), while for the C_- characteristic it is (x_-, r_-). These points are given by

$$x_{\pm} = \frac{r_3 + x_w \tan\theta_w - m_{\pm} x_3 - r_w}{\tan\theta_w - m_{\pm}} \tag{3a}$$

$$r_{\pm} = m_{\pm}(x_{\pm} - x_3) + r_3 \tag{3b}$$

where $m_{\pm}$ is the slope of the $C_{\pm}$ characteristic. It is given by

$$m_+ = \frac{r_3 - r_2}{x_3 - x_2}, \quad m_- = \frac{r_3 - r_1}{x_3 - x_1} \tag{3c,d}$$

If (x_+, r_+) lies on the 2-3 segment (Fig. 5(*a*)), the segment between (x_w, r_w) and (x_+, r_+) becomes a first approximation to the wall between these points. A predictor-corrector iteration is then used to find a more exact location of (x_+, r_+). Once (x_+, r_+) is located, it becomes the new wall point. The (x_-, r_-) intersection point on the 1-3 segment is then calculated and becomes a new wall point using the same procedure (Fig. 5(*b*)). Once the two wall points have been calculated, the procedure is repeated on the next sweep. In some instances, which depends on AR and the grid compression, only one wall point is determined per sweep.

The iteration begins by calculating (x_w, r_w) using equations (3). For the predictor step, the slope of the wall segment is set equal to θ_w. Once $(x_{\pm}, r_{\pm})$ is calculated, the corresponding flow angle $\theta_{\pm}$ calculated by

$$\theta_+ = \theta_2 + \left[\frac{(x_w - x_2)^2 + (r_w - r_2)^2}{(x_3 - x_2)^2 + (r_3 - r_2)^2}\right]^{1/2} (\theta_3 - \theta_2)$$

$$\theta_- = \theta_3 + \left[\frac{(x_w - x_1)^2 + (r_w - r_1)^2}{(x_3 - x_1)^2 + (r_3 - r_1)^2}\right]^{1/2} (\theta_1 - \theta_3)$$

The corrector calculates an updated intersection point, $(x_{\pm}, r_{\pm})$, using an average wall slope $(\theta_w + \theta_{\pm})/2$. This step is repeated until the relative change in the point location and the wall slope all satisfy a convergence criterion ϵ. This procedure terminates when the BC characteristic is reached.

The code is run in double precision on an IBM 3081 with CPU times ranging from 10 to 20 seconds per case. A global error can be evaluated by comparing the exit Mach number, M_f, produced by the kernel computation with one based on the normalized computed exit radius r_f. This Mach number is given by the well-known formula

$$r_f^2 = \frac{1}{M}\left[\frac{2}{\gamma+1}\left(1 + \frac{\gamma-1}{2} M^2\right)\right]^{(\gamma+1)/2(\gamma-1)}$$

Generally, the Mach number error, ΔM_f, is well below 10^{-4}.

3 Results

Figures 6-8 show θ^*, the kernel length x_B, and the nozzle length x_f versus M_f for $\gamma = 1.3$, 1.4, and 5/3. (Remember that all lengths are normalized by r_i). As expected, the smallest γ value requires the largest turn angle and the longest kernel and nozzle lengths. The effect is appreciable at a high exit Mach number. One can also show [9] that the ratio x_B/x_f is fairly insensitive to γ.

Figure 9 shows the Mach number along the wall for two different M_f values when $\gamma = 1.4$. The Mach number, M^*, just downstream of point A in Fig. 1 is given by $\nu(M^*) = \theta^*$, and thus exceeds unity. The rate of expansion, as expected, is greatest near the throat. Although dM/ds, where s is the arc length along the wall, is small at the exit, it is not zero. A similar phenomenon occurs in the two-dimensional case [5]. Thus, the derivative of the Mach number normal to the BC characteristic is discontinuous. This, of course, is in accord with the theory of characteristics.

The wall contour has a barely discernible inflection point near the throat; see Fig. 3(*c*). This is in contrast to the other three MLN configurations which have no inflection point [4]. Evidently, the inflection point is a result of the locally two-dimensional flow near point A adjusting to the rest of the axisymmetric flow. The location and wall slope at the inflection point are given in Table 1. The slope at this point does not greatly exceed θ^*, since it lies close to point A.

4 MLN Comparison

For the comparison, two-dimensional straight sonic line MLN results are obtained from reference [5], while curved sonic line results are obtained from reference [4]. The initial

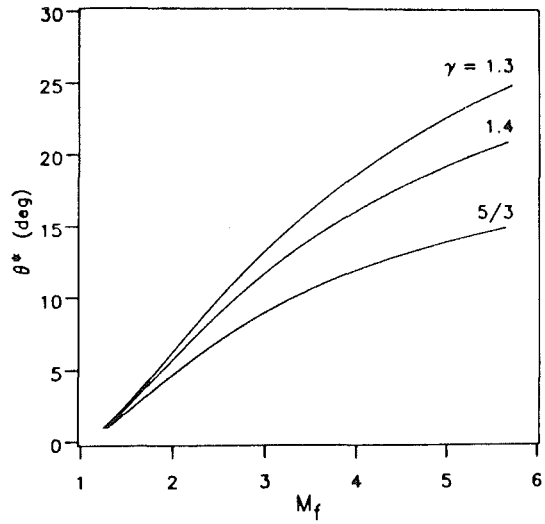

Fig. 6 Variation of θ^* versus M_f

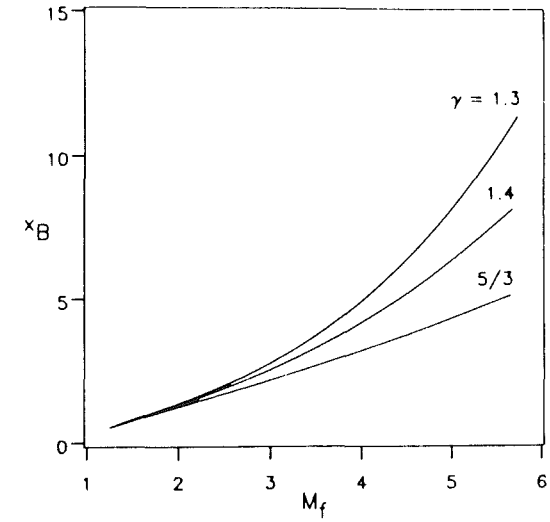

Fig. 7 Kernel length x_B versus M_f

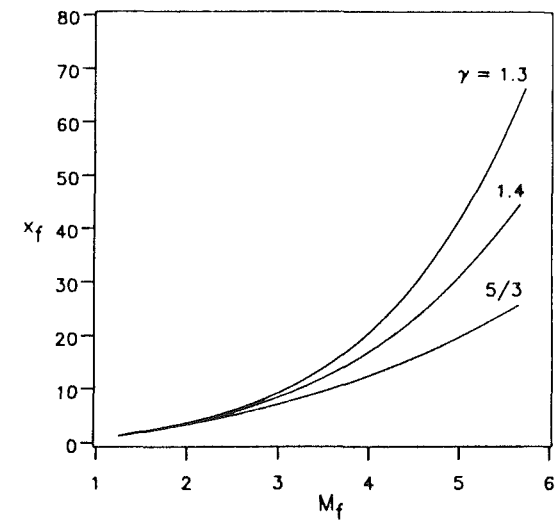

Fig. 8 Nozzle length x_f versus M_f

wall turn angle θ^* is shown in Figs. 10 and 11 for $\gamma = 1.3$ and 1.4, respectively. The slope discontinuity that occurs for the two curved sonic line MLNs is discussed in the introduction.

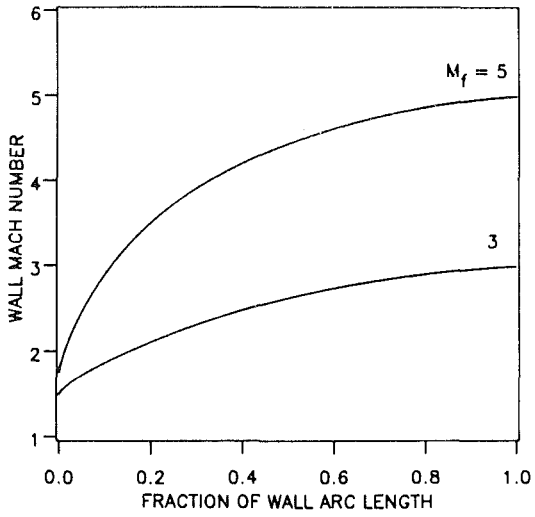

Fig. 9 Mach number along the wall for two values of M_f when $\gamma = 1.4$

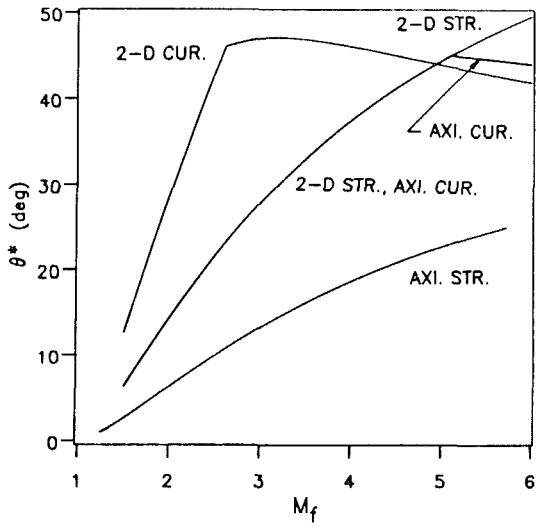

Fig. 10 Initial wall turn angle θ^* versus M_f for four MLN configurations when $\gamma = 1.3$

Table 1 Location and slope at the wall inflection point when $\gamma = 1.4$

θ^*	M_f	Inflection point		
		x	r	θ
2°	1.434	0.407	1.021	3.155°
4	1.739	0.496	1.048	5.975
6	2.037	0.576	1.081	8.606
8	2.346	0.625	1.115	11.103
10	2.681	0.690	1.156	13.492
12	3.051	0.729	1.195	15.792
14	3.472	0.765	1.235	18.015
16	3.961	0.799	1.279	20.168
18	4.544	0.834	1.325	22.256
20	5.257	0.871	1.375	24.284
22	6.160	0.889	1.419	26.254
24	7.352	0.935	1.480	28.166

Further details can be found in reference [4], which provided the results shown for the two-dimensional straight and the two curved sonic line configurations.

In Fig. 10, θ^* is the same for the axisymmetric curved and the two-dimensional straight sonic line nozzles up to an M_f of about 5.2. With an increase in γ, the point where the two solutions diverge shifts to a larger M_f value. As a consequence, this point is beyond the Mach number range shown in Fig. 11.

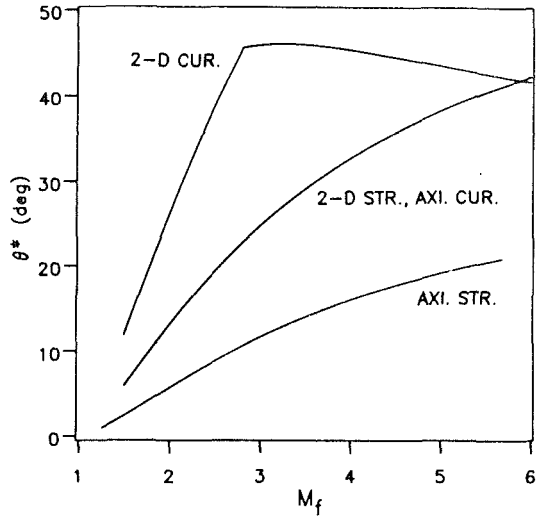

Fig. 11 Initial wall turn angle θ^* versus M_f for four MLN configurations $\gamma = 1.4$

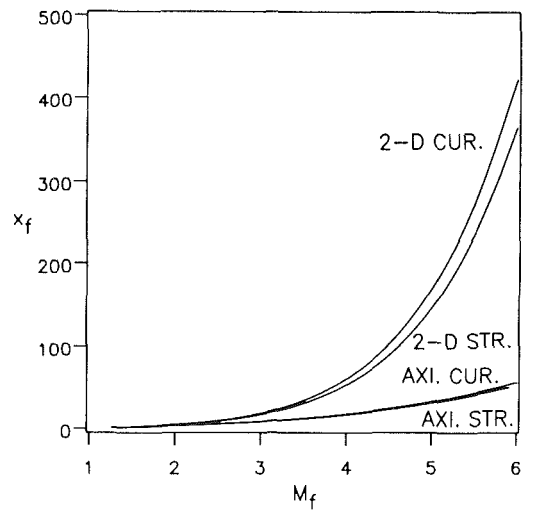

Fig. 13 Nozzle length versus M_f for four MLN configurations when $\gamma = 1.4$

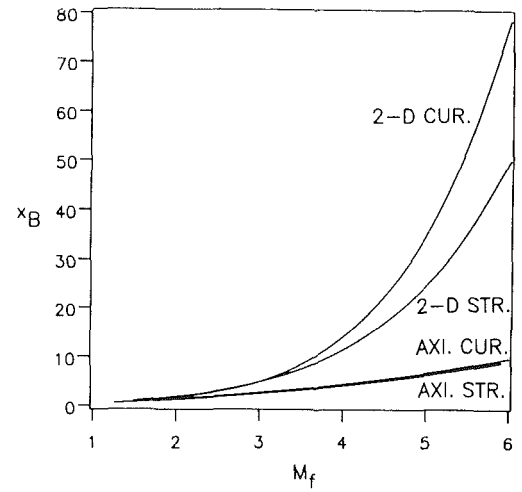

Fig. 12 Kernel length versus M_f for four MLN configurations when $\gamma = 1.4$

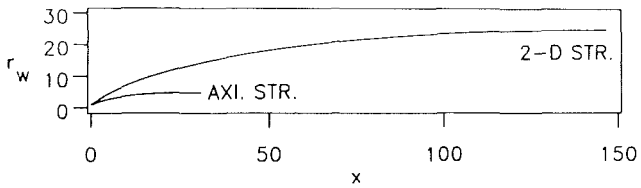

Fig. 14 Wall contour for the axisymmetric and two-dimensional MLNs with a straight sonic line when $\gamma = 1.4$ and $M_f = 5$

For a given M_f value, the comparison indicates that θ^* is significantly smaller for the axisymmetric straight sonic line MLN than for the other configurations. This conclusion holds for all γ values tested [9].

The remaining figures are for $\gamma = 1.4$. In Fig. 12 the normalized kernel length is shown. There is little difference between the two axisymmetric configurations, both of which are significantly shorter than the two-dimensional ones above an M_f value of about 2.5. This result is important for wind tunnel design because the test rhombus starts at the end of the kernel region.

Figure 13 shows the nozzle length where there is little difference between the two axisymmetric configurations and the two two-dimensional ones. Nevertheless, the axisymmetric, straight sonic line nozzle is the one with a minimum length. This result also holds at other values for γ [9].

A large disparity in size between the two straight sonic line configurations, at an $M_f = 5$, is shown in Fig. 14. The large difference in r_w at the exit is caused, in part, by the difference between r_w and r_w^2. The difference in length greatly favors the axisymmetric nozzle whenever a rapid expansion is desired, as in a gas dynamic laser or in a laser isotope separation process. What is surprising is that this advantage comes with the additional benefit of a smaller θ^*.

References

1 Shapiro, A., *Compressible Fluid Flow*, Vol. I, Chapt. 15, New York, The Ronald Press, 1953.

2 Vanco, M. R., and Goldman, L. J., "Computer Program for Design of Two-Dimensional Supersonic Nozzle with Sharp-Edged Throat," NASA TM X-1502, 1968.

3 Anderson, J. D., Jr., *Modern Compressible Flow*, Section 11.7, New York, McGraw-Hill, 1982.

4 Emanuel, G., *Gasdynamics: Theory and Applications*, New York, AIAA Educational Series, 1986.

5 Saadat, A., "Analysis of Minimum Length Two-Dimensional Nozzles," Thesis, University of Oklahoma, 1982.

6 Zucrow, M. J., and Hoffman, J. D., *Gas Dynamics*, Vol. 1, Chapter 12, and Vol. 2, Chapters 16, 17, New York, Wiley, 1976–77.

7 Foelsch, K., "The Analytical Design of an Axially Symmetric Laval Nozzle for a Parallel and Uniform Jet," *Journal of the Aeronautical Sciences*, Vol. 16, 1948, pp. 161–166, 188.

8 Dumitrescu, L. Z., "Minimum Length Axisymmetric Laval Nozzles," *AIAA Journal*, Vol. 13, 1975, p. 520.

9 Argrow, B. M., "Design and Analysis of an Axisymmetric Minimum Length Nozzle with a Straight Sonic Line," Thesis, University of Oklahoma, 1986.

10 Greenberg, R. A., Schneiderman, A. M., Ahouse, D. R., and Parmentier, E. M., "Rapid Expansion Nozzles for Gas Dynamic Lasers," *AIAA Journal*, Vol. 10, 1972, pp. 1494–1498.

11 Johanneson, N. H., and Meyer, R. E., "Axially Symmetrical Supersonic Flows Near the Center of an Expansion," *Aeronautical Quarterly*, Vol. 2, 1950, pp. 127–142.

APPENDIX

Unit Processes

Let point 3 be an interior grid point, Fig. 2(*c*), where conditions are known at points 1 and 2. The notation

$$( )_{13} = \frac{1}{2}[( )_1 + ( )_3], \quad ( )_{23} = \frac{1}{2}[( )_2 + ( )_3]$$

provides average values along the respective lines. For the first iteration, we use

$$( )_{13} = ( )_1, \quad ( )_{23} = ( )_2$$

Based on the finite-differenced form of equations (1) and (2), the unknowns are given by:

$$x_3 = \frac{E_2 - E_1}{C_{23} - C_{13}} \tag{A1}$$

$$r_3 = E_1 - C_{13} x_3 \tag{A2}$$

$$M_3 = \frac{D_1 + D_2 - B_{23} r_3 - B_{13} x_3}{A_{13} + A_{23}} \tag{A3}$$

$$\theta_3 = D_1 - A_{13} M_3 - B_{13} x_3 \tag{A4}$$

where

$$A_{j3} = \frac{[(M_{j3})^2 - 1]^{1/2}}{M_{j3}[1 + (\gamma - 1)(M_{j3})^2/2]}, \quad j = 1, 2$$

$$B_{13} = -\frac{\tan\theta_{13}}{\{[(M_{13})^2 - 1]^{1/2} + \tan\theta_{13}\} r_{13}}$$

$$B_{23} = -\frac{\tan\theta_{23}}{\{[(M_{23})^2 - 1]^{1/2} \tan\theta_{23} + 1\} r_{23}}$$

$$C_{13} = \tan[\theta_{13} - \sin^{-1}(1/M_{13})]$$

$$C_{23} = \tan\{\theta_{23} + \sin^{-1}(1/M_{23})]$$

$$D_1 = A_{13} M_1 + \theta_1 + B_{13} x_1$$

$$D_2 = A_{23} m_1 - \theta_2 + B_{23} r_2$$

$$E_j = r_j + C_{j3} x_j, \quad j = 1,2$$

For the second unit process, Fig. 2(*b*), where point 3 is adjacent to the centerline, we have $r_2 = \theta_2 = 0$. While B_{23} is indeterminate, its resolution is well known. Equations (A1), (A2), and (A4) are unchanged, while (A3) is replaced with

$$M_3 = \frac{2(D_1 - B_{13} x_3) + A_{23} M_2}{2A_{13} + A_{23}}$$

Similarly, for the third unit process, Fig. 2(*a*), we have

$$r_3 = \theta_3 = 0$$

$$x_3 = x_1 + \frac{r_1}{C_{13}}$$

$$M_3 = M_1 + \frac{\theta_1 - B_{13}(x_3 - x_1)}{A_{13}}$$

Only the first unit process is used for the transition region.

Time-Dependent Laminar Backward-Facing Step Flow in a Two-Dimensional Duct

F. Durst
Lehrstuhl für Strömungsmechanik,
Universität Erlangen-Nürnberg,
Egerlandstr. 13, 8520, Erlangen,
Federal Republic of Germany

J. C. F. Pereira
Instituto Superior Técnico,
Dept. of Mechanical Engineering,
Lisbon, Portugal

This paper presents results of numerical studies of the impulsively starting backward-facing step flow with the step being mounted in a plane, two-dimensional duct. Results are presented for Reynolds numbers of Re = 10; 368 and 648 and for the last two Reynolds numbers comparisons are given between experimental and numerical results obtained for the final steady state flow conditions. In the computational scheme, the convective terms in the momentum equations are approximated by a 13-point quadratic upstream weighted finite-difference scheme and a fully implicit first order forward differencing scheme is used to discretize the temporal derivatives. The computations show that for the higher Reynolds numbers, the flow starts to separate on the lower and *upper corners of the step yielding two disconnected recirculating flow regions for some time after the flow has been impulsively started. As time progresses, these two separated flow regions connect up and a single recirculating flow region emerges. This separated flow region stays attached to the step, grows in size and approaches, for the time $t \to \infty$, the dimensions measured and predicted for the separation region for steady laminar backward-facing flow. For the Reynolds number Re = 10 the separation starts at the bottom of the backward-facing step and the separation region enlarges with time until the steady state flow pattern is reached. At the channel wall opposite to the step and for Reynolds number Re = 368, a separated flow region is observed and it is shown to occur for some finite time period of the developing, impulsively started backward-facing step flow. Its dimensions change with time and reduce to zero before the steady state flow pattern is reached. For the higher Reynolds number Re = 648, the secondary separated flow region opposite to the wall is also present and it is shown to remain present for $t \to \infty$. Two kinds of the inlet conditions were considered; the inlet mean flow was assumed to be constant in a first study and was assumed to increase with time in a second one. The predicted flow field for $t \to \infty$ turned out to be identical for both cases. They were also identical to the flow field predicted for steady, backward-facing step flow using the same numerical grid as for the time-dependent predictions.*

1 Introduction

The development of new methods to study complex flows has been progressing for many years, resulting in new numerical prediction procedures, e.g., [1, 2] and in new experimental techniques, see [3] applicable to separated flows. These methods have now reached a stage of development that suggests their applicability to detailed studies of nonboundary layer flows. It has been demonstrated, e.g., see [4], that their complementary employment is optimal to yield physically relevant information on flows with regions of separation. Their combined usage was also attempted to carry out the present work.

Among the many flow geometries employed to carry out basic studies of separated flows, the backward-facing step has gained particular attention due to its geometrical simplicity. This simplicity has been stressed by [5–7] who provide summaries of previous investigations of backward-facing step flows in addition to their own numerical predictions and detailed laser-Doppler measurements. However, all of the work that has gained detailed attention is related to steady backward-facing step flow usually encountered for the inlet and outlet flow conditions that are independent of time.

Studies on double backward-facing steps were performed by [8] and on axisymmetric sudden expansions by [9], and [10] but it is unlikely that results of these studies can be directly transfered to the single backward-facing step flow geometry. For time-dependent inlet and outlet conditions particular flow features occur and have to be taken into account to obtain in-

Contributed by the Fluids Engineering Division and presented at the Fluids Engineering Conference, Forum on Unsteady Flow Separation, Cincinnati, Ohio, June 1987 of THE AMERICAN SOCIETY OF MECHANICAL ENGINEERS. Manuscript received by the Fluids Engineering Division, February 19, 1987.

formation on the time-variation of the flow structure, especially the time variation of the lengths of the recirculating flow regions occuring behind the step and at the opposite wall.

The above suggests that only little information exists on time-dependent backward-facing step flows as they are experienced when the flow is impulsively started. Nevertheless, there have been previous studies of time-dependent backward-facing step flows. Comparing results obtained from computations using different numerical schemes, Roache and Mueller [12], were able to deduce physical flow information regarding the separation at the base of the backward-facing step. This was found experimentally by [13] and theoretically by [14] who investigated the viscous dominated corner flow region. The same evidence that separation occurs at the backface of the step, a finite distance from the corner, was confirmed by [15] for Reynolds numbers 10 and 100. In spite of this the question of where the backward-facing step flow separates is still a subject of controversy almost two decades after the results of Roache and Mueller [12]. In many flow predictions separation is predicted to occur always at the lip of the step, e.g., see [9]. In the few time dependent flow visualization experiments, e.g., see [16], no final answer is provided to where flow separation occurs first. One of the objectives of this paper is to provide information on this subject for very low and relatively high Reynolds number backward-facing step flows.

Other investigations that should be mentioned in conjunction with the present study are those of Ahmed et al. [17, 18] who investigated the effect of Reynolds number on the stability and transition to turbulence of the flow using a random vortex method for their computations. Further work was reported by Ghia et al. [19] who employed a vorticity stream-function formulation and also employed in their computations generalized curvilinear orthogonal coordinates. The present work complements those time dependent flow analysis by investigating the influence of the inlet flow conditions on the structure of the time-dependent recirculating flow behind the step and also studies of the influence of Reynolds number on the development of the flow.

The numerical prediction procedure employed for the present study is described in Section 2 and the initial and boundary conditions are also given in this section. Numerical results are given in Section 3 and for $t \to \infty$, these are compared with predicted results obtained with a computer program for steady flows and also with results obtained by laser-Doppler anemometry for steady, backward-facing step flows in two-dimensional ducts. The last section of the paper summarizes the main findings and presents some conclusions.

2 Computer Program For Numerical Flow Studies

2.1 Governing Differential Equations. The flow to be studied in this paper is assumed to be laminar, two-dimensional, but time-dependent and the employed fluid to be Newtonian, incompressible, and of constant viscosity. With these assumptions, the continuity equation and the Navier-Stokes equations reduce to the following set of three partial differential equations:

$$\frac{\partial U_1}{\partial x_1}+\frac{\partial U_2}{\partial x_2}=0 \tag{1}$$

$$\rho\frac{\partial U_1}{\partial t}+\rho U_1\frac{\partial U_1}{\partial x_1}+\rho U_2\frac{\partial U_1}{\partial x_2}=-\frac{\partial p}{\partial x_1}+\mu\left(\frac{\partial^2 U_1}{\partial x_1^2}+\frac{\partial^2 U_1}{\partial x_2^2}\right) \tag{2}$$

$$\rho\frac{\partial U_2}{\partial t}+\rho U_1\frac{\partial U_2}{\partial x_1}+\rho U_2\frac{\partial U_2}{\partial x_2}=-\frac{\partial p}{\partial x_1}+\mu\left(\frac{\partial^2 U_2}{\partial x_1^2}+\frac{\partial^2 U_2}{\partial x_2^2}\right) \tag{3}$$

where U_1 and U_2 represent the velocity components in the x_1 and x_2 directions of a cartesian coordinate system, ρ is the fluid density, μ the fluid viscosity, and t the time.

The above set of equations can be rewritten in the form of a transport equation for the variable ϕ:

$$\frac{\partial(\rho\phi)}{\partial t}+\frac{\partial}{\partial x_1}(\rho U_1\phi)+\frac{\partial}{\partial x_2}(\rho U_2\phi)=\frac{\partial}{\partial x_1}\left(\mu\frac{\partial\phi}{\partial x_1}\right)+\frac{\partial}{\partial x_2}\left(\mu\frac{\partial\phi}{\partial x_2}\right)+S_\phi \tag{4}$$

with $\phi=1$, and $S_\phi=0$ the above equation results in the continuity equation and for $\phi=U_i$ $(i=1,2)$, and $S=-\partial p/\partial x_i$ $(i=1,2)$, the momentum equations are obtained. These equations, the boundary conditions (given in Fig. 1) and the time-varying inlet and outlet conditions define the flow problem to be studied.

2.2 Computational Scheme. The conservative finite-volume approach described by e.g., Gosman and Pun [1] was used in this investigation to discretize the terms in the continuity and momentum equations. With this method, it is necessary to approximate the convective and diffusive fluxes of the quantity under consideration at the micro-control volume faces, surrounding a grid node. These fluxes were replaced by finite difference terms employing the quadratic upstream weighted differencing scheme proposed by Leonard [20]. However in the present study the full 13-point simulation was employed. This method uses a quadratic interpolation surface oriented with the local velocity components in an upwind-like manner.

For the interpolations at each control volume face, the non-uniformity of the grid spacing was taken into consideration. Some of the details of the convection discretization procedure are given in the [24], [26].

The temporal discretization was performed by an implicit first order forward differencing scheme, and the spatial derivatives were evaluated at the new time level $t+\Delta t$. The general form of the system of algebraic equations to be solved can be expressed as:

$$A_{i,j}^{i,j}\Phi_{i,j}=\Sigma A_{i,j}^{i\pm k,j\pm l}\Phi_{i\pm k,j\pm l}+S_{\Phi_{i,j}} \tag{5}$$

where the sum Σ refers to the 12-ponts $(i\pm k, j\pm l)$ surrounding the point (i, j). The system of algebraic equations (5) was solved at each time step by a version of the strongly implicit scheme proposed by Stone [21] in which the coefficient matrix comprises nine diagonals, see Azevedo et al. [22]. The four coefficients $A_{i,j}^{i+2,j+2}$ were incorporated in the source terms; if they are not zero they are negative and contribute to the non-diagonal dominancy of the matrix to be solved.

At each time step, the solution algorithm proceeded as follows: the velocity field U_1 and U_2 were first calculated from the momentum equation for a guessed pressure field. The pressure was subsequently calculated in such a way that the velocity components satisfied the continuity equation. Hence,

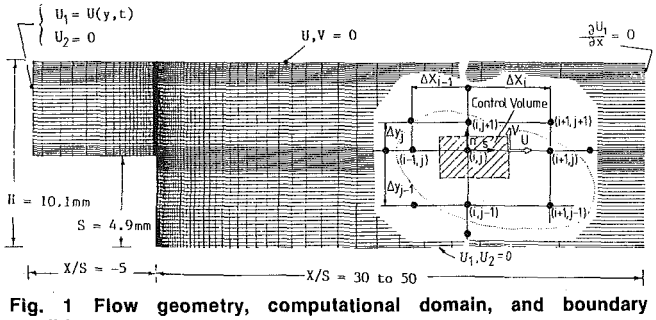

Fig. 1 Flow geometry, computational domain, and boundary conditions

the sequence of the computations was the one nowadays accepted in finite difference computations of flow fields.

The above-mentioned iteration process was continued in the described sequence until the sum of the normalized residuals for mass and momentum were less than 10^{-3}. The resulting fields for the velocity components and the pressure represented the initial values for the next time advancement.

2.3 Boundary and Initial Conditions. Particular attention was paid to a flow geometry previously used by the authors to study steady backward-facing step flows, see reference [5]. This flow geometry was made up of an inlet duct of 5.2 mm in height merging into duct of 10.1 mm height yielding an expansion ratio for 1.94. This geometry is sketched in Fig. 1. This figure also gives the boundary conditions applied in the computations. They consisted of zero slip boundary conditions at the wall, a prescribed inlet velocity at five step heights up-stream the step and zero gradient conditions for U_1 and U_2 at a distance of a minimum of four times the measured recirculation length downstream of the step expansion for the steady flow. The impulsive start of the flow at $t=0$ corresponded to an artificial situation where a zero velocity field in the entire computational domain existed except for the inlet plane where a finite velocity profile was prescribed for $t>0$ as a function of space and time. The U_2-inlet-velocity was in all calculations kept constant and set to $U_2=0$ for all points in the inlet plane and for all times. Three different U_1 profiles with the following spatial and temporal variations were considered:

(*i*) In the first test case, the prescribed $U_1(x_1=-5s, x_2, t)$ – profile corresponded to a parabolic velocity profile with its maximum being located at the centreline of the inlet duct. This inlet velocity profile was kept unaltered for the entire duration time of the computations.

(*ii*) In the second test case, the U_1-velocity profile changed with time from a top-hat profile at $t=0$ (start of the flow) to a parabolic profile when the steady state flow field was reached. The mass flow rate through the duct was kept constant for this case.

(*iii*) In the third case, a flow setup was considered for which the mean flow rate increased with time. With increasing flow rate the inlet velocity profile was assumed to change its shape in the way described for case (*ii*).

$$U_1 = U_{\max}\left[1-\left(\frac{2x_2}{h}\right)^2\right] + U_2(x_2,t) \tag{6}$$

with

$$U(x_2,t) = \sum_{n=1}^{\infty} \frac{-4(-1)^n}{\alpha^3} \cdot \exp\left(-\frac{\mu}{\rho}\alpha^2 t\right)\cos(\alpha x_2) \tag{6a}$$

and with

$$\alpha = (2n+1)\frac{\pi}{h}$$

where $h/2$ is half of the inlet channel height and $U(x_2,t)$ represents the velocity time dependence.

3 Flow Computations and Results

To carry out grid dependence investigations of the flow computations, several numerical meshes ranging from 29×24 to 85×65 grid nodes were considered. For each grid, numerical computations were obtained using different values of the time step ($5\times10^{-4}\le t\le5\times10^{-2}$ seconds), but keeping a chosen time step constant during the time marching process of the corresponding flow computation process. The distribution of the grid nodes was non-uniform in both coordinate directions allowing higher grid node concentrations in the region close to the step, along the shear region of the flow and close to both walls of the duct upstream and downstream of the step. The Reynolds number of 648 was chosen to check time and grid size dependence of the solutions. This flow turned out to be most sensitive to the discretization sizes because the flow field possessed multiple recirculation regions for which a very fine grid distribution had to be chosen to accurately predict the flow properties.

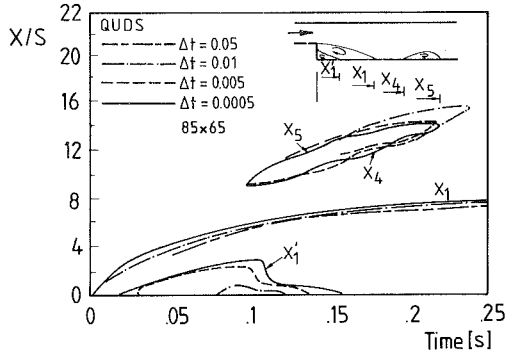

Fig. 2(*a*) Influence of time step on predicted dimensions of separated flow regions

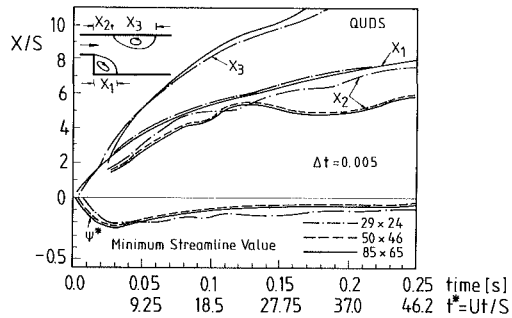

Fig. 2(*b*) Influence of grid size on predicted dimensions of separated flow regions

Figure 2(*a*) shows the time step dependence of the predicted length of the recirculating flow region attached to the step and the bottom channel wall. The numerical mesh comprised 85×65 grid nodes in the x_1 and the x_2 directions, respectively. The inlet conditions given in the last section in point (*i*) were employed in this part of the work. A time step of 5×10^{-3} proved to be small enough to compute sufficiently accurate the time variations of the flow. This finding was drawn from comparison in Fig. 2(*a*) where the reattachment lengths computed for different time steps Δt were compared with each other. The results clearly show that further refinements would not alter the predicted flow features. The sufficient agreement between the predictions with time steps of 5×10^{-3} and 5×10^{-4} seconds in the early stages of the flow development was maintained up to the establishment of the steady state flow pattern.

Figure 2(*b*) shows the dependence of the separation lengths on the numerical grid size. The main separation region, attached to the step and the recirculation region at the top channel wall are shown together with the minimum value of the nondimensionalized stream function ψ^* in the main recirculating flow region. This figure indicates that 85×65 grid notes are sufficient to capture the essential features of this flow. The physical information contained in Figs. 2(a) and 2(*b*) are discussed in section 3.3. However, it can be concluded that a constant time step Δt^* equal to 0.9, together with a grid of 85×65 grid nodes, distributed as shown in Fig. 1, are appropriate to study accurately the flow under consideration.

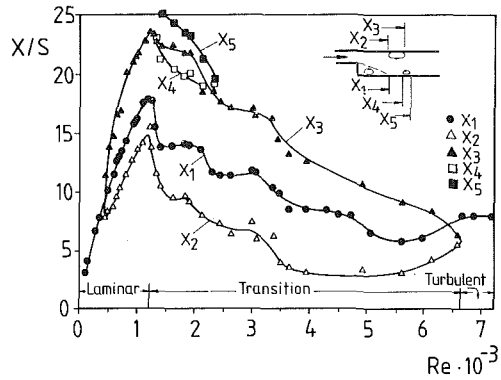

Fig. 3 Measured longitudinal dimensions of separated flow regions downstream of backward-facing step

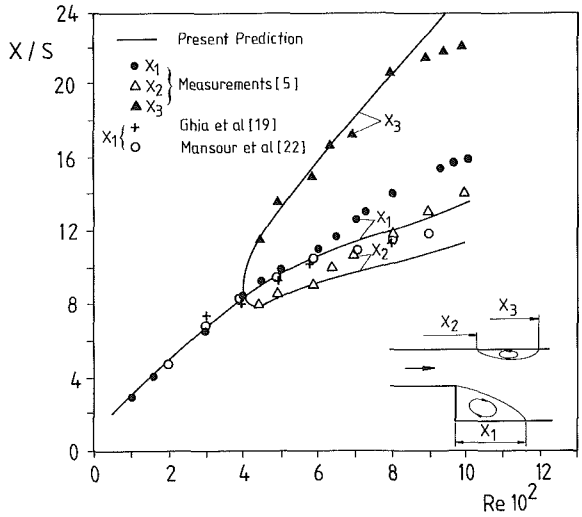

Fig. 4 Predicted longitudinal dimensions of separated flow regions downstream of backward-facing step

3.1 Steady-State Flow Results. For steady backward-facing flows, the recirculating flow regions behind the step and downstream on both sides of the channel walls were carefully investigated and their dimensions quantified with the help of the laser-Doppler anemometer described by Armaly et al. [5]. An overall representation of the longitudinal dimensions of the three separated flow regions, forming downstream of the step, is given in Fig. 3. Computational results, obtained with a computer program for predicting steady separated flows, are compared in Fig. 4 with experimental results and with predictions from other authors [19], [23]. For the Reynolds number range $Re \leq 650$, good agreement was obtained between experiments and predictions. At higher Reynolds numbers, Fig. 4 shows the agreement to be less good. The increased disagreement between experimental and numerical results at higher Reynolds numbers, i.e., in the range $650 \lesssim Re \lesssim 1200$ is caused by the occurrence of inherent three-dimensional effects in the experiments that reached the centre plane of the channel at $Re \approx 800$, see [5].

The steady state predictions were also performed with a first order upstream scheme and the results with this scheme showed that for $Re \lesssim 400$ accurate steady calculations can be obtained with coarse grids and with first order schemes. This finding can be explained by the presence of only one recirculation zone attached to the step wall and by the fact that when the flow is highly skewed with respect to the numerical mesh, the local Peclet numbers, $Pe = \Delta x U/\nu$, are very small and vice-versa and so numerical false diffusion is generally negligible. This is not the case for backward-facing step flows of higher Reynolds numbers since very complicated flow structures, incorporating multiple regions of flow separation, are present and first order solutions become strongly grid dependent, see [5, 24, 25]. Hence, higher order numerical schemes, as the 13-point quadratic upstream scheme used in this study, are only required for backward-facing step flows of $Re \geq 400$.

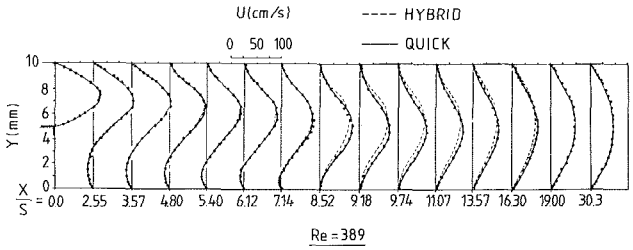

Fig. 5 Comparison between experimental and numerical results for flow field downstream of backward-facing step

In the present investigations, the emphasis of the combined experimental and numerical investigation for steady backward-facing step flow was concentrated on the Reynolds number region where two-dimensional flows existed, i.e., $Re \lesssim 650$. In this region of Reynolds numbers good agreement was obtained in the entire flow field between numerical and experimental results. This is readily seen from Fig. 5, which shows a comparison between experimental and numerical results for $Re = 389$ obtained with the quadratic upstream weighted scheme.

3.2 Unsteady Flow Results

3.2.1 Results for Re = 10. Figure 6(*a*) shows the temporal variation of the reattachment length for a flow of $Re = 10$ obtained with the quadratic scheme and using 85×65 grid points. The computational domain ends 6 step heights downstream of the step. The time step increment was chosen as 5×10^{-3} seconds ($t^* = 0.015$). Only one recirculation zone was formed during the computational time which remained of constant length after $t = 0.4$ seconds, $t^* = 1.17$ and was attached to the upper corner of the step. Figure 6(*b*) shows the calculated streamlines for various times t. These were computed from the resultant velocity field and isostreamlines were obtained by a bi-cubic interpolation. This figure clearly shows that at such low Reynolds numbers the flow starts to separate at the bottom corner of the step and no additional separation occurs at the upper corner. The separation point lies at the backface of the step and it moves upward, towards the conjectured limit position at the sharp corner as the time is increased. This is in very good agreement with the results of [12]. The same principle finding was obtained with all three inlet flow conditions described in Section 2.

3.2.2 Results for Re = 389. Experimental investigations, for $Re = 389$, under steady state flow conditions, revealed that no separation region at the wall opposite to the step existed. This can readily be deduced from Fig. 3, which indicates that multiple separation regions were only found for $Re \geq 420$. Observations suggested, however, that translational recirculating flow regions are formed during the starting phase of the flow, that disappear by the time the steady state flow is reached. To study the development of the flow for $Re < 420$, unsteady flow calculations were performed for $Re = 389$ and for the inlet condition (*i*) in section 2, i.e., it was assumed that the inlet profile was fully developed and kept constant with time for $t > 0$. This inlet condition is somewhat artificial but was meant to simulate an abruptly starting backward facing step flow.

The temporal evolution of the dimensions of the recirculation zones in the region behind a two-dimensional backward-facing step, formed on both walls of the channel, are shown in Fig. 7(*a*). The computational results show that the recirculation region on the wall opposite to the step starts to appear ap-

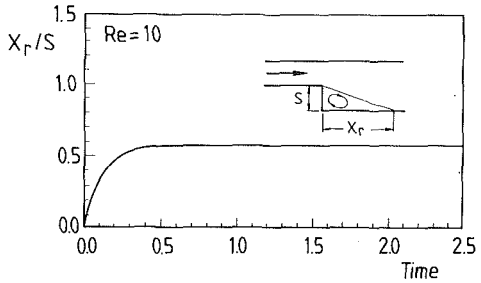

Fig. 6(a) Predicted time variation of separation length of time-varying backward-facing step flow of Re = 10

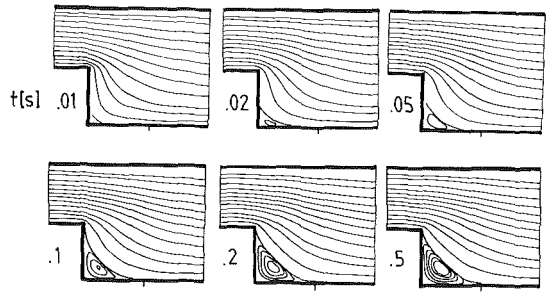

Fig. 6(b) Variation of streamline pattern with time for Re = 10

proximately at $t = 0.03$ seconds after the inlet flow was started and it disappears at approximately $t = 0.70$ seconds. This finding is in agreement with experimental studies of the steady flow for which the recirculation region at the top wall was not measured. Figure 7(a) also shows that a small separated region occurs at the lower corner of the step for some time after the starting motion. This will be discussed in the next subsection.

Figure 7(b) provides information on the strength of the time dependent recirculation region at the wall opposite to the step showing the evolution with time of the sum of the recirculating mass flow rate Q^*. It shows that the recirculation region has a maximum of strength occurring at $t = 0.13$ seconds, and continuously decreases afterwards until the recirculation zone disappears at approximately $t = 0.7$ seconds.

To provide further insight into the developing backward-facing step flow the time dependence of the streamline pattern of the separation region attached to the step was analyzed. Streamlines were computed for various times, some of which are shown in Fig. 8. These provide a good picture of the developing flow close to the step. At first, the flow separation occurred at the bottom corner of the step and then a second separation region developed at the sharp edged upper corner of the backward-facing step. The upper separation bubble reattached at the downward facing wall of the step. Both separation regions grew with time and then merged to build a single recirculating flow region. This grew further up to its steady state size. At the same stage of the flow development, a second corner separation region developed and maintained up to $t \to \infty$.

The flow visualization experiments of Honji [16], although only obtained for $t^* \approx 2$, showed separation at the corner of the step. At such a late time, the present predictions suggest that the bottom and top separation region at the step have already merged and only one separation region is seen. To investigate experimentally the complete phenomena of the developing separation, it is necessary to record the flow information much earlier than Honji [16] did in his experiments.

3.2.3 Results for Re = 648. The experimental investigations of backward-facing step flows performed by [5] for steady flow conditions showed the occurrence of a recirculation region on the channel wall opposite the step if the flow was laminar and the Reynolds number exceeded $Re \simeq 420$. This additional recirculating flow region was also found using steady state flow calculations, see Fig. 4.

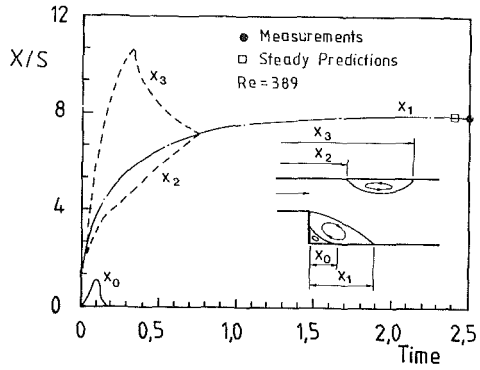

Fig. 7(a) Variations of longitudinal dimensions of separation regions for Re = 389

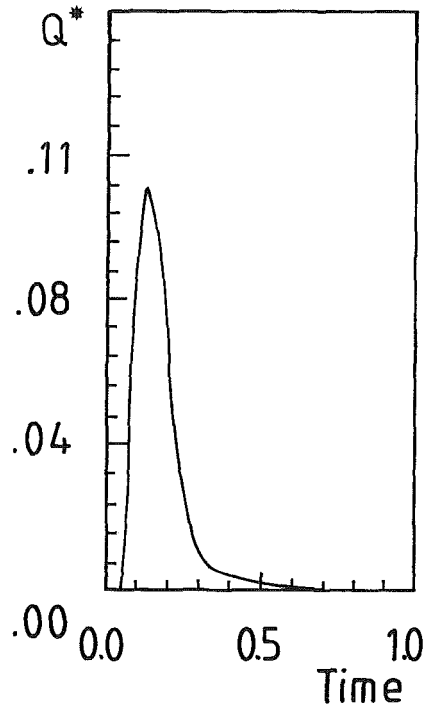

Fig. 7(b) Strength of separated flow region opposite of step as a function of time for Re = 389

To study the finite development of this flow, unsteady flow predictions were performed using 85×65 grid points. The 13-point quadratic numerical scheme was employed to eliminate numerical false diffusion errors. The Courant number based on local velocity was always less than 1 with the exception of the expansion region of the plane jet emerging from the step lip where the maximum velocity gradients were located and the mesh size was of the order of one tenth of the step height. For the results presented here the three different time dependent inlet conditions were considered as given in Section 2.

At $t = 0$ no flow passed the plane of the channel at the step. For $t > 0$ the inlet velocity profile obtained with equation (6) corresponded to a fully developed laminar channel velocity profile. The inlet mean flow rate increased from zero (for $t = 0$) to the mass flow rate corresponding to $Re = 648$.

Using the time dependent inlet velocity profiles given by equation (6), a time dependent mass flow rate through the inlet channel plane located at the backward facing step was ob-

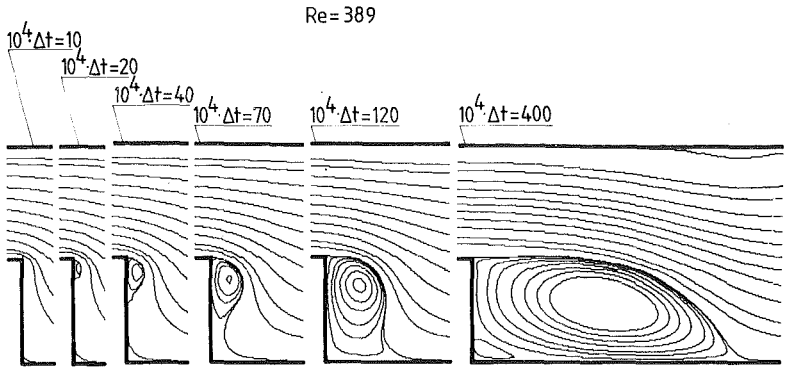

Fig. 8 Development of streamline pattern for time-dependent backward-facing step flow for Re = 389

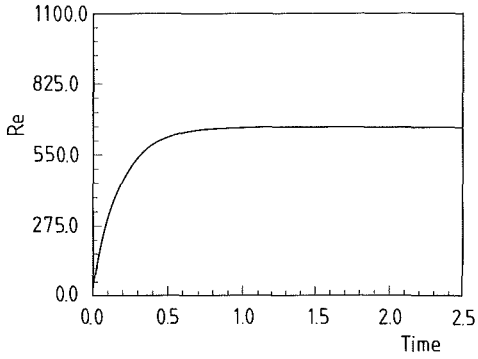

Fig. 9 Variation of mass flow rate through inlet plane of test section for Re = 648

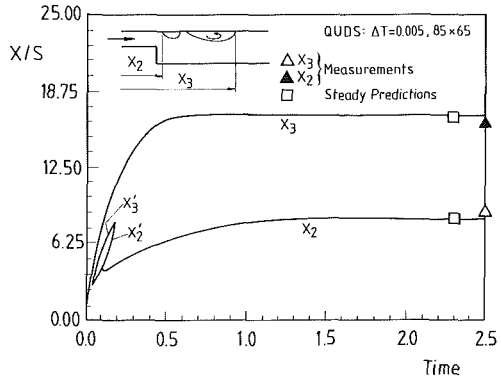

Fig. 11 Development in time of separation region opposite to backward-facing step for Re = 648

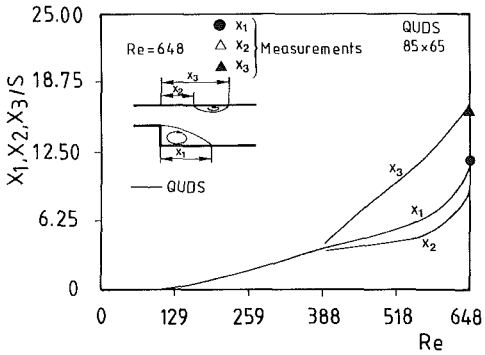

Fig. 10 Prediction of longitudinal dimensions of separation regions behind the backward-facing step for Re = 648

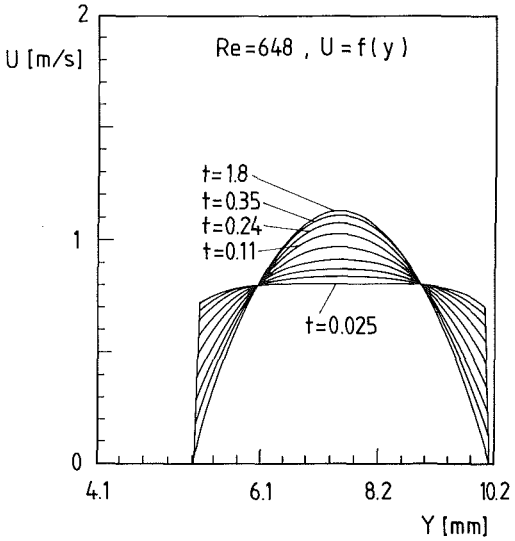

Fig. 12 Variation of inlet velocity profile with time for Re = 648

tained. Expressing this in terms of a time dependent Reynolds number of the inlet flow, yields the results given in Fig. 9. The results for the locations of detachment of reattachment obtained in the computations are indicated in Fig. 10 which allows the evolution of the longitudinal dimensions of the two separation zones to be deduced.

Figure 10 shows that the second recirculation region opposite to the step started to develop at a Reynolds number $Re \approx 410$, which is in good agreement with the Reynolds number found for steady flow conditions beyond which a separation regions exists at the wall opposite to the step, e.g. see Armaly et al. [5]. Figure 11 shows that the results of the time dependent flow calculation agreed for $t \to \infty$ with the results obtained from calculations using computer codes for steady state flow conditions. The agreement with experiments is slightly less due to occurrence of three-dimensional effects.

The second inlet profile considered for unsteady flow calculations for Re = 648 correspond to case (*iii*) of Section 2. Figure 12 shows the resulting inlet velocity profile at different times. For the final steady state flow conditions ($t \to \infty$) the inlet profile becomes that of a fully developed laminar channel flow.

The computational results are reflected in Figs. 13 and 14. For $t = 0.01$ the two separated flow regions at the backward face of the step are shown; they already had merged at $t = 0.02$. As time proceeded, the separation region attached to the step grew and a second bottom corner bubble developed together with a separation region at the wall opposite to the step. Both these secondary recirculation regions grew further, reached a maximum and than disappeared again, with the distinct phase difference between the growth and decay

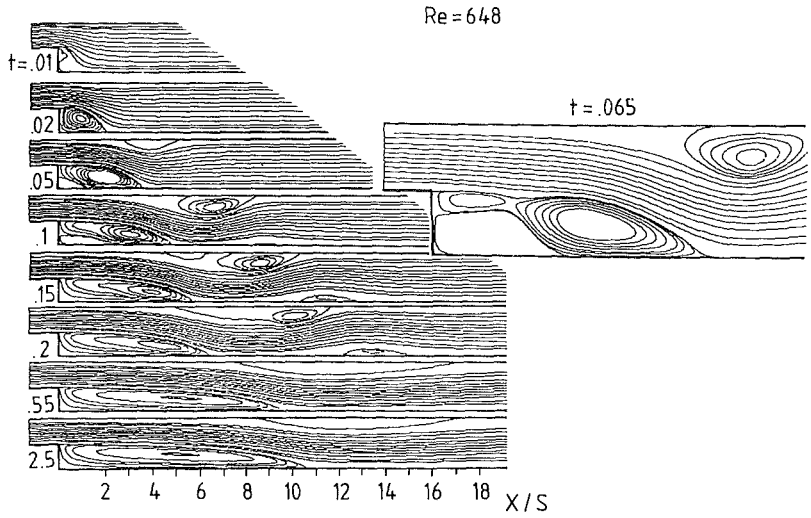

Fig. 13 Time sequence of computed streamline pattern for time-dependent backward-facing step flow at Re = 648

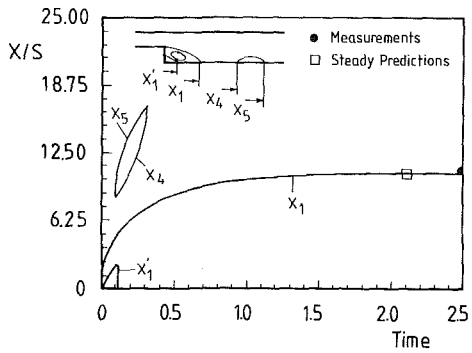

Fig. 14 Variation of longitudinal dimensions of separated flow region behind the step for Re = 648

processes. For a limited period of time a small additional recirculating flow region appeared at the wall where the step is located. This is indicated in Fig. 13 which presents the longitudinal location of detachment and reattachment of the flow at the bottom wall as a function of time.

It is interesting to note that all the essential features of the predicted flow are in good agreement with findings by Honji [16] who performed flow visualization studies of the starting flow downstream of a step at approximately the same Reynolds number. Hence, all the essential features of laminar time dependent backward-facing step flows can nowadays be predicted with sufficient accuracy to yield physically reliable flow information.

4 Conclusions

Steady and unsteady numerical predictions of laminar, viscous flow in a two-dimensional channel with sudden expansion in cross sectional area (expansion ratio 1:1.94) were performed and results were obtained for three Reynolds numbers, Re = 10, 389 and 648. The lowest Reynolds number flow was included to study the flow separation behind a step for flow conditions which previous studies have already dealt with. The numerical study orientated itself on experimental investigations carried out for steady flows. There it was found that for $Re \lesssim 420$, no recirculation flow region existed on the wall opposite to the step but recirculating flow region occurred for higher Reynolds numbers. This subdivision into a higher Reynolds number and a lower Reynolds number region resulted in the choice of the second and the third Reynolds number given above. The numerical results obtained in the present study allow the following conclusions to be drawn.

For the flow at Re = 10, separation was observed at the back face of the step below the sharp top corner. As time proceeded, the separation line moved upward reaching the top corner edge for $t \to \infty$.

Computations of the steady state flow fields obtained for $t \to \infty$ with a computation procedure for unsteady flows, were compared with steady state flow computation results. For both Reynolds numbers Re = 389 and Re = 648, the final longitudinal dimensions of the recirculating regions computed with time dependent inlet flow conditions show the same values as those computed for the corresponding inlet conditions for stationary flow fields. This indicated that the variations of the starting conditions of the flow had no influence on the final, steady state flow field.

For the flow field of Re = 389, good agreement was obtained between the steady state flow predictions and experimental results. This indicated that the predictions were sufficiently free from numerical diffusion to draw physical information from the final results.

For Re = 389, computations were performed for the time variation of the separation region attached to the step. The computational results showed that the flow initially separates at the bottom corner of the step and a second separation region occurs at the top corner. As the time progresses, both recirculating flow regions merge and a single region of the recirculating flow develops. This region increases with time to reach the final steady state recirculation region predicted and measured for backward-facing step flows.

During a transitional time period, for Re = 389, a separation region is computed at the wall opposite to the step. It occurs shortly after the flow is started and disappears before the final flow conditions for $t \to \infty$ are reached.

The unsteady flow calculations performed for Re = 648, with increasing mass flow rate at the inlet plane, showed the starting of the second recirculating flow region at the wall opposite to the step at about the Reynolds number where it is also obtained experimentally for the steady state flow conditions. After its initial occurrence, the longitudinal dimensions of the recirculating flow regions grow steadily, reaching a maximum and then decaying to a final length which agrees with the results from steady state predictions.

The longitudinal dimensions of the second recirculating flow region at the wall opposite to the step are in satisfactory agreement with those obtained experimentally. Discrepancies might be due to three-dimensional effects occurring in the

flow. The quadratic upstream discretization scheme together with a first-order implicit temporal discretization showed to be a simple and accurate solution algorithm for unsteady recirculating flows as long as very small time steps are used to decrease errors induced by the first-order temporal discretization.

It is important to note that separation regions occur on both walls of the step during the transitional period of flow development. Some of these regions vanish for $t \to \infty$ and, hence, the steady state flow does not reflect the complex flow structure that occurs during the phase of the starting step flow.

References

1 Gosman, A. D., and Pun, W. M., "Lecture Notes for Course Entitled: Calculation of Recirculating Flow," *Heat Transfer Rep.*, HTS/74/2, Imperial College, London, 1974.

2 Roache, P. J., *Computational Fluid Dynamics*, Hermosa Publishers, 1976.

3 Durst, F. and Whitelaw, J. H., "Aerodynamic Properties of Separated Gas Flows: Existing Measurement Techniques and New Optical Geometry for the Laser-Doppler Anemometer," *Heat Mass Transfer*, Vol. 4, 1971, p. 311.

4 Durst, F., and Loy, T., "Investigations of Laminar Flow in a Pipe With Sudden Contraction of Cross Section Area," *Computers & Fluids*, Vol. 13, No. 1, 1985, pp. 15–36.

5 Armaly, B. F., Durst, F., Pereira, J. C. F., and Schönung, B., "Experimental and Theoretical Investigation of Backward-Facing Step Flow," *J. Fluid Mech.*, Vol. 127, 1983, pp. 473–496.

6 Durst, F. and Tropea, C., "Turbulent Backward-Facing Step in Two-Dimensional Ducts and Channels," *Proc. Turbulent Shear Flow*, 3rd Symp. Davis, Sept. 1981.

7 Eaton, J. N., and Johnston, J. P., "An Evaluation of data for the Backward-Facing Flow," Report prepared for 1980/81 *Conference on Complex Turbulent Flows*, Stanford University.

8 Cherdron, W., Durst, F., and Whitelaw, J. H., "Asymmetric Flows and Instabilities in Symmetric Ducts With Sudden Expansions," JOURNAL OF FLUID MECH., Vol. 84, 1978, pp. 13–31.

9 Macagno, E. O., and Hung, T. N., "Computational and Experimental Study of Captative Annular Eddy," *J. Fluid Mech.*, Vol. 28, Part 1, 1967, pp. 43–64.

10 Bach, L. H., and Roschko, E. J., "Shear Layer Flow Regimes and Wave Instabilities and Reattachment Lengths Downstream of an Abrupt Linear Channel Expansion," ASME *Journal of Applied Mechanics*, Vol. 39, 1972, p. 677.

11 Durst, F. and Pereira, J. C. F., "Calculation of Laminar Backward-Facing Step Flow With Four Discretization Schemes for the Convection Terms, "*GAMM-WORKSHOP*, Bievres, France, 1983.

12 Roache, P. J., and Mueller, T. J., "Numerical Solutions of Laminar Separated Flows," *AIAA Journal*, Vol. 8, No. 3, p. 530, May 1970.

13 Hama, F. R., "Experimental Studies on the Lip Shock," *AIAA Journal*, Vol. 6, No. 2, Feb. 1968, pp. 212–219.

14 Weinbaum, S., "On the Singular Joints in the Laminar Two-Dimensional Near Wake Flow Field," *J. Fluid Mech.*, Vol. 33, Part 1, 1968, pp. 38–63.

15 Giaquinta, A. R., "Numerical Modeling of Unsteady, Separated Viscous Flow," ASME *Journal of Fluids Engineering*, Vol. 99, Dec. 1977, pp. 657–665.

16 Honji, H., "The Starting Flow Down a Step," *J. of Fluid Mech.*, Vol. 69, Part 2, 1975, pp. 229–240.

17 Ghoniem, A. F., and Cagnon, Y., "Vortex Simulation of Laminar Recirculating Flow," *J. Comp. Physics*, Vol. 68, 1987, pp. 346–377.

18 Ghoniem, A. F., and Sethian, J. A., "Effect of Reynolds Number on the Structure of Recirculating Flow," *AIAA Journal*, Vol. 25, No. 1, 1987, pp. 168–171.

19 Ghia, H. N., Oswald, G. A., and Ghia, U., "A Direct Method for the Solution of Unsteady Two-Dimensional Incompressible Navier-Stokes Equations," *2nd Symp. on Num. Phys. Aspects of Aerodynamic Flows*, California State University, Long Beach, Jan. 1987.

20 Leonard, B. P., "A Stable and Accurate Convective Modeling Procedure Based on Quadratic Upstream Interpolation," *Comp. Meths. Appl. Mech. Eng.*, Vol. 19, 1979, pp. 59–98.

21 Stone, H. L., "Iterative Solution of Implicit Approximation of Multi-Dimensional Partial Differential Equations," SIAM J. Num. Anal, Vol. 5, 1968, pp. 530–573.

22 Azevedo, J. T. L., Durst, F., and Pereira, J. C. F., "Comparison of Strongly Implicit Procedures for the Solution of the Fluid Flow Equations in Finite Difference Form," *J. Appl. Modelling*, Vol. 12, 1988, pp. 51–62.

23 Mansour, N. N., and Moin, P., "Computations of Turbulent Flows Over a Backward-Facing Step," *Fourth Symp. on Turbulent Shear Flows*, Karlsruhe, 1983.

24 Durst, F., and Pereira, J. C. F., "The Calculation of Some Steady Laminar Flows Using Various Descretization Finite Difference Schemes," Fourth Int. Conf. Num. Meth. in Laminar and Turbulent Flow, Editors, C. Taylor et al., *Pineridge Press*, U.N., 1985, pp. 551–561.

25 Durst, F., and Pereira, J. C. F., "Time-Dependent Laminar Backward-Facing Step Flow in a Two-Dimensional Duct," Forum on Unsteady Flow Separation," ASME *Fluids Engineering Spring Conference*, Cincinnati, Ohio, June 1987.

26 Durão, D. F. G., and Pereira, J. C. F., "Numerical Calculations of Laminar Flow Past a Square Cylinder," To be published in *Computer and Fluids*.

Vectorizable Implicit Algorithms for the Flux-Difference Split, Three-Dimensional Navier-Stokes Equations

P-M. Hartwich[1]
Research Scientist.

C-H. Hsu[2]
Research Scientist.

Vigyan Research Associates, Inc.,
Hampton, VA 23666-1325

C. H. Liu
Senior Research Scientist.
Analytical Methods Branch,
NASA Langley Research Center,
Hampton, VA 23665-5225
Assoc. Mem. ASME

The computational efficiency of four vectorizable implicit algorithms is assessed when applied to calculate steady-state solutions to the three-dimensional, incompressible Navier–Stokes equations in general coordinates. Two of these algorithms are characterized as hybrid schemes; that is, they combine some approximate factorization in two coordinate directions with relaxation in the remaining spatial direction. The other two algorithms utilize an approximate factorization approach which yields two-factor algorithms for three-dimensional systems. All four algorithms are implemented in identical high-resolution upwind schemes for the flux-difference split Navier–Stokes equations. These highly nonlinear schemes are obtained by extending an implicit Total Variation Diminishing (TVD) scheme recently developed for linear one-dimensional systems of hyperbolic conservation laws to the three-dimensional Navier–Stokes equations. The computations of vortical flows over a sharp-edged, thin delta wing have been chosen as numerical test cases. The convergence performance of the algorithms is discussed, and the accuracy of the computed flow field results is assessed. The validity of the present results is demonstrated by comparisons with experimental data.

Introduction

Efficient means of computing steady-state solutions to the three-dimensional Navier–Stokes equations are continuously being sought. Among others, time-dependent methods, both explicit [1,2] and implicit [3–5], have been proposed. Implicit methods are generally regarded as being more suitable for "stiff" problems because of their better numerical stability properties (e.g., [6]). The "stiffness" of physical problems described by the time-dependent Navier–Stokes equations arises from the disparate characteristic speeds and/or length scales.

Many of the current three-dimensional implicit Navier–Stokes solvers using general coordinates are inspired by the Approximate Factorization (AF) scheme by Pulliam and Steger [3]. To enhance its algorithmic and machine efficiency[3], various modifications to it have been suggested. Pulliam and Chaussee [7] proposed a diagonalization technique to decouple the system of governing equations. Thereby, the costly numerical inversion of block-tridiagonal matrices in each coordinate direction is replaced with the much simpler inversion of scalar tridiagonal matrices. Additionally, each of these tridiagonal matrices can be decomposed into an upper and a lower triangular matrix according to the sign of their eigenvalues. That allows the use of a computationally quite efficient LU-ADI algorithm [5] for the numerical inversion of the resulting six implicit factors for three-dimensional problems. However, the algorithmic efficiency is increased by going in the other direction; that is, to reduce the number of approximate factors to two [8,9] which yields less factorization error. As a side-effect, the lower number of implicit factors makes schemes with two implicit factors more accurate than three-dimensional AF schemes with three or more approximate factors. Because of these properties, only three-dimensional AF schemes with two approximate factors are considered here.

In continuation of a previous study [9] the effects of relaxation and of different formulations for the approximate factors on the algorithmic and the machine efficiency of upwind schemes are investigated. The upwinding of the inviscid fluxes gives more freedom in devising implicit algorithms since it loads up the diagonals of the implicit factors [9,10]. This feature is used to construct three-dimensional AF schemes with just two implicit factors and hybrid schemes which combine AF in crossplanes with a nonlinear updating of the residual. While sweeping back and forth in the remaining

[1] Part of this work was done while a National Research Council Postdoctoral Research Associate.

[2] Part of this work was done while an Associate Research Engineer affiliated with the University of Kansas, Lawrence, KS.

[3] Improved algorithmic efficiency means obtaining a steady-state solution within fewer time steps; improved machine efficiency means using less computer time per time step and per grid point.

Contributed by the Fluids Engineering Division for publication in the JOURNAL OF FLUIDS ENGINEERING. Manuscript received by the Fluids Engineering Division June 22, 1987.

spatial direction, this resembles a symmetric planar Gauss-Seidel (SPGS) relaxation. Upwinding also permits the generation of implicit factors that alternatively possess block-tridiagonal or block-bidiagonal structure. The inversion of block-bidiagonal matrices requires less arithmetic operations than that of block-bidiagonal matrices. However, the inversion of block-tridiagonal matrices is completely vectorizable, whereas the inversion algorithm for block-bidiagonal matrices is only vectorizable up to 55 percent.

The relative merits of four different implicit algorithms are assessed when applied to compute vortical flows around a thin, sharp-edged delta wing as steady-state solutions to the three-dimensional, incompressible Navier–Stokes equations in curvilinear coordinates. The interest in low-speed flow calculations led to the decision to solve the incompressible Navier–Stokes equations. The compressible Navier–Stokes solvers are not very well suited for flows with $M<0.3$. Their algorithmic efficiency deteriorates considerably because the governing equations become increasingly stiff due to the growing disparity of flow speed and speed of sound which goes to infinity for $M\to 0$. Furthermore, the accuracy of results computed with AF algorithms is questionable since the factorization errors increase unboundedly for decreasing Mach number (see, for instance, [11]).

The governing equations are presented in the next section. In the third section, the first-order accurate upwinding of the inviscid fluxes using flux-difference splitting is described. The extension of this upwinding to second-order accuracy is given in the fourth section. After the implicit algorithms are explained in detail, their algorithmic and machine efficiency is discussed along with the computed flow field results which are validated with experimental data.

Governing Equations

The Navier–Stokes equations for general, boundary-fitted coordinates are given in strong conservation law form:

$$(Q/J)_t+(E-E_v)_\zeta+(F-F_v)_\xi+(G-G_v)_\eta=0 \qquad (2.1)$$

with

$$\begin{bmatrix} E-E_v \\ F-F_v \\ G-G_v \end{bmatrix} = \begin{bmatrix} \zeta_x/J & 0 & 0 \\ \xi_x/J & \xi_y/J & \xi_z/J \\ \eta_x/J & \eta_y/J & \eta_z/J \end{bmatrix} \begin{bmatrix} (E-E_v)_c \\ (F-F_v)_c \\ (G-G_v)_c \end{bmatrix} \qquad (2.2)$$

and

$$E_c=(\beta u,u^2+p,uv,uw)^T$$
$$F_c=(\beta v,uv,v^2+p,vw)^T \qquad (2.3)$$
$$G_c=(\beta w,uw,vw,w^2+p)^T$$

where the Jacobian of the coordinate transformation is given by $J^{-1}=x_\zeta(y_\xi z_\eta-y_\eta z_\xi)$. Note that all $\zeta=$ constant surfaces are assumed to be parallel to x = constant surfaces. This allows for a simplified treatment of wing and wing-body geometries while it does not impede the generality of either the three-dimensional spatial differencing or of the implicit algorithms.

As pointed out by Warming and Beam [6], the most efficient implicit algorithms are those which solve the complete set of governing equations simultaneously. That requires a coupled set of governing equations. For incompressible flow, the equation of continuity is decoupled from the equations of motion. By defining a state vector

$$Q=(p,u,v,\mathrm{w})^T,$$

an artificial time-derivative of the pressure is added to the equation of continuity; thus, the incompressible Navier–Stokes equations are "recoupled," and they can be integrated like a conventional parabolic time-dependent system of equations [11,12]. As the solution of equations (2.1) approaches asymptotically a steady-state, the artificial compressibility

Nomenclature

A,B,C = Jacobians $\partial E/\partial Q$, $\partial F/\partial Q$, $\partial G/\partial Q$
CFL = Courant-Friedrichs-Lewy number
C_L = lift coefficient
C_p = pressure coefficient
$C_{p,t}$ = total pressure coefficient
D = A, B, or C
E,F,G = flux vectors
H = E, F, or G
I = identity matrix
J = Jacobian of the coordinate transformation
L = matrix whose rows are left eigenvectors
M = matrix in implicit operators of hybrid algorithms
P = dimensional static pressure
Q = state vector
R = matrix whose columns are right eigenvectors
Re = Reynolds number
RES = residual
S = artificial speed of sound
U = dimensional contravariant velocity component
V = dimensional velocity vector
W = characteristic vector
X,Y,Z = linearized Jacobians stemming from viscous shear fluxes
a,b,c = metric quantities like ξ_x/J, ξ_y/J, ξ_z/J
ℓ = root chord of delta wing (set to unity)
p = nondimensional static pressure
r = ratio of two consecutive changes in characteristic variables
u,v,w = Cartesian velocity components nondimensionalized with V_∞
x,y,z = Cartesian coordinates
Δ = difference operator
Λ = diagonal matrix with eigenvalues as entries
Φ = diagonal matrix with limiters $\phi^{\pm}_{m,\ell}$ as entries
α = angle of attack
β = amount of artificial compressibility
δ = difference operator
λ = eigenvalues
ζ,ξ,η = curvilinear coordinates
θ = ζ, ξ, or η
ρ = density
τ = time step size
ϕ = limiter

Subscripts

i,j,k = indices in ζ, ξ, η-direction in regular computational domain
ℓ = i, j, or k
m = mth component of some vector
v = denotes viscous shear fluxes
x,y,z = denotes differentiation in x-, y-, and z-direction
ζ,ξ,η = denotes differentiation in ζ-, ξ-, and η-direction
∞ = denotes freestream values

Superscripts

n = time level
$\bar{}$ = spatially averaged quantities
$\hat{}$ = temporally averaged quantities
$\tilde{}$ = denotes quantities normalized with $(a+b+c)$

vanishes and the incompressible Navier-Stokes equations are satisfied. The parameter β in equation (2.3) determines the amount of artificial compressibility allowed. Appropriate choices for β are discussed in the next section.

The Cartesian velocities u, v, w are normalized with the freestream velocity V_∞. The Cartesian coordinates x,y,z, are made dimensionless with some problem-dependent characteristic length. The pressure is nondimensionalized as $p=(P-P_\infty)/\rho V_\infty{}^2$. Since the density is simply a constant, it does not require any normalization. Assuming a constant viscosity, the viscous flux vectors are written like

$$E_{v,c}=(\mathrm{Re}\bullet J)^{-1}(0,2u_x,u_y+v_x,u_z+w_x)^T,\text{etc.} \qquad (2.4)$$

where the Cartesian derivatives are to be expanded in ζ, ξ, η space via chain rule relations.

Flux-Difference Splitting

The upwind differencing is implemented by adapting Roe's flux difference splitting [13] to incompressible flow since it preserves the strong conservation law form of equation (2.1). The widely used flux vector splitting is restricted to ideal gas flows because it either requires the inviscid fluxes being expressed in terms of density, speed of sound and Mach number [14], or it maintains a strong conservation law form only when the flux vectors are homogeneous of degree one in the state vector [10]. Common to both splitting concepts is that they are devised for one-dimensional hyperbolic conservation laws, so that they cannot be directly applied to the three-dimensional Navier-Stokes equations. First, the Navier-Stokes equations have to be taken in the limit of an infinite Reynolds number which yields the hyperbolic Euler equations. Then, the three-dimensional system of governing equations is spatially split into three quasi one-dimensional conservation laws:

$$(Q/J)_t+H_\theta=0 \qquad (3.1)$$

where $\theta=\zeta,\xi$, or η, and $H=E,F$, or G. In a Riemann problem genuinely discontinuous solutions are studied which suggests solving the conservation laws in their integral as opposed to their differential form:

$$(I/\tau J)\Delta\bar{Q}_\ell^n+\Delta_\ell\hat{H}=0 \quad (I=\text{identity matrix}) \qquad (3.2)$$

where $\Delta\bar{Q}^n=\bar{Q}^{n+1}-\bar{Q}^n$, $\hat{H}_{\ell\pm1/2}=\hat{H}(\hat{Q}_{\ell\pm1/2})$, and $\Delta_\ell()=[()_{\ell+1/2}-()_{\ell-1/2}]/\Delta\theta$ with $\ell=i$, j, or k. The sliding averages $\bar{Q}$ and $\hat{Q}$ are defined as

$$\bar{Q}_\ell^n=\Delta\theta^{-1}\int_{(\ell-1/2)\Delta\theta}^{(\ell+1/2)\Delta\theta}Q^n d\theta' \qquad (3.3a)$$

and

$$\hat{Q}_{\ell\pm1/2}=\tau^{-1}\int_t^{t+\tau}Q_{\ell\pm1/2}dt' \qquad (3.3b)$$

The flux at the interface, $\ell+1/2$, separates the positive from the negative waves which can be mathematically expressed as:

$$\hat{H}_{\ell+1/2}=\hat{H}_\ell+\Delta\hat{H}^-_{\ell+1/2}=\hat{H}_{\ell+1}-\Delta\hat{H}^+_{\ell+1/2} \qquad (3.4)$$

Upon inserting equation (3.4), equation (3.2) assumes

$$(I/\tau\mathrm{J})\Delta\bar{Q}_\ell^n+\Delta\hat{H}^-_{\ell+1/2}+\Delta\hat{H}^+_{\ell-1/2}=0 \qquad (3.5)$$

Equation (3.5) describes the influence of a right traveling wave from the left and of a left traveling wave from the right on Q at the centroidal grid point ℓ. Assuming Q to be sufficiently differentiable in the space and time intervals $\Delta\theta$ and τ, respectively, Q can be developed in Taylor series within the "computational cell" $\Delta\theta\times\tau$. Taking the effects of the coordinate transformation into account (which are encompassed in the metric coefficients in H), $\bar{Q}$ and $\hat{Q}$ can be expressed as:

$$\bar{Q}(\theta)=Q(\theta)+0(\Delta x^2,\Delta y^2,\Delta z^2) \qquad (3.6a)$$

$$\hat{Q}(t)=Q(t)+0(\tau^2) \qquad (3.6b)$$

Since the averages of Q approximate the actual function $Q(\theta,t)$ with equal order of accuracy and $0(\tau)=0(\Delta x,\Delta y,\Delta z)$, the time averages $\hat{Q}$ can be replaced with $\bar{Q}$ without loss of accuracy.

Following Roe [13], a mean value matrix $\bar{D}_{\ell+1/2}=D(\bar{Q}_\ell,\bar{Q}_{\ell+1})$ is introduced with

$$\bar{D}_{\ell+1/2}\Delta_{\ell+1/2}\bar{Q}=\Delta\bar{H}_{\ell+1/2} \qquad (3.7a)$$

$$D(\bar{Q}_\ell,\bar{Q}_\ell)=D\ell \qquad (3.7b)$$

which allows us to write (3.5) as

$$[(I/\tau J)-(\bar{D}^-_{\ell+1/2})^n\Delta_{\ell+1/2}+(\bar{D}^+_{\ell-1/2})^n\Delta_{\ell-1/2}]\Delta\bar{Q}^n$$

$$=(\bar{D}^-_{\ell+1/2})^n\Delta_{\ell+1/2}\bar{Q}^n-(\bar{D}^+_{\ell-1/2})^n\Delta_{\ell-1/2}\bar{Q}^n \qquad (3.8)$$

where

$$\bar{D}^n_{\ell\pm1/2}=(\bar{D}^+-\bar{D}^-)^n_{\ell\pm1/2}=[\bar{R}(\bar{\Lambda}^+-\bar{\Lambda}^-)\bar{L}]^n_{\ell\pm1/2} \qquad (3.9)$$

with $\Lambda^\pm=(|\Lambda|\pm\Lambda)/2$. Equation (3.8) gives an Euler-implicit time differencing of first-order accuracy, which suffices for steady state calculations. Because of condition (3.7a), the solution to (3.8) is conservative in space. It also approximates the same Riemann problem as in (3.1) or (3.2) since the eigenvalues of $\bar{D}^n_{\ell\pm1/2}$ represent the eigenvalues of $D^n_{\ell\pm1/2}$ (equation (3.7b)). The construction of $\bar{D}^n_{\ell\pm1/2}$ is accomplished in two steps. First, the analytic Jacobian $D=\partial H/\partial Q$ is formed. D is found to be a function of the metric coefficients, of the parameter β, and of the state vector Q

$$D=D(a,b,c,\beta,Q)$$

where a, b, c are the metric quantities ξ_x/J, ξ_y/J, $\xi_zJ/$, etc. For $\bar{D}^n_{\ell+1/2}$, the local values $a_{\ell+1/2}$, $b_{\ell+1/2}$, $c_{\ell+1/2}$, and $\bar{Q}^n_{\ell+1/2}$ have to be fed into the structure of D. To maintain the conservative properties of (3.8), the metrics are differenced at each grid point using a weighted-average procedure [3,9,15]. For example,

$$(\zeta_x/\mathrm{J})_{ijk}=[(\sigma_k\delta_jy)(\sigma_j\delta_kz)-(\sigma_j\delta_ky)(\sigma_k\delta_jz)]_i \qquad (3.10)$$

where, for instance, the averaging operator σ_k working on δ_jy is defined as

$$\sigma_k\delta_jy=[(\delta_jy)_{k+1}+(\delta_jy)_{k-1}]/2 \qquad (3.11)$$

with $\delta_jy=(y_{j+1}-y_{j-1})/2$. Condition (3.7$a$) is identically fulfilled, when the metrics and the quantities in the vector $\bar{Q}$ are computed from averages like $\bar{Q}_{j+1/2}=(\bar{Q}_{j+1}+\bar{Q}_j)/2$. The eigenvalues of D are:

$$\Lambda=\mathrm{diag}(\lambda_1,\lambda_2,\lambda_3,\lambda_4)=\mathrm{diag}(U-S,U+S,U,U) \qquad (3.12)$$

where $U=au+bv+cw$ and $S=[U^2+\beta(a^2+b^2+c^2)]^{1/2}$.

The stiffness of the conservation laws can be estimated by the ratio $|\lambda_{\max}/\lambda_{\min}|$. In order to prevent this ratio from assuming excessive values, large values of β which would result in a stiff system of equations should be avoided. Rizzi and Eriksson [16] proposed choosing β to be proportional to $u^2+v^2+w^2$. For viscous flows, extended regions with small velocity components might occur (e.g., secondary vortices on delta wings). Proportionally, β will decrease in those regions too, thereby increasing the amount of artificial compressibility. This triggers an incompatibility in the governing equations which results in meaningless solutions (a steady-state solution has never been obtained when β was proportional to $u^2+v^2+w^2$). Choosing β to be 0(1) (or, simply setting it to unity), ensures that all eigenvalues are of the same order and that no problems in computing a solution to equation (3.10) due to stiffness are encountered. Once the eigenvalue matrix is split according to the sign of its diagonal entries, $A^\pm$ is easily computed following (3.9). This requires the matrices R and L, whose generalized formulation reads:

$$R = \begin{bmatrix} -\beta\tilde{S} & \beta\tilde{S} & 0 & 0 \\ \tilde{a}\beta+u\tilde{\lambda}_1 & \tilde{a}\beta+u\tilde{\lambda}_2 & -\tilde{b} & -\tilde{c} \\ \tilde{b}\beta+v\tilde{\lambda}_1 & \tilde{b}\beta+v\tilde{\lambda}_2 & \tilde{a}+\tilde{c} & -\tilde{c} \\ \tilde{c}\beta+w\tilde{\lambda}_1 & \tilde{c}\beta+w\tilde{\lambda}_2 & -\tilde{b} & \tilde{a}+\tilde{b} \end{bmatrix} \tag{3.13}$$

$$L=\frac{1}{2\tilde{S}^2}\begin{bmatrix} -\tilde{\lambda}_2/\beta & \tilde{a} & \tilde{b} & \tilde{c} \\ -\tilde{\lambda}_1/\beta & \tilde{a} & \tilde{b} & \tilde{c} \\ (\tilde{\lambda}_2 d_1+\tilde{\lambda}_1 d_2)/\beta & -2\tilde{S}^2/k-\tilde{a}d_5 & 2\tilde{S}^2/k-\tilde{b}d_5 & -\tilde{c}d_5 \\ (\tilde{\lambda}_2 d_3+\tilde{\lambda}_1 d_4)/\beta & -2\tilde{S}^2/k-\tilde{a}d_6 & -\tilde{b}d_6 & 2\tilde{S}^2/k-\tilde{c}d_6 \end{bmatrix} \tag{3.14}$$

where

$$k=\tilde{a}+\tilde{b}+\tilde{c}$$

$$\tilde{a},\tilde{b},\tilde{c}=a,b,c/(a^2+b^2+c^2)^{1/2}$$

$$d_1=(r_{31}-r_{21})/k \qquad d_2=(r_{32}-r_{22})/k$$

$$d_3=(r_{41}-r_{21})/k \qquad d_4=(r_{42}-r_{22})/k$$

$$d_5=d_1+d_2 \qquad d_6=d_3+d_4$$

and quantities like $r_{31}(=\tilde{b}\beta+v\tilde{\lambda}_1)$ indicate elements of R in (3.14), and $\tilde{S}=S(u,v,w,\tilde{a},\tilde{b},\tilde{c})$, etc.

High Resolution Scheme

The scheme in equation (3.8) gives first-order accurate steady-state solutions. That means that the solutions are contaminated with a considerable amount of numerical dissipation. This artificial dissipation smears the details of the actual solution to the conservation laws in (3.1) or (3.2). The accuracy of the scheme in (3.8) is enhanced by extending it into a high resolution scheme. High resolution schemes are genuinely nonlinear schemes. They use variable difference stencils such that the schemes adapt to the local solution in order to give higher-order accurate solutions while still suppressing spurious oscillations in regions of rapid change in gradients (e.g., contact discontinuities).

Here, high resolution schemes are presented which are accurate up to second-order. They are based on a recently developed implicit TVD scheme for linear one-dimensional hyperbolic conservation laws. For the nonlinear system case, a TVD scheme cannot be constructed since the quantity which might be subject to a TVD requirement is unknown [17,18]. For linear system cases, the quantities whose total variation can be forced to diminish in time are the characteristic variables:

$$W=LQ \tag{4.1}$$

Using (4.1), the scheme in (3.8) is rewritten for constant R, L, and Λ as

$$[(1/\tau \mathrm{J})-\lambda_m^-\Delta_{\ell+1/2}+\lambda_m^+\Delta_{\ell+1/2}]\Delta\bar{w}_m^n$$

$$=\lambda_m^-\Delta_{\ell+1/2}\bar{w}_m^n-\lambda_m^+\Delta_{\ell+1/2}\bar{w}_m^n \quad (m=1,2,3,4) \tag{4.2}$$

The formulation in (4.2) describes four scalar linear hyperbolic conservation laws. The scheme in (4.2) is unconditionally TVD [18]. When $\bar{w}_m^n(\theta)$ is sufficiently differentiable, the local jumps in $\bar{w}_m^n$ are replaced with

$$\Delta_{\ell\pm1/2}\bar{w}_m^n=\partial w_m/\partial\theta|_{\ell\pm1/2}^n\Delta\theta \tag{4.3}$$

Reading equation (4.3) from right to left illustrates the aforementioned accuracy problem: the derivatives of w_m^n have to be approximated by differences which have higher accuracy rather than by the one-sided, first-order accurate differences in (4.2). This is accomplished by defining

$$\partial w_m/\partial\theta|_{\ell-1/2}^n\Delta\theta=(\bar{w}_{m,\ell}+0.5\phi_{m,\ell}^-\Delta_{\ell-1/2}\bar{w}_m)^n$$
$$-(\bar{w}_{m,\ell-1}+0.5\phi_{m,\ell-1}^+\Delta_{\ell-1/2}\bar{w}_m)^n \tag{4.4a}$$

$$\partial w_m/\partial\theta|_{\ell+1/2}^n\Delta\theta=(\bar{w}_{m,\ell+1}-0.5\phi_{m,\ell+1}^-\Delta_{\ell+1/2}\bar{w}_m)^n$$
$$-(\bar{w}_{m,\ell}-0.5\phi_{m,\ell}^+\Delta_{\ell+1/2}\bar{w}_m)^n \tag{4.4b}$$

with

$$\phi_{m,\ell}^{\pm}=\phi(r_{m,\ell}^{\pm}) \tag{4.5a}$$

and

$$r_{m,\ell}^{\pm}=\begin{cases} (\Delta_{\ell-1/2}\bar{w}_m^n/\Delta_{\ell+1/2}\bar{w}_m^n)^{\pm1} & \text{for } \Delta_{\ell\pm1/2}\bar{w}_m^n\neq0 \\ 0 & \text{for } \Delta_{\ell\pm1/2}\bar{w}_m^n=0 \end{cases} \tag{4.5b}$$

Note that the high resolution formulation applies only to $\bar{w}_m^n$, not to $\bar{w}_m^{n+1}$. Application to $\bar{w}_m^{n+1}$ would require beforehand knowledge about the function $\bar{w}_m^{n+1}$ that is simply not available. Formulation (4.4) comprises various difference approximations; the appropriate one is chosen by the TVD limiters $\phi_{m,\ell}^{\pm}$. When all ϕ_m equal zero, (4.4) is identical with (4.3). For any other combination of values for ϕ_m, equations (4.4) resemble central, one-sided, or upwind biased differences of second-order accuracy. To determine the constraints on the TVD limiters, equations (4.4) are inserted in (4.2), and the resulting expressions at location ℓ and $\ell+1$ are subtracted from each other. Using the triangle inequality, and after some simple but lengthy algebra [15], the constraints are found to be

$$\phi_{m,\ell}^{\pm}=\max(0,2\cdot\min(1,r_{m,\ell\pm1}^{\mp})) \tag{4.6}$$

In the actual computations a formulation of $\phi(r)$ is chosen that is differentiable for $r_{m,\ell}^{\pm}>0$

$$\phi_{m,j}^{\pm}=\max[0,2\cdot\min(r_{m,\ell}^{\pm}/(1+r_{m,\ell}^{\pm}),r_{m,\ell\pm1}^{\mp})] \tag{4.7}$$

Other formulations of $\phi_{m,\ell}^{\pm}$ were used. As in other comparative studies (e.g., reference [19]) the effects of $\phi_{m,\ell}^{\pm}$ on the computed results are found to be marginal. In order to extend the high resolution scheme to the nonlinear system case, first the nonlinear scalar hyperbolic conservation laws for characteristic variables are considered

$$[(1/\tau J)-\lambda_{m,\ell+1/2}^-\Delta_{\ell+1/2}+\lambda_{m,\ell-1/2}^+\Delta_{\ell-1/2}]\Delta\bar{w}_m^n$$
$$=\lambda_{m,\ell+1/2}^-[1-0.5(\phi_{m,\ell+1}^--\phi_{m,\ell}^+)]\Delta_{\ell+1/2}\bar{w}_m^n$$
$$-\lambda_{m,\ell-1/2}^+[1+0.5(\phi_{m,\ell}^--\phi_{m,\ell-1}^+)]\Delta_{\ell-1/2}\bar{w}_m^n \tag{4.8}$$

The extension of (4.8) to a conservative high resolution scheme for nonlinear systems of conservation laws is accomplished by multiplying (4.8) from the left with the set of right eigenvectors R:

$$[(I/\tau J)-(\bar{D}_{\ell+1/2}^n)^-\Delta_{\ell+1/2}+(\bar{D}_{\ell-1/2}^n)^+\Delta_{\ell-1/2}]\Delta\bar{Q}^n$$

$$= \bar{R}^n_{\ell+1/2}\{\bar{\Lambda}^-_{\ell+1/2}[I-0.5(\Phi^-_{\ell+1}-\Phi^+_{\ell})]\}^n \bar{L}^n_{\ell+1/2}\Delta_{\ell+1/2}\bar{Q}^n$$

$$-\bar{R}^n_{\ell-1/2}\{\bar{\Lambda}^+_{\ell-1/2}[I+0.5(\Phi^-_{\ell}-\Phi^+_{\ell-1})]\}^n \bar{L}^n{}_{\ell-1/2}\Delta_{\ell-1/2}\bar{Q}^n \quad (4.9)$$

where $\Phi^{\pm}_{\ell}=\text{diag}(\phi^{\pm}_1,\phi^{\pm}_2,\phi^{\pm}_3,\phi^{\pm}_4)_{\ell}$.

As usual, the high resolution scheme in (4.9) is applied independently in each coordinate direction for multidimensional flow problems, and the discrete expressions for the inviscid fluxes are summed up [15,17,18].

Implicit Algorithms

A first-order, Euler backward-time differencing for the three-dimensional Navier–Stokes equations is given by

$$[(I/\tau J)-(\bar{A}^- + \bar{X})^n_{i+1/2}\Delta_{i+1/2}+(\bar{A}^+ + \bar{X})^n_{i-1/2}\Delta_{i-1/2}$$

$$-(\bar{B}^+ + \bar{Y})^n_{j+1/2}\Delta_{j+1/2}+(\bar{B}^+ \bar{Y})^n_{j-1/2}\Delta_{j-1/2}$$

$$-(\bar{C}^- + \bar{Z})^n_{k+1/2}\Delta_{k+1/2}+(\bar{C}^+ + \bar{Z})^n_{k-1/2}\Delta_{k-1/2}]\Delta\bar{Q}^n$$

$$= -\text{RES}(\bar{Q}^n) \quad (5.1)$$

The solution is advanced in increments $\Delta\bar{Q}^n$ to compute steady-state solutions which are independent from the time-step size [6]. The residual $\text{RES}(\bar{Q}^n)$ is the discrete representation of the spatial derivatives in equations (2.1), evaluated at time level n, with the high resolution scheme applied to the inviscid fluxes. The viscous shear fluxes are centrally differenced in the usual manner (e.g., references [2–5,8,9,15]). The implicit formulation in (5.1) contains also the Jacobians of the viscous shear fluxes (i.e., $\bar{X}$, $\bar{Y}$, and $\bar{Z}$, stemming from E_v, F_v, and G_v, respectively). These Jacobians are derived as, for instance, in Pulliam and Steger [3]. After having dropped all cross derivatives in the fluxes E_v, F_v, and G_v, these "reduced" vectors are linearized by Taylor series. That produces the diagonal coefficient matrices

$$X, Y, \text{ or } Z=(\text{Re}^{-1}\bullet J)\text{diag}(0,m_1,m_2,m_3) \quad (5.2)$$

with $m_1=2a^2+b^2+c^2$, $m_2=a^2+2b^2+c^2$, and $m_3=a^2+b^2+2c^2$. For example, to obtain Y, $a=\xi_x/\text{J}$, $b=\xi_y/\text{J}$, and $c=\xi_z/\text{J}$.

Considering equation (5.1) for all grid points yields a huge system of equations with an enormous (even though sparse) matrix whose bandwidth is also very large. Since it is unacceptably expensive to invert the left-hand side (LHS) of (5.1) directly, a more economical relaxation or approximate factorization solution should be sought. To that end, four implicit algorithms are proposed in this paper. The first is a hybrid algorithm. Relaxation is used in one coordinate direction in combination with approximate factorization in the remaining two coordinate directions. The hybrid scheme avoids the τ^3 spatial splitting error incurred in the three-dimensional AF-method, which imposes a severe time-step limitation. Like a relaxation method, the hybrid scheme is unconditionally stable for the scalar equation but offers additionally the advantage of being completely vectorizable when written as

$$[M-(\bar{B}^- + \bar{Y})^n_{j+1/2}\Delta_{j+1/2}+(\bar{B}^+ + \bar{Y})^n_{j-1/2}\Delta_{j-1/2}][M^{-1}]$$

$$[M-(\bar{C}^- + \bar{Z})^n_{k+1/2}\Delta_{k+1/2}+(\bar{C}^+ + \bar{Z})^n_{k-1/2}\Delta_{k-1/2}]\Delta\bar{Q}^n$$

$$= -\text{RES}(\bar{Q}^n,\bar{Q}^{n+1}) \quad (5.3)$$

with

$$M=I/\tau J+(\bar{A}^- + \bar{X})^n_{i+1/2}+(\bar{A}^+ + \bar{X})^n_{i-1/2}$$

$\text{RES}(\bar{Q}^n,\bar{Q}^{n+1})$ indicates the nonlinear updating of the residual while sweeping back and forth in ζ-direction. Since each factor in (5.3) has the same block-tridiagonal structure as in a conventional AF algorithm, let this algorithm be termed as AF-SPGS to distinguish it from the second algorithm, which is obtained by reordering the Jacobians in (5.3) such that each implicit factor contains only the positive or the negative Jacobians

$$[M-(\bar{B}^- + \bar{Y})^n_{j+1/2}\Delta_{j+1/2}-(\bar{C}^- + \bar{Z})^n_{k+1/2}\Delta_{k+1/2}][M^{-1}]$$

$$[M+(\bar{B}^+ + \bar{Y})^n_{j-1/2}\Delta_{j-1/2}+(\bar{C}^+ + \bar{Z})^n_{k-1/2}\Delta_{k-1/2}]\Delta\bar{Q}^n$$

$$= -\text{RES}(\bar{Q}^n,\bar{Q}^{n+1}) \quad (5.4)$$

This formulation leads to an approximate LU factorization of the LHS combined with relaxation. Let this approach be termed LU-SPGS. The inversion of the upper (first implicit factor) and lower (second implicit factor) block-triangular matrices requires only 37 percent of the arithmetic operations which are necessary for the inversion of the block-tridiagonal matrices in (5.3). The drawback of the LU-SPGS is that only 55 percent of these operations can be vectorized, compared with 100 percent for the AF-SPGS method.

Both hybrid algorithms are easily convertible into time-dependent methods which exclusively use approximate factorization, but which still avoid the τ^3 spatial splitting error as in conventional AF methods, since they use only two approximate factors. Reassigning the matrices $(\bar{A}^{\pm}+\bar{X})_{i\mp1/2}$ in (5.3) yields a second approximate LU factorization

$$[(I/\tau J)-(\bar{A}^- + \bar{X})^n_{i+1/2}\Delta_{i+1/2}-(\bar{B}^- + \bar{Y})^n_{j+1/2}\Delta_{j+1/2}$$

$$+(\bar{B}^+ + \bar{Y})^n_{j-1/2}\Delta_{j-1/2}]$$

$$[(I/\tau J)+(\bar{A}^+ + \bar{X})^n_{i-1/2}\Delta_{i-1/2}-(\bar{C}^- + \bar{Z})^n_{k+1/2}\Delta_{k+1/2}$$

$$+(\bar{C}^+ + \bar{Z})^n_{k-1/2}\Delta_{k-1/2}]\Delta\bar{Q}^n=-(I/\tau J)\bullet\text{RES}(\bar{Q}^n) \quad (5.5)$$

Each implicit factor in (5.5) is composed of a block-tridiagonal matrix like in a conventional AF scheme plus a super (first implicit factor) or a sub (second implicit factor) block-diagonal matrix, which is characteristic for an approximate LU factorization. Hence, the algorithm in (5.5) is labeled AF-LU.

An analogous reassignment of the matrices $(\bar{A}^{\pm}+\bar{X})_{i\mp1/2}$ in (5.4) yields a third approximate LU factorization

$$[(I/\tau J)-(\bar{A}^- + \bar{X})^n_{i+1/2}\Delta_{i+1/2}-(\bar{B}^- + \bar{Y})^n_{j+1/2}\Delta_{j+1/2}$$

$$-(\bar{C}^- + \bar{Z})^n_{k+1/2}\Delta_{k+1/2}]$$

$$[(I/\tau J)+(\bar{A}^+ + \bar{X})^n_{i-1/2}\Delta_{i-1/2}+(\bar{B}^+ + \bar{Y})^n_{j-1/2}\Delta_{j-1/2}$$

$$+(\bar{C}^+ + \bar{Z})^n{}_{k-1/2}\Delta_{k-1/2}]\Delta\bar{Q}^n=-(I/\tau J)\bullet\text{RES}(\bar{Q}^n) \quad (5.6)$$

In this approach, termed LU-LU, the first (second) implicit factor has an upper (a lower) block-triangular structure similar to the LU-SPGS method. The arithmetic operation counts for the inversion of the implicit factors in the AF-SPGS and in the AF-LU algorithms on one hand, and of those in the LU-SPGS and LU-LU algorithms on the other hand, are identical. The difference between the respective hybrid and time-accurate methods lies in the updating of the residuals. The time-dependent methods, AF-LU and LU-LU, require two sweeps through the integration domain to advance the solution from the n^{th} to the $(n+1)^{\text{th}}$ time level. The hybrid algorithms need only one sweep since they update the residual nonlinearly.

Computational Integration Domain

The outer contour of the finite, three-dimensional integration domain around a sharp-edged delta wing (AR = 1, $t/c=0$) as shown in Fig. 1 is described by a half-hemispherical cylinder with the radius $R/c=2$. The C-H-type grids used in the flow field computations reported below, extend from one root chord upstream of the apex to one root chord aft of the trailing edge. They slice the integration domain into 66 crossplanes

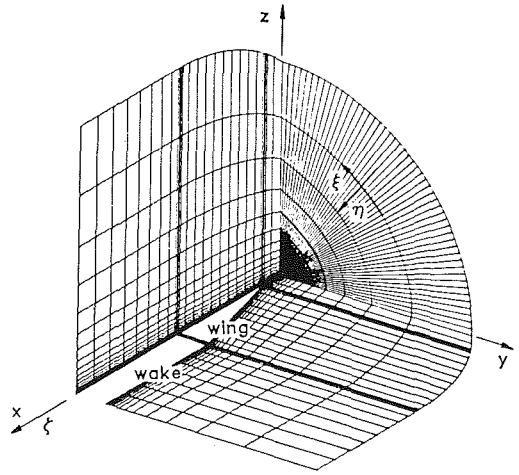

Fig. 1 Partial view of the three-dimensional integration domain around a slender delta wing

which are perpendicular to the longitudinal axis of the wing, with some clustering of the planes in the apex and trailing edge region (minimum spacing: 0.00625 root chords). In these cross-sections, C-type grids are generated from solutions to elliptic systems [20]. The coarse and the medium grids have 51 grid points in circumferential (ξ) direction; the fine grid has 101 grid points in ξ-direction. A stronger coordinate stretching in η-direction for the medium and fine grid rather than for the coarse grid, gives a finer resolution of the boundary-layer type flow along the wing surface. This is reflected by a maximum spacing in η-direction between the wing surface and the first η-constant plane encompassing the wing which is 0.0014 and 0.00025 root chord for the coarse grid and the other two, respectively.

Boundary Conditions

Unknown values of $\bar{Q}^n$ along the boundaries are updated explicitly, and $\Delta\bar{Q}^n$ is set to zero. The boundary conditions are: freestream conditions along the outer boundary except for the outflow cross-section, reflection conditions along the symmetry plane perpendicular to the wind, and no-slip conditions along the wing surface, where the normal gradient of pressure is assumed to vanish. Flow field values along the branch cut in the wake region are obtained by averaging extrapolates from above and below. The values at the outflow cross-section are computed by first-order extrapolation. The effect of the position of the outflow crossplane on the flow over the wing was assessed by expanding the wake region up to three root chords using additional crossplanes. No discernible differences in the pressure and velocity fields in the wing area were detected.

The limiters $\phi^{\pm}_{m,\ell}$ along all boundaries are set to zero, corresponding to a zeroth-order extrapolation. The initial conditions consist of the freestream values.

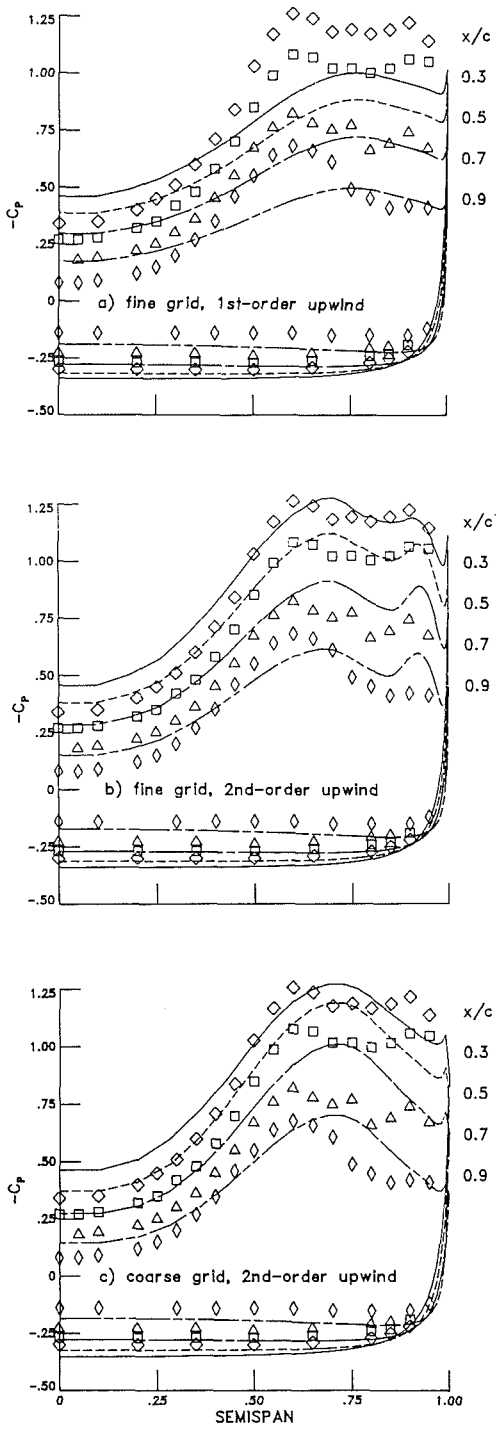

Fig. 2 Computed (lines) and measured (symbols) surface pressure coefficient distributions, AR = 1, α = 20.5 degrees, Re = 0.9 million, laminar flow

Results

The convergence performance of the four implicit algorithms is compared for steady-state calculations of incompressible, laminar (Re = 0.9 million) vortical flows around a sharp-edge delta wing.

The surface pressure distributions in Fig. 2 show comparisons between experimental data by Hummel for a similar wing [21] and three sets of computational results. The angle of attack is 20.5 degrees, and the comparison is made for $x/c = 0.3$, 0.5, 0.7, and 0.9. There are two fine grid computations with first-order (Fig. 2(*a*)) and second-order (Fig. 2(*b*)) accurate upwind differencing, and one coarse grid calculation with second-order accurate upwinding (Fig. 2(*c*)). The effect of the secondary vortex on the pressure distribution is clearly indicated in the experiment and in the high resolution calculations. In the first-order accurate results neither the position nor the strength of the primary and secondary vortices is predicted properly at any root chord station. Crossflow velocity vector plots (not shown here) demonstrate that there is a weak secondary vortex in the first-order accurate calculations (cf. reference [9]), and secondary and tertiary vortices in the high resolution computations. The primary vortex in Fig. 2(*c*)

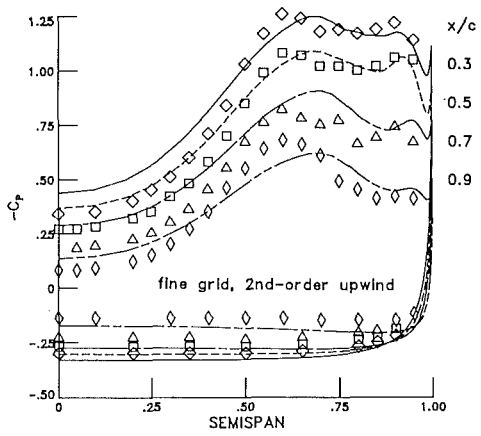

Fig. 3 Computed (lines) and measured (symbols) surface pressure coefficient distributions, AR = 1, $\alpha = 20.5$, Re = 0.9 million, flow: transitional in the computation and nominally laminar in the experiment

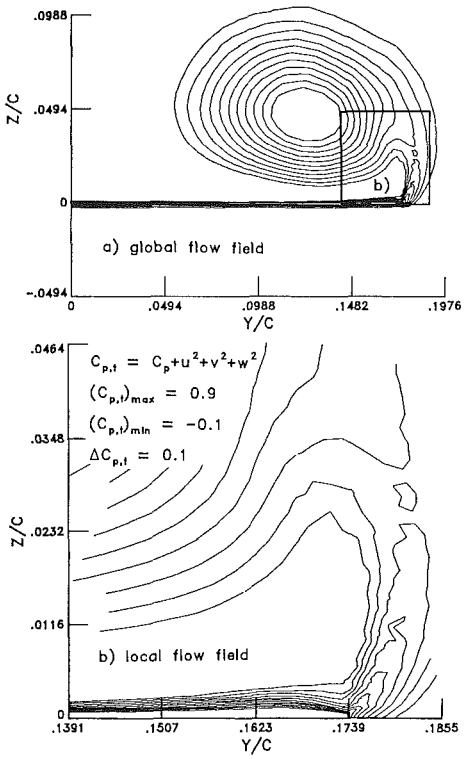

Fig. 4 Total pressure distribution in crossplane at x/c = 0.7 for a coarse grid calculation with up to second-order accurate upwinding, AR = 1, $\alpha = 20.5$ degrees, Re = 0.9 million, laminar flow

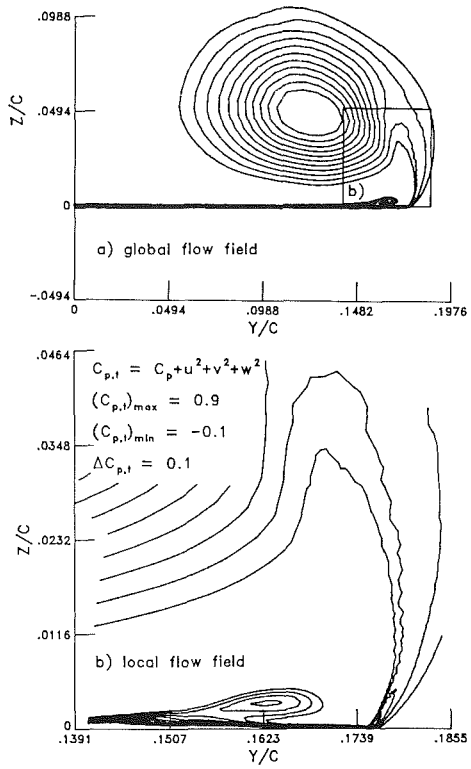

Fig. 5 Total pressure distribution in crossplane at x/c = 0.7 for a fine grid calculation with up to second-order accurate upwinding, AR = 1, $\alpha = 20.5$ degrees, Re = 0.9 million, laminar flow

is predicted in acceptable agreement with the fine grid result in Fig. 2(*b*), but the secondary and tertiary vortices are not captured. That indicates the necessity to cluster coordinate surfaces enveloping the wing, close to the wing. The grid fineness in the circumferential direction appears to be less important. The surface pressure distributions are always smooth except for a small suction spike close to the leading edge. Additional computations on the medium grid confirmed the above statements concerning the sensitivity of the flow field results toward the resolution of the flow by the grid in circumferential and radial direction. When compared to the experiment, the strength of the secondary vortex is overpredicted for $x/c \geq 0.7$ in Fig. 2(*b*). The magnitude of this disagreement is reduced when a laminar/turbulent transition is modeled in the computation. The calculated surface pressure distributions in Fig. 3 agree much better for $x/c \geq 0.7$ with the experiment than in Fig. 2. In these transitional calculations, the flow is assumed to be laminar along the windward surface and up to $x/c = 0.6$ along the leeward surface, and turbulent along the upper surface for $x/c > 0.6$ and in the wake. The eddy viscosity was calculated using a modified Baldwin-Lomax [22] turbulence model, which included, among others, the modifications as proposed by Degani and Schiff [23].

The contours of constant total pressure coefficient in Figs. 4 and 5 show the crossflow at $x/c = 0.7$ root chord station. The results in Fig. 4 (5) are computed with the up to second-order accurate upwind differencing on a coarse (fine) grid. The primary vortices in Figs. 4(*a*) and 5(*a*) appear to be quite similar and only slightly affected by the spatial resolution of the boundary-layer-like flow along the wing surface. However, a clearly developed secondary vortex as in Fig. 5(*b*) occurs only in the medium and fine grid calculations. The blowups in Figs. 4(*b*) and 5(*b*) exhibit small scale oscillations along the inner side of the shear layer that emanates from the leading edge and rolls up into the primary vortex. They are easily explained when the shear layer is considered to be a smeared vortex sheet (i.e., a smeared contact discontinuity) that is not aligned with the grid. Under such circumstances, the accuracy of high resolution schemes, which are assembled via summation of uni-dimensional discretizations, often deteriorates since they are derived with the assumption that the waves are propagated parallel to the coordinate directions (see reference [24]).

Figure 6 documents the numerical efficiency of the four implicit algorithms for the three cases shown in Figs. 2. All computations are carried out in half-precision arithmetic (i.e., seven significant decimal places) on the CDC CYBER 205 vector computers at NASA Langley (2-pipeline model) and at NASA Ames (4-pipeline model). All steady-state solutions are calculated with $\beta = 1$ and with local time stepping (CFL = 10). The L_2-norms of all residuals are driven to machine zero with

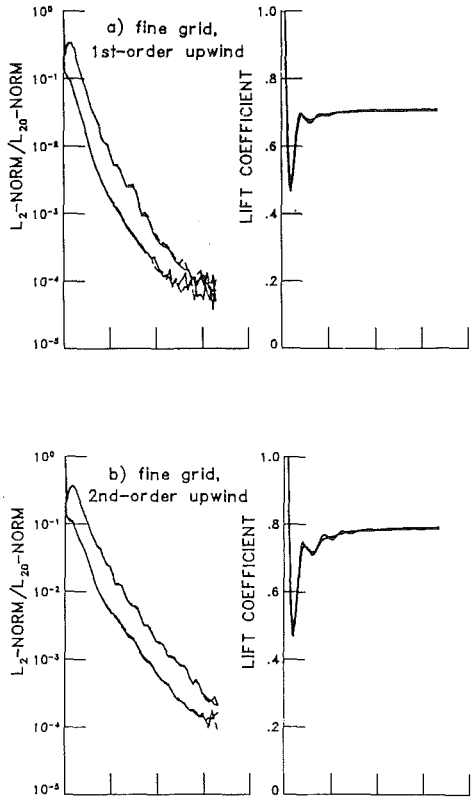

Fig. 6 Convergence summary for calculations of a vortical flow around a sharp-edged delta wing, AR = 1, $\alpha = 20.5$ degrees, Re = 0.9 million, laminar flow

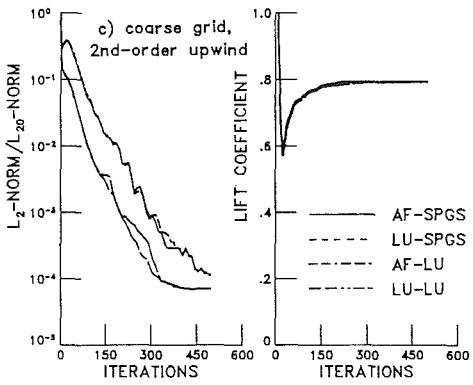

Fig. 6 Concluded

an asymptotic spectral radius of 0.973 (Fig. 6(*a*)), 0.977 (Fig. 6(*b*)), and 0.983 (Fig. 6(*c*)). The L_2-norms are scaled with the L_2-norm after the first complete update of the residual, which is about 10^{-2}. The time-dependent methods, AF-LU and LU-LU, converge within fewer iterations to an asymptotic steady-state since they reduce the L_2-norm monotonously unlike their corresponding hybrid counterparts, AF-SPGS and LU-SPGS.

Table 1 documents the computational efficiency of the four implicit algorithms. The Central Processor Unit (CPU) time per grid point and per iteration or time step is given for the CYBER 205 at NASA Ames. Multiplying these data by 1.4 gives approximately the corresponding values on the CYBER 205 at NASA Langley. The architecture of the CYBER 205 is such that it performs the better, the longer the vectors are. This is elucidated by comparing the computational efficiency of the high resolution calculations on the coarse and on a fine grid. On the coarse grid (i.e., shorter vectors), the LU-SPGS and LU-LU algorithms fare better than the AF-SPGS and AF-

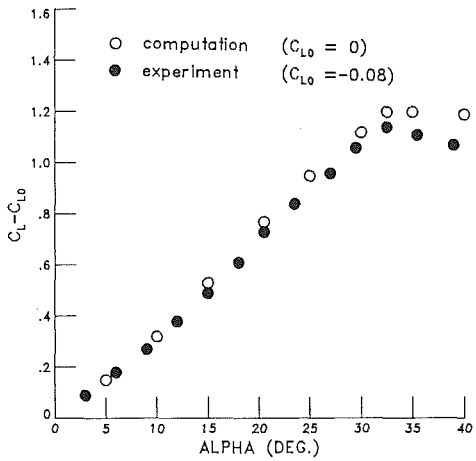

Fig. 7 Variation of lift with angle of attack, AR = 1, Re = 0.9 million, laminar flow

Table 1 CPU time per grid point and per time step or iteration (in microseconds)

	Coarse grid 2nd-order	Fine grid 2nd-order	Fine grid 1st-order
AF-SPGS	42.8	37.1	27.1
LU-SPGS	40.6	39.4	29.5
AF-LU	43.0	37.6	29.5
LU-LU	40.6	40.0	32.1

LU algorithms because they require fewer arithmetic operations. However, on the fine grid (i.e., longer vectors), the LU-SPGS and the LU-LU algorithms are slower than the AF-SPGS and AF-LU algorithms because of their lower degree of vectorizability. The first-order accurate computations on the fine grid demonstrate that they require about 25 to 35 percent less CPU time than the high resolution computations. Furthermore, the AF-LU and LU-LU are slower than both hybrid schemes since they require two sweeps through the integration domain for one update of the residual. That necessitates that three of the Jacobians on their LHSs have to be doubly computed. That disadvantage loses its impact for the high resolution computation where those Jacobians have to be computed twice anyway (once for the LHS, and once for the residual).

All four implicit algorithms maintain their performance for all fine grid computations in Fig. 7 with the high resolution scheme and with unchanged values for β and CFL. The computed linear lift is systematically higher than the measured linear lift due to the different wing geometries: the cambered wind tunnel model produces negative lift at zero angle of attack. The differences in the calculated and the measured nonlinear lift are attributed to the fact that the flow is partly turbulent in the experiment but assumed to be fully laminar in the computations (cf. measured and calculated loads in Figs. 2*b* and 3). Maximum lift is predicted at the same angle of attack as in the experiment [21], where the peak in lift is associated with the commencement of vortex breakdown at the trailing edge. Inspection of the flow field for $\alpha = 32.5$ degrees reveals that a bubble-type vortex breakdown close to the trailing edge is computed as a steady-state solution to the Navier-Stokes equations.

Conclusions

Based on flux-difference splitting, a high resolution scheme has been formulated for efficient calculations of steady-state solutions to the three-dimensional, incompressible Navier-Stokes equations in curvilinear coordinates. Four dif-

ferent implicit algorithms have been implemented in that scheme. The AF-SPGS algorithm combines a symmetric planar Gauss-Seidel (SPGS) relaxation in one coordinate direction with approximate factorization (AF) in the other two coordinate directions, where each implicit factor has block-tridiagonal structure. The LU-SPGS method combines SPGS with an approximate LU factorization (LU) which gives implicit factors with block-triangular structure. These hybrid schemes are easily converted into corresponding fully time-dependent methods, AF-LU and LU-LU. A comparative study of these algorithms reveals that their numerical efficiency is about the same. As long as a supercomputer is used whose performance does not heavily depend on vector lengths, the LU-SPGS and LU-LU algorithms are faster than their counterparts, AF-SPGS and AF-LU, because the inversion of their implicit factors requires much less arithmetic operations. Because these operations are only up to 55 percent vectorizable (as opposed to 100 percent for the AF-SPGS and AF-LU methods), they lose that advantage when run on vector computers whose performance improves with growing vector lengths, like the CDC CYBER 205.

It is planned to extend this comparative study by investigations of methods which exploit even more the speed capability of supercomputers (e.g., diagonalized, three-dimensional AF methods) or which make better use of the memory capacity of supercomputers. The latter can be accomplished by implementing elements of direct methods in the hybrid methods, which is currently being investigated.

Acknowledgments

This work of the first two authors is sponsored by the NASA Langley Research Center under Contract NAS1-17919, awarded to Vigyan Research Associates, Inc., Hampton, VA.

References

1 Swanson, R. C., and Turkel, E., "A Multistage Time-Stepping Scheme for the Navier-Stokes Equations," AIAA Paper 85-0035, Jan. 1985.

2 Vatsa, V. M., "Accurate Solutions for Transonic Viscous Flow Over Finite Wings," *Journal of Aircraft*, Vol. 24, No. 6, June 1987, pp. 377-385.

3 Pulliam, T. H., and Steger, J. L., "On Implicit Finite-Difference Simulations of Three-Dimensional Flow," AIAA Paper 78-10, Jan. 1978.

4 Lombard, C. K., Bardina, J., Venkatapathy, E., and Oliger, J., "Multi-Dimensional Formulation of CSCM—An Upwind Flux Difference Eigenvector Split Method for the Compressible Navier-Stokes Equations," AIAA Paper No. 83-1895, July 1983.

5 Obayashi, S., and Kuwahara, K., "An Approximate LU Factorization Scheme for the Compressible Navier-Stokes Equations," *J. Comput. Phys.*, Vol. 63, No. 1, Mar. 1986, pp. 157-167.

6 Warming, R. F., and Beam, R. M., "On the Construction and Application of Implicit Factored Schemes for Conservation Laws," Symposium on Computational Fluid Dynamics, *SIAM-AMS Proceedings*, Vol. 11, 1978, pp. 85-129.

7 Pulliam, T. H., and Chaussee, D. S., "A Diagonal Form of an Implicit Approximate-Factorization Algorithm," *J. Comput. Phys.*, Vol. 39, No. 2, Feb. 1981, pp. 347-363.

8 Pan, D., and Lomax, H., "A New Approximate LU Factorization Scheme for the Reynolds-Averaged Navier-Stokes Equations," AIAA Paper 86-0337, Jan. 1986.

9 Hartwich, P.-M., Hsu, C.-H., and Liu, C. H., "Implicit Hybrid Schemes for the Flux-Difference Split, Three-Dimensional Navier-Stokes Equations," *Lecture Notes in Physics*, Vol. 264, Springer-Verlag, New York, 1986, pp. 303-307.

10 Steger, J. L., and Warming, R. J., "Flux Vector Splitting of the Inviscid Gasdynamics Equations with Application to Finite-Difference Methods," *J. Comput. Phys.*, Vol. 40, No. 2, Apr. 1981, pp. 263-293.

11 Steger, J. L., and Kutler, P., "Implicit Finite-Difference Procedures for the Computation of Vortex Wakes," *AIAA J.*, Vol. 15, No. 4, Apr. 1977, pp. 581-590.

12 Chorin, A. J., "A Numerical Method for Solving Incompressible Viscous Flow Problems," *J. Comput. Phys.*, Vol. 2, No. 1, August 1967, pp. 12-26.

13 Roe, P. L., "Approximate Riemann Solvers, Parameter Vectors, and Difference Schemes," *J. Comput. Phys.*, Vol. 43, No. 2, Oct. 1981, pp. 357-372.

14 Van Leer, B., "Flux-Vector Splitting for the Euler Equations," ICASE Report No. 82-30, Sept. 1982.

15 Hartwich, P.-M., and Hsu, C.-H., "High Resolution Upwind Schemes for the Three-Dimensional Incompressible Navier-Stokes Equations," AIAA Paper No. 87-0547, Jan. 1987.

16 Rizzi, A., and Eriksson, L. E., "Computation of Inviscid Imcompressible Flow with Rotation," *J. Fluid Mech.*, Vol. 153, Apr. 1985, pp. 275-312.

17 Harten, A., "High Resolution Schemes for Hyperbolic Conservation Laws," *J. Comput. Phys.*, Vol. 49, No. 3, Mar. 1983, pp. 357-393.

18 Yee, H. C., Warming, R. F., and Harten, A., "Implicit Total Variation Diminishing (TVD) Schemes for Steady-State Calculations," *J. Comput. Phys.*, Vol. 57, No. 3, Mar. 1985, pp. 327-360.

19 Sweby, P. K., "High Resolution Schemes Using Flux Limiters for Hyperbolic Conservation Laws," *SIAM J. Numer. Anal.*, Vol. 21, No. 4, Oct. 1984, pp. 995-1011.

20 Hartwich, P.-M., "Three-Dimensional Grids as Solutions of Elliptic Systems," AIAA Paper No. 86-0430, Jan. 1986.

21 Hummel, D., "On the Vortex Formation Over a Slender Wing at Large Angles of Incidence," AGARD-CP-247, Paper No. 15, 1978.

22 Baldwin, B. S., and Lomax, H., "Thin Layer Approximation and Algebraic Model for Separated Turbulent Flows," AIAA Paper No. 78-257, Jan. 1978.

23 Degani, D., and Schiff, L. B., "Computation of Turbulent Supersonic Flows around Pointed Bodies Having Crossflow Separation," *J. Comput. Phys.*, Vol. 66, No. 1, Sept. 1986, pp. 173-196.

24 Roe, P. L., "Characteristic Based Schemes for the Euler Equations," *Ann. Rev. Fluid Mech.*, Vol. 18, 1986, pp. 337-365.

Consistent Boundary Conditions for Reduced Navier-Stokes (RNS) Scheme Applied to Three-Dimensional Viscous Flows

D. R. Reddy
Supervisor,
Turbomachinery Analysis Section,
Sverdrup Technology, Inc.,
Lewis Research Center Group
Cleveland, Ohio 44135

S. G. Rubin
Professor, Department of Aerospace
Engineering and Engineering Mechanics,
University of Cincinnati,
Cincinnati, Ohio 45221

A consistent and efficient set of boundary conditions are developed for the multi-sweep space marching pressure-elliptic Reduced Navier-Stokes (RNS) scheme as applied for three-dimensional internal viscous flow problems. No-slip boundary conditions are directly imposed on the solid walls. There is no iteration procedure required in the cross plane to ensure mass conservation across each marching plane. The finite difference equations forming the coefficient matrix are ordered such that the surface normal velocity is specified on all the solid walls; unlike external flows, a pressure boundary condition in the cross plane is not required. Since continuity is directly satisfied at all points in the flow domain, the first order momentum equations can be solved directly for the pressure without the need for a Poisson pressure correction equation. The procedure developed herein can also be applied with periodic boundary conditions. The analysis is given for general compressible flows. Incompressible flow solutions are obtained, for straight and curved ducts of square cross section, to validate the procedure. The solutions of these test cases are used to demonstrate the applicability of the RNS scheme, with the improved boundary conditions, for internal flows with strong interaction as would be encountered in ducts and turbomachinery geometries.

Introduction

The flow through advanced highly loaded turbomachinery blade rows is characterized by extensive regions of strong three-dimensional viscous-inviscid interaction. To simulate this important pressure interaction, numerical melthods that can couple the viscous and inviscid regions must be employed. In addition, efficiency and accuracy of the numerical algorithm become important considerations if these methods are to be useful in the aerodynamic design process.

A number of different approaches have been considered for the simulation of strong viscous-inviscid interaction in internal flows. Conventional full Navier-Stokes (N-S) methods, which solve the full N-S equations throughout the flow field, have been successfully used to analyze three-dimensional interacting flows in turbomachinery blade passages [1, 2]. However, these methods do not exploit the asymptotic behavior of the equations at the large Reynolds numbers typically encountered in turbomachinery flows. Consequently, these medhods require large computer storage and run times. A recently developed method in this category [1] requires 18 hr of CPU time on a VAX 11/780 computer for the prediction of end-wall flow in a cascade on a relatively coarse grid of 53 by 31 by 10 nodes.

Contributed by the Fluids Engineering Division for publication in the JOURNAL OF FLUIDS ENGINEERING. Manuscript received by the Fluids Engineering Division September 24, 1987.

Another approach is interacting boundary layer theory. This has been used by a number of researchers [3 to 7] for two-dimensonal applications, where the interaction of the inviscid flow on the boundary layer is coupled through the injection and surface boundary conditions for the inviscid and boundary layer analysis respectively. These methods are potentially very efficient; however, the evaluation of the injection condition or inviscid displacement body (due to the viscous effects), which alters the inviscid flow, can become rather involved for complex three-dimensional flows. Approximate methods normally used to evaluate this effect, such as linearized small disturbance theory, can result in considerable error. In addition, the approximation of zero normal pressure gradient through the boundary layer might not be appropriate for turbulent flows with strong pressure interaction [16].

Methods that use space marching with an approximate form of the steady N-S equations (single-pass and multipass marching methods) have been considered for a number of years to predict flows through curved ducts and turbomachinery blade cascades [8 to 11]. Single pass marching can be used for configurations where the flow is of initial value character, but multiple pass procedures are required for elliptic flows. When applied to elliptic flows, these formulations have generally introduced a Poisson equation for pressure to correct an initially assumed pressure field. This is required in lieu of the continuity equation, which is not

satisfied explicitly, in order to ensure global mass conservation. These methods are called partially parabolic or semi-elliptic methods to distinguish them from the full N-S schemes. Although these methods result in less computing time than full N-S methods, the solution of the Poisson equation, using conventional methods, still requires large computer run times for most cases. In addition, due to the uncoupled nature of the pressure correction, which is a necessity of the formulation, extremely large under-relaxation is required in high subsonic and transonic flow regions. This slows down the convergence of the iteraction procedure and thereby further increases the run time.

A method that combines the asymptotic treatment of interacting boundary layer theory and the accurate interaction simulation of the full Navier-Stokes methods is the Reduced Navier-Stokes (RNS) formulation. This scheme was originally developed for external flows [12 to 18] and later formulated for internal flows [19]. The solution procedure and the boundary conditions have been modified in this study to make the scheme more efficient for both two- and three-dimensional flows with strong interaction. As described in earlier references [14 to 19], the system of equations resulting in the RNS formulation is similar to that of the partially parabolic scheme in that streamwise diffusion effect is neglected. However, the elliptic effect or upstream influence in strongly interacting flows is simulated by a characteristic treament of the streamwise pressure gradient. The solution procedure is therefore very much different, and more direct, as compared to that of partially parabolic schemes. The equations are solved by a relaxation procedure with full coupling between pressure and velocities and without the need for a Poisson equation for the pressure correction. Detailed analysis of the RNS scheme and solutions for laminar, turbulent, subsonic, transonic, and supersonic flow regimes for a variety of external flow configurations are given in references [12 to 18]. Application of the scheme for internal flow and some preliminary results for two- and three-dimensional internal flows were presented in reference [19]. As pointed out in these references, the procedure is applicable to both inviscid and viscous flow and can be classified somewhat between interacting boundary layer theory and full Navier-Stokes solvers.

A detailed description and analysis of the RNS scheme as applicable to two-dimensional external flows are given in references [13 to 18]. Details of various stages of the evolution of the scheme leading to its present form are also given in references [13, 15 to 17]. For the sake of completeness, some of the analysis is repeated here.

The RNS equations were first considered as single sweep or PNS (Parabolized Navier-Stokes) marching procedures for supersonic flows. The first application was for hypersonic flow (20) where the contribution of the streamwise pressure gradient in the corresponding momentum equation is negligible and can therefore be neglected. The equations are mathematically parabolic, upstream influence is negligible, and an exact solution is obtained in a single marching sweep. For lower supersonic mach numbers, where the influence of the streamwise pressure gradient is not negligible, an elliptic effect associated with pressure interaction through the subsonic portion of the boundary layer introduces upstream influence [21, 22]. A single sweep methodology then leads to an ill-posed initial value problem and gives rise to exponentially growing departure solutions for a marching step size, $\Delta\xi$, less than $(\Delta\xi)_{\min}$ where $(\Delta\xi)_{\min}$ is proportional to the extent of the subsonic portion of the flow in the normal (cross stream) direction [14 and 23]. To suppress this so-called departure effect that reflects the boundary value character of the problem, researchers have used a variety of approximation techniques [20 to 24] to simulate the elliptic effect of the streamwise pressure gradient term.

In the present RNS procedure, the streamwise pressure gradient term P_ξ is split according to its characteristic behavior so that

$$P_\xi = \omega (P_\xi)_h + (1-\omega)(P_\xi)_e$$

This follows the eignevalue analysis of Vigneron et al. [25], where $0 \le \omega(\mathrm{M}) \le \omega_{\max}$ is a function of local Mach number M and

$$\omega_{\max} = \{\gamma \mathrm{M}^2/(1+(\gamma-1)\mathrm{M}^2,\ 1\}_{\min}$$

As mentioned in references [18 and 19], the portion $\omega(p\xi)h$, which is "backward" differenced during discretization, represents the "hyperbolic" or marching part of P_ξ and the term $(1-\omega)(P_\xi)_e$ represents the "elliptic" or relaxation contribution that is "forward" differenced. Note that for incompressible flow, since $\omega(0)=0$, the entire P_ξ contribution is elliptic. "Forward" differencing of $(1-\omega)(P_\xi)_e$ introduces upstream influence in the computational domain. This removes the ill-posedness found in the single sweep initial value formulation. Due to the forward differencing, the solution procedure requires multiple sweep marching or relaxation. The above treatment of the streamwise pressure gradient, with multiple sweep relaxation, leads to consistent (arbitrary $\Delta\xi$) and departure free ($\Delta\xi \to 0$) solutions for the entire range of incompressible to supersonic Mach numbers. Significantly, only the pressure (and possibly the axial velocity in the limited regions of reversed flow only) need to be stored. This results in, among, other advantages, a significant reduction in storage requirement over conventional N-S methods.

In the present study, a new consistent solution procedure is formulated, using the RNS Scheme, for three- and two-dimensional flow problems. The treatment of boundary conditions has been significantly modified, compared to the earlier procedure [19], to make the solution procedure more efficient and accurate. The application of zero injection or solid wall boundary conditions in the cross-plane is more direct in this study than in that of reference [19]. The procedure is developed for arbitrary compressible flow, but only incompressible solutions are obtained for developing flow in three-dimensional straight and curved ducts of square cross section. These solutions are compared with available experimental data and computed results.

Governing Equations

The governing equations are written in a general curvilinear coordinate system (ξ, η, and ζ) in terms of the primitive variables (u, v, w, p). The momentum equations are then rearranged to reflect the momentum balance in the directions of the contravariant velocity components (U, V, and W). This requires the appropriate combination of the Cartesian component momentum equations after transformation into the ξ, η, and ζ coordinate system. For example, the momentum equation in the U direction is written as ξ_x (x-momentum) + ξ_y (y-momentum) + ξ_z (z-momentum) (26). The final equations are given in the following matrix form.

Continuity and Momentum:

$$\partial_\xi E + \partial_\eta F + \partial_\zeta G = \partial_\xi R + \partial_\eta S + \partial_\zeta T + K$$

where

$$E = \frac{1}{J}\begin{bmatrix} \rho U \\ \rho UU \\ \rho UV \\ \rho UW \end{bmatrix}$$

$$F=\frac{1}{J}\begin{bmatrix}\rho V\\ \rho VU\\ \rho VV\\ \rho VW\end{bmatrix}$$

$$G=\frac{1}{J}\begin{bmatrix}\rho W\\ \rho WU\\ \rho WV\\ \rho WW\end{bmatrix}$$

$$R=\frac{1}{J}\begin{bmatrix}0\\ \xi_x\tau_x{}^{\xi}+\xi_y\tau_y{}^{\xi}+\xi_z\tau_z{}^{\xi}\\ \eta_x\tau_x{}^{\xi}+\eta_y\tau_y{}^{\xi}+\eta_z\tau_z{}^{\xi}\\ \zeta_x\tau_x{}^{\zeta}+\zeta_y\tau_y{}^{\zeta}+\zeta_z\tau_z{}^{\zeta}\end{bmatrix}$$

$$S=\frac{1}{J}\begin{bmatrix}0\\ \xi_x\tau_x{}^{\eta}+\xi_y\tau_y{}^{\eta}+\xi_z\tau_z{}^{\eta}\\ \eta_x\tau_x{}^{\eta}+\eta_y\tau_y{}^{\eta}+\eta_z\tau_z{}^{\eta}\\ \zeta_x\tau_x{}^{\zeta}+\zeta_y\tau_y{}^{\eta}+\zeta_z\tau_z{}^{\eta}\end{bmatrix}$$

$$T=\frac{1}{J}\begin{bmatrix}0\\ \xi_x\tau_x{}^{\zeta}+\xi_y\tau_y{}^{\zeta}+\xi_z\tau_z{}^{\zeta}\\ \eta_x\tau_x{}^{\zeta}+\eta_y\tau_y{}^{\zeta}+\eta_z\tau_z{}^{\zeta}\\ \zeta_x\tau_x{}^{\zeta}+\zeta_y\tau_y{}^{\zeta}+\zeta_z\tau_z{}^{\zeta}\end{bmatrix}$$

$$K=\frac{1}{J}\begin{bmatrix}0\\ \rho\zeta G_{\xi\rho}-g^{\xi\xi}p_{\xi}-g^{\xi\eta}p_{\eta}-g^{\xi\zeta}p_{\zeta}\\ \rho\zeta G_{\xi\rho}-g^{\xi\xi}p_{\xi}-g^{\xi\eta}p_{\eta}-g^{\eta\zeta}\rho_{\zeta}\\ \rho\zeta G_{\xi\rho}-g^{\xi\xi}p_{\xi}-g^{\xi\eta}p_{\eta}-g^{\zeta\zeta}p_{\zeta}\end{bmatrix}$$

The terms $\tau_x{}^{\xi}$, $\tau_y{}^{\xi}$, etc. appearing in the column vectors R, S, T, and K are explained in detail in Appendix A. The velocities U, V, and W are the contravariant components; all the shear stresses, as shown as Appendix A, can be expressed in terms of these components. Since one of the coordinates (ξ) represents the marching direction, it has been found that the equations expressed in this form enhance the stability of the numerical scheme. In addition, the system of equations in this form can be easily verified for an orthogonal coordinate system. For the sample problems considered in this study, an orthogonal (curvelinear) coordinate system is specified. For the present formulation, adiabatic (wall) conditions are assumed and with a Prandtl number of unity, a simplified energy equation results; i.e., total enthalpy is constant. The same algorithm can also be used for nonadiabatic wall conditions and Prandtl numbers different from unity. The energy equation written in terms of stagnation enthalpy is only weakly coupled with the remainder of the equations for low speed and even moderate supersonic flows. Therefore, the energy equation can be solved in an uncoupled manner to update the stagnation enthalpy at each marching location. To close the system, an equation of state $p=\rho RT$ and a relation for viscosity, $\mu=\mu(T)$, are required for compressible flows.

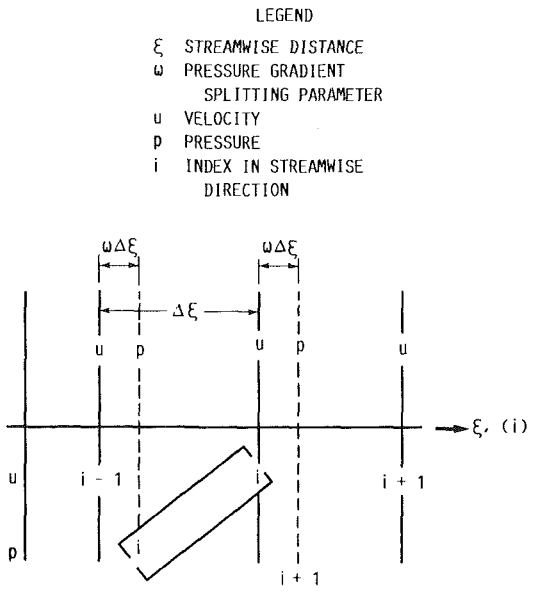

Fig. 1 Discretization in the ξ-direction

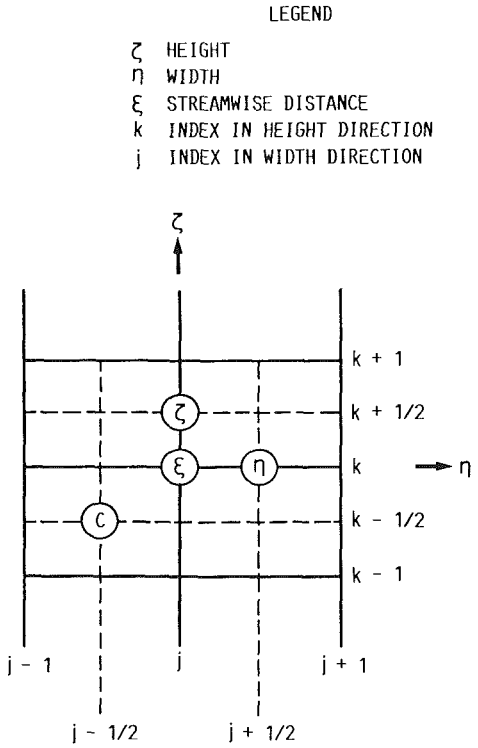

Fig. 2 Discretization in the cross-plane

In all of the momentum equations, the diffusion terms in the streamwise direction are neglected according to the RNS approximation. These terms are negligible for the coordinate system specified herein so that the RNS system closely approximates the full N-S equations. The flow Reynolds number is based on the inlet uniform velocity and the inlet hydraulic diameter of the duct. The pressure is nondimensionalized with the inlet dynamic head.

Discretization

The discretization of the governing equations is illustrated in Figs. 1 and 2. In the marching (ξ) direction the equations

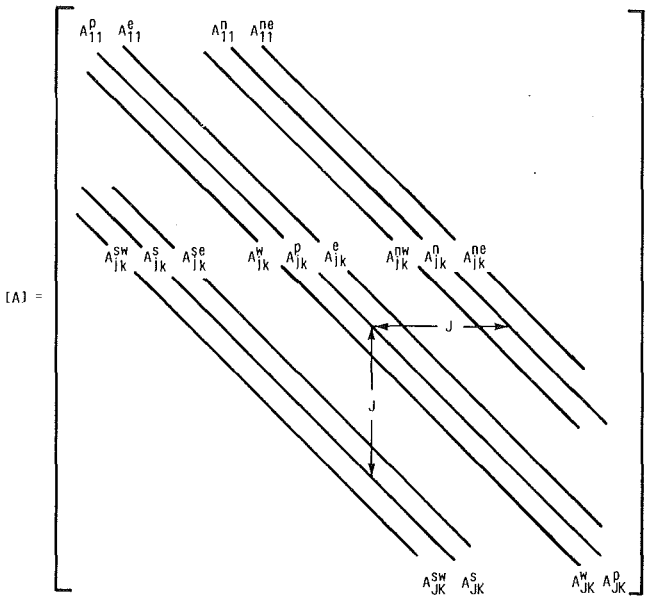

Fig. 3 Coefficient matrix for nine-point formulation

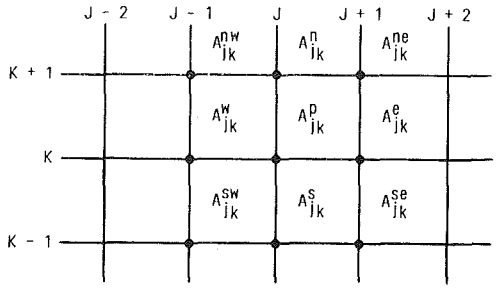

Fig. 4 Computational molecule in the cross plane

are discretized at (i), the velocity node points. In the cross-plane, the continuity, streamwise momentum and the two normal momentum equations are discretized at (c), (ξ), (η), and (ζ), respectively. All of the convective terms in the marching direction are upwind differenced. Both first-order (two point) and second-order (three point) accurate upwind differencing schemes are considered. As discussed earlier, the streamwise pressure gradient, P_ξ is differenced as:

$$P_\xi = (1-\omega_{i+1})\left\{\left[\frac{P_{i+1}^{n-1}-P_j^n}{\xi_{i+1}-\xi_i}\right]+(\Delta p_\xi)_f\right\}$$

$$+\omega_i\left\{\left[\frac{P_i^n-P_{i-1}^n}{\xi_i-\xi_{i-1}}\right]+(\Delta p_\xi)_b\right\}$$

where the subscript i is a modified index for pressure in the ξ-direction (see Fig. 1) and n is the current marching (global) sweep. The terms $(\Delta p_\xi)_f$ and $(\Delta p_\xi)_b$ are additional correction terms to produce second-order accuracy in the forward and backward directions respectively. These terms are given by:

$$(\Delta p_\xi)_f = \frac{1}{\sigma_f(1+\sigma_f)(\xi_{i+1}-\xi_i)}[(1+\sigma_f)p_{i+1}^{n-1}-p_{i+2}^{n-1}-\sigma_f p_i^n]$$

and

$$(\Delta p_\xi)_b = \frac{1}{\sigma_b(1+\sigma_b)(\xi_i-\xi_{i-1})}[\sigma_b p_i^n-(1+\sigma_b)p_{i-1}^n+p_{i-2}^n]$$

where

$$\sigma_f = (\xi_{i+1}-\xi_i)/(\xi_i-\xi_{i-1})$$

$$\sigma_b = (\xi_{i-1}-\xi_{i-2})/(\xi_i-\xi_{i-1})$$

For first order accuracy the terms $(\Delta p_\xi)_f$ and $(\Delta p_\xi)_b$ are neglected.

The discretization for p_ξ requires that the unknown pressure p_i at the marching location i, is staggered at a distance $(1-\omega)\Delta\xi$ upstream of velocity u_i, v_i, and w_i. The pressure at the grid point i is given by:

$$\tilde{p}_i = \omega_{i+1}p_i+(1-\omega_{i+1})p_{i+1}$$

The discretization of all derivatives in the η and ζ cross flow directions is done using the second-order accurate central differencing except for one of the viscous terms in each of the normal momentum equations. These terms are the diffusion terms in the same direction as the momentum direction, i.e., the second derivative with respect to η in the η-momentum equation ($\partial^2 V/\partial\eta^2$) and the corresponding term ($\partial^2 W/\partial\zeta^2$) in ζ momentum equation. Due to the nature of the discretization locations of the cross flow momentum equations, described in a later section, these terms are discretized using a retarded central differencing which is first-order accurate. Since these viscous terms are negligibly small, i.e., of order of the neglected streamwise diffusion terms, for large Reynolds numbers, the discretization in the η and ζ directions remains essentially second-order accurate in the context of the RNS approximation. As discussed in detail in reference [16], the overall accuracy of the discretization of the RNS scheme lies between first and second order; very close to second-order accuracy was observed for some examples (reference [16]). The nonlinear convective terms in the finite difference equations are qualsilinearized, with respect to the previous marching location, using a Newton linearization. The linearized equations result in a coupled system for the vector $[U, V, W, p]^T$. The system of equations can be represented by the matrix equation

$$[A]\{\phi\} = \{q\}$$

where $\{\phi\}$ is the solution vector $[U, V, W, p]^T$, $\{q\}$ is the known right hand side of the equation, and $[A]$ is the nine diagonal coefficient matrix shown in Fig. 3. The associated computational molecule is shown in Fig. 4. Each of the elements of the coefficient matrix $[A]$ is a 4 by 4 matrix corresponding to the column size [4] of the vector $\{\phi\}$. The discrete system of equations is solved for $[U, V, W, p]_{i,j,k}^T$ at each marching location i with the modifed strong implicit procedure (MSIP) of reference [27]. This method was originally developed for the scalar system describing the two-dimensional heat conduction equation [27]. It was modified by the present investigators for application to a vector system of equations in a previous study [19]. The details of the procedure are given in references 19 and 27. As mentioned in reference [19], for a two-dimensional flow the cross-plan reduces to a line and the system of equations reduces to a block tridiagonal system for $[U, V, p]_{i,j}$ which is solved by standard LU decomposition.

Boundary Conditions

The method of application of boundary conditions often dictates the efficiency of a solution algorithm. A major change in the RNS/MSIP solution procedure has been implemented in the present study by a modification of the boundary conditions as applied in the previous study [19].

Inflow and outflow boundary conditions are straight forward. Since streamwise (ξ) diffusion terms are neglected and streamwise convection terms are upwind differenced, the velocities have an initial value character (except in regions of reversed flow). Therefore the velocities must be specified only at the inflow boundary assuming that flow reversal does not occur at the outflow boundary. Due to the splitting of the streamwise pressure gradient into a forward differenced (relaxation) and backward differenced (marching) elements, a pressure condition is required at both the inflow and outflow boundaries for mach numbers $0<M<1$. For mach numbers

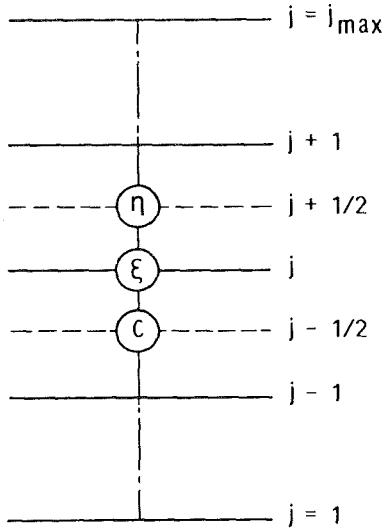

Fig. 5 Discretization for 2-D case in the normal (η) direction

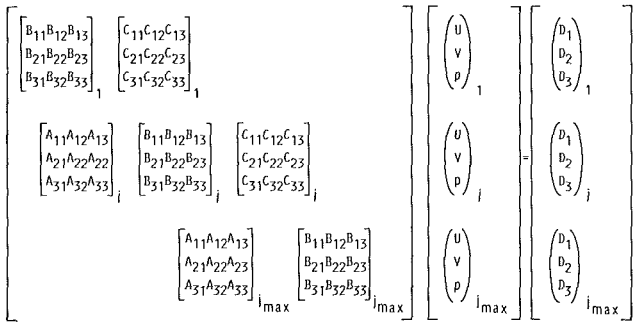

Fig. 6 Block tridiagonal system at marching location (i) for 2-D flow

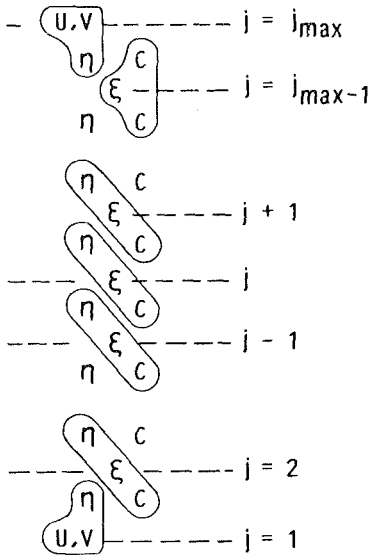

Fig. 7 Grouping of discretization governing equations in the flow field

$M \geq 1$, ω becomes unity and therefore a pressure condition is not required at the outflow boundary i.e., full marching. For incompressible flow ($\omega = 0$) a pressure condition is not required at the inflow boundary (full relaxation). For $0 < M < 1$, the staggered pressure (see Fig. 1), leads to partially prescribed pressure condition at both the inflow and outflow computational planes, since at the node point i,

$$\tilde{p}_i = \omega_{i+1} p_i^n + (1 - \omega_{i+1}) p_{i+1}^{n-1}$$

i.e., for $\omega \neq 0$, even though the pressure is prescribed at the inflow only a portion (ωp) is actually used in the computations; at the outflow $(1 - \omega)$ times the prescribed pressure is used.

In the cross plane ($\eta - \zeta$ plane), it is important to apply the boundary conditions in a consistent manner if the system of discretized equations is to be solved efficiently. To illustrate the present procedure, let us first consider the two-dimensional flow problem. The cross-plane then reduces to a line, e.g., $0 \leq \eta \leq 1$. The discretization locations for the continuity, ξ-momentum and η-momentum, associated with the system of equations to solve for $[UVp]^T$ at the node j, are denoted in Fig. 5 by (c), (ξ), and (η), respectively.

As seen in Fig. 5, the number of discrete ξ-momentum equations is $j_{max} - 2$ and the number of descrete η-momentum and continuity equations are each $j_{max} - 1$. Therefore the total number of unknowns is $3j_{max}$ (U, V, and p for each node) and the total number of discrete equation is $(3j_{max} - 4)$. For solid walls ($j = 1$ and $J = j_{max}$), each wall has two physical boundary conditions, i.e., $U = 0$ and $V = 0$. Therefore, the system is closed in so far as total number of equations plus the boundary conditions compared with the number of unknowns is concerned. However, since there are only $j_{max} - 1$ discrete η-momentum equations, the numerical solution procedure apparently requires a condition for pressure at one of the boundaries ($j = 1$ or $j = j_{max}$). This would render one of the boundary conditions on V redundant. In the previous study (19), the zero normal velocity ($V = 0$) was indirectly imposed at the outer boundary ($j = j_{max}$) through an artificial pressure boundary condition. An iterative process on this pressure boundary condition, imposed at $j = j_{max}$ was required in order to ensure global mass conservation or that the velocity $V = 0$ at $j = j_{max}$. In the present study, the zero injection conditions are directly imposed at both the boundaries without any need for the iterative artificial pressure boundary condition. This is accomplished by slightly changing the structure of the block tridiagonal matrix near the outer boundary. The block tridiagonal system at the marching location (i), for two-dimensional flow, is shown in Fig. 6. For an interior point, $2 \leq j \leq j_{max-2}$, the three equations for the unknown U, V, and p are grouped as:

$$\begin{bmatrix} \text{continuity at } j - 1/2 \\ \xi\text{-momentum at } j \\ \eta\text{-momentum at } j + 1/2 \end{bmatrix}$$

For the point next to upper boundary (the lower boundary can be chosen instead of upper boundary) we modify the grouping as follows.

$$\begin{bmatrix} \text{continuity at } (j_{max} - 1 - 1/2) \\ \xi\text{-momentum at } (j_{max} - 1) \\ \text{continuity at } (j_{max} - 1 + 1/2) \end{bmatrix}$$

For wall boundaries (i.e., $j = 1$ and $j = j_{max}$) the structure is given as follows.

For

$$j = j_{max}; \quad \begin{bmatrix} U = 0 \\ V = 0 \text{ (or specified)} \\ \eta\text{-momentum eqn at } (j_{max} - 1 + 1/2) \end{bmatrix}$$

$$j = 1 \quad \begin{bmatrix} U = 0 \\ V = 0 \text{ (or specified)} \\ \eta\text{-momentum eqn at } (1 + 1/2) \end{bmatrix}$$

The arrangement of the equations and the boundary conditions is shown in Fig. 7.

For periodic boundaries, the surface normal velocities cannot be specified. The total number of discrete equations remains $3j_{max} - 4$. However, the number of unknowns is now

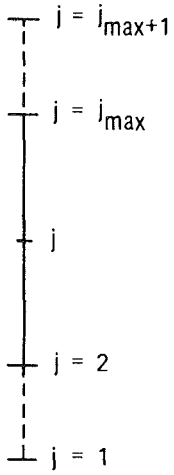

Fig. 8 Periodic boundaries for 2-D case

reduced (Fig. 8), since the values of the unknowns at $j=j_{max}$ are equal to those at $j=1$.

Therefore the total number of unknowns is now $(3j_{max}-3)$. This requires only one additional equation to close the system. This condition is obtained by applying the ξ-momentum equation at $j=j_{max}$. This relies on the fact that the location $j=j_{max}+1$ is equivalent to the location $j=2$. The resulting periodic block tridiagonal system can once again be solved using the standard LU decomposition (28).

This procedure can be directly extended to three-dimensional flows since the η and ζ momentum equations are discretized in exactly the same manner as for two-dimensional flows. The continuity equation is now dicretized at $(j-1/2, k-1/2)$ (Fig. 2). Along the lines $j_{max}-1$ and $k_{max}-1$, the arrangement of equations is as follows:

For $(j_{max}-1, k)$

$$\begin{bmatrix} \text{continuity at } (j_{max}-1/2,\ k-1/2) \\ \xi\text{-momentum at } (j_{max}-1,\ k) \\ \zeta\text{-momentum at } (j_{max}-1,\ k+1/2) \\ \text{continuity at } (j_{max}-1-1/2,\ k-1/2) \end{bmatrix}$$

with a similar form for $(j,\ k_{max}-1)$. For interior points, $2\le j\le j_{max}-1$, the arrangement is given as

$$\begin{bmatrix} \text{continuity at } (j-1/2,\ k-1/2) \\ \xi\text{-momentum at } (j,\ k) \\ \eta\text{-momentum at } (j+1//2,\ k) \\ \zeta\text{-momentum at } (j,\ k+1/2) \end{bmatrix}$$

The resulting block nine-diagonal matrix system is solved in the same manner with the MSIP scheme. The boundary conditions can be summarized as follows.

Inflow ($\xi=\xi_0$): At the inflow boundary, velocities are specified. A condition on the staggered pressure is required only for the compressible case ($\omega\neq 0$).

Outflow ($\xi=\xi_{max}$): At the outflow boundary, only one boundary condition on the staggered pressure is required. Either p or $\partial p/\partial\xi$ is specified.

Lower and left wall boundaries ($\eta=0$, and $\zeta=0$); No slip and zero injection are specified on the solid walls ($U=0$, $V=0$, and $W=0$). A boundary condition for pressure is not required. The normal momentum equations, at the corresponding boundaries, are applied to obtain the wall pressure (η-momentum equation at $\eta=0+\Delta\eta/2$ and ζ momentum equation at $\zeta=0+\Delta\zeta/2$).

Upper and right boundaries ($\eta=\eta_{max}$ and $\zeta=\zeta_{max}$): Once again zero injection and no slip are specified on the solid walls. A boundary condition for pressure is not required. The normal momentum equations are applied at the boundaries to obtain the surface pressure (η-momentum equation at $\eta=\eta_{max}-\Delta\eta/2$ and ζ-momentum equation at $\zeta=\zeta_{max}-\Delta\zeta/2$).

Solution Procedure. Starting from the inflow boundary and then at each marching location i, the block nine diagonal system shown in Fig. 3 is solved with the MSIP algorithm for $[U, V, W, p]^T$. The density and temperature for compressible flows are updated after the local iteration for the quasilinearized (U, V, W, p) have converged at each marching location i. The density and temperature are evaluated using the state and energy equations. The relaxation (marching) procedure proceeds to the downstream boundary. The terms with superscript $(n-1)$ are then updated from the previous marching sweep or global iteration. The relaxation process from the inflow to the outflow boundaries is repeated until the maximum change in the pressure field for two consecutive global iterations is less than a prescribed tolerance, e.g., 10^{-5}.

Stability

As discussed in reference [19], a detailed stability analysis of the relaxation procedure for two-dimensional incompressible flow is presented in reference [16] and a similar analysis for compressible flow is given in reference [29]. The analysis shows that the relaxation procedure for the pressure field is unconditionally stable. Since relaxation of the pressure field in the marching direction is the same for three- and two-dimensional flows, a similar conclusion can be inferred for three-dimensional flows. For the cross-plane inversion, the MSIP procedure has been shown to be unconditionally stable in reference [27]. Therefore, the overall solution procedure is postulated as unconditionally stable. No stability limitations were encountered in the present calculations.

Results

The three-dimensional flows considered in this study were chosen primarily to validate the scheme and to compare the results with available experimental data and numerical solutions obtained by other schemes. First, a simple case of laminar developing flow in a straight duct of square cross section was considered. As noted previously, the Reynolds number Re is based on the uniform inlet velocity and the hydraulic diameter H of the cross section. The velocities and lengths are nondimensionalized with respect to the inlet velocity and the hydraulic diameter respectively. The number of grid points used in the streamwise direction is 51 and in the cross plane 11 by 11. The results obtained for incompressible flow were compared with the numerical solution of Rubin and Khosla (reference [30]), obtained using a boundary layer/potential core analysis, and with the experimental data of Goldstein and Kreid (Reference [31]) (see Figs. 9 and 10). The comparison shows very good agreement of the RNS results with both the earlier numerical results and the experimental data. Next, a slightly more severe case of developing flow in circular arc (curved) duct of square cross section was considered (Fig. 11). As in the case of the straight duct, the Reynolds number is based on the uniform inlet velocity and the hydraulic diameter of the cross section. The Dean number, which is defined as $\mathrm{Re}/\sqrt{R/H}$ is 55, and Reynolds number is 205. Once again, only the incompressible flow solution was obtained, as the data for this case was readily available. The number of streamwise stations was 101, with a grid size of 15 by 15 in the cross plane. The development of the streamwise velocity profiles in the radial plane and in the trnasverse plane, from the entrance to the fully developed region, is shown in Figs. 12 and 13. The fully developed streamwise velocity profile in the radial plane was compared with the numerical solutions obtained by Kreskovsky et al. [32], who assumed a parabolic secondary flow correction to

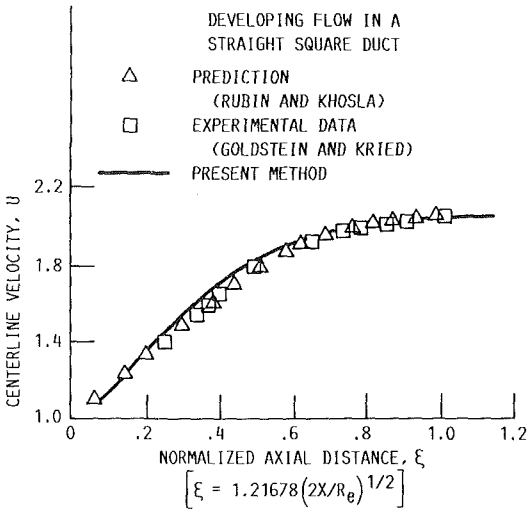

Fig. 9 Centerline velocity variation

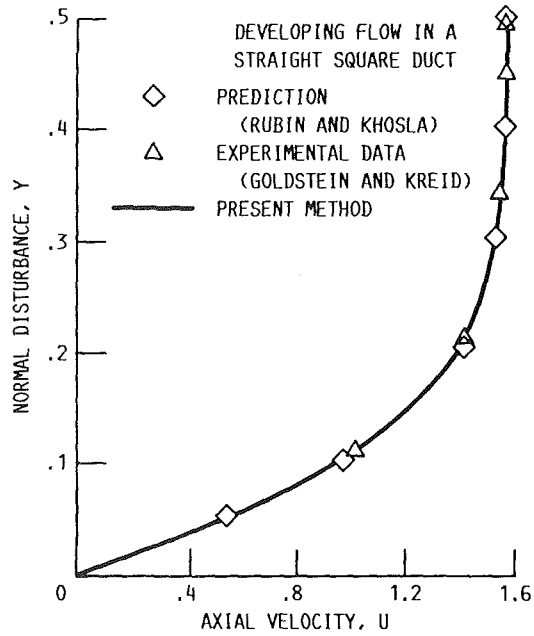

Fig. 10 Axial velocity profile at $\xi = 0.295$, $Z = 0$

the primary flow, and with the solutions of Ghia and Sokhey [9], who used a parabolic method and with the experimental data of Mori et al. [33]. The comparison, as seen in Fig. 14, shows good agreement with the numerical results. The experimental data differ from all of the numerical solutions. This disagreement of the experimental results can be attributed to possible inaccuracies in the measurements. Figure 15 shows the comparison of the fully developed secondary velocity profile in the transverse plane with those predicted by Kreskovsky et al. [32] and Ghia and Sokhey [9]. The agreement of the RNS solution with the other numerical solutions is very good. A vector plot of the fully developed secondary velocity in the cross section is given in Fig. 16. This clearly depicts the plane of symmetry and the location of the vortices that appear away from the axis and toward the outer wall due to the effects of the centrifugal force. Compressible low Mach number solutions were also obtained but are not presented here. It should be pointed out here that, the procedure of applying the boundary conditions developed in this study is aimed at improving the efficiency of the solution procedure. This procedure completely eliminated the need for any iteration procedure to satisfy global mass conservation, thereby

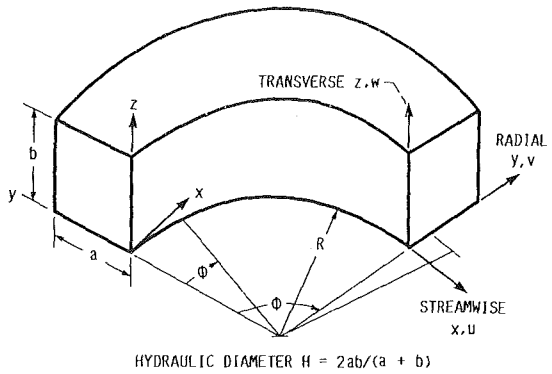

Fig. 11 Curved duct geometry and coordinate system

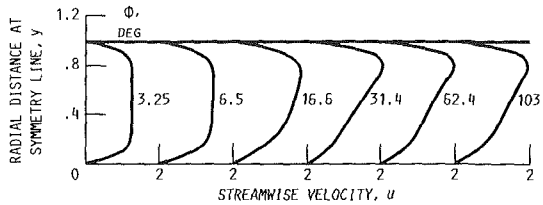

Fig. 12 Development of primary velocity profile for a circular arc duct of square cross section, Re = 205, $R/H = 14$, $K = 55$

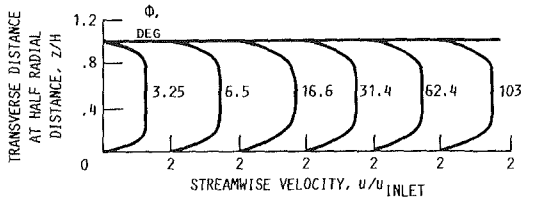

Fig. 13 Development of primary velocity profile in the transverse plane for a circular arc duct of square cross section, Re = 205, $R/H = 14$, $K = 55$

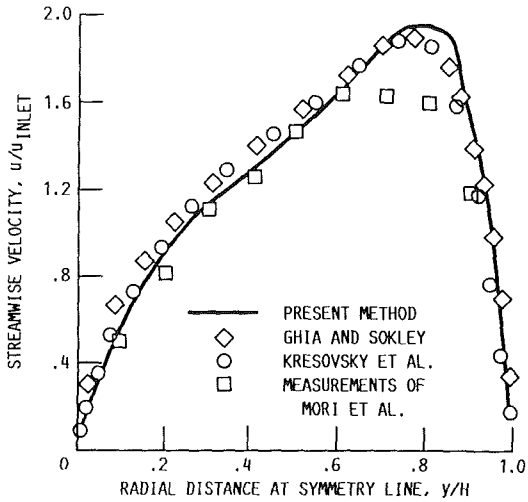

Fig. 14 Fully developed primary flow velocity profile for a circular arc duct of square cross section, $R/H = 14$, Re = 205, $K = 55$

reducing the computation time at each crossplane by a factor of three compared to that of reference [19]. The accuracy of the solution is in no way affected by the method of application of boundary conditions, since the boundary conditions in both cases were essentially the same, after the mass conservation was satisfied in the case of reference [19], at each marching plane.

Summary

A consistent procedure has been developed for the applica-

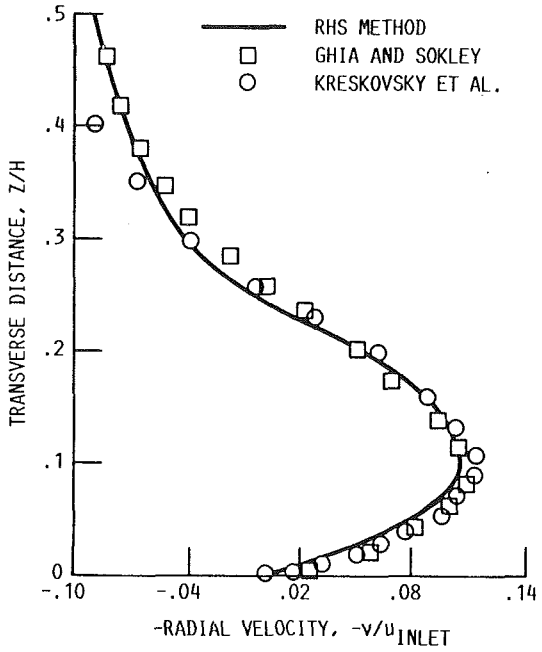

Fig. 15 Fully developed radial velocity profile at $y/H = 0.4$ for a circular arc duct of square cross section, $R/H = 14$, Re = 205, $K = 55$

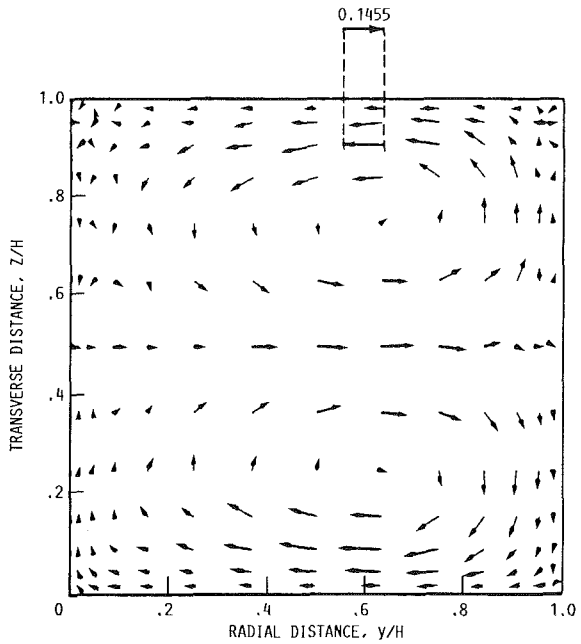

Fig. 16 Fully developed secondary flow velocity in a circular arc duct, Re = 205, $R/H = 14$, $K = 55$

tion of zero injection and pressure boundary conditions for the RNS algorithm. The matrix structure of the discretized equations has been reordered near the boundaries so the physically meaningful conditions can be applied on the boundaries in a direct manner. Global and local mass conservation is satisfied automatically without the necessity of iteration or a Poisson pressure equation. The modified strongly implicit procedure (MSIP) is used to invert the nine diagonal matrix resulting from the coupled system of equations for velocities and pressure in the cross plane. The procedure has been validated for two example cases, developing flow in straight and curved ducts of square cross section. The solutions are in good agreement with other computed results and experimental data. The scheme will be applied to more complex geometries of practical interest and to compressible flows in future studies.

Acknowledgment

This work was supported under contract No. NAS3-24105 at NASA Lewis Research Center with Dr. Peter Sockol as the project manager.

References

1 Hah, C., "A Navier-Stokes Analysis of Three-Dimensional Turbulent Flows Inside Turbine Blade Rows at Design and Off-Design Conditions," ASME *Journal of Engineering for Gas Turbines and Power*, Vol. 106, No. 2, Apr. 1984, pp. 421–429.

2 Dawes, W. N., "A Numerical Analysis of the Three-Dimensional Viscous Flow in a Transonic Compressor Rotor and Comparison with Experiment," ASME Paper 86-GT-16, June 1986.

3 Davis, R. T., and Werle, M. J., "Progress on Interacting Boundary Layer Computations at High Reynolds Number," *Numerical and Physical Aspects of Aerodynamic Flows*, T. Cebeci, Ed., Springer-Verlag, New York, 1982, pp. 187–210.

4 Vatsa, V. N., Werle, M. J., and Verdon, J. M., "Analysis of Laminar and Turbulent Symmetric Blunt Trailing-Edge Flows," United Technologies Research Center, East Hartford, CT, UTRC-R81-914986-5, Apr. 1981. (Avail. NTIS, AD-A098703).

5 Carter, J. E., and Wornom, S. F., "Solutions for Incompressible Separated Boundary Layers Including Viscous-Inviscid Interaction," Aerodynamic Analyses Requiring Advance Computers, Part 1, NASA SP-347, 1975, pp. 125–150.

6 Kim, J., Kline, S. J., and Johnston, J. P., "Investigation of Separation and Reattachment of a Turbulent Shear Layer: Flow Over a Backward-Facing Step, "Thermosciences Division, Mechanical Engineering Department, Stanford University, Report MD-37, 1978.

7 Kwon, O. K., and Pletcher, R. H., "Application of a Viscous-Inviscid Interaction Procedure to Predict Turbulent Separating Flows Over a Rearward-Facing Step," *Computation of Internal Flows: Methods and Applications*, P. M. School and K. N. Ghia, Eds., ASME, New York, 1984, pp. 73–81.

8 Pouagare, M., and Lakshiminarayana, B., "Computation of Viscous Flows in Turbomachinery Cascades With a Space-Marching Method," *Journal of Propulsion and Power*, Vol. 2, No. 3, May-June 1986, pp. 266–274.

9 Ghia, K. N., and Sokhey, J. S., "Laminary Incompressible Viscous Flow in Curved Ducts of Rectangular Cross Sections," ASME JOURNAL OF FLUIDS ENGINEERING, Vol. 99, No. 4, Dec. 1977, pp. 640–648.

10 Khalil, I. M., and Weber, W. G., "Modeling of Three-Dimensional Flow in Turning Channels," ASME *Journal of Engineering for Gas Turbines and Power*, Vol. 106, No. 3, July 1984, pp. 682–691.

11 Rhie, C. M., "Basic Calibration of a Partially-Parabolic Procedure Aimed at Centrifugal Impeller Analysis," AIAA Paper 83-0260, Jan. 1983.

12 Rubin, S. G., and Lin, A., "Marching With the Parabolized Navier-Stokes Equations," *Israel Journal of Technology*, Vol. 18, No. 1-2, 1980, pp. 21–31.

13 Rubin, S. G., "A Review of Marching Procedures for Parabolized Navier-Stokes Equations," *Numerical and Physical Aspects of Aerodynamic Flows*, T. Cebeci, Ed., Springer-Verlag, New York, 1982, pp. 171–186.

14 Rubin, S. G., and Reddy, D. R., "Global Solution Procedures for Incompressible Laminar Flow With Strong Pressure Interaction and Separation," *Numerical and Physical Aspects of Aerodynamic Flows II*, T. Cebeci, Ed., Springer-Verlag, New York, 1983, pp. 79–96.

15 Rubin, S. G., and Reddy, D. R., "Analysis of Global Pressure Relaxation for Flows With Strong Interaction and Separation," *Computers and Fluids*, Vol. 11, No. 4, 1983, pp. 281–306.

16 Reddy, D. R., "Global Pressure Relaxation Procedure for Laminar and Turbulent Incompressible Flows With Strong Interaction and Separation," Ph.D. Dissertation, University of Cincinnati, 1983.

17 Rubin, S. B., and Reddy, D. R., "Global PNS Solutions for Laminar and Turbulent Flow," AIAA Paper 83-1911, July 1983.

18 Reddy, D. R., and Rubin, S. G., "Subsonic/Transonic, Viscous/Inviscid Relaxation Procedures for Strong Pressure Interactions," AIAA Paper 84-1627, June 1984.

19 Reddy, D. R., Delaney, R. A., and Rubin, S. G., "Reduced Navier-Stokes (RNS) Relaxation Procedure for Internal Flows With Interaction," SAE Paper 851790, Oct. 1985.

20 Rudman, S., and Rubin, S. G., "Hypersonic Flow Over Slender Bodies With Sharp Leading Edges," *AIAA Journal*, Vol. 6, No. 10, Oct. 1968, pp. 1883–1890.

21 Lin, T. C., and Rubin, S. G., "Viscous Flow Over a Cone at Moderate Incidence, I. Hypersonic Tip," *Computers and Fluids*, Vol. 1, No. 1, Jan. 1973, pp. 37–57.

22 Davis, R. T., and Rubin, S. G., "Non-Navier-Stokes Viscous Flow Computations," *Computers and Fluids*, Vol. 8, No. 1, Mar. 1980, pp. 101–131.

23 Lin, A., and Rubin, S. G., "Three-Dimensional Supersonic Viscous Flow Over a Cone at Incidence," *AIAA Journal*, Vol. 20, No. 11, Nov. 1982, pp. 1500–1507.

24 Lubard, S., and Helliwell, W., "An Implicit Method For Three-Dimensional Viscous Flow With Application to Cones at Angle of Attack," *Computers and Fluids*, Vol. 3, No. 1, Mar. 1975, pp. 83–101.

25 Vigneron, Y., Tannehill, J. C., and Rakich, J. V., "Calculation of Super-

sonic Viscous Flow Over Delta Wings With Sharp Subsonic Leading Edges," AIAA Paper 78-1137, July 1978. (NASA TM-78500).

26 Katsanis, T., "Calculation of Three-Dimensional Viscous Flow Through Turbomachinery Blade Passages by Parabolic Marching," AIAA Paper 85-1408, July 1985. (NASA TM-86984).

27 Schneider, G. E., and Zedan, M., "A Modified Strongly Implicit Procedure for the Numerical Solution of Field Problems," *Numerical Heat Transfer*, Vol. 4, No. 1, Jan.-Mar. 1981, pp. 1-19.

28 Anderson, D. A., Tannehill, J. C., and Pletcher, R. H., *Computational Fluid Mechanics and Heat Transfer*, Hemisphere Publishing Corporation, Washington, D.C., 1984, pp. 551-557.

29 Ramakrishnan, S. V., and Rubin, S. G., "Global Pressure Relaxation for Steady, Compressible, Laminar, 2-Dimensional Flows With Full Pressure Coupling and Shock Waves," University of Cincinnati Report No. AFL-84-100, July 1984.

30 Rubin, S. G., Khosla, P. K., and Saari, S., "Laminar Flow in Rectangular Channels," *Computers and Fluids*, Vol. 5, No. 3, Sept. 1977, pp. 151-173.

31 Goldstein, R. J., and Kreid, D. K., "Measurement of Laminar Flow Development in a Square Duct Using Laser-Doppler Flowmeter," ASME JOURNAL OF APPLIED MECHANICS, Vol. 34, No. 4, Dec. 1967, pp. 813-818.

32 Kreskovsky, J. P., Briley, W. R., and McDonald, H., "Prediction of Laminary and Turbulent Primary and Secondary Flows in Strongly Curved Ducts," NASA CR-3388, 1981.

33 Mori, Y., Uchida, Y., and Ukon, T., "Forced Convective Heat Transfer in a Curved Channel With a Square Cross Section," *International Journal Heat and Mass Transfer*, Vol. 14, No. 11, Nov. 1971, pp. 1787-1805.

APPENDIX A

Transformation

$$\xi = \xi(x,y,z)$$
$$\eta = \eta(x,y,z)$$
$$\zeta = \zeta(x,y,z)$$

The Jacobian J is given by:

$$J = \frac{1}{x_\xi y_\eta z_\zeta + x_\zeta y_\xi z_\eta + x_\eta y_\zeta z_\xi - x_\xi y_\zeta z_\eta - x_y y_\xi z_\zeta - x_\zeta y_\eta z_\xi}$$

The contravariant components U, V, and W, written without metric renormalization (i.e., without dividing the expression for U by $\sqrt{\xi_x^2+\xi_y^2+\xi_z^2}$ and so on) are given by

$$U = \xi_x u + \xi_y v + \xi_z w$$
$$V = \eta_x u + \eta_y v + \eta_z w$$
$$W = \zeta_x u + \zeta_y v + \zeta_z w$$

where u, v, and w are the Cartesian velocity components in x, y, and z directions respectively. The shear stress terms appearing in the momentum equations are given as follows

$$\tau_x{}^\xi = \xi_x\tau_{xx} + \xi_y\tau_{xy} + \xi_z\tau_{xz}$$
$$\tau_y{}^\xi = \xi_x\tau_{xy} + \xi_y\tau_{yy} + \xi_z\tau_{zz}$$
$$\tau_z{}^\xi = \xi_x\tau_{xz} + \xi_y\tau_{yz} + \xi_z\tau_{xz}$$
$$\tau_x{}^\eta = \eta_x\tau_{xx} + \eta_y\tau_{yx} + \eta_z\tau_{xz}$$
$$\tau_y{}^\eta = \eta_x\tau_{xy} + \eta_y\tau_{yy} + \eta_z\tau_{yz}$$
$$\tau_z{}^\eta = \eta_x\tau_{xz} + \eta_y\tau_{yz} + \eta_z\tau_{zz}$$
$$\tau_x{}^\zeta = \zeta_x\tau_{xx} + \zeta_y\tau_{yx} + \zeta_z\tau_{zx}$$
$$\tau_y{}^\zeta = \zeta_x\tau_{xy} + \zeta_y\tau_{yy} + \zeta_z\tau_{zy}$$
$$\tau_z{}^\zeta = \zeta_x\tau_{xz} + \zeta_y\tau_{yz} + \zeta_z\tau_{zz}$$

where τ_{xx}, τ_{xy}, etc. are the regular Cartesian shear stress components. The Cartesian derivatives are expanded in ξ, η, and ζ space via chain rule relations such as $u_x = \xi_x u_\xi + \eta_x u_\eta + \zeta_x u_\zeta$. The Cartesian velocity components are in turn expressed in terms of the contravariant velocity components defined earlier by the following

$$u = x_\xi U + x_\eta V + x_\zeta W$$
$$v = y_\xi U + y_\eta V + y_\zeta W$$
$$w = z_\xi U + z_\eta V + z_\zeta W$$

Finally, the terms $G_{\xi\zeta}$, $g^{\xi\zeta}$, etc. appearing in the K are given as

$$G_{\xi\rho} = U((\xi_x)_\xi u + (\xi_y)_\xi v + (\xi_z)_\xi w) + V((\xi_x)_\eta u + (\xi_y)_\eta v + (\xi_z)_\eta w) + W((\xi_x)_\zeta u + (\xi_y)_\zeta v + (\xi_z)_\zeta w)$$
$$G_{\eta\rho} = U((\eta_x)_\xi u + (\eta_y)_\xi v + (\eta_z)_\xi w) = V((\eta_x)_\eta u + (\eta_y)_\eta v = (\eta_z)_\eta w) = W((\eta_x)_\zeta u + (\eta_y)_\zeta v + (\eta_z)_\zeta w)$$
$$G_{\zeta\rho} = U((\zeta_x)_\xi u + (\zeta_y)_\xi v + (\zeta_z)_\xi w) + V((\zeta_x)_\eta u + (\zeta_y)_\eta v + (\zeta_z)_\eta w) + W((\zeta_x)_\zeta u + (\zeta_y)_\zeta v + (\zeta_z)_\zeta w)$$
$$g^{\xi\xi} = \xi_x^2 + \xi_y^2 + \xi_z^2$$
$$g^{\xi\eta} = \xi_x\eta_x + \xi_y\eta_y + \xi_z\eta_z$$
$$g^{\xi\zeta} = \xi_x\zeta_x + \xi_y\zeta_y + \xi_z\zeta_z$$
$$g^{\eta\epsilon} = \xi_x\eta_x + \xi_y\eta_y + \xi_z\eta_z$$
$$g^{\eta\eta} = \eta_x^2 + \eta_y^2 + \eta_z^2$$
$$g^{\eta\zeta} = \eta_x\zeta_x + \eta_y\zeta_y + \eta_z\zeta_z$$
$$g^{\zeta\xi} = \zeta_x\xi_x + \zeta_y\xi_y + \zeta_z\xi_z$$
$$g^{\zeta\eta} = \zeta_x\eta_x + \zeta_y\eta_y + \zeta_z\eta_z$$
$$g^{\zeta\zeta} = \zeta_x\zeta_x + \zeta_y\zeta_y + \zeta_z\zeta_z$$

The Role of Eigensolutions in Nonlinear Inverse Cavity-Flow Theory

B. R. Parkin
Applied Research Laboratory,
The Pennsylvania State University,
State College, PA 16804

The method of Levi Civita is applied to an isolated fully cavitating body at zero cavitation number and adapted to the solution of the inverse problem in which one prescribes the pressure distribution on the wetted surface and then calculates the shape. The novel feature of this work is the finding that the exact theory admits the existence of a "point drag" function or eigensolution. While this fact is of no particular importance in the classical direct problem, we already know from the linearized theory that the eigensolution plays an important role. In the present discussion, the basic properties of the exact "point-drag" solution are explored under the simplest of conditions. In this way, complications which arise from non-zero cavitation numbers, free surface effects, or cascade interactions are avoided. The effects of this simple eigensolution on hydrodynamic forces and cavity shape are discussed. Finally, we give a tentative example of how this eigensolution might be used in the design process.

Introduction

The present paper bears upon the two-dimensional inverse or design problem for fully cavitating hydrofoils in which one specifies the pressure distribution on the profile wetted surface and then calculates that wetted surface shape which will satisfy this prescription. This design problem is certainly not new to airfoil designers and as far as cavity flows are concerned, both linear and nonlinear design methods have been worked out. In the realm of nonlinear approaches to the present problem, the very general method of Yim and Higgins [1] is worthy of note because it applies to single foils as well as to cascades of profiles for all cavitation numbers in the cavity-flow regime. Another approach has been discussed superficially by Khrabov [2]. Both of these contain far more generality than is required for this study at zero cavitation number. For the direct or off-design problems of exact cavity-flow theory, a good example of the present level of development is represented by the work of Furuya [3] and it is clear that now one can do both the design and off-design problems for fully cavitating hydrofoils. Thus, one can attempt to tailor the profile to an entire set of performance goals and failing that he can at least design for the best compromise among a set of conflicting requirements.

According to many authors [4–7], the inverse problem is not thought to present much of a challenge at zero cavitation number. In this case, the classical method of Levi Civita [7] can be applied to an isolated body. This view is certainly proper as long as one is content, after prescribing the pressure in the circle plane, to accept whatever correlation between points in the circle and physical planes may result. Of course, such a rudimentary approach does not lead to a useful design procedure.

The motivation for the present investigation is that none of the literature on the nonlinearized direct and inverse problems we have surveyed so far [1–8] has made use of the fact the exact theory admits the existence of a "point drag" or complementary function. While this fact is of no particular importance in the direct problem, we have already seen in the case of the linearized inverse problems [9–11] that the complementary function can play an important role. For the exact inverse theory there has been a question regarding the existence of a nonlinear eigensolution and if it does exist, should it be an admissible component of the solution [1]? Therefore, in this study, we explore these questions regarding the existence and usefulness of a "point drag" or eigensolution in the nonlinear theory under the *simplest* set of circumstances and this leads us naturally to the restrictions that the free streamline flow pertains to an isolated profile and that the flow be at zero cavitation number. These simplifications free us from the complications arising from non-zero cavitation numbers and other boundaries in the flow domain such as free surface or neighboring cascade blades.

In this paper we use the term eigensolution in the sense of thin airfoil theory as suggested by the work of Van Dyke[1]

Contributed by the Fluids Engineering Division and presented at the International Symposium on Cavitation and Propeller, Wuxi, Peoples Republic of China, 1986. Manuscript received by the Fluids Engineering Division October 26, 1986.

[1] *Perturbation Methods in Fluid Mechanics*, The Parabolic Press, Stanford, CA, 1975, pp. 48–54.

because we already know the inverse problem in the theory of fully cavitating hydrofoils is not necessarily unique. Our aim is to find a sufficiently weak singularity which can be added to the classical Levi Civita solution and can then be used to satisfy certain additional physical conditions relating to the location of the free streamline springing from the hydrofoil nose and thereby provide a unique inverse cavity-flow solution. After we have constructed the simple eigensolution, we will examine some of its properties. The actual use of this solution in the design process will be presented elsewhere, although we will start the process so that the potential usefulness of the eigensolution in design can be seen.

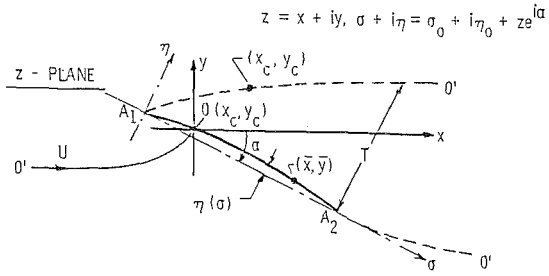

Fig. 1 Profile and cavity geometry in the physical or z-plane at zero cavitation number

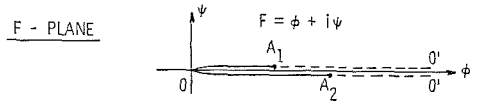

Fig. 2 Profile and cavity surfaces at zero cavitation number in the plane of the complex potential, $F = \phi + i\psi$

Flow Geometry and Conformal Mappings

The flow geometry and the principal quantities associated with the flow are illustrated in Fig. 1. The origin of coordinates in the $z = x + iy$ plane is taken at the stagnation point on the wetted surface of the hydrofoil. This point is denoted by O in Fig. 1. The chordline of the profile is inclined at the angle α with respect to the x axis and the free-stream velocity U is taken as being parallel to this axis as illustrated. The flow separation point at or near the profile nose is the point A_1 as illustrated for a sharp-nosed foil. The "upper" cavity surface is shown as the dashed curve extending from A_1 to the point O' at downstream infinity. In the case of a round-nose profile, A_1 can lie on the upper wetted surface behind the leading edge. This case is not illustrated in Fig. 1. The point A_2 denotes the location of the trailing edge of the wetted surface. The lower surface of the cavity leaves the wetted surface at A_2 and extends as shown by the dashed line to the point O' at downstream infinity.

Let the coordinates of a typical point on the wetted surface be denoted by $\bar{x}$ and $\bar{y}$ and those on the upper cavity by x_c and y_c as shown in Fig. 1. While the orientation of the profile in the z plane is convenient for purposes of analysis, the $x-y$ system is not always a convenient reference frame for foil and cavity contours. For this purpose we use a coordinate system with the abscissa along the chordline as shown by the distance σ measured from the profile nose. The ordinates of the wetted surface are then given in terms of σ as $\eta(\sigma)$ and the upper cavity ordinates are given by $\eta_c(\sigma)$. At the trailing edge of the profile, the cavity thickness is $\eta_c = T$. These quantities are also shown in Fig. 1. In the σ, η system the stagnation point O is located at (σ_o, η_o) as illustrated. The transformation between the (x, y) and (σ, η) systems is

$$\sigma + i\eta = \sigma_o + i\eta_o + ze^{i\alpha}, \tag{1}$$

where z is the complex variable, $z = x + iy$, and α is the angle of attack as measured by the inclination of the chordline with respect to the x axis and free-stream velocity U.

The conformal mappings start with the complex potential in the z plane,

$$F = \phi + i\psi, \tag{2}$$

where ϕ is the velocity potential and ψ is the stream function. As is customary, we adjust these quantities to make $\phi = 0$ at the stagnation point, O. The stream function is taken to be zero all along the stagnation streamline. Therefore, the boundaries of the flow can be represented by a cut all along the real axis in the F-plane as shown in Fig. 2. Note that the wetted surface extends from the stagnation point at O to the trailing edge at A_2 and the lower cavity surface from A_2 to O' must line along the lower surface of the cut. This is so because downstream from the stagnation point, the velocity potential increases in the flow direction and the stream function decreases outwardly from the foil or cavity surface. On the arc OA_1, the flow direction is reversed with a consequent reversal in the gradients of ϕ and ψ so that the point A_1 is on the upper edge of the cut.

The mapping which takes the F-plane into the arc and interior of the upper semi-circle in the ζ plane is

$$F = b^2\left[\cos\gamma - \frac{1}{2}\left(\zeta + \frac{1}{\zeta}\right)\right]^2. \tag{3}$$

Nomenclature

A_1 = cavity detachment point near or at profile nose
A_2 = cavity detachment point at profile trailing edge
$a = \dfrac{(\sqrt{\phi_1} - \sqrt{\phi_2})}{2}$ = see related nomenclature below
$b = \dfrac{(\sqrt{\phi_2} + \sqrt{\phi_2})}{2}$ = see related nomenclature below
C = location of eigensolution singularity on unit circle
C_D = drag coefficient
C_L = lift coefficient
$C_p(\beta)$ = pressure coefficient on wetted surface
c = profile chord length, $c = 1$
ds = element of arc length in z-plane
E = strength of eigensolution
$F = \phi + i\psi$ = complex potential in complex F-plane
ϕ = velocity profile
ψ = stream function
O = stagnation point location
O' = point at infinity
T = cavity thickness at trailing edge
U = free-stream velocity
$w = u - iv = \dfrac{dF}{dz}$ = complex velocity
Z = intermediate mapping complex plane

Corresponding points, between the F and ζ planes are indicated in Figs. 2 and 3 except for the point C which is discussed later.

Then we introduce the complex velocity,

$$w = u - iv = \frac{dF}{dz}, \tag{4}$$

in order to write

$$wdz = dF = b^2\left[\frac{1}{2}\left(\zeta+\frac{1}{\zeta}\right)-\cos\gamma\right]\left(\zeta-\frac{1}{\zeta}\right)\frac{d\zeta}{\zeta}. \tag{5}$$

These quantities are now used to define the logarithmic hodograph or ω-plane:

$$e^{-i\omega(\zeta)} = \frac{1}{U}\frac{dF}{dz} = \frac{w}{U} = \frac{q}{U}e^{-i\theta} = \exp\left[\ln\frac{q}{U} - i\theta\right]. \tag{6}$$

Therefore we have

$$\omega(\zeta) = \theta + i\ln\frac{q}{U} = \theta + i\tau, \tag{7}$$

where $\tau = \ln q/U$. On the free streamlines $q = U$ so that $\tau = 0$ there. In the ζ-plane, these free streamlines are on the real axis. At O' we know that $\theta = 0$ also.
Therefore,

$$\omega(0) = 0 \tag{8}$$

and $\omega(\zeta)$ is real when ζ is real. At the stagnation point, O, $q \to 0$ so that $\tau \to -\infty$ there. The flow directions differ by π on either side of O and so the ω-plane with the various corresponding boundaries can be represented as illustrated schematically in Fig. 4.

From equations (5), (6), and (7) we write

$$dz = dx + idy = \frac{b^2 e^{-\tau+i\theta}}{U}\left[\frac{1}{2}\left(\zeta+\frac{1}{\zeta}\right)-\cos\gamma\right] \times\left(\zeta-\frac{1}{\zeta}\right)\frac{d\zeta}{\zeta}. \tag{9}$$

On the wetted surface $\zeta = e^{i\beta}$ and equation (9) leads to

$$\left.\begin{aligned} d\bar{x} &= \frac{2b^2}{U}e^{-\tau}[\cos\gamma-\cos\beta]\sin\beta\cos\theta d\beta \\ \text{and}\quad d\bar{y} &= \frac{2b^2}{U}e^{-\tau}[\cos\gamma-\cos\beta]\sin\beta\cos\theta d\beta \end{aligned}\right\} \tag{10}$$

Note that $d\bar{y}/d\bar{x} = \tan\theta$ as it should if the wetted surface is to be a streamline. On the upper surface of the cavity $\tau = 0$ and

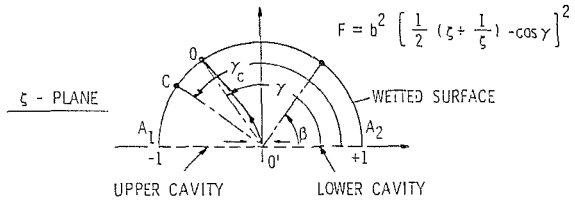

Fig. 3 The transformation shown here maps the flow from the upper half of the Z-plane into the interior of the upper unit semi-circle with the point at infinity at the origin

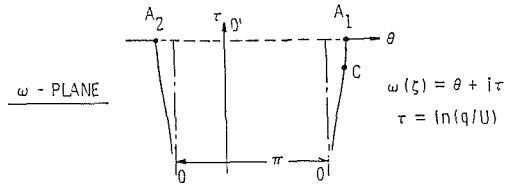

Fig. 4 Schematic diagram of the complex logarithmic hodograph in the ω-plane

arg $\zeta = \pi$ so that equation (9) leads to

$$\left.\begin{aligned} dx_c &= \frac{b^2}{U}\cos\theta\left[\frac{1}{2}\left(\zeta+\frac{1}{\zeta}\right)-\cos\gamma\right]\left(\zeta-\frac{1}{\zeta}\right)\frac{d\zeta}{\zeta} \\ dy_c &= \frac{b^2}{U}\sin\theta\left[\frac{1}{2}\left(\zeta+\frac{1}{\zeta}\right)-\cos\gamma\right]\left(\zeta-\frac{1}{\zeta}\right)\frac{d\zeta}{\zeta} \end{aligned}\right\} \tag{11}$$

provided that $-1 \le \xi \le 0$. At this point in the development ξ is the radial distance on the real axis in the ζ plane.

Returning to equation (9), we can write the square of the arc length along the wetted surface as

$$(ds)^2 = dzd\bar{z} = \left\{2\frac{b^2}{U}e^{-\tau}[\cos\gamma-\cos\beta]\sin\beta d\beta\right\}^2,$$

where we have also made use of equation (10) because it applies to the wetted surface. But from equation (7), we also have

$$\tau = \ln\frac{q}{U} = \ln\sqrt{1-C_p}, \tag{12}$$

so that

$$ds = 2\frac{b^2}{U}[(\cos\gamma-\cos\beta)\sin\beta/\sqrt{1-C_p(\beta)}]d\beta \tag{13}$$

Nomenclature (cont.)

$z = x + iy$ = complex variable in the physical (x, y) plane
α = angle of attack measured from negative real axis
δ = angular location of stagnation point measured from negative real axis
ζ = complex variable in circle plane, $\zeta = e^{i\beta}$
η = normal distance from profile chord
ξ = complex semi-circle plane, $\xi = \pi - \beta$
σ = distance along profile chord
γ = stagnation point angular location on unit circle in ζ plane ($\cos\gamma = a/b$)
γ_c = angular location of eigensolution singularity on unit circle
ϕ_1 = value of ϕ at A_1
ϕ_2 = value of ϕ at A_2
$\omega(\zeta) = \theta + i\ln\frac{q}{U} = \theta + i\tau$ = complex logarithmic hodograph
θ = flow inclination
q = flow speed

Subscripts

c = pertains to eigensolution ω_c or to the cavity surface
o = pertains to flat plate solution ω_o and other variables specifically associated with the geometric point O
0 = used on any variable having zero as its argument or limit
1 = pertains to regular part of solution ω_1

on the wetted surface. As we have noted previously, the flow directions differ by π on either side of 0. Therefore, if the sign of dz is positive on the arc OA_2, it will be negative along arc OA_1. As a result of this difference ds might have a like sign change in these two regions. Just how this might occur depends on the form of $\sqrt{1-C_p(\beta)}$ in any particular case. We will defer consideration of this question to a later place in the development.

Hydrodynamic Forces

The development of general formulae for the hydrodynamic forces on the profile depend upon certain properties of the function $\omega(\zeta)$ which result from the previously noted fact that $\omega(\zeta)$ is real when ζ is real. For then one can apply Schwartz's principle of symmetry [7] in order to write $\omega(\bar{\zeta}) = \overline{\omega(\zeta)}$ and thereby obtain the analytic continuation of $\omega(\zeta)$ into the lower half of the unit circle [6]. Thus we can write for a prescribed modulus, $|\zeta| \leq 1$, inside or on the unit circle,

$$\theta(\beta) - i\tau(\beta) = \theta(-\beta) + i\tau(-\beta),$$

or

$$\left.\begin{aligned} \tau(-\beta) &= -\tau(\beta) \\ \theta(-\beta) &= \theta(\beta) \end{aligned}\right\}. \quad \text{and} \tag{14}$$

Hence τ is an odd function of β, or Im ζ, and θ is an even function of β, or Im ζ.

Using equation (12) and the fact that $\omega(\zeta)$ is now defined inside and on the entire unit circle, one finds [7] from the calculus of residues that

$$C_L = \frac{\pi}{2}\frac{b^2}{U_c}[4\omega'(0)\cos\gamma - \omega''(0)] \tag{15}$$

and

$$C_D = \frac{\pi}{2}\frac{b^2}{U_c}[\omega'(0)]^2, \tag{16}$$

where the profile chord, c, will be taken as unity in this work. The moment can be calculated after the complete solution has been found.

The Form of $\omega(\zeta)$ Near the Stagnation Point

This is also a well known result which we shall review briefly because of later need. The form of ω near O is dominated by the fact that on a smooth contour ω jumps by the amount π. In particular, as one traces the profile surface, starting at A_1 in Fig. 1 and then passes through O while proceeding to A_2, the jump is a decrease in θ. In the ζ plane this is precisely the behavior exhibited by the real part of the analytic function $i\ln(\zeta - e^{i\gamma})$. However, this function by itself does not have the symmetry specified by equation (14) for admissible forms of ω. But if we subtract from it a similar function which has a like jump at the image of O with respect to the real axis in the ζ-plane, we preserve the necessary behavior at O and also satisfy the preceding symmetry requirements. Aside from arbitrary additive constants, this function has the form

$$i\ln\frac{\zeta - e^{i\gamma}}{\zeta - e^{-i\gamma}}.$$

Finally, we require that $\omega(0) = 0$. Because of this condition the resulting function which provides the flat plate solution is [4]

$$\omega_o(\zeta) = \theta_o + i\tau_o = -\alpha + i\ln\frac{\zeta - e^{i\gamma}}{1 - \zeta e^{i\gamma}}, \tag{17}$$

with $\gamma = \pi - \alpha$ in the case of an isolated flat-plate profile. For this case, one can show that this function has the flow direction, $\theta_o = -\alpha$ behind the stagnation point or $\theta_o = \pi - \alpha$ ahead of the stagnation point on $\zeta = e^{i\beta}$. Therefore, the wetted surface in the z-plane is a straight line through O with its trailing edge inclined at the angle $-\alpha$ with respect to the positive real axis. Moreover, since τ_o vanishes on the real axis in the ζ-plane, the free streamlines have $C_p = 0$ as required. Thus we can write equation (17) as

$$\omega_o(\zeta) = \pi H(\beta - \gamma) - \alpha + i\ln\left|\frac{\zeta - e^{i\gamma}}{1 - \zeta e^{i\gamma}}\right|, \tag{18}$$

where

$$H(\beta - \gamma) = \begin{cases} 0, & \beta < \gamma \\ 1, & \beta \geq \gamma \end{cases}$$

is the Heaviside function.

The contribution of ω_o to C_L and C_D follows from equations (15) and (16). From equations (15), (16), and (18) we get

$$C_{Lo} = 2\pi\frac{b^2}{U_c}\sin\alpha\cos\alpha \tag{19}$$

$$C_{Do} = 2\pi\frac{b^2}{U_c}\sin^2\alpha \tag{20}$$

and we see that $L/D = \cot\alpha$ as is proper for the flat plate. We can also use the relationship $C_p = 1 - e^{2\tau}$ to find the pressure distribution on the plate. The result is

$$C_{po} = \frac{4\sin\beta\sin\gamma}{(\cos\beta - \cos\gamma)^2 + (\sin\beta + \sin\gamma)^2}. \tag{21}$$

From this result, we see that when $\beta = \gamma$, $C_{po} = 1$ and when $\beta = 0$ or π, $C_{po} = 0$ as required.

Continuing the study of the flat-plate solution, we can rewrite equation (17) for points on the wetted surface as

$$\omega_o = \pi - \alpha + \gamma + i\ln\left[\frac{e^{i\gamma} - e^{i\beta}}{e^{-i\gamma} - e^{i\beta}}\right],$$

in which case

$$e^{\tau_o} = \left|\frac{e^{i\gamma} - e^{i\beta}}{e^{-i\gamma} - e^{i\beta}}\right| = \sqrt{1 - C_{po}}.$$

After some manipulation involving equation (18) and the use of equation (11), we find that

$$\sqrt{1 - C_{po}} = \frac{2|\cos\beta - \cos\gamma|}{(\cos\gamma - \cos\beta)^2 + (\sin\gamma + \sin\beta)^2}.$$

Next we can introduce $d(\sigma + i\eta) = e^{i\alpha}dz$ from equation (1) and use equation (9) with the result that

$$d(\sigma + i\eta) = 2\frac{b^2}{U}[\sin\xi + \sin\alpha\sin^2\xi - \cos\alpha\cos\xi\sin\xi]d\xi.$$

This last result implies that $\eta = 0$ as is proper for a flat plate and that $d\sigma$ is simply the arc length ds along the wetted surface measured from the profile nose where $\sigma = 0$. We can integrate this last equation from $\sigma = 0 (\xi = 0)$ to some value, $0 \leq \sigma \leq 1$ ($0 \leq \xi \leq \pi$), and get

$$s = 2\frac{b^2}{U}\left[(1 - \cos\xi)\left(1 - \frac{\cos\alpha}{2}[1 + \cos\xi]\right) + (\xi - \sin^2\xi)\frac{\sin\alpha}{2}\right]. \tag{22}$$

The profile is to have unit chord, however, so that when $\xi = \pi$, $\sigma = s = 1$ and

$$\frac{b^2}{U} = \frac{1}{4 + \pi\sin\alpha}. \tag{23}$$

When equation (23) is used in equations (19) and (20), one obtains the well known Rayleigh formulas [12].

Additional properties of the flat-plate solution which are

important for the present considerations relate to the shape of the upper surface of the cavity. In Fig. 3, ξ will be on the negative real axis for points on this part of the cavity. Therefore, let us put $\zeta = -\zeta_c$ where ζ_c is a real positive number. Then we can use $d(\sigma+i\eta) = e^{i\alpha}dz$, and write equation (9) in the form

$$d(\sigma+i\eta) = \frac{b^2}{U}\exp i[\alpha+\theta_o(\zeta_c)]d\left\{\left[\frac{1}{2}\left(\zeta_c+\frac{1}{\zeta_c}\right)-\cos\alpha\right]^2\right\}.$$

But now

$$\exp i[\alpha+\theta_o] = e^{-i\alpha}\frac{(e^{i\alpha}-\zeta_c)}{(e^{-i\alpha}-\zeta_c)}$$

and so we have

$$d(\sigma+i\eta) = \frac{1}{2}\frac{b^2}{U}\left[\zeta_c e^{-i\alpha}-2+\frac{2i\sin\alpha}{\zeta_c}+\frac{2}{\zeta_c^2}-\frac{e^{i\alpha}}{\zeta_c^3}\right]d\zeta_c.$$

The integration in this case starts at A_1 where $\zeta_c = 1$ and $\sigma = \eta = 0$ and proceeds to some value of σ_c, η_c corresponding to $1 \geq \zeta \geq 0$. This leads to the parametric representation of $\eta_c(\sigma_c)$ in terms of ζ_c which is given by

$$\sigma_c = \frac{1}{2}\frac{b^2}{U}\frac{(1-\zeta_c)^2}{\zeta_c}\left[\frac{(1+\zeta_c)^2}{2\zeta_c}\cos\alpha-2\right] \tag{24}$$

and

$$\eta_c = \frac{1}{2}\frac{b^2}{U}\sin\alpha\left[\frac{1-\zeta_c^4}{2\zeta_c^2}+2\ln\zeta_c\right]. \tag{25}$$

Equation (23) gives the value of b^2/U to be used in equations (24) and (25).

It is useful to find the ordinate of the upper surface of the cavity above the trailing edge of the wetted surface which we denote by $\eta_c(1)$. This can be done by a straightforward numerical method [18] using equations (24) and (25). It is found when the points are plotted in an $\eta_c(1)-\alpha$ plane that a linear relationship fits the data for $0 \leq \alpha \leq 10$ deg. When α is measured in degrees, this line has the equation

$$\eta_c(1) = .0294\alpha^\circ. \tag{26}$$

The corresponding relationship for α measured in radians is

$$\eta_c(1) = 1.684\alpha. \tag{27}$$

According to linearized theory [13] this latter form of the results would be $\eta_c(1) = 1.681\alpha$.

The flat-plate function $\omega_o(\zeta)$ is traditionally considered to possess all of the singular behavior of the function $\omega(\zeta)$. The shape of the smooth body is then represented by an analytic function $\omega_1(\zeta)$ which is regular inside and on the unit circle. It must also satisfy the same symmetry requirements as are imposed upon ω_o and we must also insist that $\omega_1(0) = 0$. Then one traditionally puts $\omega(\zeta) = \omega_o + \omega_1$. As mentioned previously, we will add to this customary sum a new function, $\omega_c(\zeta)$, which is the analog of the point-drag function of linearized theory. We will now explore the properties of this eigensolution.

A Simple Eigensolution

The complementary function $\omega_c = \theta_c + i\tau_c$, is to be determined from the requirements that $\tau_c = 0$ on the cavity and the foil, $\theta_c = 0$ along the stagnation streamline and that ω_c vanishes at infinity. A function which satisfies these conditions can be found most easily by considering the flow in the F-plane, Fig. 2. For example, if we take

$$\omega_c = \theta_c + i\tau_c = \frac{E}{\sqrt{F}} \tag{28}$$

where E is a real constant, we have a function which satisfies the necessary requirements. The two conditions $\omega_c(\infty) = 0$ and $q_c = U$ on both the cavity and the profile wetted surface can be satisfied by any member of the family of functions having the form F^{-m}, $0 < m < 1$. But the condition $\theta_c = 0$ along the entire stagnation streamline can be satisfied only when $m = \frac{1}{2}$. This choice for the complementary function seems to offer the advantage that it will cause less alteration of the upstream flow field inclination than other possibilities. Moreover, it is the only choice from amongst the functions F^{-m} which gives the correct branching of the flow and it appears to be the most convenient choice for further analysis. Consequently, we shall adopt this functional form for the simple eigensolution in this work. The word simple indicates that the branch point for this solution is coincident with the stagnation point at O in Fig. 1. We shall generalize this result later.

It has been noted by O. Furuya[2] that equation (28) is just the single-spiral-vortex function proposed by Tulin as a useful representation for cavity termination in the direct problem at non-zero cavitation numbers [14]. The small-scale structure of this function is responsible for its name as discussed by Tulin on page 21 of reference [14]. In connection with the present application, we may also mention Tulin's double spiral vortex model [14] which can be written as a logarithmic function [18]. It is found that the double-spiral vortex violates equation (8) and it will generally not produce a null pressure coefficient everywhere on the wetted surface. Therefore, it is not an admissible candidate for an eigenfunction. This is not to say that other logarithmic forms for an eigenfunction cannot be acceptable. This writer has not found one as yet, however. Therefore, we shall content ourselves with the form of ω_c prescribed by equation (28) and restrict the present analysis to eigensolutions of this form.

Equation (3) can be used to represent ω_c in the ζ-plane as

$$\omega_c = \frac{E}{b\left[\cos\gamma-\frac{1}{2}\left(\zeta+\frac{1}{\zeta}\right)\right]} = \frac{-2E\zeta}{b(\zeta-e^{i\gamma})(\zeta-e^{-i\gamma})}. \tag{29}$$

In the ζ-plane $\omega_c(0) = 0$ and when ζ is real, ω_c is real. Moreover, $\omega_c(\zeta)$ is an analytic function which is regular inside the unit circle and which has simple poles at $\zeta = e^{\pm i\gamma}$. Note from equation (29) that on the "nose cavity" $\theta_c \to 0+$ as $\zeta \to -0$ and on the "tail cavity" $\theta_c \to 0-$ as $\zeta \to +0$, as also illustrated in Fig. 1. From equation (6), $w_c = Ue^{-i\omega_c}$ and because of this exponentiation we see that the structure of ω_c leads to an isolated essential singularity in ω_c at the stagnation point O. The complex velocity ω_c is bounded at this point however, and a smooth foil contour will pass through $z = 0$ as will be seen below.

For points on the unit circle very near the stagnation point, $\beta = \gamma$, let $\beta = \gamma - \epsilon$ with $\epsilon \ll 1$. Then

$$\omega_c(\gamma,\epsilon) \doteq \frac{E}{\epsilon b\left[\sin\gamma+\frac{\epsilon}{2}\cos\gamma\right]}$$

and to $O(\epsilon^{-1})$, $w_c \doteq \exp -iE/\epsilon b\sin\gamma$. Therefore $|w_c| = q_c \leq 1$ as $\epsilon \to O$. Next consider an interior point, $\zeta = re^{i\gamma}$. Now let $r = 1-\rho$ with $0 \leq \rho \ll 1$. Then to $0(\rho^{-1})$, $\omega_c(\gamma,\rho) = -iE/\rho b\sin t = i\ln q_c/U$. Consequently, $q_c/U = \exp -E/\rho b\sin\gamma$ and $q_c/U \to 0$ as $\rho \to 0$. Appropriate linear combinations of these two cases can be used to consider other limiting paths but these give no new information about the boundedness of

[2] Private Communication (March 1985).

q_c/U. As a final observation we appeal to a theorem of Weierstrass[3] and assign the value of $q_c/U = 1$ at the point O on $|\zeta| = 1$. At points on the unit circle removed from O, $\zeta = e^{i\beta}$ and we have

$$\tau_c = 0 \tag{30}$$

and

$$\theta_c(\beta) = \frac{E}{b[\cos\gamma - \cos\beta]} = \frac{-E}{2b\sin\dfrac{\gamma+\beta}{2}\sin\dfrac{\gamma-\beta}{2}}. \tag{31}$$

Since $\tau_c = 0$ on the wetted surface, we expect ω_c to make no contribution to the lift although the singularity at the stagnation point should lead to a drag force. Making use of equations (15), (16), and (29), we find that

$$C_{L_c} = 0 \tag{32}$$

and

$$C_{D_c} = 2\pi\frac{E^2}{Uc}. \tag{33}$$

From equation (31) we see that the flow direction is not defined at the stagnation point, $\beta = \gamma$. If $\beta < \gamma$ however,

$$\theta_c = -\frac{E}{b[\cos\beta - \cos\gamma]} < 0$$

along the arc OA_2. If $\beta < \gamma$

$$\theta_c = \frac{E}{b[\cos\beta - \cos\gamma]} < 0,$$

along the arc OA_1. Therefore θ_c changes sign at $\beta = \gamma$ and as noted previously, the real part of ω_c has a jump of π as it passes through O. In view of equation (7) which requires that $\pi = \ln q/U$, this situation suggests a strong similarity between Fabula's "step-profile" solution for the linearized theory [15] and the present eigensolution. The present application and those of references [13] and [15] are different, however.

Simple Eigensolution Geometry

The shape of the wetted cavity surfaces follow from the relationships of equation (6) which can be expressed as

$$dz = \frac{dF}{U}e^{i\omega_c} = \frac{d(\sqrt{F^2})}{U}e^{iE/\sqrt{F}}.$$

If we put $t = E/\sqrt{F}$, we find for a profile of unit chord that

$$dz = \frac{2E^2}{U}\frac{1}{t^3}e^{it}dt = -\frac{C_{D_c}}{\pi}\frac{1}{t^3}e^{it}dt$$

which has the indefinite integral,

$$z = \frac{E^2}{U}\left\{\frac{e^{it}}{t^2} + i\frac{e^{it}}{t} + \int\frac{e^{it}}{t}dt\right\}. \tag{34}$$

Completion of this integration can be carried out in four parts starting from either side of the stagnation point where $z = 0$ and $t \to \infty$. Details of these integrations are given in reference [18]. We will give only the final outcome here. This is illustrated by the following numerical example.

We started the calculation by selecting $\delta = 70$ deg and $E/b = .01$. It is found that $\tan\alpha = .01482$ and $U/E^2 = 18{,}006$. From equations (32) and (33) we have for the cavity drag due to a profile of unit chord

$$C_{D_c} = 2\pi\frac{E^2}{U} = .00035,$$

as the contribution for this point-drag profile.

The form of equation (1) for the present calculations, giving the transformation between (x, y) and (σ, η) coordinates is

$$\sigma = .99989x - .014796y,$$

and

$$\eta = .014796x + .99989y.$$

The next phase of the calculations is the evaluation of the equations for the wetted surface and cavity contours derived from equation (34). The result of these calculations is shown in Fig. 5. In this figure, the chordline distance, σ, has been labeled as X and the ordinate, η, has been labeled as Y. Note that the Y-scale is magnified five times compared to the X-scale. The trailing edge of the wetted surface is at $X = 1$. The upper surface separation point is at $\sigma = X = .240$. The cavity thickness at $X = 1$ is $Y = T = .02980$. This point is marked to the same scale as the X-scale by the dot and the line at $X = 1$ in order to give an idea of the actual thickness of this example of a point-drag profile.

The Eigensolution

For the simple eigensolution, the restriction on the location of its point of application has allowed us to show that such a solution exists, that it definitely leads to a smoothly rounded profile nose and that it will cause an incremental thickening of the cavity depending on its strength, E. Of course, in order to explore further its possible properties, we need not restrict the eigensolution to be at the stagnation point.

For example, suppose we choose some other point C on the wetted surface. Such a point is illustrated in Fig. 3 and it happens to be located between the upper cavity separation point and the stagnation point, although C could just as well be at some other wetted-surface location. The main idea is that now $\beta = \gamma_c$ at the location of the point-drag singularity and if we simply replace equation (29) by the modified expression

$$\omega_c(\zeta) = \frac{E}{b\left[\cos\gamma_c - \dfrac{1}{2}\left(\zeta + \dfrac{1}{\zeta}\right)\right]} = \frac{-2E\zeta}{b(\zeta - e^{i\gamma_c})(\zeta - e^{-i\gamma_c})}$$

$$= \frac{iE}{b\sin\gamma_c}\left[\frac{e^{i\gamma_c}}{\zeta - e^{i\gamma_c}} - \frac{e^{-i\gamma_c}}{\zeta - e^{-i\gamma_c}}\right], \tag{29a}$$

we still have a function which satisfies those conditions needed for a complementary solution. It is clear that in the ζ-plane, $\omega_c(0) = 0$ is in agreement with equation (8). Moreover, when ζ is real ω_c is real and on the unit circle $\tau_c = 0$ everywhere except possibly at the simple poles, $\zeta = e^{\pm i\gamma_c}$. From equations (15)

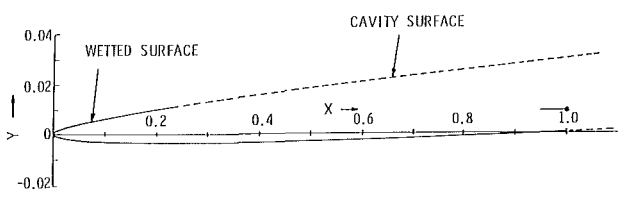

Fig. 5 The profile and cavity contours produced by an isolated eigensolution of strength $E/b = .01$ at the stagnation point $\delta = 70$ deg which produces a cavity drag $C_{D_c} = .0035$ and cavity thickness $T = .0298$. Note the distortion of the vertical scale in the plot. The line and dot at $X = 1$ show the true geometry when the vertical and horizontal axes have the same scale.

[3] See for example, Copson, E. T., *Theory of Functions of a Complex Variable*, Oxford University Press, 1946, p. 81; or Tichmarsh, *The Theory of Functions*, 2nd Edition, Oxford, 1949, pp. 93-94.

and (16) it follows that

$$C_{D_c} = 2\pi \frac{E^2}{Uc} \tag{35}$$

as before. On the other hand, because of the displacement of the point C away from O, a lift force is produced and we find that now

$$C_{L_c} = \frac{8\pi bE}{Uc} \sin \frac{\gamma+\gamma_c}{2} \sin \frac{\gamma-\gamma_c}{2}$$

$$= \frac{8\pi bE}{Uc} \sin \frac{\delta_c+\delta}{2} \sin \frac{\delta_c-\delta}{2}, \tag{36}$$

where $\gamma = \pi - \delta$ and $\gamma_c = \pi - \delta_c$ in accordance with previous convention. The profile chord, c, should be set at unity in equations (35) and (36). Equation (36) shows that $C_L = 0$ when $\delta_c = \delta$. But $\delta_c < \delta$ when the point C moves toward the point A_1, a negative lift results. In the limit as $\delta_c \to 0$, we have

$$C_{L_c} = -\frac{8\pi bE}{Uc} \sin^2 \frac{\delta}{2}.$$

If C is between O and A_2 a positive lift is produced and in the limit when C is coincident with A_2 we have

$$C_{L_c} = \frac{8\pi bE}{Uc} \cos^2 \frac{\delta}{2}.$$

If one were to let E be negative, the sign of the foregoing trends with respect to C_L would be reversed. We must insist, however, that $E \geq 0$ because this function produces a thickening of the cavity and because then $\omega_c'(0) = -2E/b$. Similarly, we have also found that $\omega_o'(0) = -2 \sin \gamma$. Thus, the effect of adding ω_o and ω_c *increases* the net drag. Neither of these functions can act to reduce it. Accordingly, we shall take equation (29*a*) as the most general form of the eigensolution which has been sought. Since both of equations (29) have simple poles on the contour $|\zeta| = 1$, they can be thought of as elementary solutions. But as we have seen in the case of the simple eigensolution, the pole at $\beta = \gamma_c$ does not lead to an unbounded value of q_c/U. Indeed, $0 \leq q_c/U \leq 1$ in the neighborhood of $\beta = \pm \gamma_c$, which can be taken to be at any point on the wetted surface when $\beta = +\gamma_c$ and we can take $q_c/U = 1$ if we wish.

The increased generality of this eigensolution does not mean that it is admissible for design use. It could be that one should restrict its location to the stagnation point. This is a question for future exploration.

Some Profile Geometry and the Flow

In any inverse design procedure, one starts the calculation by prescribing the pressure distribution or the magnitude of the velocity along the periphery of the profile. Of course, that is almost like having the solution at the outset; but not quite, because one does not know the relationship between points along the hydrofoil arc length, s, and corresponding points on the semi-circle in the ζ plane. Nevertheless, referring to Fig. 6, we can measure the arc length s from the point A_2 at the cavity-trailing edge separation point. Then the arc length increases from A_2 until one reaches the stagnation point O in Fig. 6. At O the arc length will be designated by s_o. Continuing along the periphery, one rounds the nose of the foil and arrives at the separation point A_1. At this point, the arc length is s_1. Finally we proceed along the upper surface of the cavity until we arrive at the point s_2, a distance T directly above the trailing edge, A_2. The distance T is measured perpendicularly to the profile chordline. Thus, it is parallel to the η axis in Fig. 6. Clearly, $0 < s_o < s_1 < s_2$.

A schematic diagram showing the flow speed on the wetted-surface arc and the upper surface of the cavity is illustrated in Fig. 7. This figure shows rather clearly that the designer does

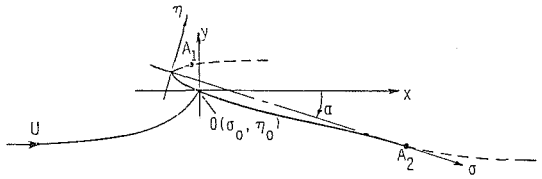

Fig. 6 The geometry of a round-nosed profile of unit chord showing the origin of σ-η coordinates at the apex of the wetted surface corresponding to (x_a, y_a) in z-plane coordinates

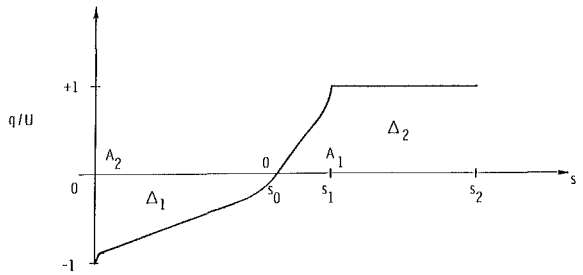

Fig. 7 Schematic diagram showing a prescribed velocity distribution on a profile and cavity arc

not have as much freedom with regard to the pressure distribution prescription as he might wish. For example, we know that $|q/U| = 1$ at $s = 0$, $s = s_1$ and in the interval, $s_1 \leq s \leq s_2$. Moreover, we take the values of $q/U \leq 0$ in the interval $0 \leq s \leq s_o$ because the flow direction on the wetted surface points in the direction opposite to the positive sense of s. Between $s_o \leq s \leq s_2$ the opposite situation holds and we count $q/U \geq 0$ in this interval. At no point in the flow can $|q/U| > 1$.

Since we prescribe the magnitude of q/U everywhere this is the same as prescribing the lift coefficient C_L. This prescribed value of C_L can be used to fix the relative position of the stagnation point s_o with respect to point s_2 if the distribution $q(s)/U$ is not too firmly fixed. One need only use the well-known Kutta-Joukowsky formula,

$$\frac{1}{2} cC_L = \frac{\Gamma}{U} = \int_0^{s_2} \left(\frac{q}{U}\right) ds,$$

where c is the profile chord and Γ is the circulation. But we can write

$$\Gamma = (\Delta_2 - \Delta_1)U,$$

where

$$\Delta_1(s_o) = \int_0^{s_o} \frac{q(s)}{U} ds$$

and

$$\Delta_2(s_o, s_2) = \int_{s_o}^{s_1} \frac{q(s)}{U} ds + (s_2 - s_1).$$

Generally one will need to solve for the ratios s_o/s_2 and s_1/s_2 numerically, starting the iteration by supposing that possibly Δ_1 and that part of Δ_2 between s_o and s_1 are triangular areas. Indeed, we will see below that the area Δ_2 must be rather closely specified in advance so that the chief freedom to be exercised by the designer is associated with Δ_1. The thought behind these observations is that whatever the approach, the design C_L and the distribution $q(s)/U$ must be consistently prescribed.

We now turn to the properties of the flow in the neighborhoods of s_o and s_1 because at s_o the flow on the wetted surface is a stagnation flow and at s_1 it is constrained by the requirements for smooth separation. For simplicity's sake we shall shift our reference point from A_2 to the point O and measure the arc length s from O. This means that the distance

along the arc from O to A_1 is $s_1 - s_o$ and we will normalize all intermediate distances s by writing $x = s/(s_1 - s_0)$.

Then it is known for a potential-flow stagnation point on a flat wall that the streamlines are equilateral hyperbolas having their separatrices as the straight wall and the normal to the wall through the stagnation point. It is also known from linearized theory [9], and it can also be shown for the exact theory, that if $x = 1$ is a separation point then $C_p(x) \sim \sqrt{1-x}$. A specific example of this general behavior can be seen by referring to the various formulae for the flat-plate velocity and pressure distributions given above in the discussion surrounding ω_o. In particular, it is easily seen that $dz/d\zeta = 0$ at the separation points $\zeta = 1$. Consequently curves of q/U and C_p will have vertical tangents at the separation points. In response to these requirements we shall consider a one-parameter family of speed distributions on the forward part of the wetted surface; namely,

$$\frac{q(x)}{U} = x[1 - \alpha\sqrt{1-x^2}(1-\sqrt{1-x^2})], \quad (0 \le x \le 1). \tag{37}$$

Although this is a rather special class of velocity distributions, it probably contains as much generality as one needs for this discussion because most often the arc length from s_o to s_1 is very small compared to the total arc length s_2. Therefore the curves of $q(x)/U$ will be very steep and the shape of one choice of distribution would hardly be discernible from some other choice, provided that the required conditions at $x = 0$ and $s = 1$ are satisfied. Other design requirements can affect this choice, but we shall not consider them here. Plots of equation (37) are given for a highly stretched length scale in Fig. 8.

This specification and cavity surface velocity for $s_1 \le s \le s_2$ makes the entire pressure distribution on the upper surface of the profile fairly well defined. In order that these results can be used conveniently in the process of reconciling the design C_L with $q(s)/U$, equation (37) should be expressed in terms of the arc-length coordinates defined in Fig. 7. Normalizing all distances by s_2 we can write

$$x = \left(\frac{s_2}{s_1 - s_o}\right)\left(\frac{s - s_o}{s_2}\right). \tag{38}$$

Having prescribed the velocity distribution for points on the periphery of the profile, one can now use equation (13) in order to derive the circle-to-profile correlation between s_o and s_2, albeit with some degree of ambiguity until the entire problem has been formulated and solved. For this correlation, we will write equation (13) in the form,

$$\frac{q(s)}{U}\,ds = 2\,\frac{b^2}{U}\,(\cos\gamma - \cos\beta)\sin\beta\,d\beta$$

$$= \frac{b^2}{U}\,d[(\cos\gamma - \cos\beta)^2], \tag{39}$$

where equation (37) defines $q(s)/U$ in the interval, $s_o \le s \le s_1$, and in the interval, $s_1 \le s \le s_2$, we have $q(s)/U = 1$. Moreover, at this point we know that when $s = s_o$, $\beta = \gamma$ and when $s = s_1$, $\beta = \pi$. From equation (37) we can put

$$(s_1 - s_o)\,dx = ds$$

and we can integrate equation (39) from s_o ($x = 0$) to x and the right-hand side of equation (39) from $\beta = \gamma$ to β. Therefore, the integral of equation (39) is

$$(s_1 - s_o)\left[\frac{x^2}{2} - a\left(\frac{1-(1-x^2)^{3/2}}{3} - \frac{x^2}{2} + \frac{x^4}{4}\right)\right]$$

$$= \frac{b^2}{U}\,(\cos\gamma - \cos\beta)^2. \tag{40}$$

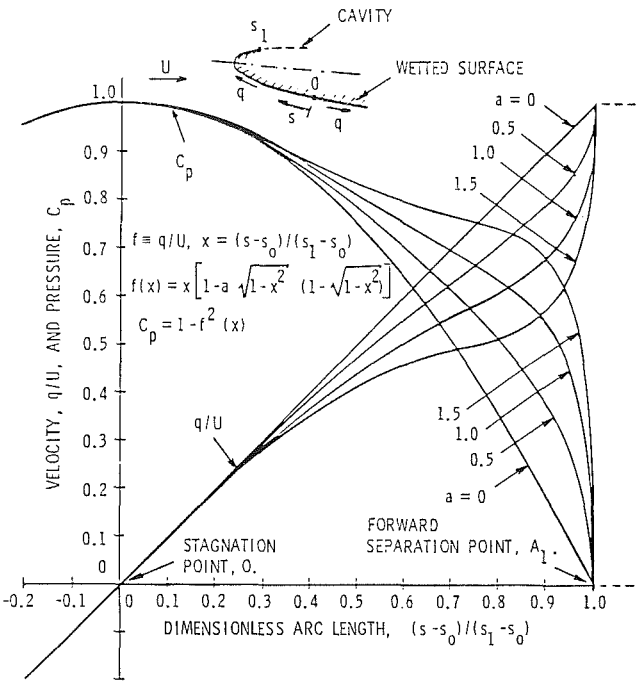

Fig. 8 A one-parameter family of velocity and pressure distributions over the nose arc of a hydrofoil

When $\beta = \pi$ and $x = 1$, equation (40) becomes

$$(s_1 - s_o)\left(1 - \frac{a}{6}\right) = 2\,\frac{b^2}{U}\,(1+\cos\gamma)^2. \tag{41}$$

Proceeding to the arc $s_1 \le s \le s_2$ along the upper surface of the cavity one may start at the point $\beta = \pi$ on the circle $|\zeta| = 1$ and move along the negative real axis toward $\zeta = -r = 0$. The velocity $q/U = 1$ everywhere along this arc and equation (11) can be used to find the differential arc-length correlation,

$$ds = -\frac{b^2}{U}\left[\frac{1}{2}\left(\frac{1}{r} + r\right) + \cos\gamma\right]\left(\frac{1}{r} - r\right)\frac{dr}{r}, \tag{42}$$

where we have taken the positive square root in view of the fact that r has been defined as a positive quantity. Starting the integration at $s = s_1$ and $r = 1$, we find

$$s - s_1 = \frac{b^2}{U}\left\{\left(\frac{1}{r} - 1\right)\left[\frac{1}{4}\left(\frac{1}{r} + 1\right) + \cos\gamma\right]\right.$$

$$\left. - (1-r)\left[\frac{1}{4}\,(1+r) + \cos\gamma\right]\right\}. \tag{43}$$

If $r = r_2$ when $s = s_2$ we can sum this special case of equation (43) and equation (41) in order to get expressions for Δ_2 in the profile and ζ planes. The considerations of this section apply to the inverse problems as a whole and we could extend the above considerations to deduce a correlation like (40) for the interval between A_2 and 0. We shall not complete the analysis here, however.

The Role of the Eigensolution

Returning to the eigensolution as given by equation (29*a*), we recall that except for the simple poles at $\zeta = e^{\pm i\gamma_c}$, the imaginary part of ω_c is zero everywhere on the unit circle and the real part suffers a jump of magnitude π at $\pm\gamma_c$ on the unit circle. On the other hand, we have found that the complex velocity has an isolated essential singularity at these poles. Moreover, because of this fact, we observed that q_c/U is bounded, being in the interval [0, 1] and according to a

theorem of Weirestrass, we can assign the value $q_c/U = 1$ at the points $\gamma_c = \pm 1$ on $|\zeta| = 1$ just as we have done before. We have also seen from an exploration of the flow due to an isolated eigensolution that the resulting profile is smooth and that its wetted surface is smooth. When the flat plate function ω_o and eigenfunction ω_c are combined, the resulting profile will have a stagnation point at $\beta = \gamma$, as we shall discuss below.

As we have remarked above, our plan is to write the logarithmic hodograph as the sum of the flat plate function ω_o, the eigenfunction ω_c and regular function ω_1. Thus

$$\omega(\zeta) = \omega_o + \omega_c + \omega_1 = \theta_o + \theta_c + \theta_1 + i\ln\left[\frac{q_o}{U}\,\frac{q_c}{U}\,\frac{q_1}{U}\right]. \quad (44)$$

Consequently,

$$\frac{q}{U} = \frac{q_o q_c q_1}{U^3}. \quad (45)$$

The composite function, q/U, is prescribed from the outset. Equation (37) which has been defined over the arc length s in the interval $[s_o, s_1]$ corresponding to the normalized variable x in the interval [0, 1], provides an example of such a composite function. The flat plate function, q_o/U, has been worked above. Here it will be written as

$$\frac{q_o}{U} = \frac{2(-\cos\beta + \cos\gamma)}{(-\cos\beta + \cos\gamma)^2 + (\sin\beta + \sin\gamma)^2}, \quad (46)$$

where the absolute sign in the numerator given previously has been replaced by ordinary brackets and we have made other changes which apply in the interval $\gamma \le \beta \le \pi$. Since $q_c/U = 1$ on $|\zeta| = 1$ the function q_1/U follows from equation (45) rewritten as $q_1/U = (q/U)/(q_o/U)$. For the example at hand, the result of this transposition cannot be used until we transform equation (46) from the ζ plane into the arc length in the interval $[s_o, s_1]$ with the help of equation (39). In particular, we find that

$$\frac{q_o}{U} = \frac{2R}{R^2 + \sin\gamma + \sqrt{\sin^2\gamma + 2R\cos\gamma - R^2}}, \quad (47)$$

where

$$R^2 = \frac{U}{b^2}(s_1 - s_o)\left[\frac{x^2}{2} - a\left(\frac{1-(1-x^2)^{3/2}}{3} - \frac{x^2}{2} + \frac{x^4}{4}\right)\right].$$

Then it follows from equation (45) that

$$\frac{q_1}{U} = \frac{(s_1 - s_o)x[1 - a\sqrt{1-x^2}(1-\sqrt{1-x^2})]}{2R/[R^2 + \sin\gamma + \sqrt{\sin^2\gamma + 2R\cos\zeta - R^2}]}. \quad (48)$$

As is true of q_o/U, the function q_1/U when represented in the ζ plane can be continued to the arc of the unit circle in the lower half of the ζ-plane in accordance with equation (14).

Now that the well behaved function q_1/U has been found along the arc OA_1, we may return to equation (44) and note that the real part of $\omega(\zeta)$ is not yet known completely even in this interval. It will be known, however, if we can find θ_1. But its complex conjugate τ_1 has just been found. Of course, we do not know τ_1 at all points of the unit circle because in this example we have not prescribed the entire pressure distribution on the wetted surface, although the way in which this can be done is certainly clear. Once that step has been carried out, τ_1 will be known on the unit circle and its conjugate θ_1 can be calculated using the customary representation of $\omega_1(\zeta)$ as a Laurent expansion, as employed by Yoshihara [8] for example. Procedures which are preferable for practical engineering calculations are usually based on the Poisson integral formula or related methods. Examples of interest for the present inverse theory are given by Theodorsen and Garrick [16] and by Parkin and Peebles [17], among others. Further discussion of these matters is beyond the scope of this paper.

In the course of designing a profile, the quantities which one specifies from the start are the design lift coefficient C_L, the pressure (velocity) distribution on the wetted surface, the cavity thickness at the trailing edge and perhaps the separation point of the upper surface of the cavity near the nose. The purpose of the eigensolution is to provide the necessary degrees of freedom which will permit the control of the cavity geometry as indicated. Added degrees of freedom can be incoporated in the prescribed pressure distribution if a parametric approach is used. It might be possible to lower the cavity drag somewhat by adjusting them although the prescription of cavity thickness is probably more important in this regard. The outcome of the design process will be coordinates of the profile and cavity shape, including the separation point; the attack angle, α; and the drag coefficient C_D. The eigensolution strength, E/b, will also be determined in the course of the calculations.

Conclusions

The chief finding of this paper is that one can construct many singular eigensolutions for the exact inverse problem of two-dimensional cavity flow at zero cavitation number. From among these, we have chosen that single eigensolution which provides the correct branching of the flow at its singularity, it also appears to offer the least disturbance to the upstream flow field inclination of any cavity flow which does not already include a point-drag solution as one of its elements. This particular choice also seems to offer the greatest analytical convenience. The physical conditions satisfied by this eigensolution are:

(1) At points on the cavity and on the wetted surface of the profile, the flow velocity is equal in magnitude to the free-stream velocity. Consequently, except for the singular point the pressure coefficient is zero on the wetted and cavity surfaces.
(2) The point-drag solution vanishes at infinity, but it does have a bounded essential singularity on the wetted surface and it produces *no singular velocities or pressures in the flow or on the profile surface.*
(3) This function produces no additional flow inclination on the entire upsteam stagnation streamline.

A specific example of the flow geometry represented by an isolated eigensolution has been given above to show how this function can produce round-nosed profiles. In general, it is found that the point-drag solution produces a widening of the cavity which is directly proportional to its strength. An incremental cavity drag accompanies this widening and this drag is proportional to the square of the eigensolution strength. No lift is produced by the point-drag function when its location coincides with that of the stagnation point on the profile surface. In contrast to the linearized theory, the complementary function singularity need not be at the stagnation point. But when the singularity is located between the stagnation point and the upper separation point, a negative incremental lift is produced. If the singularity is on the lower surface, downstream of the stagnation point, a positive life increment is found. Whether or not it is better to position the eigensolution at some point on the profile instead of at the stagnation point remains to be studied.

As a result of these findings, it appears that an eigensolution exists for the nonlinear theory of cavity flow at zero cavitation number and that it is now most likely that a similar eigensolution can be found for such fully cavitating flows at cavitation numbers which are greater than zero. The results found so far suggest that the nonlinearized theory and the linearized theories parallel one another very closely as far as the nature of their point drag solutions are concerned. But the present

results exhibit some features which are lost in the process of linearization.

Acknowledgments

This work has been supported by the Naval Sea Systems Command, Dr. Thomas E. Peirce [NSEA 63R-31] and by the David Taylor Research Center [DTRC] under the General Hydrodynamics Research Program. The author is particularly pleased to acknowledge the helpful discussions of this work by Dr. Y. T. Shen of DTRC and Dr. O. Furuya of Tetratech.

References

1 Yim, B., and Higgins, L., "A Nonlinear Design Theory of Supercavitating Cascades," ASME JOURNAL OF FLUIDS ENGINEERING, Vol. 97, No. 4, Dec. 1975, p. 430.

2 Khrabov, I. A., "Plane Problems of Cavitation Flow Around an Oblique Cascade of Profiles," *Izvestiya Akademii Nauk SSSR, Mekhanika Zhidkosti i Gaza*, No. 3, May–June 1975, pp. 149–152 [Translated: Plenum Publishing Corporation, 227 West 17th Street, New York, 1977.]

3 Furuya, O., "Exact Supercavitating Cascade Theory," ASME JOURNAL OF FLUIDS ENGINEERING, Vol. 97, No. 4, Dec. 1975, p. 430.

4 Durand, W. F. (Editor), *Aerodynamic Theory*, Vol. III, by Th. Von Karman and J. M. Burgers, Dover Publications, Inc., New York, NY, 1963, pp. 336–339.

5 Gurevich, M. I., *Theory of Jets in Ideal Fluids*, Academic Press, New York, NY, 1965, pp. 131–143.

6 Woods, L. C., *The Theory of Subsonic Plane Flow*, Cambridge University Press, London, England, 1961, pp. 443–454.

7 Milne-Thomson, L. M., *Theoretical Hydrodynamics*, Fifth Edition, The MacMillan Press, Ltd., London, England, 1968, pp. 338–348.

8 Yoshihara, H., "Optimum Fully Cavitated Hydrofoils at Zero Cavitation Number," *Journal of Aircraft*, Vol. 3, No. 4, 1966, p. 372.

9 Parkin, B. R., and Grote, R. S., "Inverse Methods in the Linearized Theory of Fully Cavitating Hydrofoils," ASME *Journal of Basic Engineering*, Vol. 86, No. 4, Dec. 1964.

10 Parkin, B. R., and Fernandez, J., "A Third Procedure for Linearized Fully-Cavitating Hydrofoil Section Design," ARL Technical Memorandum 77-186, Applied Research Laboratory, The Pennsylvania State University, July 1977.

11 Parkin, B. R., "An Extended Linearized Inverse Theory for Fully Cavitating Hydrofoil Section Design," *J. Ship Research*, Dec. 1979, p. 260; "Hydrodynamic Trends from a Generalized Design Procedure for Fully Cavitating Hydrofoil Sections," *J. Ship Research*, Dec. 1979, p. 272.

12 Lamb, Sir Horace, *Hydrodynamics*, Sixth Edition, Dover Publications, New York, NY 1945, pp. 102–103.

13 Parkin, B. R., 'Munk Integrals for Fully Cavitated Hydrofoils," *J. of the Aerospace Sciences*, Vol. 29, No. 7, July 1962, p. 775.

14 Tulin, M. P., "Supercavitating Flows – Small Perturbation Theory," *J. Ship Research*, Jan. 1964, p. 272.

15 Fabula, A. G., "Fundamental Step Profiles in Thin-Airfoil Theory with Hydrofoil Application," *J. Aerospace Sciences*, Vol. 28, No. 6, June 1961.

16 Theodorsen, T., and Garrick, I. E., "General Potential Theory of Arbitrary Wing Sections," NACA Technical Report No. 452.

17 Parkin, B. R., and Peebles, G. H., "Calculation of Hydrofoil Sections for Prescribed Pressure Distributions," Technical and Research Bulletin No. 1–17, The Society of Naval Architects and Marine Engineers, 1956.

18 Parkin, B. R., "The Role of Eigensolutions in Nonlinear Inverse Cavity-Flow Theory," ARL Technical Memorandum 85-97, Applied Research Laboratory, The Pennsylvania State University, June 1985.

P. R. Meernik[1]

M. C. Yuen
Mem. ASME

Department of Mechanical Engineering,
Northwestern University,
Evanson, IL 60201

An Optical Method for Determininig Bubble Size Distributions—Part I: Theory

A new optical technique is developed to determine the size distribution of bubbles in a two-phase flow. Implementation involves passing a narrow beam of light through the bubbly flow and monitoring the transmitted light intensity. The basic units of data are the rate at which each bubble blocks off the beam and the duration of blockage. Adding the hypothesis that the distance of closest approach between a bubble's center and the beam axis is randomly distributed, a statistical analysis yields the bubble size distribution.

1 Introduction

Multiphase flow is important in both mechanical and chemical industrial processes. A prerequisite for a better understanding of these processes is knowledge of the size distribution of the disperse phase. Many different methods, with the majority concentrating on drop size measurement, are described in the literature. A review article by Azzopardi [1] cited 131 references dating back to 1938.

The present research arose out of work on a three-phase fluidized bed system. Large bubbles introduced at the bottom of the bed broke up until typical diameters were one to two millimeters. The resulting bubbles, being small, were basically spherical, but numerous enough that even at void fractions of 5 percent the average clear optical path through the fluid was only about a centimeter.

Numerous methods have been described for obtaining bubble size information, but none of them are easily applied to the type of flow described above. Photography and related methods, the most widely used approaches, are fairly simple during the data collection stage but present analysis difficulties if large sample sizes are desired. In addition, with congested flows, a photograph will yield data on bubbles only in the vicinity of a window. Light scattering technique such as reviewed by Billet [2] is usually limited to small particles below the size of 0.1 mm diameter.

Besides photography and light scattering, another optical approach which has received considerable attention in the past ten years is laser-doppler anemometry (LDA) extended to two-phase flows. There are basically four distinct varieties of this approach which have been described. The most widely used of these utilizes a relationship between particle size and a signal characteristic such as doppler amplitude or modulation depth. The technique is most readily applied to bubble or particle sizes up to a few hundred microns (Ungut et al. [3], Yule et al. [4], Lee and Srinivasan [5, 6],) although Martin et al. [7] obtained a unique relationship between signal visibility and bubble size for diameters up to one millimeter. At its best, this approach is therefore restricted to rather small bubbles.

The second varient of LDA is that described by Durst and Zare [8]. In their technique the two light beams, either reflecting off of or refracting through a bubble, generate interference fringes in the surrounding space. Bubble size can then be calculated from the fringe spacing. The main difficulty with this method appears to be the size measurement of moving fringes as bubbles pass through the beam. The authors know of no studies of practical flows utilizing this technique.

In a more recent approach, Lee and Srinivasan [9] combine LDA determined bubble velocities with reference beam blockage times to yield diameters. This technique appears capable of yielding high quality size information, but it requires rather involved signal processing. This is especially true if number density distributions are desired.

The last LDA technique is that of Semiat and Dukler [10]. In their work, the light fringes required for LDA are generated by Ronchi gratings rather than crossed beams. This serves to simplify the optics and make the overall approach more workable in practial applications. Indeed, their work appears to be the only LDA type with which actual size distributions of relatively large bubbles (diameter up to several millimeters) have been obtained. Even so, the approach is still fairly complex when compared to the method to be presented here and its use was only demonstrated in bubbly flows of low number density.

In addition to photography and LDA methods, there are, of course, other approaches. Wu [11] describes a very simple optical method, but it is dependent upon the particles passing through the central portion of a light beam. Both fiber optic and conductivity probes (Buchholz and Schugerl [12, 13]) have also been used to determine bubbles sizes. Due to the fact that such probes must pierce the bubbles, these authors stated the techniques were applicable only down to bubble diameters of 0.6 millimeters for the conductivity probe and 1.0 millimeters for the optical probe. However, Herringe and Davis [14], also using the conductivity approach, claim detection of bubbles

[1] Present Address: General Motors Research Lab., Warren, MI.

Contributed by the Fluids Engineering Division for publication in the JOURNAL OF FLUIDS ENGINEERING. Manuscript received by the Fluids Engineering Division January 5, 1987.

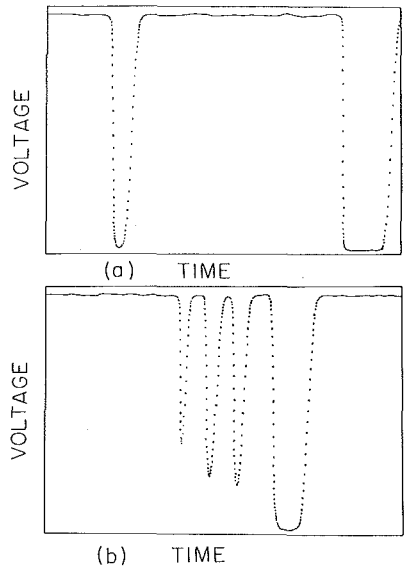

Fig. 1 Typical signals from light beam probe (50 μs between data points)

down to 0.1 millimeters with a probe whose tip diameter was 0.08 millimeters. For smaller bubbles, probe techniques suffer from the fact that bubbles may bounce off the probe or, in some cases, even stick to the probe. For organic fluids where the electrical conductivity is comparable to that of the gaseous medium, the electrical probe technique is generally not satisfactory.

Calderbank [15] described a clever and simple bubble size measurement method based upon blockage of a light beam. Regrettably, it yields only the Sauter mean diameter and requires knowledge of the local void fraction. Many other methods are presented by Azzopardi [1], but again none of them are easily applied to the type of flow under consideration.

2 The Light Beam Technique

As opposed to many of the above-mentioned methods, the light beam technique, as it will be referred to, is experimentally very simple and requires no tedious data reduction. Implementation involves passing a single light beam of known diameter and path length through the two-phase region of interest. The requirements on the beam are that its diameter should be approximately equal to that of the smallest bubbles on which data is desired and its length such that the probability of more than one bubble in the beam at once is minimal. The raw data which must be obtained for analysis are gathered by measuring the fraction of the beam which passes unblocked through the test region. The analysis procedures are involved, but once the computer routines are set up the data reduction is automatic.

This paper outlines the light beam technique and the accompanying paper by Meernik and Yuen [16] shows an application. The detail is contained in Meernik [17]. There are two keys to the light beam technique. The first is the determination from bubble signals (typical examples of which are shown in Figs. 1*a*, *b*) of both the light blockage rate and duration. Assuming the bubbles are spherical and move at a constant velocity while in the beam, the blockage rate and duration, as shown in Fig. 2, are functions of

(*a*) r = bubble radius
(*b*) s = distance of closest approach measured between the bubble's center and the light beam axis
(*c*) v = speed of the bubble in the plane perpendicular to the light beam.

With two measurable quantities and three unknowns, bubble size cannot be determined directly. However, considerable use can be made of the fact that bubbles will pass through the beam with random s values. Realization of this statistical fact is the second key item. Blockage rate and duration data, and the statistics of s, are the basis of the analysis method presented here. Before continuing, a few points concerning bubble speeds should be emphasized. First, whenever bubble

Nomenclature

$\mathbf{A}$ = matrice with element A_{ij}
A_{ij} = expected fraction of counts due to bubbles whose actual radii lie within the ith interval, but which will have apparent radii in the jth interval
$E(x)$ = expected value of a random variable, x
$f(l)$ = fraction of clear paths whose lengths are greater than l
$f_v(r)$ = u/w = ratio between the actual speed of a bubble towards the beam axis and the calculated speed (which is based upon the straight edge assumption)
$\mathbf{G}$ = diagonal matrix with element G_i
G_i = see equation (9)
$g(r,v)$ = probability per unit speed that a bubble of radius r would have a speed v in the plane perpendicular to the light beam
$\mathbf{H}$ = diagonal matrix with element h_{ij}
h_{ij} = see equation (12)
$I(r)$ = number of bubbles per unit radius about r that lie within a distance $s_m(r)$ of the beam axis per unit length of the beam
I_T = $\int_0^\infty I(r)dr$
l = length of the light beam
n = number density of bubbles
$\mathbf{N}$ = column vector with the n_i as elements
p = apparent bubble radius = $(\tau w)/2$
p_i, p_{i+1} = values defining the range of the ith apparent size interval
$\mathbf{Q}$ = column vector with element Q_i
Q_i = rate at which bubbles with apparent radius in the ith interval pass through the beam per unit length
r = bubble radius
$r_{50}(r)$ = distance bubble's center must be from the beam axis to block 50 percent of the light beam
$R(r,v,s)drdvds$ = expected rate at which bubbles with (*a*) radii between r and $r+dr$ (*b*) speeds between v and $v+dv$ (*c*) and closest approach distances between s and $s+ds$ intersect the beam per unit length
R_i = see equation (8)
$\mathbf{R}$ = column vector with element R_i
$R_{\gamma i}$ = see equation (11)
$\mathbf{R}_\gamma$ = column vector with element $R_{\gamma i}$
r_i = $(p_{i+1}+p_i)/2$
s = distance of closest approach measured

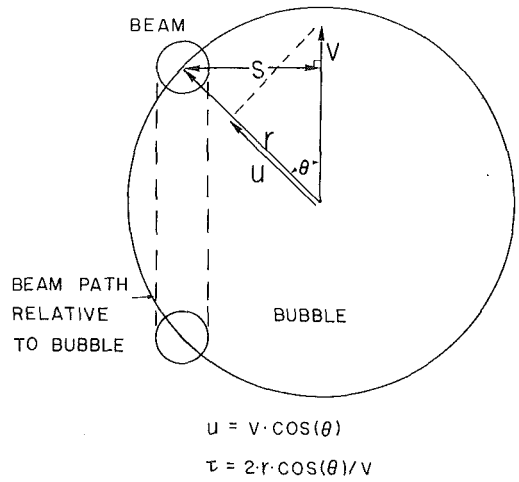

Fig. 2 Bubble/beam intersection geometry

speed is referred to, what is implied is the speed of the bubble in the plane perpendicular to the light beam. Any component of the velocity parallel to the beam does not influence the data. Secondly, although the focus of this paper is on size distributions, the technique also yields, as a function of bubble size, the mean speed of the bubbles of the plane perpendicular to the light beam.

In the following, we shall first discuss in detail the interaction of a single bubble with the light beam. Next, organization of the raw data is covered. That is followed by a determination of the relationship between actual size and speed distributions and the measured data. Finally, a means of properly normalizing the data is developed.

2a Analysis of a Bubble Encounter. Utilization of the light intensity versus time data requires a detailed analysis of a bubble-beam encounter. The analysis using geometric optics is shown in Appendix A. The result shows that for an optical system consisting of a laser beam and aligned injection and receiving optical probes of narrow field of view, any portion of the light beam intersecting a bubble will, for all practical purposes, be completely masked off.

Consider now a bubble cutting partially through the beam as shown in Fig. 2. For the present, assume the bubble's radius is sufficiently large that its edge in the region of the beam is essentially straight. By measuring the amount of light that is not blocked by the bubble, and knowing the intensity profile of the beam (Gaussian), the position of the edge of the bubble relative to the beam center can be determined. Consequently, a sequence of intensity measurements as the bubble cuts through the beam yields the bubble interface position versus time. It is thus possible to obtain

u = the component of bubble velocity towards the beam at the instant of 50 percent light blockage.

In addition, one can obtain

τ = the amount of time that a bubble blocks off more than 50 percent of the beam.

The quantities τ and u can be expressed as

$$\tau = (2/v)\,(r^2 - s^2)^{1/2} \tag{1}$$

$$u = v(r^2 - s^2)^{1/2}/r \tag{2}$$

These equations yield the values of τ and u that would be measured for a large, spherical bubble passing through the beam. However, if the edge of a bubble cutting the beam cannot be considered straight, these equations are in error. Correction for edge curvature effects can be made with the aid of the following definitions:

$r_{50}(r)$ = distance between a bubble's center and the beam axis at which it blocks 50 percent of the beam.

w = speed at which a straight edge cutting through the beam would yield the measured rate of change of light intensity at the instant of 50 percent light blockage.

and $f_v(r) = u/w$ = ratio between the actual speed of the bubble towards the beam axis and the calculated speed based upon the straightedge assumption.

Since a bubble profile must be assumed before speed can be

Nomenclature (cont.)

between the bubble's center and the light beam axis

$s_m(r)$ = maximum closest approach distance for a bubble of radius r subject to the constraint that $\beta > \beta_0$

$\tilde{\mathbf{T}}$ = system matrices for evaluating $\mathbf{Q}$ data, $-\mathbf{A}^T\mathbf{G}$

$\mathbf{T}$ = system matrix for evaluating $\mathbf{\Gamma}$ data, $-\mathbf{A}^T\mathbf{H}$

u = speed of a bubble in the direction toward the beam axis at the instant of 50 percent light blockage

v = true speed of a bubble in the plane perpendicular to the light beam

$\bar{v}_i$ = average speed of bubbles with radius in the ith interval

$\mathbf{V}$ = diagonal matrice with element $\bar{v}_i$

w = speed at which a straight edge must pass through the beam to yield the measured rate of change of light intensity at the instant of 50 percent light blockage

$z(r,p_j) = r_{50}(r) \cdot [1 - (f_r(r) \cdot p_j)/r_{50}(r)]^{1/2}$

α = void fraction

α_i = average void fraction of bubbles with radius in the ith interval

$\alpha(r)dr$ = void fraction per unit radius of bubbles with radii about r

β = maximum fraction of the light beam blocked during the passage of a given bubble

β_0 = value which β must exceed for a bubble to be considered

$\gamma = (\tau/2w)^{1/2}$ = weighting function for frequency distribution

$\mathbf{\Gamma}$ = column vector with element Γ_i

Γ_i = see equation (7)

δ_{ij} = Kronecker delta

λ = mean clear path length between bubbles

τ = time duration of the light blockage by a bubble (time during which the light beam signal is below 50 percent)

θ = angle

Superscript

T = transpose

Subscript

i = with radii in the ith interval

calculated (and a straight edge is the simplest to use), the quantity experimentally obtained is w, not u.

With the above definitions, equations (1), (2) can be rewritten to yield the measured blockage time and speed. Substituting $r_{50}(r)$ for r, and using $w = u/f_v(r)$,

$$\tau = (2/v)[r_{50}^2(r) - s^2]^{1/2} \tag{3}$$

$$w = v[r_{50}^2(r) - s^2]^{1/2}/[r_{50}(r) \cdot f_v(r)] \tag{4}$$

The two measurable quantities are thus expressible in terms of the parameters r, s, and v, along with the functions $r_{50}(r)$ and $f_v(r)$.

2b Organization of the Light Beam Data. The τ and w values can be combined to yield a new quantity

$$p = \frac{1}{2}\tau w$$

For bubbles with negligible edge curvature effects, it is easy to see that $p = r$ when $s = 0$. p will therefore be called the apparent radius. In general, for an arbitrary size bubble and arbitrary off-center distance,

$$p = (1/2)\tau w = [r_{50}^2(r) - s^2]/[r_{50}(r) \cdot f_v(r)] \tag{5}$$

From equation (5) it is seen that as the distance of closest approach between a bubble's center and the beam axis increases from zero to $r_{50}(r)$, p decreases from approximately r to zero. This is a consequence of decreases in both the time the bubble is in the beam and the component of bubble velocity toward the beam as the parameter s increases. For $s = r_{50}(r)$, the bubble, when it is closest to the beam, blocks only 50 percent of the light. The resulting signal would look similar to the first intersection shown in Fig. 1(*b*). In such a case, or anytime $s > r_{50}(r)$, there are insufficient data to determine w. A criteria must therefore be incorporated into the analysis which deletes from consideration any signal that does not drop low enough to yield usable data. For this purpose, define,

$s_m(r)$ = distance between a bubble's center and the beam axis at which some fraction, β, of the light beam is blocked.

As a practical matter, it was found convenient to require at least 75 percent beam blockage for a bubble to be counted.

With true bubble size not available, the approach taken in organizing the data was to use the apparent sizes. Specifically, the frequency of bubble intersections as a function of apparent radius was determined. The range of apparent sizes was discretized into logarithmically equal intervals and a vector **Q** defined as the relative frequency distribution of apparent sizes.

From the **Q** data vector, one can determine the product $n_i v_i$, (number density times average velocity of bubbles in each size range) but not the individual n_i and v_i values. This difficulty was overcome by weighting each bubbles contribution to the frequency distribution of apparent sizes by a function inversely proportional to the bubble's velocity. The function chosen is the square root of τ/w, which not only is inversely proportional to velocity, but is independent of the parameter, s. Thus, define

$$\gamma = (\tau/2w)^{1/2} = [r_{50}(r) \cdot f_v(r)]^{1/2}/v \tag{6}$$

Utilizing γ, the weighted frequency distribution of apparent sizes (to be labeled $\boldsymbol{\Gamma}$) can be constructed with elements

$$\Gamma_i = \sum_{p \in i\text{th interval}} \gamma \tag{7}$$

The data contained in the **Q** and $\boldsymbol{\Gamma}$ vectors are now sufficient for determining size and average speed distributions.

2c Determination of Expected Data from Assumed Size and Speed Distributions. The relationship linking actual size and speed distributions to the measured data can be determined by considering what data would result from hypothetical size and speed distributions. In particular, assume

$\alpha(r)$ = void fraction per unit radius of bubbles with radius of r,

$g(r,v)$ = probability per unit speed that a bubble of radius r would have a speed v in the plane perpendicular to the light beam,

and define

$R(r,v,s)\,dr\,dv\,ds$ = the expected frequency at which bubbles with
- (*a*) radii between r and $r + dr$
- (*b*) speed between v and $v + dv$
- (*c*) and closest approach distance between s and $s + ds$ intersect the beam per unit length and are counted.

Under the assumption that bubble/beam interactions are equally probable for s between 0 and s_m, it can be shown that

$$R(r,v,s)\,dr\,dv\,ds = (3/2\pi)\,(\alpha(r)/r^3)\,g(r,v)\,v\,dr\,dv\,ds \quad 0 < s < s_m(r)$$

$$= 0 \qquad s > s_m(r)$$

Defining R_i as the rate at which bubbles with actual radii in the interval $[p_i, p_{i+1}]$ intersect the beam, we have

$$R_i = \int_{p_i dv} dr \int_0^{s_m(r)} ds \int_0^{\infty} dv \cdot R(r,v,s).$$

If the average speed is defined as

$$\bar{v}(r) = \int_0^{\infty} g(r,v)\,v\,dv$$

and $\alpha(r)$ and $\bar{v}(r)$ are assumed to be uniform and respectively equal to α_i and $\bar{v}_i$ in the ith interval, then

$$R_i = (3/2\pi)\alpha_i \bar{v}_i \int_{p_i}^{p_{i+1}} (s_m(r)/r^3)\,dr. \tag{8}$$

This expression can be converted to explicit number density dependence by assuming that all bubbles within the ith interval have the radius

$$r_i = (p_{i+1} + p_i)/2$$

and defining

n_i = number density of bubbles whose radii fall within the ith interval.

Then

$$\alpha_i(p_{i+1} - p_i) = \frac{4}{3}\pi r_i^3 n_i$$

Now define

$$G_i = \left[2r_i^3 \cdot \int_{p_i}^{p_{i+1}} [(s_m(r)/r^3)dr]/(p_{i+1} - p_i)\right] \tag{9}$$

and rewrite equation (8) as

$$\mathbf{R} = \mathbf{GVN} \tag{10}$$

where

$$\mathbf{G} = G_i \delta_{ij} \text{ and } \mathbf{V} = \bar{v}_i \delta_{ij}$$

Similarly, the expected value of the inverse velocity weighted frequency at which bubbles in a given size range will pass through the beam, $R_{\gamma i}$, can be written as

$$R_{\gamma i} = \int_{p_i}^{p_{i+1}} dr \int_0^{s_m(r)} ds \int_0^{\infty} dv [[r_{50}(r) \cdot f_v(r)]^{1/2}/v] R(r,v,s) \tag{11}$$

By defining

$$\mathbf{H} = h_{ij} = \frac{2r_i^3 \delta_{ij}}{(p_{i+1} - p_i)} \int_{p_i}^{p_{i+1}} [[r_{50}(r) \cdot f_v(r)]^{1/2} \cdot s_m(r)/r^3] dr \quad (12)$$

Equation (11) becomes

$$\mathbf{R}_\gamma = \mathbf{HN} \quad (13)$$

In order to relate the expected values of Q_i and Γ_i to R_i and $R_{\gamma i}$, it is necessary to know the relative rate at which bubbles with radii within the ith interval intersect the beam in such a way as to have an apparent radius within the jth interval. This quantity, to be called A_{ij}, can be expressed as

$$\mathbf{A} = A_{ij} = \frac{1}{R_i} \int_{p_i}^{p_{i+1}} dr \int_{z(r,p_{j+1})}^{z(r,p_j)} ds \int_0^\infty dv \cdot R(r,v,s) \quad (14)$$

where $z(r, p_j)$ is the value of s which would result in an apparent radius of p_j for a bubble of radius r. Specifically,

$$z(r,p_j) = r_{50}(r) \cdot [1 - (f_v(r) \cdot p_j)/r_{50}(r)]^{1/2}$$

$$0 \le z(r,p_j) \le s_m(r)$$

Thus, the expected value of Γ and $\mathbf{Q}$ are given by

$$E(\mathbf{\Gamma}) = \mathbf{A}^T \mathbf{R}_\gamma \quad (15)$$

$$E(\mathbf{Q}) = \mathbf{A}^T \mathbf{R} \quad (16)$$

Substituting equation (10) and (13) into equations (15) and (16),

$$\mathbf{TN} + E(\mathbf{\Gamma}) = 0 \quad (17)$$

$$\tilde{\mathbf{T}}\mathbf{VN} + E(\mathbf{Q}) = 0 \quad (18)$$

where

$$\mathbf{T} = -\mathbf{A}^T\mathbf{H} \quad \text{and} \quad \tilde{\mathbf{T}} = -\mathbf{A}^T\mathbf{G}$$

and superscript T denotes transpose. Equations (17) and (18) can be used to determine $\mathbf{N}$ and $\mathbf{V}$ for given $\mathbf{Q}$ and $\mathbf{\Gamma}$.

In developing the above equations, it was implicitly assumed the duration of the data collection period was one unit of time. It is for that reason the rate quantities are not accompanied by a time duration. In addition, the beam length was not explicitly considered. Equation (17) will therefore yield the shape of the number density curve, but not its correct magnitude. The details of properly normalizing this information are considered next.

2d Normalizing the Number Densities. Define

$n(r)dr$ = the number density of those bubbles which have radii between r and $r + dr$,

$I(r)dr$ = the average number of bubbles per unit length of the beam with radii between r and $r + dr$ and whose centers lie within a distance $s_m(r)$ of the beam axis.

From these definitions, it follows that the average number of bubbles per unit length is

$$I_T = \int_0^\infty I(r)dr = \int_0^\infty \pi s_m^2(r) n(r) dr \quad (19)$$

The quantity I_T can be determined by passing a light beam through a distance l of the fluid and monitoring the transmitted light fraction. Whenever a bubble's center is within the distance $s_m(r)$ of the beam axis, the transmitted light will be less than $(1 - \beta)$. Conversely, whenever the transmitted light is measured and found to be greater than $(1 - \beta)$, this indicates there are not bubbles within a distance $s_m(r)$ of the beam axis. If this sampling is done multiple times, a determination can be made of the fraction of paths which have clear path lengths (i.e., no bubbles within $s_m(r)$ of the beam axis) greater than l. This quantity will be labeled $f(l)$.

The concept of a mean clear path length, defined by

$$\lambda = 1/I_T$$

can be used to relate I_T to $f(l)$. If a random spatial distribution of bubbles is assumed, the fraction of paths with a clear path length greater than a given distance, l, will be

$$f(l) = \exp(-l/\lambda) = \exp(-l \cdot I_T)$$

Knowing the value of f yields

$$I_T = -\ln(f)/l \quad (20)$$

Substituting I_T from equation (20) into equation (19), the proper normalizing factor for $\mathbf{N}$ is determined.

3 Statistical Analysis of the Light Beam Data

As shown, it is possible to take the light beam data (i.e., the vectors $\mathbf{Q}$ and $\mathbf{\Gamma}$) and calculate the size distribution and average speeds which would have these measured quantities as the theoretically expected values. In the measured data, however, there are statistical fluctuations which mask the true expectation values. Thus, the desire is not to determine the bubble size distribution for which these $\mathbf{Q}$ and $\mathbf{\Gamma}$ would be precisely the expected values, but rather what is wanted is the "smooth" distribution for which the data would constitute a likely set of measurements.

If the form of the functions describing the size distribution and average speed were known a priori, then a straightforward least squares process to determine the curve parameters could be used. Some arguments concerning the type of equation which should fit the speed data could be made, but there is very little literature on bubble size distributions. Thus, rather than force the data to fit a specific type of equation, a general approach was taken utilizing cubic splines, which would let the data determine the shape of the size distribution.

In the inversion procedure with cubic splines, both the large and small ends of the number density distributions often show a significant amount of uncertainty. At the large end, the uncertainty is due to a shortage of statistics on the very large bubbles. This is a limitation of the technique and a point which must be considered in deciding whether the technique is appropriate to a given problem. At the small end, the difficulty is due to "pollution" of the small bubble statistics by large and medium size bubbles which passed through the beam off-center. In the author's experience, however, the void fraction contribution from the small bubbles with poor statistics was completely negligible.

4 Testing the Analysis Procedures

The computations involved in analyzing a set of data are rather involved. Thus, to ensure proper functioning of the routines, a test was performed on a set of data for which the "true" size distribution was known. Such a data set was obtained via a Monte Carlo simulation program. Input consisted of specified size and speed distributions, and the code's output was a simulated set of data. Shown in Fig. 3 are both the specified void fraction distribution and the distribution generated by analyzing 2000 simulated bubble intersections. The error bars indicate the statistical uncertainty due to the finite amount of data. The closeness of the match gives assurance that the methods specified are sound in both theory and implementation.

5 Accuracy Evaluation of the Light Beam Method

It has been shown how the data collected from the light beam probe can be analyzed to yield size distributions and average velocities. This work was based on the assumptions that the bubbles were spherical and that they traveled in straight lines at constant speeds while in the beam. Just how rigidly these assumptions must hold will now be considered.

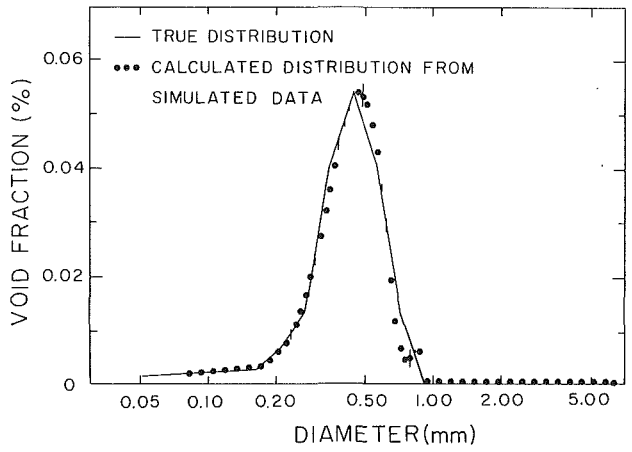

Fig. 3 Void fraction distribution from Monte Carlo simulated data

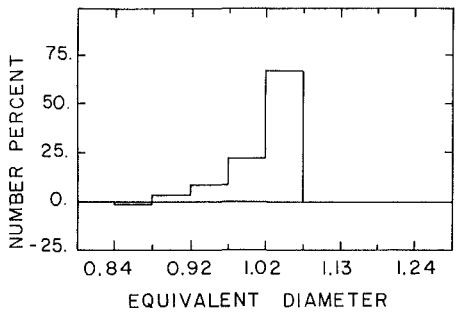

Fig. 4 Equivalent sphere number density distributions for randomly oriented oblate ellipsoids with dimensions of 0.9 × 1.05 × 1.05 units and volume of a unit sphere

5a Effects of Nonspherical Bubbles in the Data. The bubbles that pass through the beam will not be perfectly spherical and will, therefore, generate apparent size distributions different than those of spheres. It is generally known (Clift et al. [18]) that small bubbles take on an oblate ellipsoid shape, with the short dimension oriented vertically, when surface tension is not quite sufficient to keep them spherical. If such bubbles rise through the beam with no horizontal motion or tilting of the vertical axis, their resulting signals will be interpreted as being due to spheres with diameters approximately equal to the short dimension of the ellipsoid. In turbulent flows, however, due to wobble and movement in random directions, bubbles will yield signals which indicate a spread of diameters. To study these effects, a computer simulation involving random orientations of an oblate ellipsoid was undertaken. The result, shown in Fig. 4, is a distribution of sphere sizes which would produce the same data. In Fig. 4, the horizontal scale is logarithmic with sphere size distribution divided into logarithmically equal interval. If the short dimension of the ellipsoid were aligned with the flow, the percentage number in the column with sphere diameter between .88 and .92 would be 100 percent. For random distribution, the data is smeared with a bias toward the 1.05 diameter. The negative number percent between diameters .84 and .88 is a consequence of an apparent size distribution which is impossible to obtain with spheres. For nonspherical bubbles, it is clear that the resolution of the method will decrease with increasing deviations from sphericity, but for small deviations (less than 20 percent difference between principle diameters), the results will remain fairly reliable.

5b The Constant Speed Assumption. The effects of assuming the bubbles having a constant velocity while in the beam can be determined through a relaxation of that requirement. The result, from Meernik [17], is that small constant accelerations introduce, to the first degree, no biases in the data. Once again, therefore, the effect of bubbles not conforming to a stated assumption is simply a decrease in the method's resolution.

7 Summary and Conclusion

The described light beam technique can be used to determine the size distribution of spherical, or nearly spherical, bubbles. Implementation of the method involves monitoring the transmitted intensity of a collimated light beam passing through the bubbly media. The light beam diameter should be less than the diameter of the smallest bubbles on which data are desired, while the optical path length should be long enough to accommodate the largest bubbles but short enough so that the probability of two bubbles crossing the optical path simultaneously is small. For each bubble that passes through the beam, the duration of the light blockage and the rate at which the bubble cuts through the beam is measured. By assuming the distance of closest approach between any bubble's center and beam axis to be random, a statistical analysis of a collection of data yields size distributions.

Acknowledgment

This research was partially supported by the Department of Energy.

References

1 Azzopardi, B. J., "Measurement of Drop Sizes," *Int. J. Heat Mass Transfer*, Vol. 22, 1979, p. 1245.

2 Billet, M. L., "Cavitation Nuclei Measurements with an Optical System," ASME JOURNAL OF FLUIDS ENGINEERING, Vol. 108, 1986, p. 366.

3 Ungut, A., Yule, A. J., Taylor, D. S., and Chigier, N. A., "Particle Size Measurement by Laser Anemometry," *J. Energy*, Vol. 2, 1978, pp. 330–336.

4 Yule, A. J., Chigier, N. A., Atkam, S., and Ungut, A., "Particle Size and Velocity Measurement by Laser Anemometry," *J. Energy*, Vol. 1, 1977, pp. 220–228.

5 Lee, S. L., and Srinivasan, J., "Measurement of Local Size and Velocity Probability Density Distributions in Two-Phase Suspension Flows by Laser-Doppler Technique," *Int. J. Multiphase Flow*, Vol. 4, 1978a, pp. 141–155.

6 Lee, S. L., and Srinivasan, J., "An Experimental Investigation of Dilute Two-Phase Dispersed Flow Using LDA Technique," *Proc. 1978 Heat Transfer and Fluid Mech. Inst.*, Stanford Univ. Press, Stanford, 1978b, pp. 88–102.

7 Martin, W. W., Adbelmessih, A. H., Liska, J. J., and Durst, F., "Characteristics of Laser-Doppler Signals from Bubbles," *Int. J. Multiphase Flow*, Vol. 7, 1981, pp. 439–460.

8 Durst, F., and Zare, M., "Laser Doppler Measurements in Two-Phase Flows," U. Karlsruhe, SFB-80/TM/63, 1975.

9 Lee, S. L., and Srinivasan, J., "An LDA Technique for IN SITU Simultaneous Velocity and Size Measurement of Large Particles in a Two-Phase Suspension Flow," *Int. J. Multiphase Flow*, Vol. 8, 1982, p. 47.

10 Semiat, R., and Dukler, A. E., "Simultaneous Measurement of Size and Velocity of Bubbles or Drops: A New Optical Technique," *AIChE J.*, Vol. 27, 1981, p. 148.

11 Wu, J., "Fast Moving Suspended Particles: Measurements of Their Size and Velocity," *Appl. Opt.*, Vol. 16, 1977, p. 596.

12 Buchholz, R., and Schugerl, K., "Bubble Column Bioreactors," *European J. Appl. Microbiol. Biotechnol.*, Vol. 6, 1979a, p. 301.

13 Buchholz, R., and Schugerl, K., "Methods for Measuring Bubble Size in Bubble Column Bioreactors," *European J. Appl. Microbiol. Biotechnol.*, Vol. 6, 1979b, p. 314.

14 Herringe, R. A., and Davis, M. R., "Structural Development of Gas-Liquid Mixture Flows," *J. Fluid Mech.*, Vol. 73, 1976, pp. 97–123.

15 Calderbank, P. H., "Physical Rate Processes in Industrial Fermentation, Part I: The Interfacial Area in Gas Liquid Contacting with Mechanical Agitation," *Trans. Inst. Chem. Engrs.*, Vol. 36, 1958, p. 443.

16 Meernik, P. R., and Yuen, M. C., "An Optical Method for Determining Bubble Size Distributions – Part II: Application to Bubble Size Measurement in a Three Phase Fluidized Bed," published in this issue pp.

17 Meernik, P. R., "An Optical Technique for the Determination of Bubble Size Distributions and Its Application to a Three-Phase Fluidized Bed System," Ph.D. Dissertation, Northwestern University, 1983.

18 Clift, R. Grace, J. R., and Webber, M. E., "Bubbles, Drops and Particles," Academic Press, New York, N.Y., 1978.

APPENDIX A

Laser Beam Refraction by a Bubble

Figure 2 of reference [16] shows a typical laser beam system for the present study. Both the laser injection and receiving probes which are 10 mm apart have a tip with an inside diameter of 0.38 mm to minimize flow disturbance and to provide a narrow field of view. The two probes are initially aligned such that a Gaussian laser beam from the injection probe, which is focused by a 100 mm focal length lens to give a beam waist diameter of approximately 120 μm, will be collected in the receiving probe by a 1 mm diameter optical fiber. The field of view of the receiving probe is such that a refraction of the laser beam by an angle of 0.02 radian is sufficient to miss the light collecting optical fiber inside the receiving probe. This means that for the present system, a light ring at $s = 0.2\,r$ will not be collected by the present probe. Detail of the probe design is shown in reference [17].

For a finite size Gaussian beam, even if the beam axis passes through the center of the bubble ($s=0$), not all the beam energy will be collected by the receiving optics. For the present optics with a Gaussian laser beam diameter of 120 μm ($1/e^2$ diameter), the maximum fractions of beam energy that are collected is significant only for bubble diameters above 2.5 mm. For example, at $r = 1.0$ mm, the fraction is .05, at $r = 2.5$ mm, the fraction is 0.29 and at $r = 5$ mm, the fraction is 0.75. Thus, if the beam passes centrally through a large bubble (larger than 2.5 mm), a signal such as shown in Fig. A1 could result. However, the same signal could result from two bubbles passing through the beam very close together.

In our particular work, in which the number of large bubbles was small compared to the number of bubbles less than 2.5 mm in diameter, we guarded against the possibility of counting two small bubbles as a single large bubble. A set of four criteria were developed which were required to be satisfied before the signal would be interpreted as coming from a single large bubble.

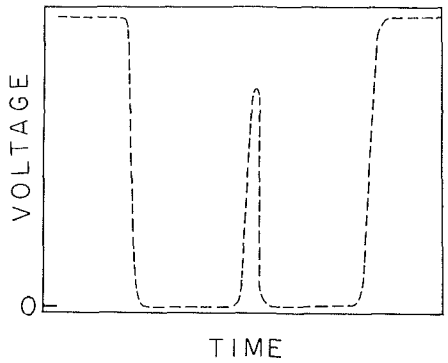

Fig. A1 Signals from light beam probe near center of the bubble

1. The signal had to go to zero on both sides of the central hump.
2. The maximum value of the hump had to be less than 30 percent of the full signal.
3. Speeds determined from the entrance and exit slopes had to agree within 15 percent.
4. The difference in duration of the two halves of the signal had to be less than 30 percent of the total signal duration.

These criteria are admittedly somewhat arbitrary, and will result in the dismissal of at most a few percent of the data on the largest bubbles. It is, however, a reasonable means of dealing with those relatively few cases in which the bubble cannot be considered opaque.

An Optical Method for Determining Bubble Size Distributions—Part II: Application to Bubble Size Measurement in a Three-Phase Fluidized Bed

P. R. Meernik[1]

M. C. Yuen
Mem. ASME

Department of Mechanical Engineering,
Northwestern University,
Evanston, IL 60201

The light beam technique, described in Part I of a paper with the same title, was applied to a three-phase system (nitrogen, organic solvents, and glass particles) to study the equilibrium bubble size distributions. A range of liquid and gas flow rates, with respective superficial velocities of 1–8 cm/sec and 0.1–1.1 cm/s; and various particles, 2 mm diameter by 5 mm long cylinders and 1 to 5 mm diameter spheres, were considered. Typical average bubble diameters were measured to be in the range of 1.2 to 2 mm. For the range of flow conditions considered, the Sauter mean diameters, normalized by particle size, were found to be proportional to the Eotvos number and essentially independent of the liquid and gas fluxes.

1 Introduction

The purpose of developing the bubble size measurement technique, presented in the previous paper by Meernik and Yuen [1], was to determine the factors controlling bubble sizes in a three-phase fluidized bed. In this paper we describe the application of the light beam method of measuring bubble sizes and, based upon collected data, develop a nondimensional expression relating bubble sizes to system parameters.

A fair amount of literature exists concerning different aspects of three-phase fluidized beds. Of these who have measured bubble sizes, Massimilla [2], Rigby et al. [3], and Page and Harrison [4] confined themselves to beds of small particles (about one millimeter in diameter or less). With water as the liquid phase, this resulted in average bubble sizes in the 4 to 20 mm range. The smaller sizes were generally measured at the gas distributor, with diameters increasing due to coalescence as the bubbles rose through the bed. Those who have studied beds of larger particles, one to eight millimeter diameters, include Lee [5], Kim et al. [6, 7], Bruce and Revel-Chion [8], and Lee and Buckley [9]. References [6–8] looked at gas fluxes in ranges of industrial importance (superficial velocities of approximately 5 cm/s and higher) and measured average bubble sizes from 6 to 80 millimeters. Reference [5] provides some information on a water fluidized bed of six millimeter diameter particles in which air bubbles broke up until average diameters of roughly 2.4 millimeters were achieved. The gas flux was 4 cm/s. In references [9], information is provided on bubbles in both water and octanol fluidized beds of four and six millimeter diameter particles. At low gas fluxes with the six millimeter particles, average bubble sizes were stated to be 1.9 mm and 1.3 mm for, respectively, water and octanol. These diameters given by reference [5], along with reference [9], are much less than those quoted by the other two investigators for beds of six millimeter diameter particles. The discrepancy is probably due to the fact that reference [8] used a rather short settled bed height (32 cm), while references [6 and 7] were primarily interested in much higher gas fluxes (superficial velocities up to 53 cm/s).

Despite the above investigations, there is currently very little understanding of the breakup and coalescence mechanisms which determine bubble sizes in three-phase fluidized beds. Due to this lack of understanding, one cannot, working from information in the above cited papers, predict with much confidence what bubble sizes would be expected in other systems with different fluids and/or particles. This paper addresses that problem.

2 Experiment

Before considering the hardware involved in applying the light beam technique, the fluidized bed system (Fig. 1) in which the measurements were made will be described. The column containing the bed was approximately 3.66 m high and 15.2 cm in diameter. It was made up of four, 61 cm long, pyrex glass pipe sections. These sections were separated and held in place by four spool pieces. These pieces had both 2.54 cm and 1.27 cm diameter access ports. Inlet and outlet plenums made up the remainder of the column.

Accessory equipment associated with storing and moving the liquid included a .435 m^3 holding tank and a magnetic

[1]Present Address: General Motors Research Lab., Warren, MI.

Contributed by the Fluids Engineering Division for publication in the JOURNAL OF FLUIDS ENGINEERING. Manuscript received by the Fluids Engineering Division January 15, 1987.

Table 1 Fluid properties

Chemical	Density (gm/cm^3)	Viscosity (cP) 10^{-3} NS/m^3	Surface tension 10^{-3} N/m	Refractive index	% in mixture
Dipropylene Glycol Monomethyl Ether	0.95[1]	3.2[2]	28.8[2]	1.419[1]	66
Diphenyl Ether	1.07[3]	3.9[2]	42. [4]	1.579[2]	34
Mixture	0.99[1]	3.2[1]	29. [1]	1.474[2]	66

[1]20 °C, [2]25 °C, [3]30 °C, [4]Calculated based upon chemical formula.

Table 2 Particulate properties

Particles	Density (gm/cm^3)	Average dimensions (mm)	Type of glass
2 × 4 mm Cylinders	2.24	Diam. 2.1, Length 5.7	Pyrex
1 mm Spheres	2.49	1.10 ± 0.10	Soda Lime
2 mm Spheres	2.49	2.04 ± 0.07	Soda Lime
3 mm Spheres	2.49	2.99 ± 0.07	Soda Lime
5 mm Spheres	2.49	4.96 ± 0.06	Soda Lime

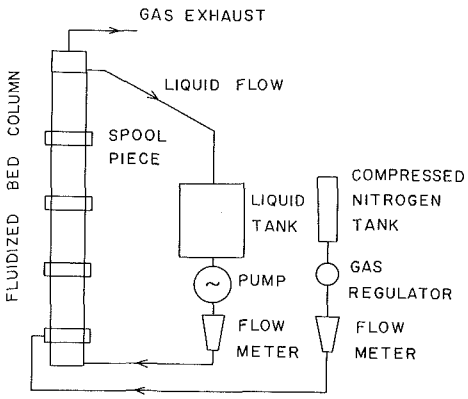

Fig. 1 Schematic of experimental setup

drive pump. The gas supply was provided by tanks of nitrogen. It was routed into the column via the bottom most spool piece and a gas sparger. The sparger was a length of .95 cm diameter copper tubing which spanned the diameter of the column. Five, 1.6 mm diameter holes spaced approximately 2.54 cm apart served as a means of injecting relatively large bubbles (a few centimeters or so in diameter) into the bottom of the bed.

The initial solids used in the column were pyrex glass cylinders. These were nominally 2 mm in diameter and 5 mm long. The fluid used was a mixture of two organic solvents in a proportion such that the refractive index of the fluid matched that of the glass cylinders. The intention was to make possible the use of optical techniques within the bed. Property values of the constituent fluids and the mixture are given in Table 1.

In addition to the pyrex glass cylinders, spherical glass balls with diameters of 1, 2, 3, and 5 mm were used. Basic data on the solids are provided in Table 2. The settled bed heights were approximately 70 cm.

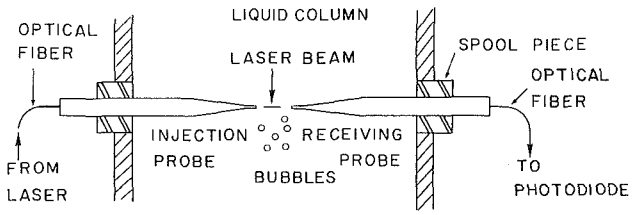

Fig 2 Light beam method

Figure 2 indicates the hardware arrangement used to implement the light beam method. The configuration was dictated by beam length and diameter considerations. Beam length must be short enough to minimize the possibility of more than one bubble in the beam at once, yet long enough to allow larger bubbles to pass through the beam. In regards to the beam diameter, it must be less than the diameter of the smallest bubbles on which size information is desired. For the present experiment, where bubble sizes were primarily in the range of 0.1 mm to 4 mm, a beam diameter of 0.1 mm and

Nomenclature

d_m = Sauter mean bubble diameter
d_s = particle diameter
E_o = $\sigma/[\Delta\rho d_s^2 g]$ Eotvos number
F_r = $u_l/[d_s g]^{1/2}$ Froude number
g = gravitational acceleration
p = apparent bubble radius
Q_i = number of bubbles with apparent radius in the ith interval
R_e = $\Delta\rho u_l d_s/\mu$ Reynolds number
u_l = liquid superficial velocity
u_g = gas superficial velocity
w = speed at which a straight edge must pass through the beam to yield the measured rate of change of light intensity at the instant of 50 percent light blockage
α = void fraction
γ = $(\tau/2w)^{1/2}$ = weighting function for frequency distribution
Γ_i = summation of the quantities γ associated with bubbles in the ith apparent size range
μ = liquid viscosity
ρ = liquid density
$\Delta\rho$ = $\rho_s - \rho_l$
σ = surface tension
τ = time duration of the light blockage by a bubble (time during which the light beam signal is below 50 percent)

Subscript

d = diameter
g = gas
l = liquid
s = solid
t = total

Table 3 Experimental condition

	u_l (cm/s)	u_g (cm/s)	α
Cylinders	2 to 7	0.14 to 1.1	.01 to .09
5 mm Sphere	4 to 8	0.14 to .44	.01 to .04
3 mm Sphere	1 to 8	0.14 to .44	.01 to .04
2 mm Sphere	4 to 6.5	0.14	.01

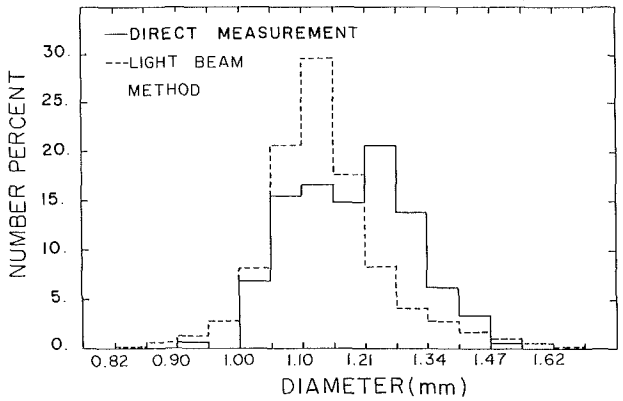

Fig. 3 Comparison of size distributions of glass balls by light beam method and direct measurement

beam lengths of 10 mm or less were used. Thus, with a column diameter of 15.2 cm, it was necessary to use probes, as shown in Fig. 2, for light injection and collection. Besides being necessary, the use of probes makes possible local measurements. To minimize flow disturbance, the probe tips, consisting of an optical fiber enclosed in stainless steel tubing, were made as small as possible (0.8 mm diameter).

The light source used was a 5 mw He-Ne laser. To simplify alignment problems, an optical fiber carried the light to the light injection probe. A single mode fiber was chosen so that both the coherency of the laser light and the desirable Gaussian distribution of the light intensity would be maintained. The light receiving probe, through a lens system, focused the transmitted light into another optical fiber which finally carried the light to a photodiode. The photodiode's output was amplified and fed to a mini-computer for digitization, storage, and subsequent analysis. The detail is described in Meernik [10].

For quantitative interpretation of experimental data, a precise measurement of beam diameter was required. The calibration was performed, at the start of a data collection session, by passing a piece of stainless steel tubing (diameter of 0.82 mm) through the beam roughly ten times. Based upon how quickly the beam was cut off, and for how long, each passage through the beam yielded a beam diameter. The average value obtained from this process was used during the subsequent collection of data. The beam diameter, generally determined to within two percent, depended primarily on the focusing optics and secondarily on the alignment of the beam through the probes.

Typical signals from the light beam probe are shown in Fig. 1 of Meernik and Yuen [1]. The time interval between data points is 50 microseconds. It was found that roughly 2000 such intersections yielded sufficient data for a reasonable analysis of the size distribution.

As described in Meernik and Yuen [1], information from each bubble intersection is reduced to the duration of blockage (τ) and the light blockage rate (w). The apparent radius p and weighting function γ are then immediately given by

$$p = \tau w/2$$

and

$$\gamma = (\tau/2w)^{1/2}$$

With the range of apparent radii discretized into logarithmically equal intervals (100 intervals at 5 percent increments), Q_i and Γ_i are calculated according to reference [1]. Analysis of these distributions then leads to the average density distribution. The entire procedure is involved, but a computer program rendered the data analysis automatic.

As an overall check of the light beam technique, the following test was performed. With the fluid level in the experimental column approximately 30 cm above the probes, glass balls with an average diameter of 1.2 mm were sprayed with a stream of air into the top of the column. Light beam data were then collected as the balls fell through the beam.

Histograms of the glass ball size distribution as determined by both the light beam method and measurements on optically magnified particles are shown in Fig 3. As can be seen, there is only about a five percent difference between the means of the two distributions although in a given size range the difference can be as large as 50 percent. The sample size was large enough that the differences are considered to be primarily due to systematic rather than statistical error. In particular some of the difference is believed to be a consequence of the nonideal spheres (approximate average difference between maximum and minimum diameters for a given ball was 5 percent), and the relative coarseness of the measurement intervals when compared to the width of the distribution. Based upon this information, the mean bubble size data presented in this paper is expected to have errors of less than 5 percent.

Returning now to the fluidized bed system, data collected with the light beam method involved a range of liquid flows such that bed conditions from incipient fluidization up to at least 75 percent bed expansion were achieved for all but the five millimeter diameter particles. The maximum bed expansion with the five millimeter spheres, 40 percent, was somewhat less due to the limited flow capacity of the system. Gas flow rates were generally restricted so that void fractions remained below five percent. This limitation was due to difficulties, to be discussed below, in obtaining good data at higher void fractions. Table 3 depicts the range of conditions at which data were obtained for each of the different particle sizes.

Void fractions above five percent resulted in data collection problems. Probes had to be close enough together to minimize occurences of multiple bubbles in the beam, but separated enough to allow physical passage of the larger bubbles between the probes. In most cases, calculated size distribution curves showed reasonable safety margins between the largest measured bubble sizes and the largest sizes that could be measured. Answers to questions concerning multiple bubbles in the beam, however, were not quite so straightforward.

The possibility of biased data due to simultaneous bubble intersections was investigated by collecting sets of data at identical flow conditions but using different beam lengths. The results show that if the blockage time fraction is below 15 percent, the effect of different beam lengths on the data is negligible. Blockage fractions greater than that quantity showed progressively greater effects on the size distribution curves. Of all the data presented in this paper, only those few cases having gas superficial velocity of 1.0 cm/s or higher involve blockage fractions greater than 15 percent.

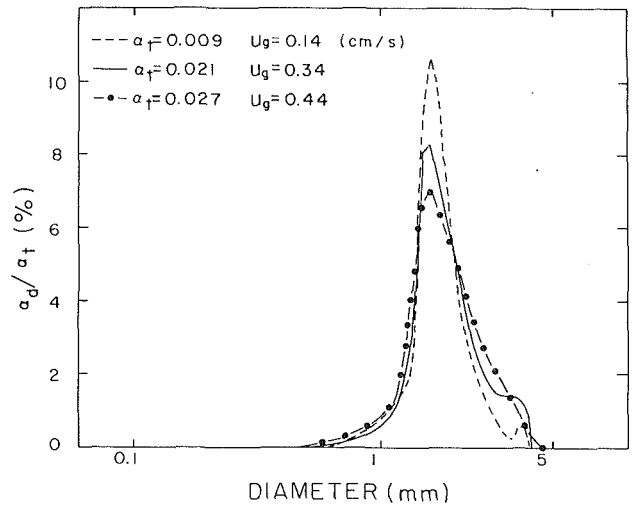

Fig. 4 Normalized bubble size distributions for a fixed liquid flux (cylinders, $u_1 = 4.01$ cm/s)

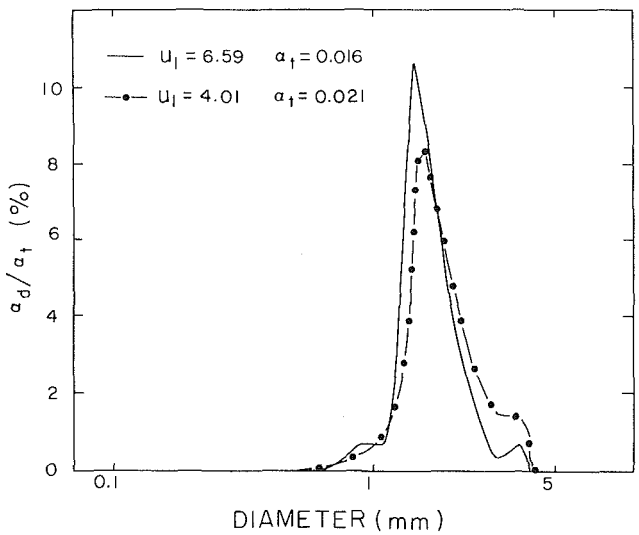

Fig. 5 Normalized bubble size distributions for a fixed gas flux (cylinders, $u_g = 0.34$ cm/s)

Before going on to the results, let us address the question of data collection within the fluidized bed. As should be clear from the use of glass particles and a liquid of the same refractive index, one goal of this research effort was to obtain bubble size information within the bed. However, even though one could see through the bed, the quality of data obtained within the bed was very poor.

Visual observations revealed that the bubbles travel very erratically in the bed. They essentially "bounce" along with frequent stops when they get stuck beneath groups of particles. As a confirmation check that this was indeed the problem, one set of data was obtained with the probes just above the top of the bed and another with them just below. For each set, the average percent difference between the beam entrance and exit speeds were calculated. Theoretically, for steady bubble velocities through the beam, the two speeds should be identical. For the case of the problem just above the bed, the average difference was 10 percent, but the probes within the bed the figure was 32 percent. Clearly the bubbles in the bed were not passing through the beam in a steady manner and data collection within the bed was deemed unfeasible.

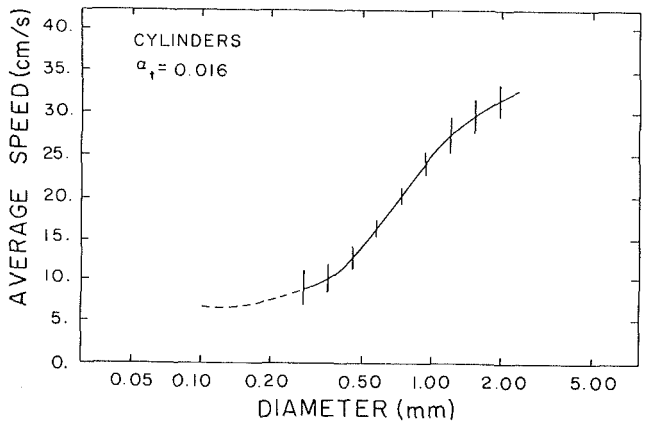

Fig. 6 Bubble speed distribution (cylinders, $u_1 = 6.59$ cm/s, $u_g = 0.34$ cm/s)

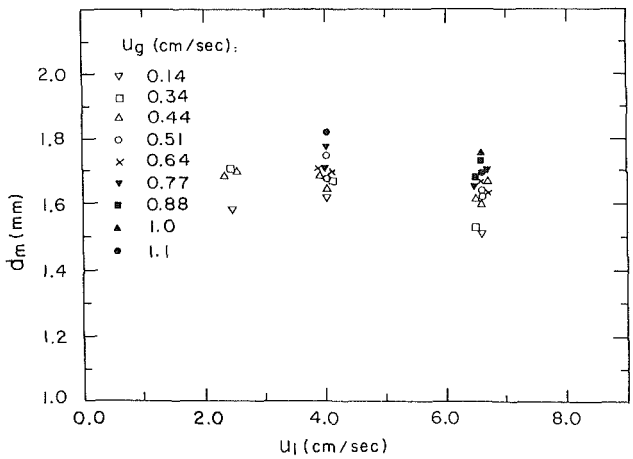

Fig. 7 Effect of liquid flow rate on Sauter mean diameter (cylinders)

3 Experimental Results

3a Cylindrical Particles. The most extensive data was obtained using the cylindrical particles of pyrex glass. Figures 4 and 5 show measured bubble size distributions at the column centerline, for a representative sample of liquid and gas flow rates. As can be seen, the bulk of the void fraction distribution for each of these cases falls within a fairly narrow size range of bubbles. Figure 4 shows the size distribution curves for a fixed liquid flux and increasing gas flux. It appears that the relative volume of gas in the larger bubbles increases slightly with the gas flow rate. Figure 5 shows, for a fixed gas flux and varying liquid flux, that large bubbles are more thoroughly broken up at the higher liquid flux.

Even though the emphasis of this paper is on bubble number density and size distribution, nevertheless the bubble speed distribution can also be calculated. Figure 6 shows a typical distribution as a function of bubble diameter. The bars represent the statistical uncertainty due to the finite sample size. The data cut-off at about 0.3 mm diameter is due to the contamination of data in the smaller apparent size range by the larger bubbles. Because the small bubbles contribute insignificantly to the total gas volume, the lack of good speed information on them has virtually no effect on the void fraction distribution.

Figure 7 is a summary plot of the Sauter mean diameters obtained with cylindrical particles. These diameters have a small increasing trend with increasing gas flux, and a slight decreasing trend with increasing liquid flux.

Figure 8 shows the nearly uniform Sauter mean diameter

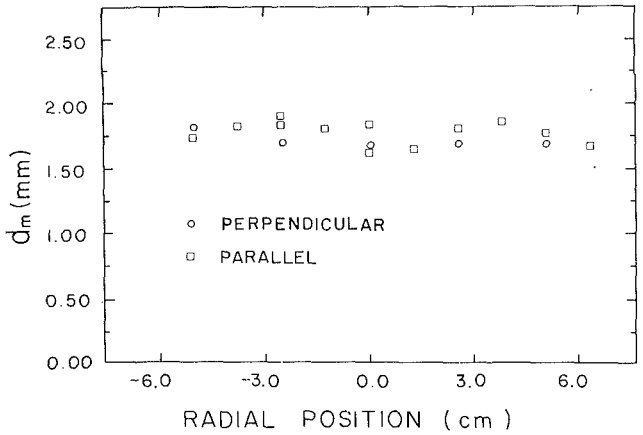

Fig. 8 Radial distribution of Sauter mean diameter (cylinders, u_1 = 4.01 cm/s, u_g = 0.34 cm/s)

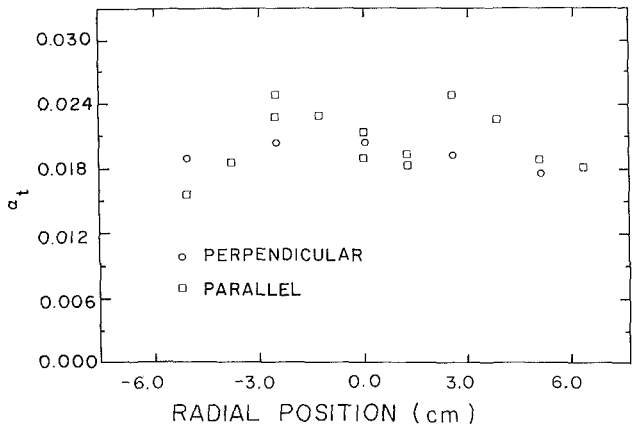

Fig. 9 Radial distribution of void fraction (cylinders, u_1 = 4.01 cm/s, u_g = 0.34 cm/s)

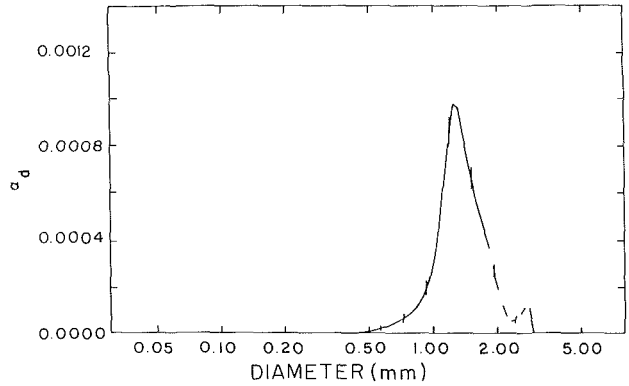

Fig. 10 Bubble size distribution (5 mm spheres, $u_1 = 6.59$ cm/s, $u_g = 0.14$ cm/s, $\alpha = 0.011$)

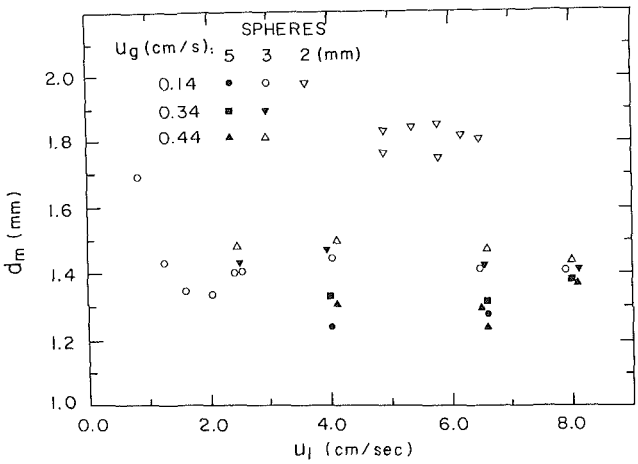

Fig. 11 Sauter mean diameters versus liquid flow rate

obtained with traverses both parallel and perpendicular to the gas sparger. Figure 9 shows the corresponding void fraction distributions. It indicates some radial variation along the axis parallel to the gas sparger, a possible consequence of recirculation patterns in the bed.

3b Spherical Particles. To check the dependence of bubble size distributions on particle size, beds of uniformly sized glass balls with diameters of 1.0, 2.0, 3.0, and 5.0 millimeters were studied. The physical characteristics of these balls were provided in Table 2. The bubble size distributions obtained with them have essentially the same characteristics as those obtained with the cylinders, except for shifts in the mean sizes. A typical size distribution curve for a bed of 5 mm spheres is shown in Fig 10. The error bars in this figure indicate the statistical uncertainty in the size distribution due purely to the finite amount of data collected. Other possible error sources, including multiple bubbles in the beam, bubbles too large to pass between the probes, the measurement of beam diameter, and effects of nonspherical bubbles have been considered elsewhere in this set of papers. The dashed portion of the curve indicates the number of counts in an interval (i.e., Q_i) dropped below four. The interval with maximum counts typically had 50 to 100.

Figure 11 shows the Sauter meam diameters of bubbles for the 2 mm, 3 mm, and 5 mm diameter beds as a function of liquid and gas flow rate. The experimental data indicates that bubble diameter is primarily a function of particle diameter and is relatively independent of both the liquid and gas flow rate. The only exception is the data for 3 mm diameter particles with u_g at 0.14 cm/s and u_l below the minimum fluidizing velocity of 2.4 cm/s. For this case, the mean bubble size reaches a minimum just before fluidization. At still lower liquid flow rates the mean bubble size increases. The data also show that the larger particles are more effective in breaking up bubbles; thus the mean sizes of the bubbles increase with decreasing size of the particles.

With a bed of two millimeter diameter spheres, visual observation shows that even at the low gas flow rate of 0.14 cm/s, relatively large bubbles (up to 1 cm in diameter) pass through the bed at the low liquid flow rates. Apparently, 2 mm diameter particles are marginal in breaking up large bubbles and require the assistance of fluid motion produced at the higher liquid fluxes. As a consequence, data were only taken for the 2 mm particles at a superficial gas velocity of .14 cm/s and superficial liquid velocities above 4.9 cm/s.

One millimeter diameter spheres resulted in essentially no breakup of large bubbles. Due to large, nonspherical bubbles, no light beam data were taken. One visual observation was that the bed height did decrease when gas flow was initiated. No such decrease was noted with any of the other particles.

4 Analysis of Results

Two definite patterns emerged from the bubble size distribution data. First, at void fractions of a few percent and with particles larger than the two millimeter diameter spheres, the bubbles are fairly uniform in size and generally smaller than the associated particles. Bubble sizes vary with particle sizes, but are nearly independent of the liquid and gas fluxes. Secondly, the smaller particles appear to lack the ability to break up large bubbles. The two millimeter spheres are only

capable of such action at very low void fractions, while the one millimeter spheres are apparently incapable of generating sufficient force to cause any bubble breakup.

In order to account for these patterns, a two-stage bubble breakup model is proposed. The first stage concerns the initial break up of large bubbles and will be essentially qualitative. The second stage is quantitative and concerns the achievement of stable size distributions.

Based on the present experimental results and visual observations of the fluidized bed systems, it was apparent that the larger particles were far more efficient at breaking up large bubbles than were the smaller particles. Previous models, typified by that of Henriksen and Ostergaard [11], concentrated on the breakup of a large bubble by a single particle falling through the central portion of the roof of the bubble. The breakup mechanism in that case is due to Taylor instability. More pertinent to fluidized beds, where particles are densely packed, we propose a stripping model. It is hypothesized that when a large bubble rises through the fluidized bed, the interaction of particles with the edge of the bubble strips off quantities of gas whose volume, order of magnitude wise, is roughly equal to that of the particle. For the following reasons, such a mechanism would account for the inability of small particles to break up large bubbles:

1) Small particles would be less likely to pass through the edge of the bubble since the "edge" for a small particle is a much smaller region that for a large one.

2) Small particles near the edge would be much more likely to be swept around the bubble with the liquid flow than would large particles.

3) Small particles that did pass through the edge of the bubble would strip off smaller volumes of gas than would large particles.

The second stage of the bubble breakup model involves the achievement of an equilibrium bubble size distribution in a bed of given size particles. To begin, it seems likely the mean bubble size in a stable distribution of bubble sizes should be expressable as

$$d_m = f_1(\rho_1, \rho_s, d_s, \sigma, \mu, u_1, g)$$

where d_m = Sauter mean bubble diameter
d_s = particle diameter
ρ_1 = liquid density
ρ_s = solid density
σ = surface tension
μ = viscosity
u_1 = liquid superficial velocity
$\Delta\rho = \rho_s - \rho_1$

By limiting consideration to size distributions in the case of low void fractions, the inclusion of gas superficial velocity is avoided. Through dimensional analysis, the functional dependence of mean diameter on the above quantities can be written as

$$d_m/d_s = f_2(\Delta\rho/\rho_1, \sigma/(\Delta\rho d_s^2 g), \Delta\rho u_1 d_s/\mu, u_1/(d_s g)^{1/2})$$

The dimensionless groups in this expression are:

$\Delta\rho/\rho_1$ = ratio of the solid-liquid density difference to the liquid density
$\sigma/(\Delta\rho d_s^2 g)$ = Eo (Eotvos number)
$\Delta\rho u_1 d_s/\mu$ = Re (Reynolds number)
and $u_1/(d_s g)^{1/2}$ = Fr (Froude number)

To obtain an explicit functional relationship between mean bubble size and particle size, we make a few simplifying assumptions. First, the slight bubble size dependence upon liquid flow rate exhibited in the data will be ignored. This makes it possible to delete the individual Re and Fr numbers

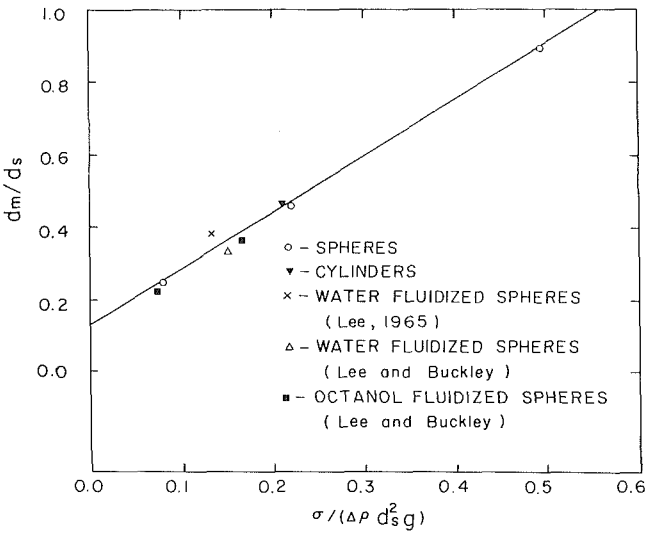

Fig. 12 Dimensionless bubble size versus Eotvos number

from consideration and replace them with the single dimensionless group

$$\Delta\rho d_s^{3/2} g^{1/2}/\mu = \text{Re/Fr}$$

Next, since there was little variation in the density of the particles (the spheres were all of the same density and the pyrex cylinders only slightly less dense) and only one fluid was used, the term $\Delta\rho/\rho_1$, is nearly constant. It will be thus ignored. This leaves only the Eotvos number and the Re/Fr group.

From a physical point of view, one would expect the term involving surface tension, the Eotvos number, to be the most important. Furthermore, visual observations of bubbles moving through the bed of cylindrical particle showed that as they rose, they often become trapped temporarily beneath a particle or group of particles. During these moments, it is likely that the forces on the bubbles are the largest attained during the course of a bubble's travels. Thus, it should be at these times that a bubble is most likely to break up. Taking the ratio of the surface tension generated pressure to the dynamic pressure that would exit on such a trapped bubble leads to the Eotvos number.

Now, based upon data from different size spheres, d_m/d_s is plotted versus $\sigma/(\Delta\rho d_s^2 g)$. The numbers for this plot, Fig. 12, are given in Table 4. The straight line is based upon the 2, 3, and 5 millimeter diameter particle data, and a least squares calculation. Its equation is,

$$d_m = d_s[1.544(\sigma/(\Delta\rho d_s^2 g)) + 0.143]$$

Reference [4] and reference [8] provide the only other bubble data available on beds of large particles with relatively low gas fluxes. Their data are also summarized in Table 4 and plotted in Fig. 12. As can be seen, the correlation is quite good.

The question of a critical particle size for the break up of large bubbles can now be considered. If a particle is not capable of generating sufficient force to produce a bubble whose size is roughly that of the particle, then, according to the proposed model, large bubble breakup will not occur. By setting d_m equal to d_s in the correlation, the critical diameter can be determined to be 1.89 millimeters for glass particles in our system. While this value is consistent with the data, it could be argued that reasonably efficient breakup of large bubbles requires a particle size somewhat greater than 2 millimeters. Adding 25 percent to the calculated critical size, a value of 2.4 millimeters results. Using this same procedure with water properties, a glass particle size of 3.7 millimeters should be required for efficient breakup of bubbles. This

Table 4 Data for bubble size correlation

Particles	Fluid	Sauter mean diameter	d_m/d_s	$\sigma/(\Delta\rho d_s^2 g)$
5 mm Spheres	Solvents	0.133[1]	0.266	0.0789
3 mm Spheres	Solvents	0.144[1]	0.480	0.219
2 mm Spheres	Solvents	0.181[1]	0.905	0.493
Cylinders	Solvents	0.161	0.481[2]	0.211
6 mm Spheres	Water	0.24	0.400	0.132
6 mm Spheres*	Water	0.19	0.317	0.137
6 mm Spheres*	Octanol	0.13	0.217	0.0700
4 mm Spheres*	Octanol	0.13	0.325	0.157

Sphere density = 2.49 gm/cm^3
*Sphere density = 2.45 gm/cm^3
Cylinder density = 2.24 gm/cm^3

Solvent mixture properties: Density = 0.99 gm/cm^3, Surface tension = .029 N/m

Water properties: Density = 1.00 gm/cm^3, Surface tension = .07 N/m

Octonol properties: Density = 0.83 gm/cm^3, Surface tension = .04 N/m

[1]Based upon data at gas fluxes below 0.5 cm/s and bed expansions greater than 20 percent.
[2]Based upon a volume equivalent diameter of 0.335 cm.

value for water is in very good agreement with literature values summarized by Vasalos et al. [12]. From this reference, it appears the critical particle size in water (assuming a solid density of 2.5 gm/cm) is between 3 and 4 millimeters.

5 Conclusions

The light beam method is shown to be a very good means of obtaining size information on small bubbles at void fractions up to about 1 percent. In a three-phase fluidized bed of nitrogen, organic solvent, and glass particles, the experimental data show that the mean equilibrium bubble size is nearly independent of liquid and gas flow and dependent primarily on particle size. In addition, it was shown that the average bubble size could be correlated very well with particle and fluid properties via the Eotvos number.

Acknowledgment

This research was partially supported by the Department of Energy.

References

1 Meernik, P., and Yuen, M. C., "An Optical Method for Determining Bubble Size Distributions—Part I: Theory," published in this issue pp. 00.

2 Massimilla, L., Solimando, A., and Squillace, E., "Gas Dispersion in Solid-Liquid Fluidized Beds," *Brit. Chem. Eng.*, Vol. 6, 1961, p. 632.

3 Rigby, G. R., Van Blockland, G. P., Park, W. H., and Capes, C. E., "Properties of Bubbles in Three Phase Fluidized Beds as Measured by an Electroresistivity Probe," *Chem. Eng. Sci.*, Vol. 25, 1970, p. 1729.

4 Page, R. E., and Harrison, D., "The Size Distribution of Gas Bubbles Leaving a Three-Phase Fluidized Bed," *Powder Tech.*, Vol. 6, 1972, p. 245.

5 Lee, J. C., *Proc. 3rd European Symp. Chem. React. Eng.*, Pergamon Press, 1965, p. 211.

6 Kim, S. D., Baker, C. G. J., and Bergougnou, M. A., "Hold-up and Axial Mixing Characteristics of Two and Three Phase Fluidized Beds," *Can. J. Chem. Eng.*, Vol. 50, 1972, p. 696.

7 Kim, S. D., Baker, C. G. J., and Bergougnou, M. A., "Phase Holdup Characteristics of Three Phase Fluidized Beds," *Can. J. Chem. Eng.*, Vol. 53, 1977, p. 134.

8 Bruce, Y. N., and Revel-Chion, L., "Bed Porosity in Three-Phase Fluidization," *Powder Tech.*, Vol. 10, 1976, pp. 243–249.

9 Lee, J. C., and Buckley, P. S., *Biological Fluidized Bed Treatment of Water and Wastewater*, Halstead Press, Chapter 4, 1981.

10 Meernik, P., "An Optical Technique for the Determination of Bubble Size Distributions and Its Application to a Three-Phase Fluidized Bed System," Ph.D. dissertation, Northwestern University, 1983.

11 Henriksen, H. K., and Ostergaard, K., "On the Mechanism of Break-up of Large Bubbles in Liquids and Three-Phase Fluidized Beds," *Chem. Eng. Sci.*, Vol. 29, 1974, p. 629.

12 Vasalos, I. A., Bild, E. M., Rundell, D. N., and Taterson, D. F., "H-Coal Fluid Dynamics Final Technical Progress Report," AMOCO Oil Company, U.S. Dept. of Energy Contract No. DE-AC05-77ET-10149, 1980.

Journal of Fluids Engineering

Technical Brief

On the Drag Coefficient and the Correct Integration of the Equation of Motion of Particles in Gases

E. E. Michaelides[1]

Nomenclature

c_D = drag coefficient
d = particle diameter
Re = Reynolds number
Re_p = particle Reynolds number
t^* = particle relaxation time
t^+ = dimensionless time
U = gas velocity
U_s = particle velocity
U_s^+ = dimensionless particle velocity
x^+ = dimensionless distance
μ = gas viscosity
ρ_f = gas density
ρ_p = particle density

Introduction

A great deal of work has been accomplished in the area of air particle flows during the last decade. The application of numerical techniques in fluid flows resulted in high activity on the subject of computational fluid mechanics with particles. Among the models developed for the treatment of particle flows in air is the Particle-Source-In Cell (PSI-CELL) model first introduced by Crowe and his coworkers [1]. The techniques of this model were subsequently used by others, including the works in the references [2–6]. In order to make the numerical calculations easier all the above use an integrated form of the equation of motion for the particles. The particle drag coefficient is the main input to this equation and is obtained by an empirical relation [7, 8]. The choice of this empirical coefficient is paramount to the accuracy of the solution of the particle equation of motion.

This short note aims at pointing out how an exact solution to the particle equation of motion can be obtained using the drag coefficient from [7, 8]. It also shows the discrepancies in the obtained results stemming from other approximate solutions or from different drag coefficient expressions.

The Simplified Particle Motion Equation and Its Solution

It is assumed here that $\rho_p/\rho_f \gg 1$ and therefore, the added mass and Basset force terms are neglected. The particle equation of motion will be solved for horizontal motion and for constant fluid velocity, U. Under these conditions, the equation of motion for the particle is:

$$\frac{dU_s^+}{dt^+} = \frac{\mathrm{Re}_p}{24} c_D (1 - U_s^+) \tag{1}$$

where

$$U_s^+ = U_s/U, \tag{1a}$$

$$\mathrm{Re}_p = \frac{d\rho_f |U - U_s|}{\mu} = \frac{d\rho_f U}{\mu} |1 - U_s^+| = \mathrm{Re}\,|1 - U_s^+|. \tag{1b}$$

and

$$t^+ = \frac{t}{t^*} = \frac{t}{\dfrac{\rho d^2}{18\mu}} \tag{1c}$$

The drag coefficient term c_D is given by an empirical relation, such as Stokes Law ($c_D = 24/\mathrm{Re}_p$) or a modification of it ($c_D = 24\,(1 + 0.15\ \mathrm{Re}_p^{0.687})/\mathrm{Re}_p$) which was proposed in [8] and used in [1–6] or by another expression, such as Allen's ($c_D = 30\mathrm{Re}_p^{-0.625}$), [9]. It must be pointed out that this list of expressions is by no means exhaustive. Other expressions for c_D are abundant in the literature.

Substitution of these expressions in (1) yields the following three expressions:

From Stokes Law:

$$\frac{dU_s^+}{dt^+} = 1 - U_s^+, \tag{2a}$$

From the modified Stokes Law, [8]:

$$\frac{dU_s^+}{dt^+} = (1 - U_s^+)[1 + 0.15\mathrm{Re}^{0.687}\,|1 - U_s^+|^{0.687}], \tag{2b}$$

and from Allen's expression:

$$\frac{dU_s^+}{dt^+} = \frac{5}{4}(1 - U_s^+)\mathrm{Re}^{0.375}\,|1 - U_s^+|^{0.375} \tag{2c}$$

The initial condition for the above equations is determined by the particular problem to be solved. It is assumed here for simplicity that the particle started from rest ($U_s^+(0) = 0$). Then the integration of the three equations (2*a*), (2*b*), and (2*c*) yields:

$$U_s^+ = 1 - e^{-t^+} \tag{3a}$$

$$U_s^+ = 1 - [(1 + 0.15\mathrm{Re}^{0.687})e^{0.687t^+} - 0.15\mathrm{Re}^{0.687}]^{\frac{-1}{0.687}}, \tag{3b}$$

and

$$U_s^+ = 1 - [0.469\mathrm{Re}^{0.375}t^+ + 1]^{\frac{-1}{0.375}} \tag{3c}$$

[1]Department of Mechanical Engineering, University of Delaware, Newark, Del. 19716.

Contributed by the Fluids Engineering Division of The American Society of Mechanical Engineers. Manuscript received by the Fluids Engineer Division September 8, 1987.

Equation (3*b*) is the exact and correct solution to the equation (2*b*), where the modified Stokes Law is taken for the drag coefficient. It is different than the expression used in references [1-6], which is:

$$U_s^+ = 1 - (1 - U_{s0}^+)e^{-f\Delta t^+} \tag{4}$$

with

$$f = 1 + 0.15\ \mathrm{Re}_p^{\ 0.687},$$

and $U_{s0}{}^+$ is the solids velocity at the end of the previous time interval.

The difference is due to the assumption that the term in square brackets in equation (2*b*) is constant over the interval Δt^+. This term is not constant, since it contains the solids velocity U_s^+, which is the dependent variable in the differential equation.

At the two limits $t^+ = 0$ and $t^+ = \infty$ all the above equations give identical results for the velocity U_s^+, namely $U_s^+ = 0$ and $U_s^+ = 1$. Between those two values for t^+, however, there is considerable disagreement among the expressions. This disagreement depends on the actual value of t^+ and the parameter Re. The results of equation (4) are always higher than the results of equation (3*b*), because using constant f is tantamount to assuming higher drag coefficient throughout the particle motion.

One way to minimize the velocity discrepancy is to realize that the term in square brackets in equation (2*b*) is not constant and hence to use an updated expression for f after every time step Δt^+. It appears that this updating was used in the original derivation of equation [1] for obtaining particle velocities. However, others (e.g., [5]) have not updated the values for the parameter f. The resulting error in the first case depends on the time step Δt^+ used for the numerical calculations, because this determines how often f is updated. Figure 1 shows the absolute fractional differences of equation (4) and (3*c*) from equation (3*b*) as a function of t^+ and for Re = 500. Two values have been used for Δt^+, $0.02t^+$, and $0.1t^+$. It is observed that Allen's expression results to a maximum error of 11 percent in estimating the particle velocity at $t^+ = 0.1$. Equation (4) when not updated results in high fractional difference, but when updated to take into account the variation of f, this error is smaller. The results of the solution when f is updated approach those of equation (3*b*) when Δt^+ tends to zero. Actually when $\Delta t^+ = 0.02t^+$ almost all of the fractional differences are less than 5 percent. The definition of the absolute fractional differences for Fig. 1 are as follows:

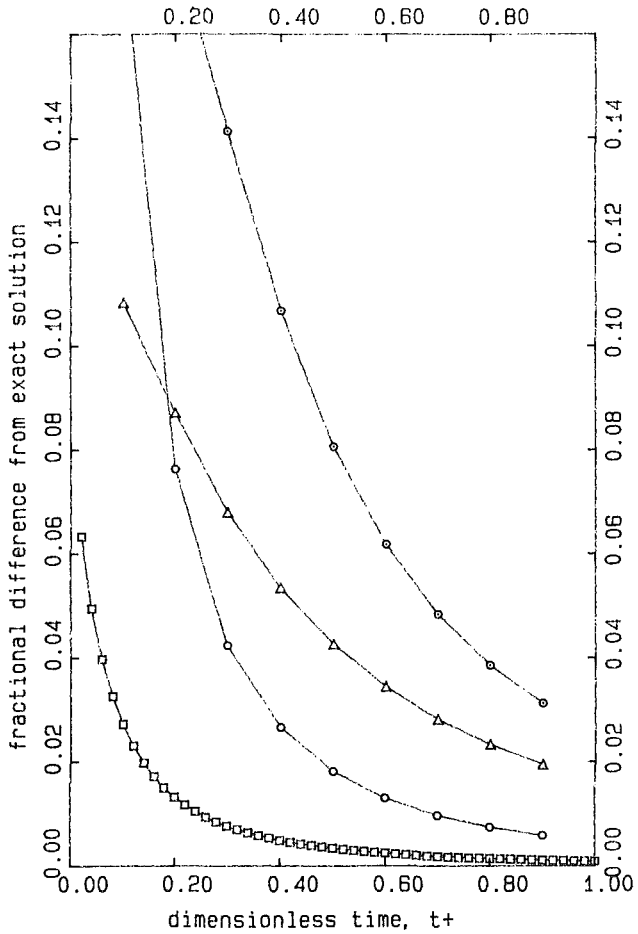

Fig. 1 Fractional differences of the various expressions from equation (3*b*):

- ⊙ from equation (4) without updating f;
- ○ from equation (4) with f updated, and $\Delta t = 0.1t^+$
- □ from equation (4) with f updated, and $\Delta t^+ = 0.02t^+$;
- △ from Allen's expression, equation (3*c*).

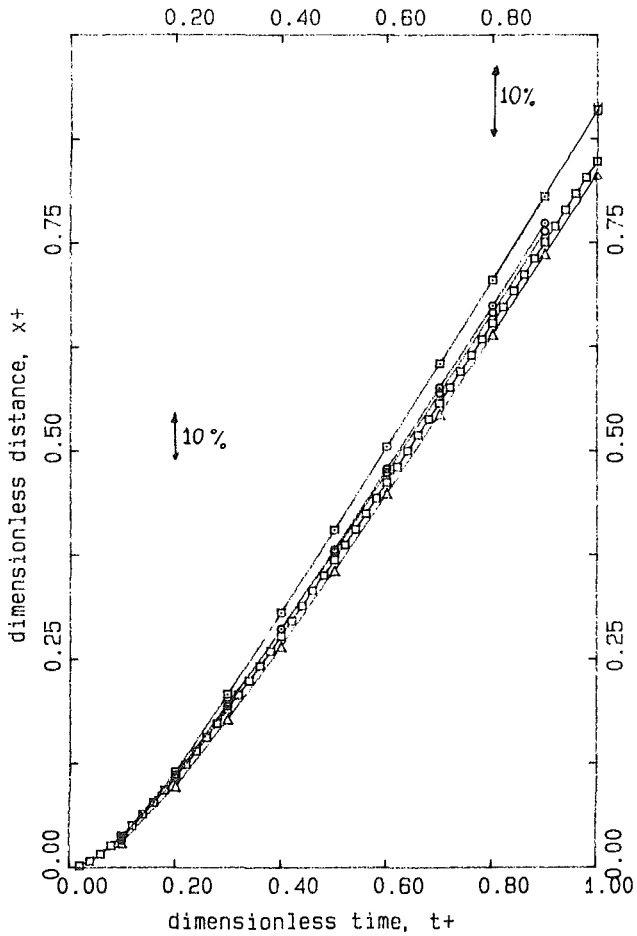

Fig. 2 Dimensionless distances traveled by the particle.

- △ using equation (3*b*)
- □ using equation (4) with $\Delta t^+ = 0.02t^+$;
- ○ using equation 4 with $\Delta t^+ = 0.1t^+$;
- ⊡ using equation 4 without updating f;
- ⊙ using equation 3*c*.

$$e_j = \frac{|U_{s1}^+ - U_{si}^+|}{U_{s1}}, \tag{5}$$

where U_{s1}^+ is the value from expression (3*b*) and U_{si}^+ is the value from (4) or (3*c*) at the same t^+ and Re. It must be pointed out that these differences depend on Re and that they become smaller when Re is less than 500. When $\mathrm{Re} < 1$ these differences are always less than 2 percent.

It must be pointed out that upon integration equations (3*a*) and (3*c*) yield simple algebraic expressions for the position of the particle. Equation (3*b*) may be integrated by a recursion formula to yield a converging series [10]. The results for the dimensionless position of the particle

$$x^+ = \int_0^t U_s^+ \, dt^+ \tag{6}$$

are depicted in Fig. 2. It is observed that the results from expression (3*b*) are always lower, but very close to those obtained from Allen's expression equation (3*c*) and equation (4) with f updated in intervals of $0.02t^+$. Larger errors in x^+ (about 10 percent eventually) are obtained when f is not updated or when it is updated every $0.1t^+$. Again when $\Delta t^+ \to 0$ the results from expression (4) for x^+ are the same as those of equation (3*b*).

The above results for the velocity of the particles and the distance covered serve to illustrate the importance of using the exact expression for the velocity of the particles or the proper choice of Δt^+ when an approximate solution is chosen.

Calculations have shown that if the final error in velocity and position at time $t^+ = 1$ and for $\mathrm{Re} = 500$ is to be less than 5 percent, then in expression (4) the condition for Δt^+ for which the parameter f is updated has to be $\Delta t^+ < 0.1t^+$. The use of expression (4) is not recommended to be used in fast varying velocity fields because the choice of Δt^+ would impose a very low value for the time step in the problem. In contrast, the exact equation (3*b*) may be used at all times.

3 Conclusions

The accurate evaluation of the drag coefficient c_D for particle motion in fluids plays a very important role in the calculation of the velocity of an accelerating or decelerating particle. Similarly the rigorous solution of the equation of motion of a particle is paramount for the determination of the particle velocity and position as a function of time. This short note gives analytical solutions to the particle equation of motion for several expressions of c_D and points out the differences between them.

References

1 Crowe, C. T., Sharma, M. P., and Stock, D. E., "The Particle Source in Cell (PSI-CELL) Model for Gas Droplet Flows," ASME JOURNAL OF FLUIDS ENGINEERING, Vol. 99, No. 2, 1977, pp. 325–332.

2 Durst, F., Milojevic, D., and Schonung, B., "Eulerian and Lagrangian Predictions of Particulate Two-Phase Flows: A Numerical Study," *Appl. Math Modeling*, Vol. 8, 1984, pp. 101–115.

3 Shahnam, M., and Jurewicz, J. T., "Particle Motion Near the Inlet of a Sampling Probe," *Gas-Solid Flows-1986*, ed. J. T. Jurewicz, 1986, pp. 145–150.

4 Kallio, G. A., and Stock, D. E., "Turbulent Particle Dispersion: A Comparison Between Lagrangian and Eulerian Modeling Approaches," *Gas-Solid Flows-1986*, ed. J. T. Jurewicz, 1986, ASME, pp. 23–29.

5 Ushimoru, K., and Butler, G. W., "Numerical Simulation of Gas-Solid Flow in an Electrostatic Precipitator," *Gas-Solid Flows*, ed. J. T. Jurewicz, 1984, ASME, pp. 87–96.

6 Chen, P. P., and Crowe, C. T., "On the Monte-Carlo Method for Modeling Particle Dispersion in Turbulence," *Gas-Solid Flows*, ed. J. T. Jurewicz, ASME 1984, pp. 37–41.

7 Wallis, G. B., *One Dimensional Two-Phase Flow*, McGraw-Hill, New York, 1969.

8 Rowe, P. N., "The Drag Coefficient of a Sphere," *Trans. Inst. Chem. Engin.*, Vol. 39, 1961, pp. 175–181.

9 Govier, G. W., and Aziz, K., *The Flow of Complex Mixtures in Pipes*, R. Krieger Publ., Huntington, 1977 (repr.).

10 Gradshteyn, I. S., and Ryzhix, I. M., *Tables of Integrals Series and Products*, ed. by A. Jeffrey, Acad. Press, Orlando, 1980.

Journal of Fluids Engineering

Discussion

The Trailing Edge of a Pitching Airfoil at High Reduced Frequencies[1]

James S. Uhlman, Jr. The authors state that no inviscid trailing edge model is appropriate when the reduced frequency, k, exceeds a value of about 2.4 and they attribute this phenomenon to a breakdown of the boundary-layer assumption of small pressure gradient normal to the shear layer. This condition may also be expressed as a violation of the parallel flow assumption of boundary-layer theory which may be stated as the requirement that the ratio of the boundary-layer thickness, δ, to the radius of curvature of the trailing edge streamline, R, must remain small, i.e.,

$$\frac{\delta}{R} << 1.$$

However, if, due to an increase in the reduced frequency, the radius of curvature of the trailing edge streamline has become small enough to violate this condition then it appears that a decrease in the boundary-layer thickness (at constant reduced frequency) could result in the subsequent resatisfaction of the condition.

This parallel flow condition may be restated in terms of the important dimensionless variables of the problem, namely the reduced frequency,

$$k = \frac{\omega L}{U_\infty}$$

and the Reynolds number,

$$\mathrm{Re} = \frac{U_\infty L}{\nu}$$

It is well known that, in the laminar regime, the boundary-layer thickness is related to the Reynolds number by

$$\delta \propto \mathrm{Re}^{-1/2}.$$

In order to obtain a relation between the radius of curvature of the trailing edge streamline and the reduced frequency it will be assumed that the Euler equations in local cylindrical coordinates may be used [1] i.e.,

$$\frac{\partial u}{\partial t} + u\frac{\partial u}{\partial s} = -\frac{1}{\rho}\frac{\partial p}{\partial s}$$

and

$$\frac{\partial v}{\partial t} - \frac{u^2}{R} = \frac{-1}{\rho}\frac{\partial p}{\partial n}$$

where s and u are the coordinate and velocity along the streamline, n and v are the coordinate and velocity normal to the streamline and p is the pressure. If it is assumed that the pressure gradient normal to trailing edge streamline is small, which follows from the standard boundary-layer assumption or from the experimental data for the case of low reduced frequencies, then

$$R \cong \frac{u^2}{\partial v/\partial t}$$

Now if it is assumed that the velocity normal to the streamline, v, is sinusoidal and that the velocity along the streamline, u, is just a perturbation away from the freestream value then it is evident that

$$R \propto k^{-1}$$

Therefore the parallel flow assumption becomes

$$\frac{\delta}{R} = C\frac{k}{\mathrm{Re}^{1/2}} << 1$$

where the parameter, C, is independent of k. Based on this expression it appears that a quadrupling of the Reynolds number should result in a doubling of the reduced frequency which is attainable before the inviscid flow models are no longer applicable. Does the data of the authors support this hypothesis and do the authors plan any higher Reynolds number experiments in order to examine the effect of Reynolds number?

Additional Reference

1 Li, W. H., and S. H. Lam, *Principles of Fluid Mechanics*, Addison-Wesley Inc., Reading, Mass., 1964.

S. A. Kinnas.[3] First, I would like to congratulate the authors for such a fine piece of work. It is very useful for the hydronamicist to know how physical or nonphysical his assumptions are. Especially, for either steady or unsteady flows around hydrofoils it is well known that the Kutta condition is very important for the prediction of the pressure distributions and therefore forces and moments on the foil.

The authors present experimental evidence in support of the Giesing – Maskell condition at the trailing edge. They also give the range of the validity of that condition. They finally suggest a new similarity parameter rather than the commonly used reduced frequency in order to represent the local trailing edge flow. I read their work with great interest and I would like to make the following points:

1) How important is the geometry of the trailing edge? For example do the authors expect the same range of validity for the Giesing-Maskell condition for different sharp trialing edge angles? It is my intuition that the range of validity should be affected.

[1] By D. R. Poling and D. P. Telionis, published in the December 1987 issue of the JOURNAL OF FLUIDS ENGINEERING, Vol. 109.

[2] Manager, Theoretical Hydrodynamics, Gould Inc./Ocean Systems Division, Middletown, R.I. 02840.

[3] Research Engineer, Department of Ocean Engineering, M.I.T., Cambridge, Mass. 02139.

2) How does the steady loading and hence the steady value of circulation affect their conclusions?

3) Is there a similar investigation available for a hydrofoil subject to an incoming gust? In other words, are there any experimental results of the same sort as described in reference [2], but for a broader reduced frequency range? If yes, is the range of their parameter ℓ the same as for the pitching hydrofoil?

4) Is there any experimental evidence of the quasi-steady Kutta condition for low values of the reduced frequency? In other words have the authors observed if the wake indeed detaches from the trailing edge along the bisector line? This probably would not be important for the pressure distributions as shown in reference 6, but it would be nice to know.

Finally, I would like to encourage the authors in continuing working in this important field. I would like also to ask them to keep me updated on their work. We, at MIT, are working currently in developing an unsteady propeller panel code and we are very interested in their conclusions with regard to the unsteady Kutta condition.

Authors' Closure

Response of Authors to Comments of J. S. Ulmann

The discusser's argument is certainly valid. After all, the ultimate control of circulation rests upon viscosity. And it is at the trailing edge that for attached flow, viscosity influences the entire flow field. So indeed we anticipate that the range of the validity of the Giesing-Marskell condition should be a function of the Reynolds number. Unfortunately our experimental results are limited to Reynolds numbers of the order of 10^4.

Response of Authors to Comments of S. A. Kinnas

We feel that the geometry of the trailing edge should not affect the validity of the Giesing-Maskell condition. This condition is based on strong physical ground as discussed in detail in the references of the paper. The experimental results presented here verify the validity of the condition up to $l=0.32$. This parameter is defined on page 413 of the paper. We also feel that the radius of curvature as well should not affect the condition, as long of course as it is small.

We have run some experiments for an airfoil at a fixed angle of attack but immersed in a wavy stream, namely a stream with a nearly sinusoidal gust (see reference [2] in the paper). This is the case of finite steady or rather time-averaged loading. Once again it was determined that the Giesing-Maskell condition is satisfied. However, these data were confined to a narrower range of reduced frequencies.

There is ample pressure data supporting the classical Kutta condition for low reduced frequencies as referenced in our paper. To our knowledge though, no flow visualization is available for this case, and therefore there is no hard evidence that for steady or low-frequency oscillatory flow, the stagnation streamline bisects the trailing-edge angle.

It may be appropriate here to note that our Fig. 12 is perhaps the most interesting piece of flow visualization but in the final version of the paper, was reproduced very poorly. This is perhaps because it is a color print. We would be happy to share the original of our prints with anyone who expresses interest.

Erosion Due to Impingement of Cavitating Jet[1]

R. Balachandar.[2] Professors Yamaguchi and Shimizu are to be congratulated for this stimulating paper. The authors have presented a large quantity of experimental data from systematic tests. However, there are a few points which need further discussion.

(1) A rather interesting observation can be made from Fig. 17.[3] One notes that as L (distance between outlet edge of nozzle and specimen) increases, the weight loss increases. A maximum weight loss occurs at a critical value of L for a given set of inlet and outlet pressures. However, with a further increase in L, the weight loss decreases. This can possibly be explained as follows:

As L is increased, the time available for the bubbles to grow increases and larger bubbles impinge on the specimen surface rather explosively leading to increased damage. Beyond the critical value of L, though the time available for the bubbles to grow is large, the local pressures also drop and the bubbles impinge less explosively. This leads to reduced erosion. It would be interesting to realize why the weight loss values exhibit a peak for $L<15$ as in Fig. 8. Further, one notes from Fig. 12, that as P_d is gradually reduced, the weight loss increases and at a critical P_d the weight loss is maximum. A further decrease in P_d results in decreased damage. This observation is consistent with the behavior found from weight loss measurements conducted in cavitating venturi tunnels and rotating disk apparatus behind two-dimensional bluff bodies {21–23}. As one reduces the cavitation number of the flow, the zone enveloped by the bubbles will increase. This is somewhat similar to an increase in the length of cavity behind two-dimensional bluff bodies with a decrease in cavitation number. The bubble size will be larger and hence possess more damage potential. However, the other effect of reducing the cavitation number by reducing the pressure is to reduce the collapse pressure of the bubbles and therefore their ability to impact material damage is limited.

(2) It would be interesting to reanalyze the data by arranging the results in a suitable nondimensional form so as to eliminate size scale effects.

Additional References

21 Ramamurthy, A. S., and Bhaskaran, P., "Source Size and Frequency Effects on Cavitation Noise and Damage," ASME JOURNAL OF FLUIDS ENGINEERING, Vol. 97, No. 3, 1975, pp. 384–386.

22 Ramamurthy, A. S., and Bhaskaran, P., "Velocity Exponents for Cavitation Noise and Damage," ASME JOURNAL OF FLUIDS ENGINEERING, Vol. 101, No. 3, 1979, pp. 69–75.

23 Balachandar, R., Ranganathan, Y., and Ramamurthy, A. S., "Evaluation of Cavitation Damage Characteristics Using a Profilometer," Accepted for publication in the *Journal of Mech. Engg. Sci.*, Proc. of Inst. of Mech. Enggs. London, 1988.

Authors' Closure

The authors would like to express their gratitude to Dr. Balachandar for his discussion to the paper.

The mass loss had generally has two peaks as pointed out in the paper. For convenience the peak near the jet exit and other are designated the first peak and the second peak, respectively. The relationship between the mass loss and the stand-off distance depends on the configuration of the test cell as shown in Fig. 10. Recent experiments [24] show that it also depends

[1] By A. Yamaguchi and S. Shimizu, published in the December 1987 issue of the JOURNAL OF FLUIDS ENGINEERING, Vol. 109.

[2] Research Assistant, Department of Civil Engineering, Concordia University, Montreal, Quebec, Canada.

[3] Figures are as referred to in the paper.

2) How does the steady loading and hence the steady value of circulation affect their conclusions?

3) Is there a similar investigation available for a hydrofoil subject to an incoming gust? In other words, are there any experimental results of the same sort as described in reference [2], but for a broader reduced frequency range? If yes, is the range of their parameter ℓ the same as for the pitching hydrofoil?

4) Is there any experimental evidence of the quasi-steady Kutta condition for low values of the reduced frequency? In other words have the authors observed if the wake indeed detaches from the trailing edge along the bisector line? This probably would not be important for the pressure distributions as shown in reference 6, but it would be nice to know.

Finally, I would like to encourage the authors in continuing working in this important field. I would like also to ask them to keep me updated on their work. We, at MIT, are working currently in developing an unsteady propeller panel code and we are very interested in their conclusions with regard to the unsteady Kutta condition.

Authors' Closure

Response of Authors to Comments of J. S. Ulmann

The discusser's argument is certainly valid. After all, the ultimate control of circulation rests upon viscosity. And it is at the trailing edge that for attached flow, viscosity influences the entire flow field. So indeed we anticipate that the range of the validity of the Giesing-Marskell condition should be a function of the Reynolds number. Unfortunately our experimental results are limited to Reynolds numbers of the order of 10^4.

Response of Authors to Comments of S. A. Kinnas

We feel that the geometry of the trailing edge should not affect the validity of the Giesing-Maskell condition. This condition is based on strong physical ground as discussed in detail in the references of the paper. The experimental results presented here verify the validity of the condition up to $l=0.32$. This parameter is defined on page 413 of the paper. We also feel that the radius of curvature as well should not affect the condition, as long of course as it is small.

We have run some experiments for an airfoil at a fixed angle of attack but immersed in a wavy stream, namely a stream with a nearly sinusoidal gust (see reference [2] in the paper). This is the case of finite steady or rather time-averaged loading. Once again it was determined that the Giesing-Maskell condition is satisfied. However, these data were confined to a narrower range of reduced frequencies.

There is ample pressure data supporting the classical Kutta condition for low reduced frequencies as referenced in our paper. To our knowledge though, no flow visualization is available for this case, and therefore there is no hard evidence that for steady or low-frequency oscillatory flow, the stagnation streamline bisects the trailing-edge angle.

It may be appropriate here to note that our Fig. 12 is perhaps the most interesting piece of flow visualization but in the final version of the paper, was reproduced very poorly. This is perhaps because it is a color print. We would be happy to share the original of our prints with anyone who expresses interest.

Erosion Due to Impingement of Cavitating Jet[1]

R. Balachandar.[2] Professors Yamaguchi and Shimizu are to be congratulated for this stimulating paper. The authors have presented a large quantity of experimental data from systematic tests. However, there are a few points which need further discussion.

(1) A rather interesting observation can be made from Fig. 17.[3] One notes that as L (distance between outlet edge of nozzle and specimen) increases, the weight loss increases. A maximum weight loss occurs at a critical value of L for a given set of inlet and outlet pressures. However, with a further increase in L, the weight loss decreases. This can possibly be explained as follows:

As L is increased, the time available for the bubbles to grow increases and larger bubbles impinge on the specimen surface rather explosively leading to increased damage. Beyond the critical value of L, though the time available for the bubbles to grow is large, the local pressures also drop and the bubbles impinge less explosively. This leads to reduced erosion. It would be interesting to realize why the weight loss values exhibit a peak for $L<15$ as in Fig. 8. Further, one notes from Fig. 12, that as P_d is gradually reduced, the weight loss increases and at a critical P_d the weight loss is maximum. A further decrease in P_d results in decreased damage. This observation is consistent with the behavior found from weight loss measurements conducted in cavitating venturi tunnels and rotating disk apparatus behind two-dimensional bluff bodies {21–23}. As one reduces the cavitation number of the flow, the zone enveloped by the bubbles will increase. This is somewhat similar to an increase in the length of cavity behind two-dimensional bluff bodies with a decrease in cavitation number. The bubble size will be larger and hence possess more damage potential. However, the other effect of reducing the cavitation number by reducing the pressure is to reduce the collapse pressure of the bubbles and therefore their ability to impact material damage is limited.

(2) It would be interesting to reanalyze the data by arranging the results in a suitable nondimensional form so as to eliminate size scale effects.

Additional References

21 Ramamurthy, A. S., and Bhaskaran, P., "Source Size and Frequency Effects on Cavitation Noise and Damage," ASME JOURNAL OF FLUIDS ENGINEERING, Vol. 97, No. 3, 1975, pp. 384–386.

22 Ramamurthy, A. S., and Bhaskaran, P., "Velocity Exponents for Cavitation Noise and Damage," ASME JOURNAL OF FLUIDS ENGINEERING, Vol. 101, No. 3, 1979, pp. 69–75.

23 Balachandar, R., Ranganathan, Y., and Ramamurthy, A. S., "Evaluation of Cavitation Damage Characteristics Using a Profilometer," Accepted for publication in the *Journal of Mech. Engg. Sci.*, Proc. of Inst. of Mech. Enggs. London, 1988.

Authors' Closure

The authors would like to express their gratitude to Dr. Balachandar for his discussion to the paper.

The mass loss had generally has two peaks as pointed out in the paper. For convenience the peak near the jet exit and other are designated the first peak and the second peak, respectively. The relationship between the mass loss and the stand-off distance depends on the configuration of the test cell as shown in Fig. 10. Recent experiments [24] show that it also depends

[1] By A. Yamaguchi and S. Shimizu, published in the December 1987 issue of the JOURNAL OF FLUIDS ENGINEERING, Vol. 109.

[2] Research Assistant, Department of Civil Engineering, Concordia University, Montreal, Quebec, Canada.

[3] Figures are as referred to in the paper.

on the test liquid. The experiments in hydraulic oil conducted by using apparatus 2 with nozzle holder A show that the mass loss has only one peak and the stand-off distance to give the maximum mass loss corresponds to the second peak of HWBF. Dr. Balachandar's explanations on the effects of the stand-off distance and P_d seems to be appropriate when the stand-off distance is relatively large. However, when the stand-off distance is relatively small, the effect of the pressure distribution in the impingement region on cavity behavior becomes important. Because of this reason, there exists a complex relationship between the mass loss and P_d as shown in Figs. 11 and 12 for $L = 10$ mm and 12.5 mm.

The mechanism of erosion due to impingement of cavitating jet has not yet been sufficiently clarified. Further work to clarify scale effect is necessary.

Additional Reference

24 S. Shimizu, and A. Yamaguchi, Cavitation Erosion in Hydraulic Oil, HWCFs, and Tap Water, unpublished.

Temperature Effects on Single Bubble Collapse and Induced Impulsive Pressure[1]

F. G. Hammitt.[2] Paper deals with the very interesting problem of effects of water temperature on vibratory cavitation damage, which conventionally maximizes roughly midway between freezing and boiling points of any liquid yet tested.

Present tests were at constant liquid pressure. However, we (U-M) and others find approximately the same thing happens for constant suppressure pressure (i.e., NPSH) tests rather than constant pressure.[3]

Paper's new measurements of bubble shapes and impulsive wall pressure add very valuable new information to this highly complex problem, and should help considerably in its more complete understanding. Also the use of Schleiren pictures is valuable.

Authors' Closure

The authors wish to express their thanks to Professor Hammitt for his valuable discussion to our paper. In the present paper, we have made an experimental investigation of the temperature effects on the single bubble collapse and the induced impulsive pressure at constant liquid pressure. Viewing that vibratory cavitation damage is closely related with the collapse of a bubble cluster, it must be significantly influenced by not only the liquid temperature effect but also the suppression pressure effect, as you pointed out. The finding that the damage rate indicates a maximum for the both effects, suggests that number and size of bubbles as well as surrounding pressure vary with those effects. We examined here only one effect of the liquid temperature. However, we are now planning a systematic investigation of two bubbles in water at various temperatures and pressures, which is a basic problem of multi-bubble system.

[1] By A. Shima, Y. Tomita, and T. Ohno published in the June 1987 issue of the JOURNAL OF FLUIDS ENGINEERING, Vol. 110, pp. 194–199.

[2] Professor Emeritus, Department of Mechanical Engineering, The University of Michigan, Ann Arbor, Mich. 48109-1221.

[3] F. G. Hammit, *Cavitation and Multiphase Flow Phenomenon*, McGraw-Hill, 1980.

on the test liquid. The experiments in hydraulic oil conducted by using apparatus 2 with nozzle holder A show that the mass loss has only one peak and the stand-off distance to give the maximum mass loss corresponds to the second peak of HWBF. Dr. Balachandar's explanations on the effects of the stand-off distance and P_d seems to be appropriate when the stand-off distance is relatively large. However, when the stand-off distance is relatively small, the effect of the pressure distribution in the impingement region on cavity behavior becomes important. Because of this reason, there exists a complex relationship between the mass loss and P_d as shown in Figs. 11 and 12 for $L = 10$ mm and 12.5 mm.

The mechanism of erosion due to impingement of cavitating jet has not yet been sufficiently clarified. Further work to clarify scale effect is necessary.

Additional Reference

24 S. Shimizu, and A. Yamaguchi, Cavitation Erosion in Hydraulic Oil, HWCFs, and Tap Water, unpublished.

Temperature Effects on Single Bubble Collapse and Induced Impulsive Pressure[1]

F. G. Hammitt.[2] Paper deals with the very interesting problem of effects of water temperature on vibratory cavitation damage, which conventionally maximizes roughly midway between freezing and boiling points of any liquid yet tested.

Present tests were at constant liquid pressure. However, we (U-M) and others find approximately the same thing happens for constant suppressure pressure (i.e., NPSH) tests rather than constant pressure.[3]

Paper's new measurements of bubble shapes and impulsive wall pressure add very valuable new information to this highly complex problem, and should help considerably in its more complete understanding. Also the use of Schleiren pictures is valuable.

Authors' Closure

The authors wish to express their thanks to Professor Hammitt for his valuable discussion to our paper. In the present paper, we have made an experimental investigation of the temperature effects on the single bubble collapse and the induced impulsive pressure at constant liquid pressure. Viewing that vibratory cavitation damage is closely related with the collapse of a bubble cluster, it must be significantly influenced by not only the liquid temperature effect but also the suppression pressure effect, as you pointed out. The finding that the damage rate indicates a maximum for the both effects, suggests that number and size of bubbles as well as surrounding pressure vary with those effects. We examined here only one effect of the liquid temperature. However, we are now planning a systematic investigation of two bubbles in water at various temperatures and pressures, which is a basic problem of multi-bubble system.

[1] By A. Shima, Y. Tomita, and T. Ohno published in the June 1987 issue of the JOURNAL OF FLUIDS ENGINEERING, Vol. 110, pp. 194–199.

[2] Professor Emeritus, Department of Mechanical Engineering, The University of Michigan, Ann Arbor, Mich. 48109-1221.

[3] F. G. Hammit, *Cavitation and Multiphase Flow Phenomenon*, McGraw-Hill, 1980.

